COPPE
Instituto Alberto Luiz Coimbra de Pós-Graduação e Pesquisa de Engenharia
UFRJ

CHROMATOGRAPHIC SEPARATION OF PRAZIQUANTEL RACEMATE USING SIMULATED MOVING BED: FROM UNIT DESIGN TO DYNAMIC STUDIES WITH ONLINE MEASUREMENTS

Felipe Coelho Cunha

Tese de Doutorado apresentada ao Programa de Pós-graduação em Engenharia Química, COPPE, da Universidade Federal do Rio de Janeiro, como parte dos requisitos necessários à obtenção do título de Doutor em Engenharia Química.

Orientadores: Amaro Gomes Barreto Jr.
Argimiro Resende Secchi
Maurício Bezerra de Souza Jr.

Rio de Janeiro
Maio de 2021

CHROMATOGRAPHIC SEPARATION OF PRAZIQUANTEL RACEMATE USING SIMULATED MOVING BED: FROM UNIT DESIGN TO DYNAMIC STUDIES WITH ONLINE MEASUREMENTS

Felipe Coelho Cunha

TESE SUBMETIDA AO CORPO DOCENTE DO INSTITUTO ALBERTO LUIZ COIMBRA DE PÓS-GRADUAÇÃO E PESQUISA DE ENGENHARIA DA UNIVERSIDADE FEDERAL DO RIO DE JANEIRO COMO PARTE DOS REQUISITOS NECESSÁRIOS PARA A OBTENÇÃO DO GRAU DE DOUTOR EM CIÊNCIAS EM ENGENHARIA QUÍMICA.

Orientadores: Amaro Gomes Barreto Jr.
Argimiro Resende Secchi
Maurício Bezerra de Souza Jr.

Aprovada por: Prof. Amaro Gomes Barreto Jr.
Prof. Argimiro Resende Secchi
Prof. Maurício Bezerra de Souza Jr.
Prof. Príamo Albuquerque Melo Junior
Prof. André Luiz Hemerly Costa
Profa. Diana Cristina Silva de Azevedo

RIO DE JANEIRO, RJ – BRASIL
MAIO DE 2021

Cunha, Felipe Coelho

Chromatographic separation of praziquantel racemate using Simulated Moving Bed: from unit design to dynamic studies with online measurements/Felipe Coelho Cunha. – Rio de Janeiro: UFRJ/COPPE, 2021.

XXIII, 166 p.: il.; 29, 7cm.

Orientadores: Amaro Gomes Barreto Jr.
Argimiro Resende Secchi
Maurício Bezerra de Souza Jr.

Tese (doutorado) – UFRJ/COPPE/Programa de Engenharia Química, 2021.

Referências Bibliográficas: p. 93 – 104.

1. Chromatography continuous process. 2. Simulated Moving Bed. 3. Praziquantel. 4. Online measurement. 5. Process dynamics. I. Barreto Jr., Amaro Gomes *et al.* II. Universidade Federal do Rio de Janeiro, COPPE, Programa de Engenharia Química. III. Título.

"You cannot step into the same river twice, for other waters are continually flowing on."
Heraclitus of Ephesus
(c.535-c.475 BC)

Acknowledgments

First of all, I would like to thanks my wife and my son. They are part of me, and without them, the way should be less colorful and less motivating. Helga and Thor, I love both of you.

My mom and dad, who are also responsible for this work, thank you very much. Without them, the chances to make this work should be at least smaller.

I would like to thanks my brother, Guilherme; we lived great moments together throughout our lives. Special thanks to his daughter, Chloé, who I still do not know, but I look forward to knowing her.

To my friends from LABCADS: Rafael, Torraca (the pokemon hunter) and Reinaldo. There is still one friend that deserves a memorable line, Rômulo Holanda; he was my right-hand man, whom I came up to be an advisor in his undergraduate final project; thank you so much!

All teachers and professors I had all my life shared with me, the most powerful tool ever: **knowledge**. Special thanks to my advisors Amaro, Argimiro and Maurício.

To the CNPQ and my wife again, for the financial support, thank you very much.

Resumo da Tese apresentada à COPPE/UFRJ como parte dos requisitos necessários para a obtenção do grau de Doutor em Ciências (D.Sc.)

SEPARAÇÃO CROMATOGRÁFICA POR LEITO MÓVEL SIMULADO DE RACEMATO DE PRAZIQUANTEL: DO PROJETO DA UNIDADE AOS ESTUDOS DINÂMICOS COM MEDIÇÕES ONLINE

Felipe Coelho Cunha

Maio/2021

Orientadores: Amaro Gomes Barreto Jr.
Argimiro Resende Secchi
Maurício Bezerra de Souza Jr.

Programa: Engenharia Química

Este trabalho estudou o processo de separação por cromatografia contínua conhecido como Leito Móvel Simulado (LMS) com o intuito de separar a mistura racêmica de praziquantel (PZQ), utilizada no combate à esquistossomose. A unidade de LMS construída foi validada e comparada com as encontradas na literatura para a separação do racemato de praziquantel. Cinco dos oito parâmetros de desempenho da unidade construída foram superiores aos encontrados na literatura, apesar da concentração de alimentação de praziquantel ser, aproximadamente, 10 vezes inferior ao utilizado pela literatura. Além disso, a atual unidade foi capaz de atingir o estado estacionário cíclico 10 vezes mais rápido. Na medição em linha de concentração com o equipamento *chiral detector* (JASCO modelo CD-2095) foi observado absorção não-linear dos sinais de ultravioleta-vis e dicroísmo circular até mesmo em misturas com baixa concentração, e o modelo empírico utilizado apresentou bom ajuste. A partir de experimentos em malha aberta, com o equipamento *chiral detector* acoplado à unidade de LMS, concluiu-se que: (1) um degrau na concentração de alimentação revelou que a influência dos tubos, válvulas e bombas presentes na unidade entre as colunas cromatográficas tiveram como principal consequência um atraso nas concentrações de saída, enquanto que os efeitos cinéticos puderam ser desprezados e (2) os degraus aplicados nas vazões volumétricas revelaram a importância de incluir no modelo matemático as flutuações inerentes aos experimentos realizados.

Abstract of Thesis presented to COPPE/UFRJ as a partial fulfillment of the requirements for the degree of Doctor of Science (D.Sc.)

CHROMATOGRAPHIC SEPARATION OF PRAZIQUANTEL RACEMATE USING SIMULATED MOVING BED: FROM UNIT DESIGN TO DYNAMIC STUDIES WITH ONLINE MEASUREMENTS

Felipe Coelho Cunha

May/2021

Advisors: Amaro Gomes Barreto Jr.
Argimiro Resende Secchi
Maurício Bezerra de Souza Jr.

Department: Chemical Engineering

This work studied a continuous chromatographic separation process known as Simulated Moving Bed (SMB) aiming the separation of the racemic mixture of praziquantel (PZQ). This racemate is primarily used to fight against schistosomiasis. The built-in-house SMB unit was validated and compared to that of the literature about concerning the praziquantel separation. Five of the eight performance parameters were superior to those in the literature, despite the feed-concentration of praziquantel being approximately ten times lower. Its dynamics was, approximately, ten times faster than those. Nonlinear absorption of ultraviolet-vis and circular dichroism signals were observed in the concentration measurement with the *chiral detector* equipment (JASCO model CD-2095), even in mixtures with low concentrations, however, the empirical model used showed a good fit. Based on an experimental open-loop study, with the *chiral detector* equipment coupled to the SMB unit, the following conclusions can be presented: (1) A step-change in the feed concentration revealed that the influence of the pumps, valves, and pipes located in between the columns had as a consequence a time lag to be accounted in future mathematical models, while their kinetic effects in the built-in-house SMB could be neglected and (2) A step-change in some volumetric flow rates revealed the importance to include in the mathematical model the fluctuations inherent to the experiments carried out.

Contents

List of Figures

List of Tables

List of Symbols

Γ	Metric used to compare experimental and simulated ϕ, p. 72
Ω	Total subset, p. 55
Ω^{cal}	Calibration set, p. 55
Ω^{mix}	Subset of mixed enantiomers, p. 55
Ω^{pur}	Subset of pure enantiomers, p. 55
Ω^{val}	Validation set, p. 55
α	Mass transfer units number, p. 30
β_k	Constraint to be satisfied for each zone, p. 14
ϵ_t	Total porosity, p. 23
ϵ_{int}	Interstitial porosity, p. 13
γ	Root of Sum of Squared Residuals, p. 39
$\lambda_{k,q}$	Parameters associated to UV signal equation, p. 55
ω	Element representing the pair of signals and pair of enantiomer concentrations, p. 140
ϕ	Slope of the line drawn near the inflection point in the dynamic part of the curve, p. 72
$\psi_{k,q}$	Parameters associated to CD signal equation, p. 55
ζ_F	smaller root of the quadratic equation, p. 16
ζ_G	bigger root of the quadratic equation, p. 16
b	Adsorption interaction constant, p. 16
q_m	Maximum adsorption capacity, p. 16

A_L	Left-circularly polarized light, p. 51
A_R	Right-circularly polarized light, p. 51
$A_{i,j}$	*van Deemter* parameter for component i and column j, p. 42
C_F	Feed concentration, p. 16
$C_{i,j}$	*van Deemter* parameter for component i and column j, p. 42
C	Concentration of enantiomer, p. 33
D_{axial}	Axial diffusion coefficient, p. 23
DC	Desorbent consumption, p. 35
HETP	Height Equivalent to a Theoretical Plate, p. 27
H	Henry constant, p. 13
N_{column}	Number of columns, p. 35
N	Number of theoretical plates, p. 27
Pe	*Péclet* number, p. 30
Pr	Productivity, p. 35
Pur	Optical purity, p. 35
Q_D	Desorbent volumetric flow rate, p. 14
Q_F	Feed volumetric flow rate, p. 14
Q_R	Raffinate volumetric flow rate, p. 14
Q_X	Extract volumetric flow rate, p. 14
Q_j	Volumetric flow rate of the liquid phase for each zone, p. 13
Q_s	Cross section area, p. 13
Q_{solid}	Volumetric flow rate of the solid phase in the TMB, p. 13
Rec	Recovery, p. 35
Res	Residuals between observed and simulated data, p. 60
S_{CD}	Circular dichroism signal obtained from *Chiral Detector equipment*, p. 55

S_{UV}	Ultraviolet-visible signal obtained from *Chiral Detector equipment*, p. 55
V_{column}	Chromatographic column volume, p. 25
A or D	Dextropraziquantel, p. 8
B or L	Levopraziquantel, p. 8
L	Chromatographic column length, p. 13
i	Refers to component A or B, p. 23
j	Refers to SMB chromatographic column, p. 13
k	Refers to SMB zone, p. 12
k	k power of the L-PZQ concentration, p. 55
out	Refers to outlet stream, p. 35
q	q power of the D-PZQ concentration, p. 55
r	Refers to the elements composing the subset of mixed enantiomers, p. 55
sim	Refers to the simulated data, p. 39
s	Refers to the switching time interval, p. 33
y	Counter for switching time, p. 36
g	G-factor or anisotropy factor, p. 51
k_{eff}	Effective mass transfer coefficient, p. 23
m_k	Flow rate ratio for each zone, p. 14
m_{ads}	Adsorvent mass, p. 20
q_e	Concentration in equilibrium with the solid phase, p. 43
q	Mass concentration in the adsorbed-phase, p. 36
t_i	Retention time of component i, p. 25
t_o	Dead time, p. 23
$t_{d,R}$	Dead time value in the raffinate, p. 76

$t_{d,X}$	Dead time value in the extract, p. 76
t_{switch}	Switching time, p. 13
t	Time, p. 36
u_m	Effective velocity, p. 36
u_{int}	Interstitial velocity, p. 12
u_{solid}	Solid velocity in the TMB, p. 12

List of Abbreviations

CD	Circular Dichroism, p. 50
CSP	Chiral Stationary Phase, p. 19
CSS	Cyclic Steady State, p. 12
D-PZQ	Dextropraziquantel, p. 4
HPLC	High Performance Liquid Chromatography, p. 7
L-PZQ	Levopraziquantel, p. 4
MCTA	Microcrystalline Cellulose TriAcetate, p. 19
MSE	Mean Square Error, p. 58
NMPC	Nonlinear Model Predictive Control, p. 18
NTD	Neglected Tropical Diseases, p. 1
PC	Preventive Chemotherapy, p. 2
PZQ	Praziquantel, p. 2
RSSR	Root of Sum of Squared Residuals, p. 39
SMB	Simulated Moving Bed, p. 5
TMB	True Moving Bed, p. 6
TTBB	1,3,5-tri-*tert*-butylbenzene, p. 19
UV	Ultraviolet, p. 20
WHO	World Health Organization, p. 1
ee	Enantiomeric excess, p. 51

Chapter 1

Introduction

1.1 Contextualization

Neglected Tropical Diseases (NTDs) are a set of contagious diseases that have been causing suffering and death to many people worldwide, specially those from low-income countries. NTDs are responsible for around 534,000 death worldwide every year, and individuals are usually contaminated by two or more NTDs [3]. The World Health Organization (WHO) estimates that these diseases can be found in around 149 countries, affecting more than one billion people nowadays [4]. They are neglected because most developed countries have already vanished them from their territories, while in undeveloped countries (most of them situated in tropical and subtropical areas), NTDs are still an open issue. Furthermore, in these tropical and subtropical countries, usually, the most impoverished areas are seriously affected. The well-known physical and emotional injuries caused to people are strictly related to bad side effects to the economy of the affected countries, as they directly influence a person's ability to work properly, keep children out of school, and so forth [3].

Schistosomiasis is one of the most well-known NTDs, and it has infected human being at least for four millennia, as some schistosomiasis' eggs were found in Egyptian mummies (3,000 years ago) and Chinese mummies (2,100 years ago) [5]. This disease is endemic, and it is caused by parasitic helminths of the family *Schistosomatidae* (and genus *Schistosoma*) conditioned to the presence of snails (intermediate hosts) of aquatic habits (genus *Biomphalaria*) [5, 6]. The symptoms are related to worms' eggs deposited in intestinal or urogenital parts of the human body; it depends on each species. Intestinal ones in advanced cases could promote the liver and spleen enlargement and hypertension of the abdominal blood vessels. At the same time, urogenital ones in advanced cases can cause fibrosis of the bladder, and ureter and the kidney can also be damaged. Bladder cancer and infertility could be later complications too [7]. There are also evidences that urogenital schistosomiasis

has a relationship with HIV infection [8]. This disease has been making about 207 million people suffer daily (approximately 90% of those infected are Africans) [3].

The regular treatment recommended by WHO is not focused on individual treatment; it is focused on collective treatment, called "preventive chemotherapy" (PC). Once a risk area is identified, all humans in this area need to be medicated, and the frequency it happens is related to the number of school-age children living in this area. PC seems to be an excellent alternative to individual ones because gives a more practical and faster solution to cover more significant at-risk areas. It is important to emphasize that in most affected countries, the healthcare system is inadequate to promote individual diagnosis efficiently. Countries like China and Egypt have adopted preventive chemotherapy, and good results have been achieved [9]. This large-scale control is possible thanks to praziquantel (PZQ), which is used to treat all forms of schistosomiasis safely and effectively. Besides all sense of urgency, until 2009, only 7% of the affected population was adequately treated in Africa [9], for instance, Nigeria had about 64 million people (24% of the population) requiring preventive chemotherapy, and Ethiopia had about 23 million people (9% of the population) in 2014 [10]. Nigeria and Ethiopia, for instance, have a significant proportion of school-age children (between 5 and 14 years old) indicated to require PC, Nigeria almost 100% and Ethiopia approximately 50 % of them.

In November 2016, a three-day meeting promoted by WHO at Geneva came up with discussions related to offering regular treatment to at least 75% of the world's pre-school and school-aged children contaminated by schistosomiasis and soil-transmitted helminthiases. One of the topics debated among specialists was how to find ways to stimulate medicine production proportionally to current demand [11]. WHO has been acting in the international scenario to increase the access to PZQ sufficient to treat about 100 million children of school-aged per year; this is a very ambitious plan. An average treatment is estimated to cost US$ 0.20 - 0.30 per person per year [9]. Therefore, treating 100 million children would cost US$ 30,000,000/year. If a comparison is made between this cost and the global sales of the pharmaceutical industry in 2008 (US$ 773 billion) [12], the conclusion is: the costs to treat 100 million children is just 0.004% of the global sales. It helps to understand why private companies are not interested in producing and developing medicines against schistosomiasis; this market is not profitable to them. One could think, the affected countries should develop their medicines trying to solve their problems. Nevertheless, it is a fact that the pharmaceutical industry is an R&D (research and development) intensive industry. It requires a high level of qualification of their professionals and government priority and compromises to assume this task should be strictly necessary, as private companies will not assume it. Unfortunately, most of the time, both facts are not accomplished in undeveloped countries. However, there

are few exceptions. For instance, one of the most promising research was developed by FIOCRUZ (Fundação Oswaldo Cruz) in Brazil, where a vaccine development has been making progress and has just begun phase II of tests. The reader could find more information on reference [13].

Schistosomiasis in Brazil

There were about 1,500,000 people (almost 100% of them are school-aged children) living at-risk areas in 2014. According to WHO [14], Brazil has adopted individual diagnosis as a regular treatment, instead of the indicated preventive chemotherapy. Brazil is one of the two countries in the Americas indicated to this treatment; the other one is Venezuela [14]. In 2010, only approximately 39,800 people were treated for schistosomiasis. Although statistical numbers are from different years (2010 and 2014), they evidence the great urgency to raise the number of people being treated for schistosomiasis in Brazil.

1.1.1 Praziquantel enantiomers

Praziquantel is anthelminthic against a broad spectrum of parasitic trematodes and cestodes [15]. Thanks to this particular feature, this substance is included in the "WHO Model List of Essential Medicines" [16]. However, its administration is oral (*i.e.*, tablet form). Unfortunately, tablet form does not include all groups of humans in the regular treatment. Pre-school aged children (under five years of age) are not able to swallow these tablets, leading, therefore, to the discontinuation of this treatment. Under the current policy, these children have been treated just into primary school (up to 6 years of age) [17]. Furthermore, Bustinduy *et al.* [18] found that higher doses of praziquantel are required to treat pre-school aged children (>60 mg/kg), while the adequated doses for adults is about 40 mg/kg. Regular commercial tablets contain the racemic mixture [19], in which levopraziquantel (L-PZQ) is the active principle, while the dextropraziquantel (D-PZQ) is not, and, moreover, the latter is much bitter than the former [20]. Therefore, just half of the mass of the commercial tablets are composed of the active ingredient, and they can not be chewed. Research is still in progress to generate a pioneering medicine to fight against many parasitic diseases mainly using racemates (*e.g.*, capsules), or L- and D-PZQ in different proportions (*e.g.*, orally dispersible tablets). The former focus on the encapsulation of the praziquantel racemate [21–24] and the latter focus on orally dispersible tablets with one-fourth the size of commercial ones, the tablets are under development by a public-private cooperation called *Pediatric Praziquantel Consortium*, in which the main goal is a tablet richer in the L-PZQ [25]. Despite the big issue involving pre-school aged children, worms resistant to the traditional

active principle are raising concern too [26–30].To overcome this issue new molecular formulas have been studied, using the praziquantel racemate (rac-PZQ) as starting point. Synthesis of PZQ derivatives can be primarily found in the literature [31–33]; modifications of PZQ molecules aiming to kill juvenile worms are also a concern [34–36]. These promising study areas use rac-PZQ, which indicates that studies using optically pure L-PZQ should be a suitable area to be explored. Regardless of L-PZQ importance, optically pure D-PZQ has its importance in developing chemical routes aiming at racemization [37]. Unfortunately, current chemical routes are ineffective in addressing large-scale production and more studies are needed, which will demand optically pure D-PZQ. Further interests in the optically pure enantiomers are studies of the mechanism of PZQ action against *Schistosoma* bodies, in order to better understand the phenomena involving parasites and PZQ, like the resistance of the formers to the latter [26, 27, 36, 38, 39]. Summing up, the pure enantiomers have their importance in different researches involving PZQ studies and those are not available nowadays because separation is expensive, thanks to a lack of efficient separation processes.

The depicted scenario requires a solution involving multidisciplinary groups of professionals (*i.e.*, pharmaceuticals, engineers, politicians, physicians, and so forth). The present work is included on a broader project formed by multidisciplinary professionals, aiming to develop a medicine that could help millions of children around the world to fight against one of the most disseminated diseases in undeveloped countries, schistosomiasis. That project involves three Brazilian institutions (School of Chemistry/UFRJ, Chemical Engineering Program/COPPE/UFRJ, and FIOCRUZ).

1.2 Objectives

1.2.1 Main Objective

The separation itself is not the biggest challenge, but a separation of the racemic mixture on a large scale and at the same time minimizing cost and maximizing profit and yield is the biggest challenge. As it will be formally presented later (Chapter 2), the chromatographic process used to separate the racemic mixture of PZQ has some particular features like long time delays, distributed parameters, and mixed discrete and continuous time. These characteristics make the SMB dynamics peculiar, and studying its dynamics is fundamental for further studies taking into account control issues. Therefore, the main objective can be formally presented as:

- Study of the dynamic behavior of a Simulated Moving Bed (SMB) semi-preparative unit and proposal of an online concentration measurement system

for enantiomers in the outlet streams.

1.2.2 Specific Objectives

Aiming to accomplish the main objective, the specific objectives are:

1. Design and construction of a real SMB chromatographic unit in a semi-preparative scale;
   (a) Basic project (using AutoCad®);
   (b) Detailed project;
   (c) Executive project:
      i. Assembly of the equipment, tubing and skid;
      ii. Supervisory system (using LabView®); and
2. Validation of the actual SMB unit;
3. *Chiral detector* equipment calibration;
4. Coupling the SMB unit with the *Chiral detector* equipment; and
5. Study of the system dynamics, by introducing disturbances and comparing experimental with simulated responses.

1.3 Document arrangement

This document is arranged into 5 chapters, bibliographic references, and 11 appendices.

- **Chapter 1**: the first part provides a brief and general contextualization of this work, to answer the following question: what is this work for? The second part gives shortly the main objective and the specific objectives related to it. Finally, this third part serves as a summary extension, which introduces the main features of each chapter presented in this thesis, providing the reader with more information than the "Contents" part does. Serving, therefore, as a helpful shortcut to getting the issue of interest;
- **Chapter 2**: the main concepts related to chromatography and SMB are presented. The SMB is presented, making analogies between the SMB and the TMB (True Moving Bed) process. The main results of this chapter are: (1) experimental determination of the main chromatographic column parameters,

(2) first experiments using the new SMB unit to validate it, (3) comparison to other PZQ separations using SMB in literature and (4) fine adjustment of zone-2 flow rate with the help of simulations using software developed in our group. Part of the content of this chapter was published in the *Chirality* journal [40] and another article is being written including more details about the SMB unit automation (see Appendix K);

- **Chapter 3**: the *chiral detector* equipment was calibrated with pure enantiomers and mixed enantiomers and, right after a validation procedure was executed using just the mixing solutions. The method used to calibrate and validate the empirical models was the **L**eave-**O**ne-**O**ut **C**ross-**V**alidation (LOOCV). The content of this chapter was published in the Journal of *Spectrochimica Acta Part A: Molecular and Biomolecular Spectroscopy* [41];

- **Chapter 4**: the results coming from the previous chapters served as a basis for the generation and discussion of the results obtained in the coupling of the SMB unit and the *chiral detector* equipment. Step changes in flow rates delivered by pumps were the perturbation applied;

- **Chapter 5**: this chapter collects all the conclusions, which came up from the discussion of the previous chapters.

Chapter 2

SMB Chromatographic Process

This chapter provides the main concepts involving SMB process and its use to separate praziquantel racemate. After that, the materials and methodology were presented. The latter contains the chromatographic column characterization and how the SMB experiments were carried out. In the results and discussion section, the calculated parameters of the chromatographic columns are shown. The region of operation of the isotherm was determined, and PZQ separation using the chiral stationary phase (CSP) of Chiralcel^{TM} OZ was compared to other CSPs in the literature.

2.1 Main SMB concept

The High-Performance Liquid Chromatography (HPLC) is also known as elution chromatography. It consists of injecting at the column's inlet a feed solution that will be carried throughout the column by a pumped solvent. Thanks to different thermodynamic interactions, the solutes present in the feed solution will move with different velocities inside the column. As a consequence, in diluted concentrations, separation of the substances will take place. The pure solutes could be obtained if flasks were placed sequentially at the column outlet. This is a straightforward process, but, unfortunately, it is very limited too. As mentioned, the feed solution needs to be injected as a pulse, which provides just a minor contact between the solid and liquid phase, and, worse, the contact between phases decreases as the injected mass flows along the column. Decreasing, consequently, the efficiency of the process. This explains why HPLC is commonly used just for analytical purposes.

Fortunately, in 1961, Donald Broughton and Clarence Gerhold invented an interesting process [42], which combined the HPLC concept and the efficiency of a counter-current process. Nowadays, this sort of process is the so-called *Simulated Moving Bed* (SMB) Chromatography.

Instead of explaining the SMB process, in which the solid phase does not move, a

similar, however idealized, process will be introduced first. Its name is *True Moving Bed* (TMB). The word "True" means a hypothetical motion of the solid phase [1]. At first, it will be idealized a column in a circle format, and the solid phase could be put into perpetual motion. Furthermore, this round column has two outlet streams and two inlet streams (see Figure 2.1a). One of the inlets adds pure solvent (also called desorbent or eluent), and the other inlet adds the feed solution (A + B). One of the outlets withdraws the extracted solute, while the other one the raffinated solute. It is not difficult to identify two extreme situations in the TMB process. They are:

1. **First extreme situation**: if the solid motion is too fast, all solutes are going to be carried out together in the same direction of the solid phase.

2. **Second extreme situation**: if liquid motion is too fast, all solutes are going to be carried out together in the same direction of the liquid phase.

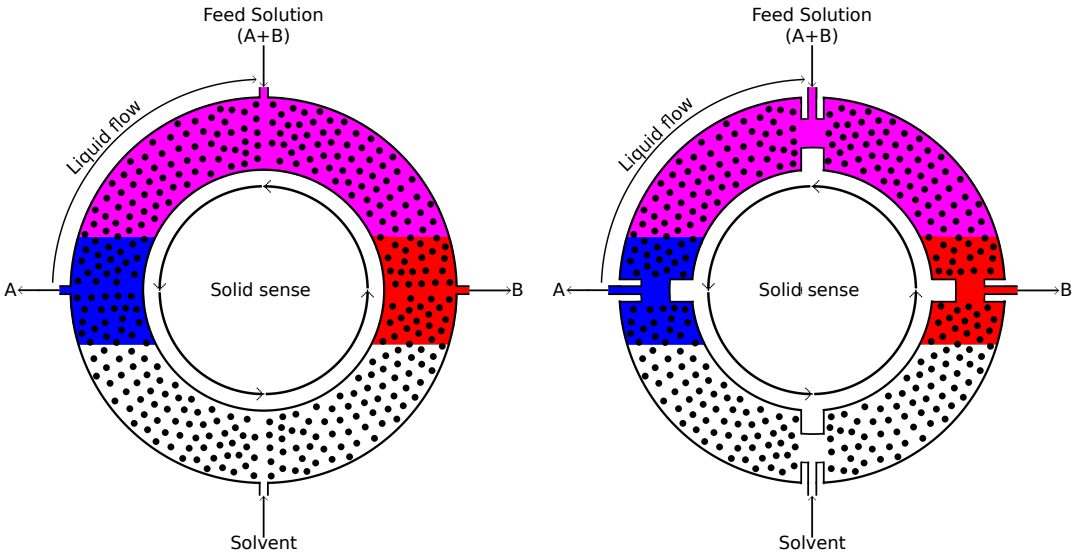

(a) One circular column (b) Four curved columns

Figure 2.1: Idealized True Moving Bed (TMB).

At this point, it is easy to understand that the desired situation lies in between these two extreme scenarios. In Figure 2.1a, this desired scenario is illustrated, where one of the solutes (more retained by the solid phase) is carried by the solid phase and the other solute (less retained by the solid phase) by the liquid phase. By appropriate adjustment of flow rates, it is possible to collect one of the solutes (A) in the extract outlet and the other one (B) in the raffinate outlet. Now following the steps right below, it is possible to go from the hypothetical TMB to the true SMB:

[1] Many inconvenient come from the solid motion, for instance, increase in pressure drop, extract stream contamination by the solid phase, etc. [43].

1. the single circular column is divided into four "curved" columns, and the inlets and outlets are situated in between the columns (Figure 2.1b);

2. "the curved" columns now are represented by rectangular columns illustration (change from Figure 2.1b to Figure 2.2a); and

3. hypothetical solid motion is ceased, and inlets and outlets start to switch periodically in the same direction as fluid flow (Figure 2.2).

The first step breaks the singular circular column idealization. The second step changes the representation from curved to rectangular shape, to turn the illustration more intuitive with reality. Finally, the third step stops the solid motion, and it starts to switch the inlets and outlets, so the relative movement between phases is still obeyed (the liquid phase effective velocity needs to increase obeying Equation 2.1, discussed in the next section). In other words, the counter-current nature of the process is still valid. It is easy to notice the change from the TMB, where the solid phase was in motion, to SMB, where the solid phase has no motion but still experiences a relative counter-current motion. After this explanation, it is clear to understand the central concept of the SMB and why the word *simulated* composes the process name, as relative motion is experienced, the solid phase motion is literally simulated. The SMB process is used in many industrial segments, which require complex separation tasks of similar compounds, like petrochemicals, pharmaceuticals, and sugars [44].

2.2 Comparison between TMB and SMB

The inlet and outlet streams divide an SMB process not only physically but functionally too. These different areas are called zones. For instance, zone 1 begins with the eluent inlet stream and ends with the extract outlet stream; zone 2 begins with the extract outlet stream and ends with the racemic solution inlet stream, and so on until zone 4. Observing Figure 2.3, one can see just one column per zone, totalizing 4 columns in this process. However, there is no maximum limit of columns per zone. Each zone has its role in the SMB process. They are (in the following A represents the more retained solute and B the less retained one):

- **Zone 1** is responsible for regenerating the solid phase. The beginning of this zone is the eluent port. The concentration of A is very high in the solid phase at the end of this zone. It is essential to notice that in this zone, pure solvent comes in, so the chemical potential indicates a more favorable situation of solute A to pass from the solid phase to the liquid phase, regenerating, therefore, the solid phase;

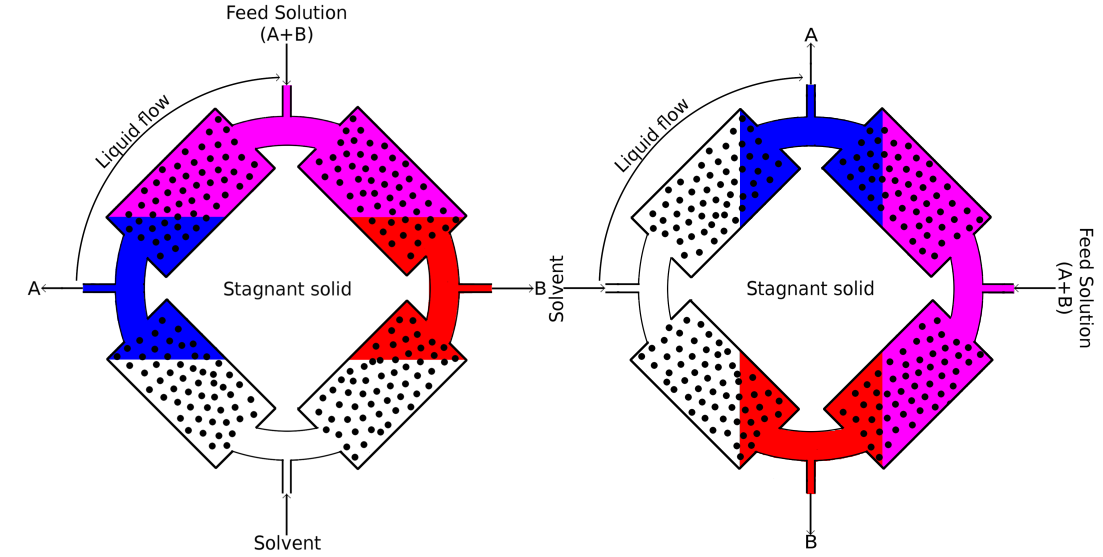

(a) t_{switch} (b) 2 t_{switch}

(c) 3 t_{switch} (d) 4 t_{switch}

Figure 2.2: Switching time changes during one cycle.

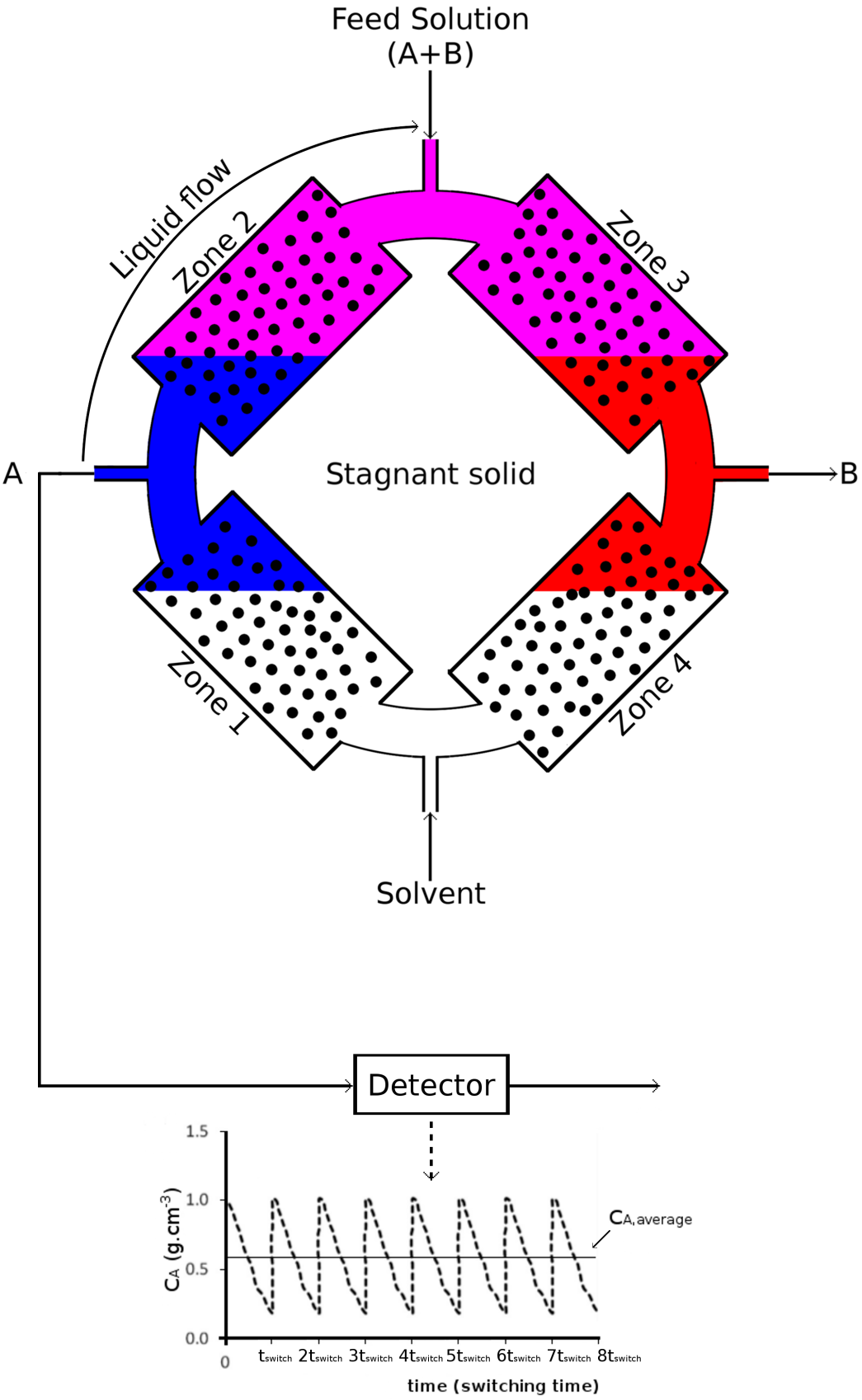

Figure 2.3: Representation of zones and the CSS.

- **Zone 2** and **Zone 3**: enriches the solid phase with A and liquid phase with B; and
- **Zone 4** is responsible for regenerating the liquid phase. The concentration of B is very high in the liquid phase at the beginning of this zone. So the chemical potential indicates a more favorable situation of solute B to pass from the liquid phase to the solid phase, regenerating, therefore, the liquid phase.

It does not matter how many columns are inside each zone in a *standard SMB behavior* (*i.e.*, constant switching time to all zones); all columns will perform the same function imposed by each zone. The more columns per zone, the better its performance. In a limiting situation, in which each zone has infinity columns, the SMB behavior is going to tend to the TMB behavior [45]. This information is of great importance to define which SMB modeling strategy to be used (Subsection 2.2.1). The periodically switching streams promote a permanently transient behavior to the process, that means never a stationary state will be achieved (see Figure 2.3). This characteristic makes any control and optimization strategy much more complex, especially if the instantaneous concentration is taken into account. But fortunately, after a specific operation time, the transient behavior starts to repeat over time in a cyclic behavior, which is called Cyclic Steady State (CSS). Thanks to this cyclic behavior, it is possible to make a different approach based on the average concentration (see Figure 2.3) and not on instantaneous one. This approach makes things easier, once a classical approach based on ordinary steady-state behavior could be done. Thanks to the complexity involving an SMB process and to perform some separation continuously from its racemic mixture without any unpredicted interruption, it is indispensable to studies about the process dynamics to develop model-based control strategies applied to SMB.

2.2.1 Equivalence between TMB and SMB

To keep the relative motion between phases, the liquid velocity in the SMB (u_{int}^{SMB}) is the sum of the liquid velocity in the TMB (u_{int}^{TMB}) and solid velocity (u_{solid}):

$$u_{int,k}^{SMB} = u_{int,k}^{TMB} + u_{solid}, \tag{2.1}$$

where $u_{int,k}^{SMB}$ is the liquid interstitial velocity in the zone k of the SMB (cm.min^{-1}), $u_{int,k}^{TMB}$ is the liquid interstitial velocity in the zone k of the TMB (cm.min^{-1}) and u_{solid} is the solid velocity in the TMB (cm.min^{-1}).

As explained in the previous section, the switching of streams confers the "simulated" solid movement. Therefore, there is a link between switching time in the

SMB and the solid motion in the TMB:

$$u_{solid} = \frac{L}{t_{switch}}, \tag{2.2}$$

where L is the chromatographic column length (cm), t_{switch} is the switching time (min) in the SMB process. Equations 2.1 and 2.2 are more useful if they could be rewritten in terms of volumetric flow rate in each zone k. The equations relate velocities and volumetric flow rate:

$$Q_k^{SMB} = \epsilon_{int,j}\ u_{int,k}^{SMB}\ A_s \tag{2.3a}$$

$$Q_k^{TMB} = \epsilon_{int,j}\ u_{int,k}^{TMB}\ A_s \tag{2.3b}$$

$$Q_{solid} = (1 - \epsilon_{int,j})\ u_{solid}\ A_s, \tag{2.3c}$$

where A_s is the cross-section area (cm^2) and $\epsilon_{int,j}$ is the interstitial porosity in the chromatographic column j (-). Substituting Equations 2.3 in Equations 2.1 and 2.2. Moreover, rearranging them, it is obtained:

$$Q_k^{SMB} = Q_k^{TMB} + \frac{\epsilon_{int,j}}{1 - \epsilon_{int,j}} Q_{solid} \tag{2.4a}$$

$$Q_{solid} = \frac{(1 - \epsilon_{int,j}) V_{column}}{t_{switch}} \tag{2.4b}$$

2.2.2 Equilibrium Theory (Triangle Theory)

Linear isotherm

A standard design method used to get preliminary flow rates and switching times for the SMB consists of calculating the flow rates for the TMB and, in the sequence, convert them to the SMB process (Equations 2.4a and 2.4b). The first step is to define mathematically the role of each zone considering a binary system, linear adsorption isotherm, and ideal model for a TMB process (for more details, see [46],[45]):

$$\textbf{Zone 1} : H_A < \frac{Q_1^{TMB}}{Q_{solid}} \tag{2.5a}$$

$$\textbf{Zone 2} : H_B < \frac{Q_2^{TMB}}{Q_{solid}} < H_A \tag{2.5b}$$

$$\textbf{Zone 3} : H_B < \frac{Q_3^{TMB}}{Q_{solid}} < H_A \text{ and } Q_3^{TMB} > Q_2^{TMB} \tag{2.5c}$$

$$\textbf{Zone 4} : \quad \frac{Q_4^{TMB}}{Q_{solid}} < H_B \tag{2.5d}$$

If the set of volumetric flow rate obeys the above inequalities, a pure less-retained solute B will be collected in the raffinate stream and the more-retained solute A in the extract stream. Considering the constraints for each zone are satisfied by a margin "β_1", "β_2", "β_3" and "β_4", respectively, for zone 1, zone 2, zone 3, and zone 4 ($\beta = [\beta_1, \beta_2, \beta_3, \beta_4] > 1$). Equations 2.5 turns to:

$$m_1 = \frac{Q_1^{TMB}}{Q_{solid}} = \beta_1 H_A \tag{2.6a}$$

$$m_2 = \frac{Q_2^{TMB}}{Q_{solid}} = \beta_2 H_B \tag{2.6b}$$

$$m_3 = \frac{Q_3^{TMB}}{Q_{solid}} = \frac{H_A}{\beta_3} \tag{2.6c}$$

$$m_4 = \frac{Q_4^{TMB}}{Q_{solid}} = \frac{H_B}{\beta_4} \tag{2.6d}$$

where m_k is the flow rate ratio (-) of the zone k.

Adding the macroscopic mass balance equations coming from each node:

$$Q_D = Q_1^{TMB} - Q_4^{TMB} \tag{2.7a}$$

$$Q_X = Q_1^{TMB} - Q_2^{TMB} \tag{2.7b}$$

$$Q_F = Q_3^{TMB} - Q_2^{TMB} \tag{2.7c}$$

$$Q_R = Q_3^{TMB} - Q_4^{TMB} \tag{2.7d}$$

where Q_D, Q_X, Q_F and Q_R are the external volumetric flow rates of desorbent, extract, feed, and raffinate streams (mL.min^{-1}), respectively.

Equations 2.4, 2.6, and 2.7 are sufficient to define all the flow rates. The suggested procedure could be seen in Figure 2.4.

The separation takes place effectively in zones 2 and 3. It is common to plot them, as shown in Figure 2.5. The separation region has the shape of a triangle

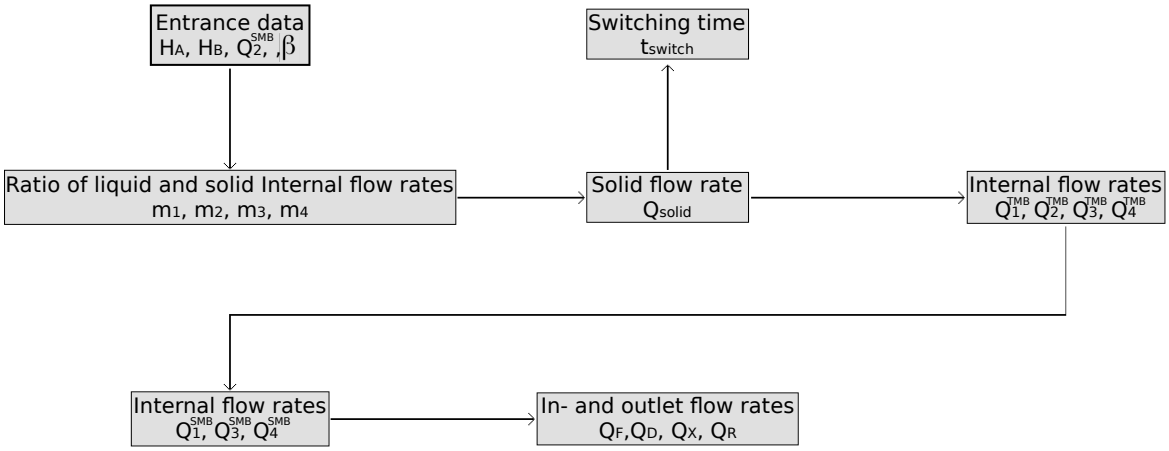

Figure 2.4: Procedure used to calculate the flow rates and the flow rate ratios.

(that is why the name is also triangle theory) and the regeneration region has a rectangular shape.

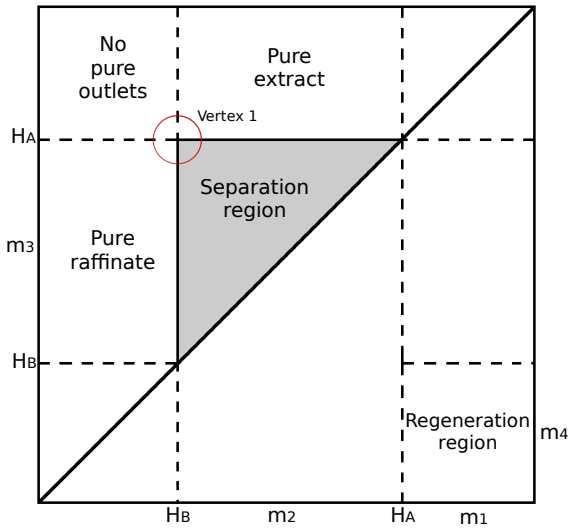

Figure 2.5: The so-called triangle theory after plotting m_3 vs. m_2 and m_4 vs. m_1 considering linear isotherm.

It is worthwhile mentioning that vertex 1 (see Figure 2.5) represents the point of maximum productivity, but it is essential to remember that this theory was conceived with some strong assumptions in mind, they are:

1. Linear adsorption isotherm;

2. Neglected dispersion effects throughout the column;

3. Instantaneous equilibrium between phases;

4. Isothermal operation; and

5. Infinite number of columns per zone (thanks to the equivalence between TMB and SMB).

Hence, the most powerful feature of this theory relies on reasonable estimates of the flow rates. Moreover, due to the above assumptions, operating in vertex 1 is not a reliable choice [45], so process control strategies are of utmost importance. Every process suffers influence from the surrounding environment; therefore the variables of the process have a natural stochastic behavior. Bearing that in mind, reliable models to define control strategies need to be developed to allow the best performance possible.

Nonlinear isotherm

In order to make the triangle theory closer to reality, the linear isotherm can be substituted for a nonlinear isotherm:

$$q_{e,i} = \frac{q_m b_i C_i}{1 + \sum_{i=A,B} (b_i C_i)}, \tag{2.8a}$$

$$b_i = \frac{H_i}{q_m}, \tag{2.8b}$$

where q_m is the maximum adsorption capacity ($\mathrm{gL^{-1}}$) and b_i is the adsorption interaction constant of each enantiomer i ($\mathrm{Lg^{-1}}$). Fortunately, the bounds of the separation regions can be explicitly obtained if practically no interaction between desorbent and CSP is observed [47]. The equations necessary to draw the triangle and regeneration borders illustrated in Figure 2.6 are summarized below (more details could be found elsewhere [47],[48]):

$$H_A = m_{1,min} < m_1 < \infty; \tag{2.9a}$$

$$0 < m_4 < m_{4,max}; \tag{2.9b}$$

where

$$m_{4,max} = \frac{1}{2}\left\{ H_B + m_3 + b_B C_{F,B} (m_3 - m_2) - \sqrt{\left[H_B + m_3 + b_B C_{F,B} (m_3 - m_2)\right]^2 - 4 H_B m_3} \right\}.$$

The lines of the entire separation region are:

Straight line b-w:

$$[H_A - H_B\,(1 + b_A C_{F,A})]\,m_2 + b_A C_{F,A} H_B m_3 = H_B\,(H_A - H_B)\,; \tag{2.10}$$

Straight line w-v:

$$[H_A - \zeta_G\,(1 + b_A C_{F,A})]\,m_2 + b_A C_{F,A} \zeta_G m_3 = \zeta_G\,(H_A - \zeta_G)\,; \tag{2.11}$$

Curve v-a:

$$m_3 = m_2 + \frac{\left(\sqrt{H_A} - \sqrt{m_2}\right)^2}{b_A C_{F,A}}; \tag{2.12}$$

Straight line a-b:

$$m_3 = m_2 \tag{2.13}$$

The intersection points are:

Point a: (H_A,H_A)

Point b: (H_B,H_B)

Point v: ($\frac{\zeta_G^2}{H_A}$, $\frac{\zeta_G[\zeta_F(H_A-\zeta_G)(H_A-H_B)+H_B\zeta_G(H_A-\zeta_F)]}{H_A H_B(H_A-\zeta_F)}$)

Point w: ($\frac{H_B\zeta_G}{H_A}$, $\frac{\zeta_G[\zeta_F(H_A-H_B)+H_B(H_B-\zeta_F)]}{H_B(H_A-\zeta_F)}$)

It is essential to highlight that $\zeta_G > \zeta_F > 0$, which are calculated by finding the roots of the quadratic equation below:

$$(1 + b_A C_{F,A} + b_B C_{F,B})\,\zeta^2 - [H_B(1 + b_A C_{F,A}) + H_A(1 + b_B C_{F,B})]\,\zeta + H_A H_B = 0 \tag{2.14}$$

The m_2 versus m_3 plane and m_1 versus m_4 plane can be seen in Figure 2.6.

Unlike the linear isotherm, in the nonlinear isotherm, the separation boundaries vary according to the enantiomeric feed concentration.

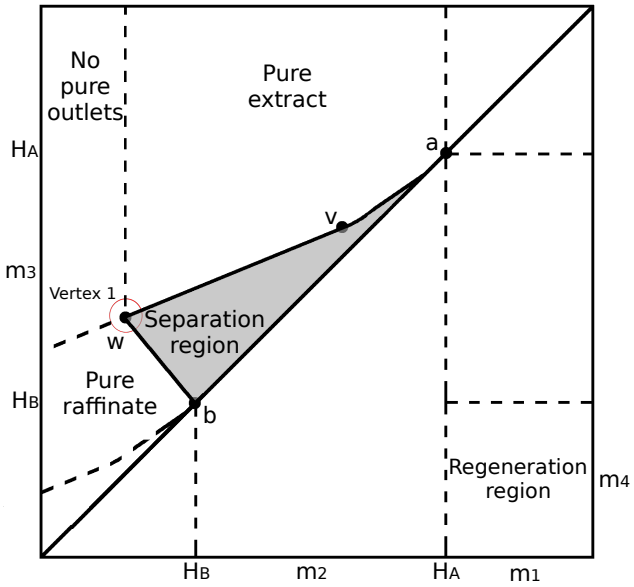

Figure 2.6: The triangle theory after plotting m_3 vs. m_2 and m_4 vs. m_1 considering nonlinear isotherm.

2.3 Separation of praziquantel using simulated moving bed technology

In 1993, Ching *et al.* [1] were the first, to the best of our knowledge, to use SMB to separate a racemic mixture of praziquantel aiming to achieve the semi-preparative scale. Some particularities need to be pointed out from their work: (1) **M**icrocrystalline **C**ellulose **T**ri**A**cetate (MCTA) was used as an adsorbent, (2) the chromatographic process was composed by 4 chromatographic columns, (3) the feed concentration was 50 g.L^{-1} of a praziquantel racemic mixture in methanol, (4) methanol was used as a desorbent, and (5) the SMB process did not recycle the desorbent (*i.e.*, absence of zone 4). The disposal of the columns in each zone was 1:1:2 (zone 1 : zone 2 : zone 3). This configuration achieved 90.1% of D-PZQ in the extract stream and 93.7% of L-PZQ in the raffinate stream. Lim *et al.* [2], in 1995, used an SMB with a similar configuration as the previous work but using 8 chromatographic columns instead of 4 and disposed of as (1:4:3). The raffinate stream presented 97.5% of L-PZQ. In order to get pure L-PZQ, crystallization process was coupled right after the raffinate stream. The process got an overall production of 11.7 g.day^{-1} and an overall L-PZQ recovery of approximately 80%. In our research group, Andrade Neto *et al.* [49] made a theoretical study adopting adaptative **N**onlinear **M**odel **P**redictive **C**ontrol (NMPC) strategies to separate praziquantel racemate using SMB chromatography. The controller's performance was tested in many different situations (i.e., pumps and switching valves malfunction and setpoint tracking). The controller showed fast and smooth responses, even when the param-

eter estimation was included in the control strategies to solve plant-model mismatch situations. The outlined control strategies were accomplished, and for the first time, a model based on first principle equations was satisfactorily used. Furthermore, the presence of zone 4 evidences the recycling of the desorbent, that means, less fresh desorbent should be consumed, which increases the efficiency of the process. This is an exciting scenario that allows further studies involving racemization [37] and synthesis of PZQ analogs to fight against resistant and immature parasites [32–36]. The actual SMB unit used in the present work is going to provide crucial information for a better understanding of the dynamics of the SMB process and the consequent updating of mathematical models for the development of control strategies, like NMPC, to provide in a semi-preparative scale enantiomers with different optical purities, maximum productivity, and minimum desorbent consumption.

2.4 Polysaccharide-based Chiral Stationary Phases

Many works are found in the 1990s using Microcrystalline Cellulose TriAcetate (MCTA), a polysaccharide-based Chiral Stationary Phase (CSP), to separate racemic mixtures like PZQ [2, 50, 51]. It became prevalent thanks to its high loadability and good enantioselectivity features. However the non-existence of support materials conferred to these adsorbents poor mechanical stability [52]. In order to overcome this issue, adsorbents started to be coated on macroporous silica surfaces [52]. Nowadays, new CSPs and almost all of them are still polysaccharide-based [53, 54]. The main idea behind the technology development of CSPs in the last three decades was mainly related to the substituents allocated in the aromatic rings of the phenyl moiety of these polysaccharides [55]. Thanks to it, the cellulose tris(3-chloro-4-methylphenylcarbamate) (commercially available with the name Chiralcel^{TM} OZ) has a great chiral recognition feature and, at the same time, poor solubility in polar desorbents usually used in chromatographic separations (e.g., ethanol). Furthermore, PZQ is freely soluble in alcohol [56] (an important feature when working on the preparative scale). On the other hand, the CSPs commercially available as Chiralcel^{TM} OD, Chiralcel^{TM} OJ, and Chiralpak^{TM} AD are not compatible with high polar desorbents, and additionally, the separation factor of Chiralcel^{TM} OZ for PZQ ($\alpha = 1.9$) is greater than Chiralcel^{TM} OD, Chiralcel^{TM} OJ, and Chiralpak^{TM} AD [2].

2.5 Materials and methods

2.5.1 Materials

Solvent and Solutes

The solvent used was the ethanol HPLC grade provided by Tedia (Brazil). The solutes used were 1,3,5-tri-*tert*-butylbenzene (TTBB) 97%, provided by Sigma-Aldrich (USA) and a solid racemic mixture of praziquantel (PZQ), kindly provided by LASiFA - Farmanguinhos/Fiocruz (Brazil).

Lab Consumables

The lab consumables used were: (1) Kitasato flask of size 1000 mL, (2) Büchner funnel, (3) membrane made of PTFE and supported by polyethylene, average pore size of 0.22 μm and membrane diameter of 47 mm provided by Millipore, and (4) Schott flask.

2.5.2 Equipment

The equipment used:

1. **for filtration of ethanol was**:
   - vacuum pump, model 131, provided by Prismatec;
2. **for HPLC characterizations and analysis were (all provided by JASCO Co. - see Figure 2.7)**:
   (a) one HPLC pump, model PU-2087;
   (b) one autosampler, model AS-2059;
   (c) one column oven, model CO-2060;
   (d) one chromatographic column, model Chiracel OZ®, provided by Diacel Co with the following characteristics:
      - particles were coated with the selective material *tris*(3-chloro-4-methylphenylcarbamate) cellulose;
      - monodispersed particle diameter: 20 μm;
      - 4.8 g of CSP (m_{ads});
      - internal diameter: 10 mm;
      - length: 100 mm;
   (e) one multi-wavelength UV/Vis detector, model UV-2077;

(f) one computer equipped with the ChromNav software (JASCO Co. software)

3. **for SMB separations were (see Figure 2.8)**:

- one in-line degasser, model DG-2080-54, provided by JASCO Co.;
- four HPLC pumps, model PU-2086 provided by JASCO Co.;
- six valves with 8 dead-end streams (bore 0.40 mm) provided by ViCi®;
- six chromatographic columns, model Chiracel OZ®, provided by Diacel Co;
- six valves with microelectronic actuator and two positions, provided by ViCi®;
- two stainless steel proportional relief valves series R3A for high pressure, model SS-4R3A, provided by swagelok;
- no-break, model "Laser Senoidal 4200 VA", provided by NHS;
- three Data AcQuisition (DAQ) instruments, model NI USB-6501, provided by National Instruments; and
- one computer equipped with LabView 2012, intel Core i7 (4th generation), 16 gigabyte RAM memory (DDR3), 6 DB9 ports and 8 USB ports.

All experiments were carried out inside HPLC or SMB processes.

2.6 Experimental Methodology

2.6.1 Chromatographic column characterization

It was determined that some crucial parameters related to each chromatographic column were necessary to represent the nature of the process in the used models. They are total porosity for each column j ($\epsilon_{t,j}$), Henry coefficient for each solute i in each column j ($H_{i,j}$), the axial diffusion coefficient for each solute i in each column j ($D_{axial,i,j}$ - $cm^2.min^{-1}$) and effective mass transfer coefficient for each solute i in each column j ($k_{eff,i,j}$ - min^{-1}).

In order to determine the $\epsilon_{t,j}$ of the columns, a solution of 2 $g.L^{-1}$ of TTBB in ethanol was used. The other parameters were determined using 1 $g.L^{-1}$ of a racemic mixture of PZQ in ethanol. Despite the differences in solutions concentration, the experimental methodology was the same, and it is presented below:

1. Experimental procedure to obtain the parameters using the HPLC system:

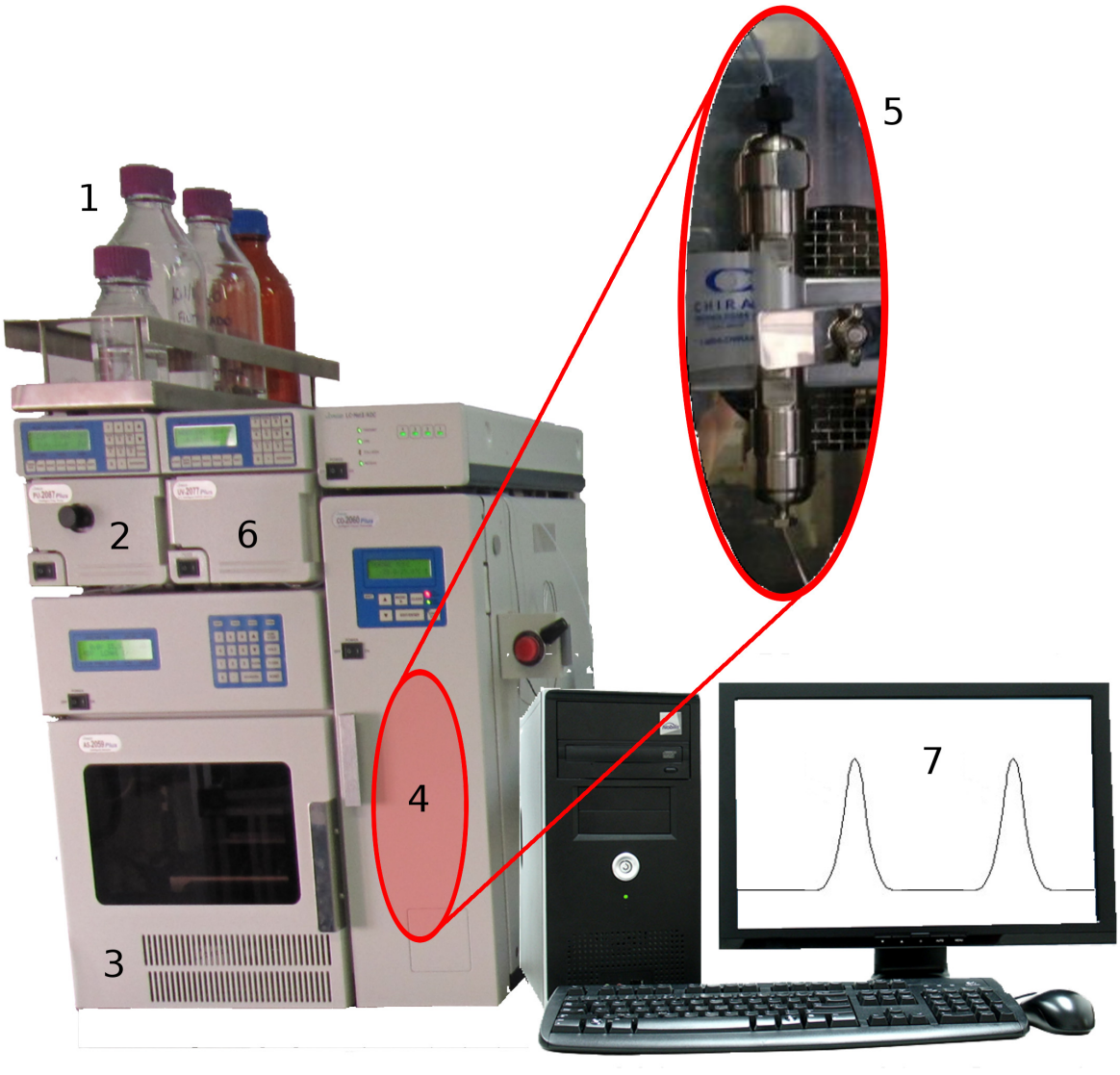

Figure 2.7: Photo of the HPLC system used. **Solvent path**: (1) Solvent flask; (2) HPLC pump; (4) column oven; (5) chromatographic column; (6) UV/Vis detector and (7) software analysis. **Solute path**: (3) autosampler; (4) column oven; (5) chromatographic column; (6) UV/Vis detector and (7) software analysis.

Figure 2.8: Photo of the SMB system used. (1) Solvent flasks; (2) degasser; (3) HPLC pump; (4) valves with 8 dead-end streams; (5) chromatographic columns; (6) valves with two positions and (7) interface.

(a) the vial containing the ethanol solution (of TTBB or racemic mixture of PZQ) was conditioned inside the auto-sampler;

(b) 20 μL of this solution was automatically injected into the HPLC system. The solute was carried till the chromatographic column installed inside the column oven with 25°C of temperature;

(c) After getting throughout the column, the solute was conducted by the eluent flow until the UV/Vis detector, in which the wavelength was set to 210 nm to determine its retention time [2].

This procedure was repeated for seven different eluent flow rates (0.5, 1.0, 2.0, 3.0, 4.0, 5.0, 6.0 mL.min^{-1}), which one identified by a number (number 1 for 0.5 mL.min^{-1}, 2 for 1.0 mL.min^{-1}, until 7 for 6 mL.min^{-1}). For each flow rate, the experiments were replicated three times, and they were identified by the letters *a*, *b*, and *c*. For instance, $t_{o,j,1a}$ represents the first replica of the experiments carried out at 0.5 mL.min^{-1} inside the column *j*, $t_{o,j,3b}$ represents the second replica of the experiments carried out at 2.0 mL.min^{-1} inside the column *j*, and so on. This nomenclature was adopted to all experimental and calculated data obtained.

Total Porosity ($\epsilon_{t,j}$)

Table 2.1 illustrates the disposal of experimental and calculated data used to calculate $\epsilon_{t,j}$, where the identified experimental data were obtained straight from HPLC system.

The calculated data were obtained by the equations below:

- Retention time average of the flow rate replica in the column *j* ($\bar{t}_{o,j,n}$):

$$\bar{t}_{o,j,n} = \frac{t_{o,j,na} + t_{o,j,nb} + t_{o,j,nc}}{3}, \text{for } n = 1, 2, 3, 4, 5, 6 \text{ or } 7. \tag{2.15}$$

- Retention time variance of the flow rate replica in the column *j* ($(\delta t_{o,j,n})^2$):

$$(\delta t_{o,j,n})^2 = \frac{(t_{o,j,na} - \bar{t}_{o,j,n})^2 + (t_{o,j,nb} - \bar{t}_{o,j,n})^2 + (t_{o,j,nc} - \bar{t}_{o,j,n})^2}{2}. \tag{2.16}$$

- Retention time standard deviation of the flow rate replica in the column *j* ($\delta t_{o,j,n}$):

$$\delta t_{o,j,n} = \pm\sqrt{(\delta t_{o,j,n})^2}. \tag{2.17}$$

- Non-linear regression method:

It consists of solving the optimization problem stated below:

[2]The TTBB retention time is also called dead time (one could find a detailed explanation elsewhere [57])

Table 2.1: Experimental data for each column j

	Experimental data		Calculated data		
Exp. n^o	$\dot{V}_n$ (mL.min^{-1})	$t_{o,j,nm}$ (min)	$\bar{t}_{o,j,n}$(min)	$\delta t_{o,j,n}$(min)	$(\delta t_{o,j,n})^2$(min^2)
1	0.5	$t_{o,j,1a}$ $t_{o,j,1b}$ $t_{o,j,1c}$	$\bar{t}_{o,j,1}$	$\delta t_{o,j,1}$	$(\delta t_{o,j,1})^2$
2	1.0	$t_{o,j,2a}$ $t_{o,j,2b}$ $t_{o,j,2c}$	$\bar{t}_{o,j,2}$	$\delta t_{o,j,2}$	$(\delta t_{o,j,2})^2$
3	2.0	$t_{o,j,3a}$ $t_{o,j,3b}$ $t_{o,j,3c}$	$\bar{t}_{o,j,3}$	$\delta t_{o,j,3}$	$(\delta t_{o,j,3})^2$
4	3.0	$t_{o,j,4a}$ $t_{o,j,4b}$ $t_{o,j,4c}$	$\bar{t}_{o,j,4}$	$\delta t_{o,j,4}$	$(\delta t_{o,j,4})^2$
5	4.0	$t_{o,j,5a}$ $t_{o,j,5b}$ $t_{o,j,5c}$	$\bar{t}_{o,j,5}$	$\delta t_{o,j,5}$	$(\delta t_{o,j,5})^2$
6	5.0	$t_{o,j,6a}$ $t_{o,j,6b}$ $t_{o,j,6c}$	$\bar{t}_{o,j,6}$	$\delta t_{o,j,6}$	$(\delta t_{o,j,6})^2$
7	6.0	$t_{o,j,7a}$ $t_{o,j,7b}$ $t_{o,j,7c}$	$\bar{t}_{o,j,7}$	$\delta t_{o,j,7}$	$(\delta t_{o,j,7})^2$

$$\begin{aligned} &\min\ S(\epsilon_{t,j}) \\ &\text{subjected to: } \epsilon_{t,j} \in [0,1], \end{aligned} \tag{2.18}$$

where $S(\epsilon_{t,j})$ represents the objective function defined as:

$$S(\epsilon_{t,j}) = \sum_{n=1}^{7} \left[\frac{\bar{t}^{calc}_{o,j,n}(\epsilon_{t,j}) - \bar{t}_{o,j,n}}{\delta t_{o,j,n}} \right]^2 . \tag{2.19}$$

Knowing the liquid flow rate, the $\bar{t}^{calc}_{o,j,n}(\epsilon_{t,j})$ was calculated as:

$$\bar{t}^{calc}_{o,j,n}(\epsilon_{t,j}) = \frac{\epsilon_{t,j} V_{column}}{Q_n},$$

This experimental procedure was performed on all columns. Table 2.6 shows the total porosity calculated for each column j, the involved error, and the correlation coefficient.

Henry Constant ($\mathbf{H}_{i,j}$)

Table 2.2 illustrates the experimental and calculated data used to calculate $H_{i,j}$, where the column identified as *Experimental data* were obtained straight from HPLC system.

Table 2.2: Experimental data for each enantiomer i in each column j

	Experimental data		Calculated data		
Exp. n^o	$\dot{V}_n$ (mL.min^{-1})	$t_{i,j,m}$ (min)	$\bar{t}_{i,j,n}$(min)	$\delta t_{i,j,n}$(min)	$(\delta t_{i,j,n})^2$(min^2)
1	0.5	$t_{i,j,1a}$ $t_{i,j,1b}$ $t_{i,j,1c}$	$\bar{t}_{i,j,1}$	$\delta t_{i,j,1}$	$(\delta t_{i,j,1})^2$
2	1.0	$t_{i,j,2a}$ $t_{i,j,2b}$ $t_{i,j,2c}$	$\bar{t}_{i,j,2}$	$\delta t_{i,j,2}$	$(\delta t_{i,j,2})^2$
3	2.0	$t_{i,j,3a}$ $t_{i,j,3b}$ $t_{i,j,3c}$	$\bar{t}_{i,j,3}$	$\delta t_{i,j,3}$	$(\delta t_{i,j,3})^2$
4	3.0	$t_{i,j,4a}$ $t_{i,j,4b}$ $t_{i,j,4c}$	$\bar{t}_{i,j,4}$	$\delta t_{i,j,4}$	$(\delta t_{i,j,4})^2$
5	4.0	$t_{i,j,5a}$ $t_{i,j,5b}$ $t_{i,j,5c}$	$\bar{t}_{i,j,5}$	$\delta t_{i,j,5}$	$(\delta t_{i,j,5})^2$
6	5.0	$t_{i,j,6a}$ $t_{i,j,6b}$ $t_{i,j,6c}$	$\bar{t}_{i,j,6}$	$\delta t_{i,j,6}$	$(\delta t_{i,j,6})^2$
7	6.0	$t_{i,j,7a}$ $t_{i,j,7b}$ $t_{i,j,7c}$	$\bar{t}_{i,j,7}$	$\delta t_{i,j,7}$	$(\delta t_{i,j,7})^2$

The calculated data were obtained by the equations below:

- Retention time average of the flow rate replica in the column *j* ($\bar{t}_{i,j,n}$):

$$\bar{t}_{i,j,n} = \frac{t_{i,j,na} + t_{i,j,nb} + t_{i,j,nc}}{3}, \text{for } n = 1, 2, 3, 4, 5, 6 \text{ or } 7. \tag{2.20}$$

- Retention time variance of the flow rate replica in the column *j* ($\delta t_{i,j,n})^2$):

$$(\delta t_{i,j,n})^2 = \frac{(t_{i,j,na} - \bar{t}_{i,j,n})^2 + (t_{i,j,nb} - \bar{t}_{i,j,n})^2 + (t_{i,j,nc} - \bar{t}_{i,j,n})^2}{2}. \tag{2.21}$$

- Retention time standard deviation of the flow rate replica in the column *j* ($\delta t_{i,j,n}$):

$$\delta t_{i,j,n} = \pm\sqrt{(\delta t_{i,j,n})^2}. \tag{2.22}$$

- Relationship between $\bar{t}_{i,j,n}$ and $\bar{t}_{o,j,n}$:

Plotting experimental data $\bar{t}_{i,j,n}$ versus $\bar{t}_{o,j,n}$, it was observed a linear relationship between them. Therefore,

$$\bar{t}_{i,j,n} = d_{i,j} \cdot \bar{t}_{o,j,n}, \tag{2.23}$$

where $d_{i,j}$ was experimentally determined by Equation 2.24:

$$d_{i,j} = \frac{\sum_{n=1}^{7} \left(\bar{t}_{i,j,n} - \bar{\bar{t}}_{i,j}\right)^2}{\sum_{n=1}^{7} \left[\left(\bar{t}_{i,j,n} - \bar{\bar{t}}_{i,j}\right) \cdot \left(\bar{t}_{o,j,n} - \bar{\bar{t}}_{o,j}\right)\right]}, \tag{2.24}$$

where $\bar{\bar{t}}_{i,j,n}$ is the mean of all retention time averages for enantiomer i in the column j:

$$\bar{\bar{t}}_{i,j} = \frac{\sum_{n=1}^{7} \bar{t}_{i,j,n}}{n}. \tag{2.25}$$

- Henry coefficient calculation ($H_{i,j}$):

From Equation 2.26 [58]:

$$\bar{t}_{i,j,n} = \bar{t}_{o,j,n} \left(1 + \frac{1 - \epsilon_{t,j}}{\epsilon_{t,j}} H_{i,j}\right). \tag{2.26}$$

Moreover, substituting Equation 2.23 into Equation 2.26, it was possible to write:

$$d_{i,j} = 1 + \frac{1 - \epsilon_{t,j}}{\epsilon_{t,j}} H_{i,j}. \tag{2.27}$$

Rearranging it:

$$H_{i,j} = \frac{(d_{i,j} - 1)\, \epsilon_{t,j}}{1 - \epsilon_{t,j}}. \tag{2.28}$$

This experimental procedure was performed on all columns.

Apparent axial dispersion ($D_{app,i,j}$) and effective mass transfer coefficients ($k_{eff,i,j}$)

Tables 2.3 and 2.4 illustrate the disposal of experimental and calculated data used to calculate $D_{app,i,j}$ and $k_{eff,i,j}$, where the identified experimental data were obtained straight from the HPLC system. The main concepts related to theoretical plates, HETP, and van Deemter's equation, are presented in Appendix E.

The calculated data were obtained by the equations below:

- Number of theoretical plates average of the flow rate replica in the

Table 2.3: Experimental data for each enantiomer i in each column j

	Experimental data		Calculated data		
Exp. n^o	$\dot{V}_n$ (mL.min^{-1})	$N_{i,j,m}$ (-)	$\overline{N}_{i,j,n}$(-)	$\delta N_{i,j,n}$(-)	$(\delta N_{i,j,n})^2$(-)
1	0.5	$N_{i,j,1a}$ $N_{i,j,1b}$ $N_{i,j,1c}$	$\overline{N}_{i,j,1}$	$\delta N_{i,j,1}$	$(\delta N_{i,j,1})^2$
2	1.0	$N_{i,j,2a}$ $N_{i,j,2b}$ $N_{i,j,2c}$	$\overline{N}_{i,j,2}$	$\delta N_{i,j,2}$	$(\delta N_{i,j,2})^2$
3	2.0	$N_{i,j,3a}$ $N_{i,j,3b}$ $N_{i,j,3c}$	$\overline{N}_{i,j,3}$	$\delta N_{i,j,3}$	$(\delta N_{i,j,3})^2$
4	3.0	$N_{i,j,4a}$ $N_{i,j,4b}$ $N_{i,j,4c}$	$\overline{N}_{i,j,4}$	$\delta N_{i,j,4}$	$(\delta N_{i,j,4})^2$
5	4.0	$N_{i,j,5a}$ $N_{i,j,5b}$ $N_{i,j,5c}$	$\overline{N}_{i,j,5}$	$\delta N_{i,j,5}$	$(\delta N_{i,j,5})^2$
6	5.0	$N_{i,j,6a}$ $N_{i,j,6b}$ $N_{i,j,6c}$	$\overline{N}_{i,j,6}$	$\delta N_{i,j,6}$	$(\delta N_{i,j,6})^2$
7	6.0	$N_{i,j,7a}$ $N_{i,j,7b}$ $N_{i,j,7c}$	$\overline{N}_{i,j,7}$	$\delta N_{i,j,7}$	$(\delta N_{i,j,7})^2$

column *j* ($\overline{N}_{i,j,n}$):

$$\overline{N}_{i,j,n} = \frac{N_{i,j,na} + N_{i,j,nb} + N_{i,j,nc}}{3}, \text{for } n = 1, 2, 3, 4, 5, 6 \text{ or } 7. \tag{2.29}$$

- Number of theoretical plates variance of the flow rate replica in the column *j* ($(\delta N_{i,j,n})^2$):

$$(\delta N_{i,j,n})^2 = \frac{(N_{i,j,na} - \overline{N}_{i,j,n})^2 + (N_{i,j,nb} - \overline{N}_{i,j,n})^2 + (N_{i,j,nc} - \overline{N}_{i,j,n})^2}{2}. \tag{2.30}$$

- Number of theoretical plates standard deviation of the flow rate replica in the column *j* ($\delta N_{i,j,n}$):

$$\delta N_{i,j,n} = \pm\sqrt{(\delta N_{i,j,n})^2}. \tag{2.31}$$

- Conversion of $\mathbf{N}_{i,j,n}$ to $\mathbf{HETP}_{i,j,n}$:

$$\overline{HETP}_{i,j,n} = \frac{L}{\overline{N}_{i,j,n}}.$$

- Conversion of Q_n to $u_{m,j,n}$:

$$u_{m,j,n} = \frac{Q_n}{\epsilon_{t,j} A_s}.$$

Table 2.4: Calculated data for each enantiomer i in each column j

Exp. n^o	$u_{m,j,n}$ (cm.min^{-1})	$HETP_{i,j,n}$ (-)
1	$u_{m,j,1}$	$HETP_{i,j,1a}$
		$HETP_{i,j,1b}$
		$HETP_{i,j,1c}$
2	$u_{m,j,2}$	$HETP_{i,j,2a}$
		$HETP_{i,j,2b}$
		$HETP_{i,j,2c}$
3	$u_{m,j,3}$	$HETP_{i,j,3a}$
		$HETP_{i,j,3b}$
		$HETP_{i,j,3c}$
4	$u_{m,j,4}$	$HETP_{i,j,4a}$
		$HETP_{i,j,4b}$
		$HETP_{i,j,4c}$
5	$u_{m,j,5}$	$HETP_{i,j,5a}$
		$HETP_{i,j,5b}$
		$HETP_{i,j,5c}$
6	$u_{m,j,6}$	$HETP_{i,j,6a}$
		$HETP_{i,j,6b}$
		$HETP_{i,j,6c}$
7	$u_{m,j,7}$	$HETP_{i,j,7a}$
		$HETP_{i,j,7b}$
		$HETP_{i,j,7c}$
$\overline{HETP}_{i,j,n}$(cm)	$\delta HETP_{i,j,n}$(cm)	$(\delta HETP_{i,j,n})^2$(cm^2)
$\overline{HETP}_{i,j,1}$	$\delta HETP_{i,j,1}$	$(\delta HETP_{i,j,1})^2$
$\overline{HETP}_{i,j,2}$	$\delta HETP_{i,j,2}$	$(\delta HETP_{i,j,2})^2$
$\overline{HETP}_{i,j,3}$	$\delta HETP_{i,j,3}$	$(\delta HETP_{i,j,3})^2$
$\overline{HETP}_{i,j,4}$	$\delta HETP_{i,j,4}$	$(\delta HETP_{i,j,4})^2$
$\overline{HETP}_{i,j,5}$	$\delta HETP_{i,j,5}$	$(\delta HETP_{i,j,5})^2$
$\overline{HETP}_{i,j,6}$	$\delta HETP_{i,j,6}$	$(\delta HETP_{i,j,6})^2$
$\overline{HETP}_{i,j,7}$	$\delta HETP_{i,j,7}$	$(\delta HETP_{i,j,7})^2$

- HETP average of the flow rate replica in the column *j* ($\overline{HETP}_{i,j,n}$):

$$\overline{HETP}_{i,j,n} = \frac{HETP_{i,j,na} + HETP_{i,j,nb} + HETP_{i,j,nc}}{3}, \text{for } n = 1, 2, 3, 4, 5, 6 \text{ or } 7. \tag{2.32}$$

- HETP variance of the flow rate replica in the column *j* ($(\delta HETP_{i,j,n})^2$):

$$\begin{aligned}(\delta HETP_{i,j,n})^2 = &\frac{(HETP_{i,j,na} - \overline{HETP}_{i,j,n})^2}{2} \\ &+ \frac{(HETP_{i,j,nb} - \overline{HETP}_{i,j,n})^2}{2} \\ &+ \frac{(HETP_{i,j,nc} - \overline{HETP}_{i,j,n})^2}{2}.\end{aligned} \tag{2.33}$$

- HETP standard deviation of the flow rate replica in the column *j* ($\delta HETP_{i,j,n}$)

$$\delta HETP_{i,j,n} = \pm\sqrt{(\delta HETP_{i,j,n})^2}. \tag{2.34}$$

The van Deemter equation plus the data of Table 2.4 were used to calculate the apparent diffusion coefficient ($D_{app,i,j}$) and the effective mass transfer coefficient ($k_{eff,i,j}$) for each enantiomer i inside each column j (more details see [45, 57, 58]). From the *van Deemter* equation:

$$\overline{HETP}^{calc}_{i,j,n} = A_{i,j} + C_{i,j}u_{m,j,n}. \tag{2.35}$$

From the experiments, it was possible to define the parameters by linear regression:

$$C_{i,j} = \frac{\sum_{n=1}^{7}\left[\left(\overline{HETP}_{i,j,n} - \overline{\overline{HETP}}_{i,j}\right)\cdot\left(u_{m,j,n} - \overline{u}_{m,j}\right)\right]}{\sum_{n=1}^{7}\left(u_{m,j,n} - \overline{u}_{m,j}\right)^2}, \tag{2.36a}$$

$$A_{i,j} = \overline{\overline{HETP}}_{i,j} - C_{i,j}\overline{u}_{m,j}, \tag{2.36b}$$

where,

$$\overline{\overline{HETP}}_{i,j} = \frac{\sum_{n=1}^{7}\overline{HETP}_{i,j,n}}{7}, \text{ and,} \tag{2.37a}$$

$$\overline{u}_{m,j} = \frac{\sum_{n=1}^{7}u_{m,j,n}}{7}.. \tag{2.37b}$$

- $D_{app,i,j,n}$ and $k_{eff,i,j,n}$ calculation:

The parameters $A_{i,j}$ and $C_{i,j}$ are well described in the literature (see [58]), and

their equations can be rearranged as follows:

$$D_{app,i,j,n} = \frac{A_{i,j} u_{m,j,n}}{2}, \tag{2.38a}$$

$$k_{eff,i,j} = 2\left(\frac{k_{0,i,j}}{1+k_{0,i,j}}\right)^2 \frac{1}{k_{0,i,j} C_{i,j}}, \tag{2.38b}$$

$$k_{0,i,j} = H_{i,j} \frac{(1-\epsilon_{t,j})}{\epsilon_{t,j}}. \tag{2.38c}$$

As the apparent diffusion coefficient ($D_{app,i,j,n}$) is dependent on the effective velocity ($u_{m,j,n}$), this one was not presented in a table, just the effective mass transfer coefficient ($k_{eff,i,j}$).

The *Péclet* number ($Pe_{i,j}$) and the number of mass transfer units ($\alpha_{i,j}$) for the species i in a column j were formally presented because they will be used in some moment of the text:

$$Pe_j = \frac{u_{m,j,n}.L}{D_{axial,j,n}}; \tag{2.39a}$$

$$\alpha_{i,j} = \frac{k_{eff,i,j}.L}{u_{solid}}. \tag{2.39b}$$

As the difference between the axial dispersion coefficient of species A and B where less than 10% and are isomers, they were stuck together, taking the average value:

$$D_{app,j,n} = \frac{D_{app,A,j,n} + D_{app,B,j,n}}{2}. \tag{2.40}$$

This experimental procedure was performed on all columns.

2.6.2 SMB unit experiment

The chromatographic unit used was presented in Figure 2.8. The pump flow rates and the valve switching time of the SMB unit were calculated using the equilibrium theory. The SMB unit was located in an air-conditioned room in order to provide an isothermal condition.

The experiments were carried out in the SMB unit with one chromatographic column in zone 1, two chromatographic columns in zone 2, two chromatographic columns in zone 3, and one chromatographic column in zone 4; normally this conformation is represented by [1,2,2,1] and the configuration used was represented in Figure 2.9. There was a pump installed in zone 2 and no pump in the raffinate stream in this configuration. Previous experiences coming from [62] were used to choose the configuration adopted in this work. The experiments were divided into

two stages: (1) SMB running with solvent in both inlet streams for 1 cycle (see Figure 2.9a) and (2) SMB running with solvent and solute(s) for 5 cycles (see Figure 2.9b), totalizing 6 cycles per experiment. Each experiment was carried out three times (*n=1,2 and 3*).

First Stage:

Objective: To measure the volumetric flow rates of the outlet streams at each switching time during the entire cycle of the first stage. The following procedure was adopted:

1. the pump's flow rates were calculated in the light of the triangle theory;
2. the SMB unit was switched on;
3. with the aid of a 5 mL volumetric flask and a stopwatch, the flow rate of the outlet streams were measured.

This procedure was repeated in each switching time interval (*i.e.*, 6 times, as it was necessary 6 switching times to complete one cycle). Therefore, an average flow rate in the extract ($Q_{X,n}$) and raffinate stream ($Q_{R,n}$) of the n^{th} experiment could be calculated:

$$\overline{Q}_{k,n} = \frac{\sum_{s=1}^{6} Q_{k,s,n}}{6} \tag{2.41}$$

where Q represents the flow rates ($mL.min^{-1}$), their subscript k and s represent external or internal flow rates and the specific switching time interval, respectively. The latter subscript was defined as

$$s = \{s \in \mathbb{N} \ / \ 1 \leq s \leq 6\}.$$

From these flow rates, the other external ones were calculated as follows:

$$\overline{Q}_{F,n} = \frac{\overline{C}_{i,X,n}\overline{Q}_{X,n} + \overline{C}_{i,R,n}\overline{Q}_{R,n}}{\overline{C}_{i,F,n}} \tag{2.42}$$

and

$$\overline{Q}_{D,n} = \overline{Q}_{X,n} + \overline{Q}_{R,n} - \overline{Q}_{F,n}. \tag{2.43}$$

To determine the internal flow rates, one of them must be known as a priori; in this case, Q_2 is known because an HPLC pump can set it. Unlike the external flow rates that could be determined experimentally (or inferred), the internal flow rate could not be measured or inferred. Therefore a posteriori adjustment of Q_2 was

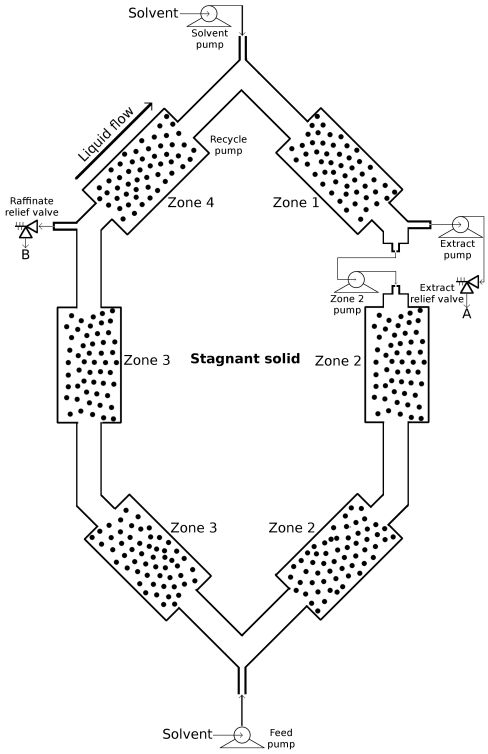

(a) Just solvent inlet

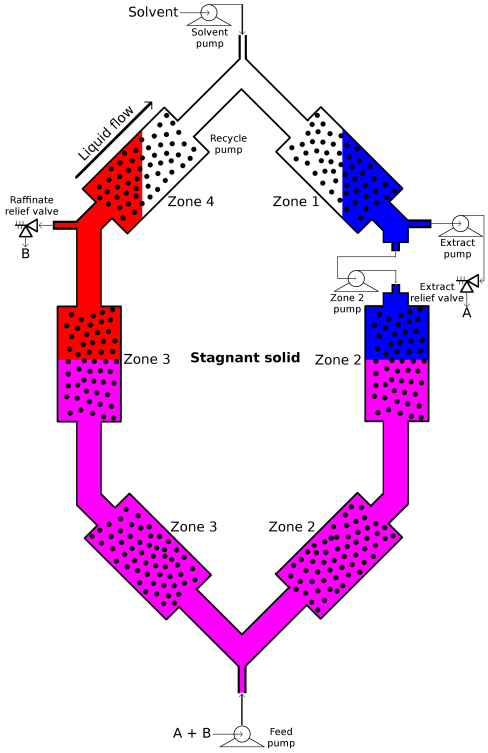

(b) Solute and solvent inlet

Figure 2.9: Illustration of the (a) first part and (b) second part of the SMB experiment.

made, and it was presented in the next section. Once Q_2 was set, the other internal flow rates could be calculated:

$$\overline{Q}_{1,n} = \overline{Q}_{2,n} + \overline{Q}_{X,n}; \tag{2.44a}$$

$$\overline{Q}_{3,n} = \overline{Q}_{2,n} + \overline{Q}_{F,n}; \tag{2.44b}$$

$$\overline{Q}_{4,n} = \overline{Q}_{2,n} + \overline{Q}_{F,n} - \overline{Q}_{R,n}; \tag{2.44c}$$

It is important to note that the flow rates have been determined so far for only one experiment *n*. After the third repetition of each experiment, all the flow rates and their experimental dispersions were calculated:

$$\overline{Q} = \frac{\sum_{n=1}^{3} Q_n}{3} \tag{2.45a}$$

$$\delta Q = \sqrt{\frac{\sum_{n=1}^{3} \left(Q_n - \overline{Q}\right)^2}{2}}, \tag{2.45b}$$

where Q represents any internal or external flow rate ($mL.min^{-1}$). They were displayed in Table C.1.

Right after the first stage, the solvent flask in the feed pump was substituted by the racemic solution flask (without shutting the SMB unit down), promoting a step in the solute concentration inside the SMB unit. Starting, therefore, the second stage.

Second Stage:

It is the SMB experiment itself (see Table C.1). The SMB unit worked for 5 cycles [3]. The entire volume of each outlet stream in the sixth switching time of the fifth cycle was collected; in the sequence, part of the collected volume was conditioned in separated vials and analyzed following the filtration and experimental procedures presented at the beginning of Section 2.6.1 (procedure 1 and 2). The concentration of the racemate in ethanol used in the feed stream of all experiments was approximately 1 $g.L^{-1}$.

The HPLC was previously calibrated for both enantiomers, $Area\ [\mu V.s] = 1941799.C_{A\ or\ B}\ [g.L^{-1}] - 8219$, with coefficient of determination (R^2) equal to 0.999.

The flow rates of the experiments were estimated in the linear region of the isotherm. Below, a brief explanation is given of the main features of the five carried-

[3]Previous experiments were carried out to certify that the unit was operating in the CSS after 5 cycles. Furthermore, Figure 4.5 corroborates this.

out experiments aiming to obtain pure stream(s):

- **Run 1**: inside the triangle of separation in Figure 2.5;
- **Run 2**: inside the area of pure extract and contaminated raffinate in Figure 2.5;
- **Run 3**: inside the area of contaminated extract and pure raffinate in Figure 2.5;
- **Run 4**: on the maximum productivity point on the triangle of separation top vertex in Figure 2.5; and
- **Run 5**: inside the triangle of separation in Figure 2.5, these runs had the highest feed concentration among all the carried out runs.

Typical chromatograms obtained in the extract and raffinate streams of each run is presented in Appendix D. In Table C.1, more details about the runs can be seen.

SMB performance parameters

Runnings were compared to each other using the performance parameters below [45]:

$$Pur_{i,out} = \frac{\overline{C}_{i,out}}{\overline{C}_{A,out} + \overline{C}_{B,out}}; \tag{2.46a}$$

$$Rec_{i,out} = \frac{\overline{Q}_{out}\overline{C}_{i,out}}{\overline{Q}_F\overline{C}_{i,F}}; \tag{2.46b}$$

$$Pr_i = \frac{(60.24).\overline{Q}_{out}\overline{C}_{i,out}}{m_{ads}\ N_{column}};\ \text{and} \tag{2.46c}$$

$$DC = \frac{\overline{Q}_D + \overline{Q}_F}{\overline{Q}_F.\ \left(\overline{C}_{A,F} + \overline{C}_{B,F}\right)}. \tag{2.46d}$$

where $Pur_{i,out}$ is the optical purity of component i (A or B) in the outlet stream (extract or raffinate) (%), $Rec_{i,out}$ is the recovery of component i in the outlet stream, Pr_i is the productivity of component i ($g.kg_{ads}^{-1}.day^{-1}$), DC is the desorbent consumption ($L.g_{rac}^{-1}$), $\overline{C}_{i,out}$ is the mean concentration of component i in the outlet stream ($g_i.L^{-1}$), $\overline{Q}_{out}$ is the mean flow rate in the outlet stream ($mL.min^{-1}$), $\overline{Q}_F$ is the mean flow rate in the racemic mixture inlet stream ($mL.min^{-1}$), $\overline{C}_{i,F}$ is the mean concentration of component i in the racemic mixture inlet stream ($g.L^{-1}$), N_{column} is the number of chromatographic columns in the SMB unit (-), m_{ads} is the mass of adsorbent in each column (kg_{ads}), and $\overline{Q}_D$ is the mean flow rate in the desorbent inlet ($mL.min^{-1}$). The mean concentrations were defined as [45]:

$$\overline{C}_{i,out} = \int_{t}^{t+t_{switch}} \frac{C_{i,out}}{t_{switch}} \, \mathrm{d}t, \tag{2.47}$$

where t_{switch} (min) is the switching time.

2.6.3 Simulation of SMB experiments

The simulated data coming from the second stage was carried out by software named SiMoBed. The software was developed during the dissertation of ANDRADE [59] using MatLab® R2016a (student license). The modeling strategy adopted by this software was the direct approach for four-zone SMB and the chromatographic columns distribution was 1 for zone 1, 2 for zone 2, 2 for zone 3 and 1 for zone 4 (1-2-2-1). The liquid-phase and solid-phase mass balance for the component i in the jth chromatographic column was:

$$\underbrace{\overline{\epsilon}_t \, \frac{\partial C_{i,j}}{\partial t}}_{\text{acc. term in fluid phase}} + \underbrace{\overline{\epsilon}_t \, u_{m,j} \frac{\partial C_{i,j}}{\partial x}}_{\text{advection term}} + \underbrace{(1-\overline{\epsilon}_t) \, \frac{\partial q_{i,j}}{\partial t}}_{\text{acc. term in solid phase}} = \underbrace{\overline{\epsilon}_t \, D_{app,j} \frac{\partial^2 C_{i,j}}{\partial x^2}}_{\text{axial dispersion term}} \tag{2.48}$$

and

$$\frac{\partial q_{i,j}}{\partial t} = k_{eff,i,j}(q_{e,i,j} - q_{i,j}) \tag{2.49}$$

with the initial and boundary conditions:

$$IC : C_{i,j}^{[y]}(0,x) = C_{i,j}^{[y-1]}(t_{switch},x) \tag{2.50a}$$

$$BC : \begin{cases} x = 0 : C_{i,j}^{[k]} = C_{i,j}|_{x=0} - \frac{D_{app,j}}{u_{m,j}} \frac{\partial C_{i,j}}{\partial x}|_{x=0} \\ x = L : \frac{\partial C_{i,j}}{\partial x}|_{x=L} = 0 \end{cases} \tag{2.50b}$$

where $C_{i,j}$ is the concentration of component i in the column j (g.L^{-1}), $u_{m,j}$ is the effective velocity in the column j (cm.min^{-1}), x is the axial coordinate (cm), $\overline{\epsilon}_t$ is the average total porosity (-), $q_{i,j}$ is the mass concentration of component i in the adsorbed-phase of the column j (g.L^{-1}), $C_{i,j}^{[k]}$ is the concentration of component i in the column j located at zone k (g.L^{-1}), L is the column length (cm) - the same for all columns, superscript y and k count the switching time intervals and zone, respectively, and t is the time (min), defined below:

$$t = \{t \in \mathbb{R} \ / \ 0 \leq t \leq t_{switch}\}.$$

The modeling strategy adopted requires the calculation of the column inlet con-

centration if the column is the first of its zone. This calculation was made as follow:

First column of zone 1:

$$C_{i,j}^{[1]} = \frac{Q_4 . C_{i,j-1}^{[4]}|_{x=L}}{Q_1}. \tag{2.51}$$

First column of zone 3:

$$C_{i,j}^{[3]} = \frac{Q_2 . C_{i,j-1}^{[2]}|_{x=L} + Q_F . C_{F,i}}{Q_3}. \tag{2.52}$$

The other columns:

$$C_{i,j}^{[k]} = C_{i,j-1}|_{x=L}, \tag{2.53}$$

where $C_{F,i}$ is the feed stream concentration of component i.

The effective velocity in the column j is defined below ($u_{m,j}$):

$$u_{m,j} = \frac{Q_j}{\epsilon_t \ A_s}, \tag{2.54}$$

where A_s is the chromatographic column cross-section area (cm^2).

The constitutive equations used were the thermodynamic equilibrium governed by the binary Langmuir (nonlinear) isotherm:

$$q_{e,i,j} = \frac{\overline{q}_m \overline{b}_i C_{i,j}}{1 + \sum_{i=A,B} \left(\overline{b}_i C_{i,j} \right)} \tag{2.55a}$$

$$\overline{b}_i = \frac{\overline{H}_i}{\overline{q}_m}, \tag{2.55b}$$

the subscript j has vanished from thermodynamic parameters ($\overline{H}_i$,$\overline{b}_i$, and $\overline{q}_m$) and $\overline{\epsilon}_t$ because an average of the values of each column was used [4]

From the overall mass balance in the nodes, it is possible to write:

[4]The chromatographic columns belong to the same manufacturer, and they are of the same model, even so, they were not the same, minor discrepancies among them exist, therefore an average was computed.

$$\textbf{Zone 1: } Q_1 = Q_D + Q_4 \text{ and } u_{m,1} = \frac{Q_1}{\bar{\epsilon}_t.A_s}; \tag{2.56a}$$

$$\textbf{Zone 2: } Q_2 = Q_1 + Q_X \text{ and } u_{m,2} = \frac{Q_2}{\bar{\epsilon}_t.A_s}; \tag{2.56b}$$

$$\textbf{Zone 3: } Q_3 = Q_2 + Q_F \text{ and } u_{m,3} = \frac{Q_3}{\bar{\epsilon}_t.A_s}; \tag{2.56c}$$

$$\textbf{Zone 4: } Q_4 = Q_3 + Q_R \text{ and } u_{m,4} = \frac{Q_4}{\bar{\epsilon}_t.A_s}, \tag{2.56d}$$

where A_s is the chromatographic column cross-section area (cm^2), and it is the same to all columns, Q_k is the volumetric flow rates in zone k ($cm^3.min^{-1}$), Q_D, Q_F, Q_X, and Q_R are the desorbent, feed, extract, and raffinate volumetric flow rates ($cm^3.min^{-1}$), respectively. The linear system composed by Equations 2.56 has a unique solution if one of the internal flow rates could be determined. In this case a HPLC pump is responsible for setting the flow rate in zone 2 (Q_2).

- Spatial Discretization

The spatial discretization approach adopted by the software was the Finite Differences Method. It was used to approximate the model equation in the discretized spatial domain. After discretization, a single Partial Differential Equation (PDE) becomes a n Ordinary Differential Equations (ODEs) system with time, t, as independent variable. In this method, the first derivative was approximated by a first-order backward approximation (*upwind differentiating scheme*) as follows:

$$\frac{\partial C_{i,j}(t,x)}{\partial x} \approx \frac{C_{i,j}(t)|_\eta - C_{i,j}(t)|_{\eta-1}}{\Delta x}. \tag{2.57}$$

A central finite differences equation approximated the second derivative:

$$\frac{\partial^2 C_{i,j}(t,x)}{\partial x^2} \approx \frac{C_{i,j}(t)|_{\eta+1} - 2C_{i,j}(t)|_\eta + C_{i,j}(t)|_{\eta-1}}{(\Delta x)^2}. \tag{2.58}$$

The subscript η determines the spatial position in coordinate x_η when the continuous domain is transformed into a discrete one with n internal elements spaced by a length of Δx and is defined as:

$$\eta = \{\eta \in \mathbb{Z} \ / \ 0 < \eta \leq n\}.$$

Therefore the Equation 2.48 can be approximated by the set of n ODEs:

$$\frac{dC_{i,j}|_{\eta}}{dt} + u_{m,j}\frac{C_{i,j}(t)|_{\eta} + C_{i,j}(t)|_{\eta-1}}{\Delta x} + \frac{1-\bar{\epsilon}_t}{\bar{\epsilon}_t}\frac{dq_{i,j}|_{\eta}}{dt} = ... \\ ... = D_{app,j}\frac{C_{i,j}(t)|_{\eta+1} - 2C_{i,j}(t)|_{\eta} + C_{i,j}(t)|_{\eta-1}}{(\Delta x)^2}. \tag{2.59}$$

The boundary conditions after discretization becomes:

$$BC: \begin{cases} x = 0 : C_{i,j}|_{\eta=0} = \frac{C_{i,j}^{[k]} - \frac{D_{app,j}}{u_{m,j}} C_{i,j}|_{\eta=1}}{1 - \frac{D_{app,j}}{u_{m,j}}} \\ x = L : C_{i,j}|_{\eta=n+1} = C_{i,j}|_{\eta=n} \end{cases} \tag{2.60a}$$

The number of n internal elements was chosen by a mesh test performed by ANDRADE [59]. The number of elements tested was 15, 30, 60, 120, and 240. A mesh was considered refined when the maximum difference between the CSS concentrations obtained with two subsequent meshes was lesser than one percent. The two last meshes accomplished the criterion; therefore, the chosen one was 120 elements.

The method of lines approach adopted as a solution strategy resulted in a stiff ODE system, thanks to the steep moving fronts of concentrations imposed by periodic switching. Therefore, an implicit 5^{th} order BDF integration algorithm was used to solve the system of ODEs using MatLab© (*ode15s*). The disadvantage of high computational costs required to build the jacobian matrix, to solve the nonlinear algebraic system at each integration step, was surpassed because sparse algebra was used to solve the sparse ODE system (more details see elsewhere [59]).

Table 2.5 shows the provided information to the software to run the simulations in this chapter.

Adjustment of the volumetric flow rate of zone 2 (Q_2)

It was previously assumed that the HPLC pump in zone 2 delivered exactly the set value. As the flow rates delivered by the external HPLC pumps (*i.e.*, feed, extract, and desorbent streams) showed discrepancies between the set and delivered values, the same can happen to the HPLC pump in zone 2. In light of it, the experimental flow rates, switching time and racemic concentration, and the Henry constants and porosity were used to simulate the SMB. Afterward, the simulated outlet concentrations were compared to experimental ones by using the **R**oot of **S**um of **S**quared **R**esiduals (RSSR), γ:

Table 2.5: Simulation parameters

More- and Less-retained components parameters (A and B)			
Thermodynamic parameters		$C_{A,F}(g.mL^{-1})$	$C_{B,F}(g.mL^{-1})$
Table 2.8 and Table F.1		Table C.1	Table C.1
Column parameters			
L_{column} (cm)	D_{column} (cm)	ρ_{ads} ($g.cm^{-3}$)	$\epsilon_{t,j}$ (-)
10	1	1.00	Table 2.8
SMB parameters			
Nº of columns	Columns per zone [z_1 z_2 z_3 z_4]		Nº of cycles
6	[1 2 2 1]		5 (2^{nd} stage)
t_{switch} (min)		$Q^{SMB}_{1,2,3,4}$ ($mL.min^{-1}$)	
Table C.1		Table C.1	
Solver control			
Nº of internal elements		Jacobian	
120		Numerical	
Abs. tolerance		Rel. tolerance	
10^{-8}		10^{-8}	
Integrator			
ode15s - Variable order BDF method			
Discretization method			
First order backwards finite difference (first derivative) Central finite difference (second derivative)			

$$\gamma = \sqrt{\left(\overline{C}_{A,X} - \overline{C}^{\,nlin}_{A,X}\right)^2 + \left(\overline{C}_{B,X} - \overline{C}^{\,nlin}_{B,X}\right)^2 + \left(\overline{C}_{A,R} - \overline{C}^{\,nlin}_{A,R}\right)^2 + \left(\overline{C}_{B,R} - \overline{C}^{\,nlin}_{B,R}\right)^2}, \tag{2.61}$$

where the superscript *nlin* denotes the simulation carried out in the nonlinear isotherm, the absence of superscript in the equation above implies that the data was experimentally determined.

For all the experiments, fifteen simulations were carried out, the difference among them was the increment of the Q_2 about the original one: -25%, -20%, -15%, -12%, -10%, -5%, -1% , 0%, 1%, 5%, 10%, 12%, 15%, 20% and 25%. The original runnings (*i.e.*, 0% Q_2) can be found in Appendix C. As Q_2 changed, the other internal flow rates were recalculated, in order to satisfy the mass balance.

2.7 Results and Discussion

2.7.1 Calculated parameters

The total porosity of each column j, their experimental error, and correlation coefficients are shown in Table 2.6. It is crucial to notice that the relative difference between the lowest and the highest porosity is less than 1%. Nevertheless, this insignificant difference can make a massive difference in SMB runnings with many completed cycles because cumulative error should occur due to the cyclic nature of the process.

Table 2.6: Porosity of each column, calculated error and determination coefficients

Column j	$\epsilon_{t,j}$ (-)	$\delta\epsilon_{t,j}$ (-)	R_j^2 (-)
1	0.7410		0.999
2	0.7389		0.999
3	0.7384	$\pm$ 0.0006	0.999
4	0.7455		0.998
5	0.7446		0.999
6	0.7427		0.999

The Henry coefficient for each solute (A or B) of each column j, their experimental error, and determination coefficients are shown in Table 2.7. The same discussion made for porosity is valid for the Henry coefficients.

Table 2.7: Henry constants, their errors and determination coefficients

Column j	$H_{A,j}(-)$	$\delta H_{A,j}$ (-)	$R_{A,j}^2$
1	9.38		0.999
2	9.11		0.999
3	9.28	$\pm$ 0.04	0.999
4	9.55		0.997
5	9.38		0.999
6	9.30		0.999
Column j	$H_{B,j}(-)$	$\delta H_{B,j}$ (-)	$R_{B,j}^2$
1	5.05		0.999
2	4.91		0.999
3	5.01	$\pm$ 0.02	0.999
4	5.15		0.995
5	5.04		0.999
6	5.01		0.999

The average porosity ($\overline{\epsilon}_t$), average Henry constant for each enantiomer ($\overline{H}_A$ and $\overline{H}_B$), and their experimental error among the columns in the SMB are shown in

Table 2.8. Typical chromatograms originated from these experiments can be found in Appendix D.

Table 2.8: Calculated average porosity and average Henry constants and corresponding experimental errors

$\overline{\epsilon}_t$	0.742	$\pm$ 0.003
$\overline{H}_A$	9.33	$\pm$ 0.15
$\overline{H}_B$	5.03	$\pm$ 0.08

It is essential to highlight that errors coming from Table 2.6 and Table 2.7 represent the experimental dispersion coming from the HPLC experiments. In contrast, the errors in Table 2.8 represent the dispersion among the chromatographic columns used in the SMB unit.

The effective mass transfer coefficient for each solute (A or B) of each column j, their experimental error, and determination coefficients are shown in Table 2.9. This mass transfer coefficient accounts for many kinetic effects that take place inside each chromatographic column.

Table 2.9: Effective mass transfer coefficients ($k_{eff,i,j}$), their errors and the determination coefficients

Column j	$k_{eff,A,j}(min^{-1})$	$\delta k_{eff,A,j}(min^{-1})$	$R^2_{A,j}$
1	46	$\pm$ 4	0.995
2	55	$\pm$ 4	0.997
3	45	$\pm$ 3	0.997
4	44	$\pm$ 4	0.997
5	47	$\pm$ 4	0.997
6	45	$\pm$ 4	0.998
Column j	$k_{eff,B,j}(min^{-1})$	$\delta k_{eff,B,j}(min^{-1})$	$R^2_{B,j}$
1	78	$\pm$ 2	0.996
2	92	$\pm$ 2	0.997
3	76	$\pm$ 2	0.997
4	75	$\pm$ 2	0.998
5	79	$\pm$ 2	0.997
6	77	$\pm$ 2	0.998

All the above parameters plus the diffusion coefficients helped to compose and, consequently, to interpret the phenomena involved in the SMB runnings.

2.7.2 Evaluation of mass transfer phenomena inside the chromatographic columns

The analysis of the *Péclet* number (Pe) for each column j can be made by recalling the Equations 2.38a and 2.39a:

$$D_{app,i,j,n} = \frac{A_{i,j} u_{m,j,n}}{2},$$
$$Pe_{i,j} = \frac{u_{m,j,n}.L}{D_{app,i,j,n}}$$

The $A_{i,j}$ (see Table 2.10) is an experimental parameter that depends on the enantiomer i and the chromatographic column j.

Table 2.10: $A_{i,j}$ and $C_{i,j}$ parameters

Column j	$A_{A,j}$	$C_{A,j}$	$A_{B,j}$	$C_{B,j}$
1	0.0072	0.0078	0.0060	0.0060
2	0.0085	0.0066	0.0072	0.0050
3	0.0063	0.0080	0.0057	0.0061
4	0.0062	0.0081	0.0056	0.0061
5	0.0069	0.0077	0.0060	0.0059
6	0.0063	0.0080	0.0058	0.0060

Substituting one into another, it gives:

$$Pe_{i,j} = \frac{2 \cdot L}{A_{i,j}} \tag{2.63}$$

Table 2.11: *Péclet* number of species A and B for each column

Column j	$Pe_{A,j}$	$Pe_{B,j}$
1	2,765	3,335
2	2,340	2,777
3	3,163	3,535
4	3,223	3,541
5	2,914	3,359
6	3,151	3,461

The analysis of the *Péclet* number for all columns and enantiomers indicates that advective transport rate is at least 2340 times greater than the dispersive transport rate. This magnitude means that dispersive transport phenomena can be neglected inside the chromatographic columns used in the built SMB unit and, therefore, the advective transport prevails.

Another important adimensional number to be examined is the mass transfer units for species i in a column j, $\alpha_{i,j}$. Recalling Equation 2.39b:

$$\alpha_{i,j} = \frac{k_{eff,i,j} \cdot L}{u_{solid}}.$$

This adimensional number will change if the switching time of the experiment changes, as it is related to the solid velocity (u_{solid}). All the experiments were carried out in the standard operation mode (*i.e.*, all the valves operated with constant and equal switching time interval throughout the cycles), therefore in the same experiment, the $\alpha_{i,j}$ varies with the effective mass transfer coefficient for each solute (A or B) of each column j, $k_{eff,i,j}$. Table 2.12 shows that for each experiment the value of $\alpha_{A,4}$ for the enantiomer in the chromatographic column with the smallest effective mass transfer coefficient (see Table 2.9).

Table 2.12: Adimensional number mass transfer units for species A in column *4*, $\alpha_{A,4}$

	Run 1	*Run 2*	*Run 3*	*Run 4*	*Run 5*
$\alpha_{A,4}$	157	388	291	385	157

From Table 2.12, it can be observed that mass transfer between the liquid and the solid phase is at least 157 times greater than the solid convective motion in an idealized TMB process. Translating to the SMB process, the shorter the switching time, the less the influence of the liquid-solid mass transfer at the expense of the influence of the relative movement of the solid phase.

Summing up, the axial dispersion and the mass transfer between liquid and solid phases can be neglected inside the column. This equilibrium assumption vanishes the necessity of a mass balance on the solid phase side because as soon as the solid phase and liquid phase get in contact with each other, equilibrium adsorption is immediately established in the solid-fluid interface and inside the adsorbent particle, because mass transfer effects are too fast and, consequently, they are not considered a limiting step:

$$\frac{\partial q_{i,j}}{\partial t} = \frac{\partial q_{e,i,j}}{\partial t}, \tag{2.64}$$

$q_{e,i,j}$ is the concentration of component i in the column j in equilibrium with the solid phase ($\mathrm{g.L^{-1}}$).

Therefore, Equation 2.48 becomes:

$$\underbrace{\bar{\epsilon}_t \frac{\partial C_{i,j}}{\partial t}}_{\text{acc. term in fluid phase}} + \underbrace{\bar{\epsilon}_t \, u_{m,j} \frac{\partial C_{i,j}}{\partial x}}_{\text{advection term}} + \underbrace{(1 - \bar{\epsilon}_t) \frac{\partial q_{e,i,j}}{\partial t}}_{\text{acc. term in solid phase}} = 0 \tag{2.65}$$

Equation 2.65 is known as the *ideal model*. It can predict advective motion throughout the interstitial space of the column and adsorption equilibrium of solutes in the surface of the solid phase. In order to complete the set of equations, only the constitutive equation is now required (*i.e.*, isotherm equation).

Previous work developed in our laboratory evaluated adsorption isotherms between PZQ enantiomers and the same CSP used in this work [60]. The *binary Langmuir* was the isotherm that was most suited to experimental data [60]. Another study has been developed in our group, and it extended the results to the column of this work, Chiralcel^{TM} OZ [61]. The parameters can be found in Appendix F.

2.7.3 PZQ separation using SMB process with Chiralcel^{TM} OZ as CSP

The main results of each experiment can be seen in Table 2.13 and Figure 2.10.

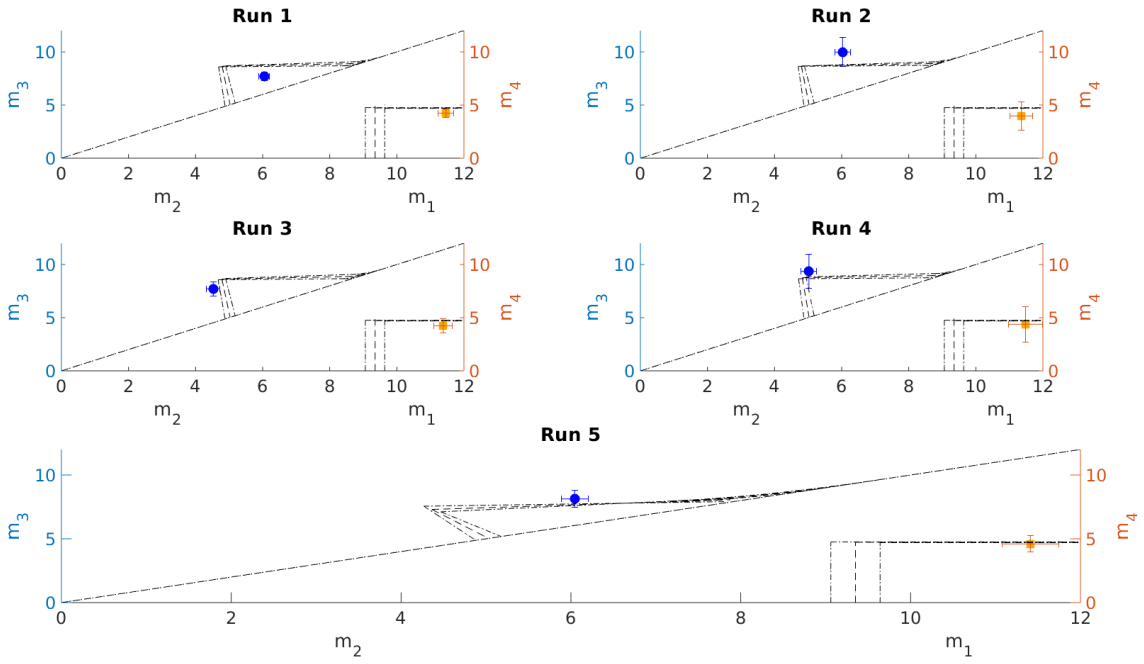

Figure 2.10: Separation region (circle dots) and regeneration region (square dots) of the *Run 1*, *Run 2*, *Run 3*, *Run 4*, and *Run 5*. The variation in the separation- and regeneration-region frontiers represented by dotted lines are due to thermodynamic parameters uncertainties and feed concentration experimental errors.

The first experiment (*Run 1*) was proposed intentionally inside the area of total separation/regeneration (see Figure 2.10). In this conservative scenario, the SMB unit operation is robust, that means, the variation of the enantiomers adsorption equilibrium constants due to room temperature changes (*i.e.*, oscillation of the thermodynamic parameters), feed concentration, column porosity, and fluctuations of the flow rate delivered by the pumps should not have an important role in the sepa-

ration, these are regular perturbations ignored by the equilibrium-theory approach [62, 63]. Therefore, the expected scenario would be the total separation of both outlet streams (raffinate and extract). However, the optical purity of the D-PZQ (A) in the extract stream was 97%, and the optical purity of the L-PZQ (B) in the raffinate stream was 100%. Despite the high optical purity in the extract stream, the complete separation did not occur mainly because the number of columns per zone is finite; the fifth fundamental consideration imposed by the equilibrium theory (*i.e.*, infinity columns per zone) could never be satisfied. Zones 2 and 3 are responsible for separating the racemic mixture of praziquantel (PZQ) from the racemic mixture inlet (Q_F), and they had two chromatographic columns each. It is a situation very far from the infinity number of chromatographic columns imposed by the TMB approach used to calculate the flow rate of the zones. The same discussion is valid for zones 1 and 4, responsible for regenerating the solid and liquid phases, respectively, and each zone had only one chromatographic column. It can be noticed that the frontier between inside and near (but outside) the borders of the separation area can be tiny and therefore dificult to be distinguished.

Table 2.13: Comparison of our work, Ching *et al.*** [1] and Lim *et al.*** [2]

	Run 1	Run 2	Run 3	Run 4	Run 5	Ching *et al.**	Lim *et al.**
$\overline{C}^{\#}_{\text{A or B},F}$	0.55 ± 0.03	0.53 ± 0.05	0.57 ± 0.01	0.46 ± 0.02	2.02 ± 0.04	25	25
$\text{Pur}^{\#}_{A,X}$	97 ± 2	99 ± 1	98.6 ± 0.2	98 ± 1	98 ± 1	90.1	85.9
$\text{Pur}^{\#}_{B,R}$	100 ± 0	68 ± 2	100 ± 0	78 ± 2	97.1 ± 0.2	93.7	97.5
$\text{Rec}^{\#}_{A,X}$	94 ± 10	47 ± 4	96 ± 3	71 ± 6	90 ± 4	94	98
$\text{Rec}^{\#}_{B,R}$	104 ± 10	102 ± 3	100 ± 3	97 ± 3	103 ± 5	90	84
$\text{Pr}^{\#}_{A}$	24 ± 4	11 ± 1	27 ± 2	16 ± 3	107 ± 4	115	n.a
$\text{Pr}^{\#}_{B}$	27 ± 3	26 ± 1	28,4 ± 0.5	22 ± 2	125 ± 2	110	n.a
DC	4.8 ± 0.4	2.5 ± 0.3	2.8 ± 0.1	2.9 ± 0.3	1.06 ± 0.02	0.29	0.35
$\text{t}^{\#}_{switch}$	3.55	8.78	6.58	8.71	3.55	45.0	30.0

* dispersion of the experiments **n**ot **a**vailable (n.a)
**A and B are the D-PZQ and L-PZQ, respectively
$\overline{C}$=[gL^{-1}] ; Pur=[-] ; Rec=[-] ; Pr=[g kg^{-1}_{ads} day^{-1}] ; DC=[$g_i L^{-1}$] ; t_{switch}=[min]

In comparison with *Run 1*, the scenario proposed by the second experiment (*Run 2*) kept constant the flow rate ratios in zones 1, 2, and 4, but flow rate ratio in zone 3 increased enough to shift the experiment into the contaminated raffinate area (see Figure 2.10). The expected results matched the experimental observations. The extract stream optical purity of the D-PZQ was 100%, and the raffinate stream optical purity of the L-PZQ was contaminated mainly by the D-PZQ. As almost no L-PZQ was detected in the extract stream, its recovery in the raffinate stream was 100%. On the other hand, the D-PZQ went out as a contaminant in the raffinate stream, this was the reason to observe a dropping in its recovery and, consequently, a drop in its productivity, while the productivity of L-PZQ remained the same as *Run 1*.

The third experiment (*Run 3*) maintained the constant flow rate ratios in zones 1,

3, and 4, while the flow rate ratio in zone 2 decreased enough to shift the experiment into the contaminated extract area (see Figure 2.10). Therefore, high recoveries of both enantiomers helped to maintain the productivity of both enantiomers in the same level of *Run 1*. The L-PZQ, 98.6%, slightly contaminated the extract stream, and the optical purity of the L-PZQ in the raffinate was 100%. This experiment ran outside but close to the triangle of separation.

The fourth experiment (*Run 4*) intended to shift the SMB unit near the vertex of the triangle. At this point, the separation should still occur, but now with maximum productivity and less (but not minimum) desorbent consumption. This situation is a desired operating point, but unfortunately, it is not a robust operation because operation turns to be very sensitive to temperature changes (*i.e.*, oscillation of thermodynamic parameters), fluctuations of the flow rate delivered by the pumps, and a finite number of columns in a real SMB unit. As expected, the operation ran out of the separation area, culminating in the contamination of the raffinate stream and a highly purified extract stream. This experiment evidences the necessity of good control strategies in order to shift the SMB unit operation as near as possible to the triangle vertex. The *Run 1*, *Run 2*, *Run 3*, and *Run 4* validated the built-in-house SMB unit.

The fifth experiment (*Run 5*) was carried out aiming at a semi-preparative scale. As a consequence, the productivity increased, and the desorbent consumption decreased, both significantly. This situation evidences the most crucial reason to operate a real SMB unit in higher concentrations (*i.e.*, nonlinear region of the isotherms).

Despite the concentration of the racemic mixture in Ching *et al.* [1] and Lim *et al.* [2] experiments being approximately ten times greater than the fifth experiment (*Run 5*). Almost all our SMB unit performance parameters were very near or even superior (see Table 2.13). In *Run 5*, the performance parameters related to the extract stream were very similar or superior in comparison to Ching *et al.* [1] and Lim *et al.* [2]; the high optical purity of D-PZQ is the performance parameter that stands out. In contrast, the others vary approximately on the same level. The raffinate stream produced L-PZQ with 97.1% optical purity, 100% recovery, and productivity 14% greater than the Ching *et al.* [1] experiment. It is an exciting scenario because L-PZQ is the component of significant interest, thanks to its ability to kill parasitic worms. The comparison of productivity with Lim *et al.* [2] was not possible because any information that could calculate the total quantity of CSP was found. These are fascinating results because an excellent production of high-purity streams could be produced continuously by our SMB unit. The fifth experiment did not overcome the desorbent consumption parameter; this happened due to the high feed concentration of the racemic mixture in the compared works. But, the desorbent consumption in *Run 5* decreased 4.5 times in comparison to *Run 1*, thanks

to the increase in the feed concentration from 1 to 4 gL^{-1} of the racemate. It is important to emphasize that the feed concentrations reported in literature works are 12.5 times higher than in *Run 5*. The presence of zone 4 (*i.e.*, desorbent recycle stream) decreases the fresh desorbent consumption, which is highly desired towards the preparative scale.

Another important feature was the much faster dynamic of the present SMB unit. It is a consequence of the use of cellulose tris(3-chloro-4-methylphenylcarbamate) (Chiralcel^{TM} OZ) as CSP. This CSP improved a lot the separation efficiency due to the better mechanical stability in comparison to MCTA and its molecular structure, which has particular substituents situated in the aromatic rings of the polysaccharide phenyl moiety (for more details, see [55, 64]). The latter feature makes this CSP not soluble in polar desorbents (like ethanol), and this is highly desirable, as PZQ has excellent solubility in ethanol. Besides that, the interstitial porosity in each chromatographic column was very high, allowing an excellent interface between liquid and solid phases. Our unit achieved the Cyclic Steady State (CSS) much faster, approximately 106 minutes in *Run 5*, while the work of Ching et al. [1] achieved the CSS in 540 minutes (= 9 hours), and the work of Lim *et al.* [2] was not evident when the SMB unit achieved the CSS, but 30 minutes to switch the valves, 8 chromatographic columns and MCTA as CSP should make the unit achieve the CSS in some hours (> 106 minutes).

Run 1, *Run 3* and *Run 5* produced high purity of both streams, especially for *Run 1* and *Run 3*, which produced 100% purity of L-PZQ in the raffinate stream. The importance of L-PZQ is not restricted to being the active principle against *Schistosoma*. Modifications in the L-PZQ molecular structure have been the subject of research to make L-PZQ more active against more resistant parasites and juvenile ones. Moreover, all the raffinate streams produced L-PZQ in a concentration higher than the produced D-PZQ in the extract streams.

All runnings produced high purity of D-PZQ in the extract stream. This situation is of utmost importance for racemization studies; once a racemate is produced from pure D-PZQ. Producing racemate from pure D-PZQ should allow better process performance parameters once part of the extract outlet stream could be reintroduced in the racemic solution inlet stream.

2.7.4 Adjustment of the volumetric flow rate of zone 2 (Q_2)

As explained in the methodology section of this chapter, the external flow rates could be experimentally determined or inferred, but the internal ones could not. With the help of the software developed in our group [59] and presented in Section 2.6.3, the calculated enantiomeric concentrations in the outlet streams were compared with

the experimental ones, both in the CSS, by the Root of Sum of Squared Residuals (RSSR), γ. As can be observed from Figure 2.11, the Q_2 changes of 5% and 10% presented null γ for almost all the experiments carried out (*i.e.*, *Run 1*, *Run 2*, *Run 3*, and *Run 4*).

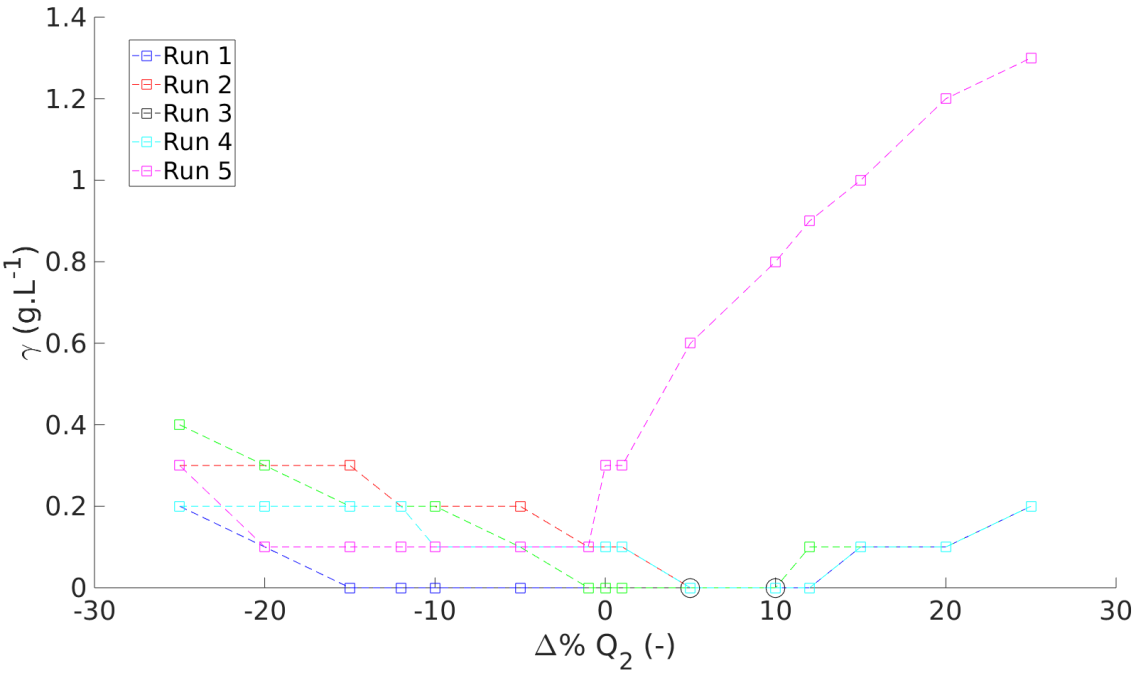

Figure 2.11: The behavior of γ vs. $\Delta\%$ Q_2. The 5% and 10% change in Q_2 were highlighted because almost all runnings presented null γ between these values.

2.8 Conclusions

The built SMB unit was tested in different conditions, and almost all of them kept at least one high optical purity stream. In *Run 1* and *Run 3*, the L-PZQ was produced in the raffinate stream with 100% optical purity. In *Run 2*, the extract stream was produced with 100% of optical purity. When the optical purity was high, the recovery percentage and productivity were kept high too. The time needed to achieve the CSS was also advantageous compared with the literature due to the shorter switching time and better stationary phase. Many performance parameters surpassed the literature works, which used high concentration, 50 $g.L^{-1}$ of the racemic mixture. The built-in-house SMB unit can operate with better performance parameters but using lower rac-PZQ concentration.

The SMB unit design, together with the high-performance cellulose tris(3-chloro-4-methyl-phenylcarbamate) (Chiralcel^{TM} OZ) as a CSP, allowed to separate the enantiomers efficiently. It is essential to keep in mind that the active principle, L-PZQ, is desired, but also the D-PZQ is needed with high optical purity too, as both

of them could be required for many different applications.

The software developed in our group was an advantage to determine the real Q_2 better once the external flow rates and outlet and inlet concentrations are available to feed the simulator. The determination of Q_2 helped to interpret better the SMB separations that occurred in the CSS because it allowed simulating the experiments more realistically without imposing a TMB model to interpret the results as done in the equilibrium theory. However, the intrinsic dynamics of each experiment cannot yet be determined without proper online measuring equipment, which could quantify each enantiomer in the outlet streams. This issue is the subject of the next chapter.

Chapter 3

Online measurement of praziquantel

The main focus of this chapter is to calibrate and validate the *chiral detector* equipment responsible for measuring the concentration of different enantiomers, even if both enantiomers are in the same solution.

3.1 Introduction

There is a growing need for analytical and preparative separation methods, and, consequently, there is a rising demand for fast and accurate chiral identification coming from these methods. Many separation-based methods have been used to identify chiral enantiomers (*i.e.*, HPLC and gas chromatography). However, these techniques require much time to identify enantiomers, making them unsuitable for online measurements [65, 66]. Fortunately, new methods for the determination of enantiomers have emerged, and spectroscopy is one of them.

Spectroscopy has high sensitivity, good selectivity, and high response speed. Many techniques, including ultraviolet and visible (UV-vis) and circular dichroism (CD) spectroscopy, have been explored. The former, when combined with other spectroscopy techniques, offers essential information, for instance, about molecular structures [67] and material characterization [68, 69]. CD spectra are an essential tool to recognize and quantify chiral enantiomers (*e.g.*, for medical diagnostics) [70–74], to determine absolute configurations and secondary structures of macromolecules [75–83], and so forth. Many types of research and reviews about UV-vis and CD absorption can be found elsewhere [67, 84, 85].

CD spectroscopy was the chosen technique because it handles the quantification of enantiomers with high precision and fast response [86]. This technique responds directly to the intrinsic optical activity of chiral molecules [71, 87]; this means that

the chiral center of the molecule interacts with the incident polarized electromagnetic radiation by electronic absorption at a wavelength [81]. This interaction allows selective detection while achiral compounds surrounding the chiral molecules are transparent [88]. The first usage of this technique was to study absolute configurations and secondary structures of macromolecules in the 1960s [85]. In 1980, DRAKE *et al.* [89] used for the first time information coming simultaneously from the CD absorption (difference absorption of left- and right-circularly polarized light, $\Delta A = A_L - A_R$) and UV-vis (average absorption of A_L and A_R, $A = \overline{A}_L + \overline{A}_R$ [84]) to calculate their ratio, known as g-factor (also known as anisotropy or dissymmetry factor). The authors observed an invariant and equal, but opposite in sign, g-factor values for the extremes of enantiomeric excess (ee), indicating pure fractions of each enantiomer. Equation 3.1 shows the relationship between ee and g-factor (g):

$$g = \frac{\Delta A}{A} \propto \frac{C_1 - C_2}{C_1 + C_2} = ee, \tag{3.1}$$

where C is the enantiomer concentration, and subscripts 1 and 2 denote a generic pair of enantiomers. It was also observed that in-between these limits, the ee of intermediate fractions could be determined too. The output of UV-vis and CD instruments are usually measured in *Abs* and *mdeg* (ellipticity), respectively [84].

After that, many works came using this approach [80, 90–97]. BERTUCCI *et al.* [90] and SALVADORI *et al.* [91] studied the simultaneous absorption of UV-vis and CD coming from an HPLC using a chiral stationary phase; the g-factor approach was used to optimize the collection of enantiomeric fractions with high purity in preparative chromatography and the last one used the information coming from CD to recognize the absolute stereochemistry of the eluted enantiomers. ZUKOWSKI *et al.* [92] used CD-UV detectors in series for g-factor calculation. The main advantage of this approach is the possibility to choose a different wavelength for UV and CD absorptions, which permitted to choose a wavelength of maximum sensitivity in the CD detector; on the other hand, the detection was limited in situations of large or small ee. BERTUCCI *et al.* [80] and SONG *et al.* [95] used simultaneous absorption of CD and UV-vis in a nonchiral HPLC system to validate the relationship between ee and g-factor for different enantiomeric drugs and glucose, respectively. SANCHEZ *et al.* [93] created a method to measure the ee of mixtures of bupivacaine enantiomers using the anisotropy factor. LECOEUR-LORIN *et al.* [94] studied a molecule with two chiral center, benzoxathiepin, and an a-factor was defined as a dimensionless parameter related to diastereoisomers (analogous to g-factor for stereoisomers with one chiral center). The UV-vis and CD absorption were simultaneously recorded, and a relationship among diastereoisomeric purity, enantiomeric purity, and a-factor was proposed. HAN e MARTIN [96] calculated the

g-factor coming from membrane permeate to get its ee of 1-phenylethanol. TANG *et al.* [97] studied the nonlinear absorption for CD and UV to calculate the ee for different enantiomers in order to test the developed method.

The main drawback of the use of the g-factor is that enantiomer concentrations remain unknown. For many analytical purposes, concentration could not be essential to be determined. However, for preparative purposes, concentration is vital to be known in order to accomplish control tasks mainly in continuous chromatographic separations [49, 98, 99]. Besides that, most works usually studied the limiting case, where the ee and g-factor have a linear relationship. This limiting case is known as the Beer-Lambert-Bouguer law [100, 101]. In short, this law works when the average distances between molecules in a solvent (*e.g.*, enantiomers) are not small enough to affect the charge distribution of surrounding molecules. This scenario vanishes at higher concentrations or even when concentration is not too high, but there are significant associations between solvent-enantiomer, enantiomer-enantiomer, or both. [100, 102].

The novelty of this chapter is the development of an online measurement system for enantiomers using an empirical mathematical relationship between UV-vis/CD signals recorded simultaneously and the concentration of each praziquantel enantiomer, which have significant nonlinear behavior even at small concentrations.

3.2 Materials and methods

3.2.1 Materials

- Ethanol HPLC grade was the solvent, provided by Biograde (Brazil);
- Racemic mixture of praziquantel with pharmaceutical-grade was manufactured by Yixing Xingyu Medical Chemical Co. and provided by Farmanguinhos (Rio de Janeiro, Brazil), and their molecular structure formula is presented in Figure 3.1 .

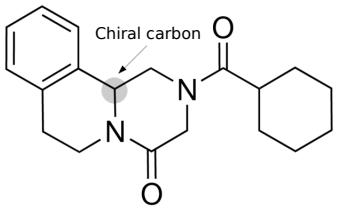

Figure 3.1: Molecular structure of praziquantel.

3.2.2 Equipment

The equipment used in the HPLC system and in the SMB unit was described in Section 2.5.1.

The calibration was done using a *Chiral Detector* [1] (CD-2095) and an HPLC pump (PU-2086), both provided by Jasco Company.

3.2.3 Racemate separation into pure enantiomers

The pure levo-praziquantel (L-PZQ) and pure dextro-praziquantel (D-PZQ) were obtained by separating a racemate using the build-in-house SMB unit. Three runnings were made with a 5 $g.L^{-1}$ of racemate in the feed stream. These runnings produced raffinate streams with a purity of 99.6% $\pm$ 0.2 of L-PZQ and extract streams with 98.8% $\pm$ 0.3 of D-PZQ. The resulting raffinate streams were reallocated in the SMB feed stream again to get L-PZQ with 100% purity. The same procedure was followed for the extract streams to get pure D-PZQ.

3.2.4 Determination of the wavelength by spectrum measurement

An amount of 1800 μL of a solution of well-known concentration of praziquantel in ethanol was injected into an HPLC without a chromatographic column and HPLC pump set to 1 $mL.min^{-1}$. This injection was repeated for different concentrations and for each enantiomer (0.25, 0.50, 0.75, 1.00, 1.25, 1.75, 2.00, 2.25, 2.50, 2.75, 3.00 and 3.50 $g.L^{-1}$). For each concentration, the experiments were replicated three times. The baseline spectrum and in the sequence the sample spectrum was measured by stopped-flow scanning. The latter spectrum was measured at the peak top of the chromatogram. Each output gave a CD and a UV spectrum for each concentration and each enantiomer. The spectrum scanning range was fixed from 220 to 420 nm. A Hg-Xe lamp and a monochromator with a relatively wide spectral bandwidth (20 nm) were used.

For a fixed wavelength, plots of concentration versus signal were compared for the two enantiomers to find the relationship closer to a linear correlation between the signal and concentration. This comparison was made using the coefficient of determination (R^2).

[1] This equipment records simultaneously the UV-vis and CD signals.

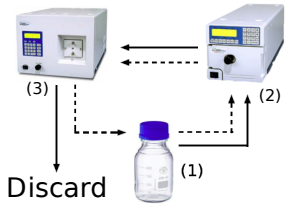

Figure 3.2: **Dotted line circuit:** baseline establishment. **Full line circuit:** Uv-vis and CD data recorder for a fixed concentration and wavelength. The solvent flow rate of 1 mL.min^{-1} in both circuits. (1) pure ethanol (dotted circuit)/ praziquantel solution (full circuit) flask, (2) HPLC pump, and (3) Chiral detector.

3.2.5 Collection of UV-vis and CD data for each PZQ solution

The methodology below was used to collect UV-vis and CD data for each PZQ solution (see Figure 3.2):

1. Ethanol was run in a closed-circuit (dotted line circuit) with an HPLC pump (2) and a CD-2095 (3). The solvent flow rate was 1 mL.min^{-1};

2. the autozero key was pressed in the CD-2095 when the CD signal voltage was oscillating in-between 0±0.03V;

3. after a baseline was observed for both signals; the circuit was changed from closed-circuit (dotted line circuit) to open-circuit (full line circuit). Therefore, the flask of pure ethanol (dotted line circuit) was substituted by a flask with a solution of well-known PZQ concentration (full line circuit);

4. after a new baseline was established for both signals, the points were recorded, and subsequently, the mean value and experimental dispersion were calculated using LabView® software.

The output ranges set in the CD-2095 were 0.04 Abs.(10.mV)$^{-1}$ and 0.0005 deg.(10.mV)$^{-1}$.

This procedure was repeated for different concentrations of pure enantiomers (see Table H.1) and mixtures with the total concentration of enantiomers of 0.25, 0.75 and 1.00 g.L^{-1} (see Table H.2). From these tables, it is possible to see that the concentration range in which the calibration is valid is between 0 and 1.25 gL^{-1}.

3.2.6 Calibration and validation procedure

The method **L**eave-**O**ne-**O**ut **C**ross-**V**alidation (LOOCV) is a particular case of the cross-validation method, and it was used in this work. In this method, the data of

mixtures is repeatedly split into a validation set (Ω_j^{val}) and a calibration (or training) set (Ω_j^{cal}). Mathematically, it can be written in the following way:

$$\Omega^{pur} = \{\omega_1^{pur}, \omega_2^{pur}, ..., \omega_{10}^{pur}\};$$
$$\Omega^{mix} = \{\omega_1^{mix}, \omega_2^{mix}, ..., \omega_{r-1}^{mix}, \omega_r^{mix}, \omega_{r+1}^{mix}, ..., \omega_{14}^{mix}\}.$$

The pair of signals and the related pair of enantiomer concentrations ($\overline{S}_{UV}$: $\overline{S}_{CD}//C_D$: C_L) were represented by ω in the subsets. Their labels are in Table H.1 and Table H.2. The union of these two subsets gives the total set, Ω:

$$\Omega = \Omega^{pur} \cup \Omega^{mix}.$$

The LOOCV method used consists of leaving the *r-th* element out of the subset Ω^{mix}, which was used as the *r-th* validation set (Ω_j^{val}), defined as follows:

$$\Omega_r^{val} = \{\omega_r^{mix} \in \Omega^{mix}\},$$

where r is the subscript defined as

$$r = \{r \in \mathbb{N} \mid 1 \leq r \leq 14\}.$$

Consequently, the *r-th* calibration set, Ω^{cal}, is defined as

$$\Omega_r^{cal} = \Omega \backslash \Omega_r^{val},$$

that means Ω_r^{cal} is composed of all the elements present in the total set, Ω, minus the *r-th* element composing the validation set, Ω_r^{val}.

The Calibration step (see Section 3.2.7) was the first to be executed and, right after, the validation step (see Section 3.2.8) was executed for each empirical mathematical model that followed the expansions below for each calibration subset (r):

$$\hat{\mathbf{S}}_{UV,r} = \sum_{k=0}^{m}\sum_{q=0}^{p}\{\lambda_{kq,r}\mathbf{C}_{L,r}^{k}\mathbf{C}_{D,r}^{q}\} = \mathbf{f}_r^{UV}\left(\lambda_{kq,r}\right), \tag{3.3}$$

$$\hat{\mathbf{S}}_{CD,r} = \sum_{k=0}^{m}\sum_{q=0}^{p}\{\psi_{kq,r}\mathbf{C}_{L,r}^{k}\mathbf{C}_{D,r}^{q}\} = \mathbf{f}_r^{CD}\left(\psi_{kq,r}\right), \tag{3.4}$$

where $\hat{\mathrm{S}}_{UV,r}$ is the computed UV signal (*Abs*), $\hat{\mathrm{S}}_{CD,r}$ is the computed CD signal (*mdeg*), $\mathbf{C}_{L,r}$ is the *r-th* calibration set vector of experimental L-PZQ concentration ($g.L^{-1}$), $\mathbf{C}_{D,r}$ is the *r-th* calibration set vector of experimental D-PZQ concentration ($g.L^{-1}$), $\lambda_{k,q}$ is the parameter associated with UV signal equation, $\psi_{k,q}$ is the parameter associated with CD signal equation, m and p are the upper limits of k and q, respectively, and are defined as

$$m, p = \{m, p \in \mathbb{N} \mid 0 \leq m, p \leq 2\}.$$

The different upper limits generated five different polynomial equations used in the calibration process (see Equation 3.7).

$$\hat{\mathbf{S}}_{UV,r} = \begin{cases} \sum_{q=0}^{1}\{\lambda_{0q,r}\mathbf{C}_{D,r}^{q}\} + \sum_{k=0}^{1}\{\lambda_{k0,r}\mathbf{C}_{L,r}^{k}\} = \mathbf{f}_{1,r}^{UV} \\ \sum_{k=0}^{1}\sum_{q=0}^{1}\{\lambda_{kq,r}\mathbf{C}_{L}^{k}\mathbf{C}_{D}^{q}\} = \mathbf{f}_{2,r}^{UV} \\ \sum_{k=0}^{1}\sum_{q=0}^{2}\{\lambda_{kq,r}\mathbf{C}_{L}^{k}\mathbf{C}_{D}^{q}\} = \mathbf{f}_{3,r}^{UV} \\ \sum_{k=0}^{2}\sum_{q=0}^{1}\{\lambda_{kq,r}\mathbf{C}_{L}^{k}\mathbf{C}_{D}^{q}\} = \mathbf{f}_{4,r}^{UV} \\ \sum_{k=0}^{2}\sum_{q=0}^{2}\{\lambda_{kq,r}\mathbf{C}_{L}^{k}\mathbf{C}_{D}^{q}\} = \mathbf{f}_{5,r}^{UV} \end{cases} \tag{3.5}$$

It is essential to highlight that the function $\mathbf{f}_{1,r}^{UV}$ in Equation 3.7 does not have interaction terms added to the polynomial equation, which means $\mathbf{f}_{1,r}^{UV}$ says that each enantiomer gives the same contribution as if it were pure to the UV signal.

The $\psi_{kq,r}$ parameters were estimated analogously by replacing UV data with CD data and the discussion about the $\mathbf{f}_{1,r}^{CD}$ is similar (Equation 3.6).

$$\hat{\mathbf{S}}_{CD,r} = \begin{cases} \sum_{q=0}^{1}\{\psi_{0q,r}\mathbf{C}_{D,r}^{q}\} + \sum_{k=0}^{1}\{\psi_{k0,r}\mathbf{C}_{L,r}^{k}\} = \mathbf{f}_{1,r}^{CD} \\ \sum_{k=0}^{1}\sum_{q=0}^{1}\{\psi_{kq,r}\mathbf{C}_{L,r}^{k}\mathbf{C}_{D,r}^{q}\} = \mathbf{f}_{2,r}^{CD} \\ \sum_{k=0}^{1}\sum_{q=0}^{2}\{\psi_{kq,r}\mathbf{C}_{L,r}^{k}\mathbf{C}_{D,r}^{q}\} = \mathbf{f}_{3,r}^{CD} \\ \sum_{k=0}^{2}\sum_{q=0}^{1}\{\psi_{kq,r}\mathbf{C}_{L,r}^{k}\mathbf{C}_{D,r}^{q}\} = \mathbf{f}_{4,r}^{CD} \\ \sum_{k=0}^{2}\sum_{q=0}^{2}\{\psi_{kq,r}\mathbf{C}_{L,r}^{k}\mathbf{C}_{D,r}^{q}\} = \mathbf{f}_{5,r}^{CD} \end{cases} \tag{3.6}$$

3.2.7 Calibration

The calibration was performed with Matlab® tool lsqcurvefit to find the best value of the objective function, $G(\hat{C}_{i,r})$, to find the parameters $\lambda_{kq,r}$, and $\psi_{kq,r}$.

The problem solved for each calibration subset (r) was:

$$\begin{cases} \min\limits_{\lambda_{kq,r},\psi_{kq,r}} G(\lambda_{kq,r}, \psi_{kq,r}) \\ G(\lambda_{kq,r}, \psi_{kq,r}) = \left(\mathrm{S}_{UV,r} - \hat{\mathrm{S}}_{UV,r}\right)^2 + \left(\mathrm{S}_{CD,r} - \hat{\mathrm{S}}_{CD,r}\right)^2 \end{cases} \tag{3.7}$$

where $\lambda_{kq,r}$ is the parameter of the *r-th* calibration set (Abs L^{k+q} $\mathrm{g}^{-(k+q)}$), $\psi_{kq,r}$ is the parameter of the *r-th* calibration set (mdeg L^{k+q} $\mathrm{g}^{-(k+q)}$), $\mathrm{S}_{UV,r}$ and $\hat{\mathrm{S}}_{UV,r}$ are the *r-th* calibration set of observed and predicted UV signals (Abs), respectively,

$S_{CD,r}$ and $\hat{S}_{CD,r}$ are the *r-th* calibration set of observed and predicted CD signals (mdeg), respectively, and the initial guess for each parameter is zero.

3.2.8 Validation

The validation problem used Matlab® tool lsqnonlin to find the best value of the objective function, $F(\hat{C}_{i,r})$, to compute the concentrations. The problem solved was:

$$\begin{cases} \min\limits_{\hat{C}_{i,r}} F(\hat{C}_{i,r}) \\ F(\hat{C}_{i,r}) = \left(S_{UV,r} - \hat{S}_{UV,r}\right)^2 + \left(S_{CD,r} - \hat{S}_{CD,r}\right)^2 \\ \text{subjected to: } \hat{C}_{i,r} \in [0, 1.25] \end{cases} \tag{3.8}$$

where $S_{UV,r}$ and $\hat{S}_{UV,r}$ are the *r-th* validation set of observed and predicted UV signals (Abs), respectively, $S_{CD,r}$ and $\hat{S}_{CD,r}$ are the *r-th* validation set of observed and predicted CD signals (mdeg), respectively, and the initial guess for each enantiomer concentration is zero. For the sake of clarity, Equations 3.3 and 3.4 were rewritten. However, now the parameters $\lambda_{kq,r}$, and $\psi_{kq,r}$ are known from the *r-th* calibration procedure (see Subsection 3.2.7), and the L- and D-PZQ concentrations were calculated:

$$\hat{\mathbf{S}}_{UV,r} = \sum_{k=0}^{m}\sum_{q=0}^{p}\{\lambda_{kq,r}\hat{\mathbf{C}}_{L,r}^{k}\hat{\mathbf{C}}_{D,r}^{q}\} = \mathbf{f}_{r}^{UV}\left(\hat{\mathbf{C}}_{L,r}, \hat{\mathbf{C}}_{D,r}\right), \tag{3.9}$$

$$\hat{\mathbf{S}}_{CD,r} = \sum_{k=0}^{m}\sum_{q=0}^{p}\{\psi_{kq,r}\hat{\mathbf{C}}_{L,r}^{k}\hat{\mathbf{C}}_{D,r}^{q}\} = \mathbf{f}_{r}^{CD}\left(\hat{\mathbf{C}}_{L,r}, \hat{\mathbf{C}}_{D,r}\right), \tag{3.10}$$

where $\hat{\mathbf{C}}_{L,r}$ and $\hat{\mathbf{C}}_{D,r}$ are the *r-th* validation set of calculated concentrations of L- and D-PZQ ($g.L^{-1}$), respectively. These calculated concentrations were compared with the experimental ones using the metric called total Mean Square Error, MSE_t (see Equation 3.12).

Total Mean Square Error metric

The metric adopted to compare different models performance was the **M**ean **S**quare **E**rror (MSE), which is the average of the n sum of squared error of each validation set r for each enantiomer i:

$$MSE_i = \frac{\sum\limits_{r=1}^{n}\left(C_{i,r} - \hat{C}_{i,r}\right)^2}{n}, \tag{3.11}$$

where n is the total number of observations ($n = 14$), $C_{i,r}$ is the observed concentration of enantiomer i in the *r-th* validation set ($g.L^{-1}$) and the $\hat{C}_{i,r}$ is the predicted

concentration of enantiomer i in the *r-th* validation set ($g.L^{-1}$). As two MSE were generated, one for each enantiomer (L-PZQ and D-PZQ), both were summed in order to get a total, MSE_t:

$$MSE_t = MSE_L + MSE_D \tag{3.12}$$

This metric was used to evaluate the performance of each model.

3.3 Results and Discussion

3.3.1 Wavelength determination

There is a range of wavelengths in which the CD signal of D-PZQ is negative and of L-PZQ is positive. That means the wavelength of interest is in between this range. The enantiomers' spectra become indistinct for longer wavelengths and near-zero; the same is observed for longer wavelengths in the UV spectra. Every tested concentration presented opposite signs in between 238 nm and 252 nm, as can be seen in Table I.1. Figure I.1 illustrates a typical spectrum observed.

The range of concentration between 0.25 to 1.25 g.L^{-1} was chosen in the wavelength of 242 nm because a linear relationship between the signals and concentrations of the pure enantiomers was observed. Equation 3.13 provides the four linear equations fitted for absorption signal ($\overline{S}_{UV}$), in Abs, and circular dichroism signal ($\overline{S}_{CD}$), in mdeg, for each pure enantiomer.

$$\overline{S}_{UV,L} = 0.20.C_L + 0.03 \qquad R^2 = 0.99 \tag{3.13a}$$
$$\overline{S}_{CD,L} = 4.48.C_L + 1.31 \qquad R^2 = 0.99 \tag{3.13b}$$
$$\overline{S}_{UV,D} = 0.13.C_D + 0.03 \qquad R^2 = 0.99 \tag{3.13c}$$
$$\overline{S}_{CD,D} = -3.33.C_D - 0.13 \qquad R^2 = 0.97 \tag{3.13d}$$

From these equations, it is possible to state that each enantiomer absorbs UV-vis and CD signal differently from each other, which means there is no symmetry in absorption. Furthermore, there are linear correlations between signal and concentration of each pure enantiomer in the selected wavelength and concentration interval.

3.3.2 Searching for the best empiric model

After the calibration and validation steps were applied, the MSE$_t$ of all tested empiric models were calculated and, therefore, Figure 3.3 could be built. The predictions

of L-PZQ concentration were systematically better than the D-PZQ concentration. Thanks to the inability to predict interactions (nonlinear terms) between the enantiomers in the mixtures, the 3-parameters model for both equations of the system presented the worst prediction of D-PZQ concentration. Keeping the 3 parameters fixed in the UV equation and increasing the number of parameters in the CD equation, it could be seen in a general way that the MSE of both enantiomers decreased in comparison to the 3-parameters CD equation. Therefore, the terms predicting the interaction between both enantiomers in the mixture are of utmost importance.

3.3.3 Best empiric model

The smallest value of MSE_t found was 0.005, and it was predicted by the model composed of 6 parameters in the UV and CD equations:

$$\begin{cases} \mathrm{S}_{UV} = \sum_{k=0}^{2}\sum_{q=0}^{1}\{\lambda_{kq}\hat{C}_L^k\hat{C}_D^q\} & R^2 = 0.98 \\ \mathrm{S}_{CD} = \sum_{k=0}^{2}\sum_{q=0}^{1}\{\psi_{kq}\hat{C}_L^k\hat{C}_D^q\} & R^2 = 0.99 \end{cases} \tag{3.14}$$

The calculated parameters are presented in Table 3.1.

Table 3.1: Estimated model parameters and their standard deviations

$\overline{\lambda}_{00} \pm \delta\lambda_{00}$	$\overline{\lambda}_{01} \pm \delta\lambda_{01}$	$\overline{\lambda}_{10} \pm \delta\lambda_{10}$
0.040 ± 0.003	0.119 ± 0.003	0.183 ± 0.009
$\overline{\lambda}_{11} \pm \delta\lambda_{11}$	$\overline{\lambda}_{20} \pm \delta\lambda_{20}$	$\overline{\lambda}_{21} \pm \delta\lambda_{21}$
0.005 ± 0.014	0.009 ± 0.006	0.493 ± 0.012
$\overline{\psi}_{00} \pm \delta\psi_{00}$	$\overline{\psi}_{01} \pm \delta\psi_{01}$	$\overline{\psi}_{10} \pm \delta\psi_{10}$
-0.513 ± 0.073	-2.971 ± 0.077	9.899 ± 0.195
$\overline{\psi}_{11} \pm \delta\psi_{11}$	$\overline{\psi}_{20} \pm \delta\psi_{20}$	$\overline{\psi}_{21} \pm \delta\psi_{21}$
-17.041 ± 0.560	-3.405 ± 0.118	9.396 ± 1.432

units: λ_{kq} = [Abs L^{k+q} $\mathrm{g}^{-(k+q)}$], ψ_{kq} = [mdeg L^{k+q} $\mathrm{g}^{-(k+q)}$]

The parameters mean values in Table 3.1 were calculated as follows:

$$\overline{\lambda}_{kq} = \frac{\sum_{r=1}^{n}\{\lambda_{kq,r}\}}{n} \tag{3.15}$$

and

$$\overline{\psi}_{kq} = \frac{\sum_{r=1}^{n}\{\psi_{kq,r}\}}{n} \tag{3.16}$$

Their standard deviations were calculated as follows:

$$\delta\lambda_{kq} = \pm\sqrt{\frac{\sum_{r=1}^{n}\{\lambda_{kq,r} - \overline{\lambda}_{kq}\}^2}{n-1}} \tag{3.17}$$

and

$$\delta\psi_{kq} = \pm\sqrt{\frac{\sum_{r=1}^{n}\{\psi_{kq,r} - \overline{\psi}_{kq}\}^2}{n-1}} \tag{3.18}$$

The comparison between the calculated and the observed concentrations coming from the validation step was displayed in Figure 3.4. The residuals of the concentrations of the enantiomers were evaluated as follows:

$$Res_{L,r} = \hat{C}_{L,r} - C_{L,r} \tag{3.19}$$

$$Res_{D,r} = \hat{C}_{D,r} - C_{D,r}, \tag{3.20}$$

and plotted together with the predicted concentrations ($\hat{C}_{i,r}$) in Figure 3.4. The residuals appear to be generally distributed near zero, suggesting that the chosen model fitted well the data.

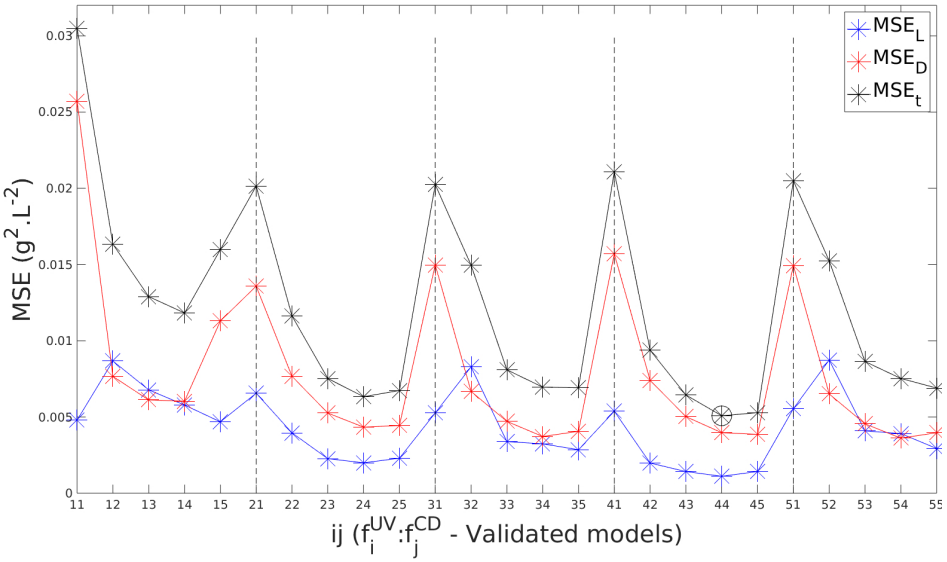

Figure 3.3: MSE_D, MSE_L and MSE_t for the validated models. They were composed by one of the UV-vis (Equation 3.7) and CD (Equation 3.6) Equations.

It is essential to highlight that Equation 3.14 has the upper limit of the k-th power higher than the upper limit of q-th power and bearing in mind that the former is the power of L-PZQ concentration, it adds a power two in the C_L-terms,

$$\begin{cases} \lambda_{20}C_L^2 + \lambda_{21}C_L^2C_D \\ \psi_{20}C_L^2 + \psi_{21}C_L^2C_D. \end{cases} \tag{3.21}$$

The terms exposed by Equation 3.21 allowed to increase the predictability of L-PZQ in the mixtures and without compromise the predictability of D-PZQ in the same mixture. The comparison of MSE_D of other pairs of equations shows that even when the q-th power of C_D is high, the predictability of D-PZQ did not improve.

In Table 3.2 the standard deviations of $\overline{\lambda}_{11}$ and $\overline{\lambda}_{20}$ show that these parameters could not have significant meaning; therefore, two hypothesis were formulated - the *null* hypotheses H_o and the *alternative* hypothesis H_a. They are:

- H_0: The parameters $\overline{\lambda}_{11}$ and $\overline{\lambda}_{20}$ are essential to predict calculations.
- H_a: The parameters $\overline{\lambda}_{11}$ and $\overline{\lambda}_{20}$ are not essential to predict calculations.

Table 3.2: Estimated model parameters and their confidence intervals

$\overline{\lambda}_{00} \pm$ ci	$\overline{\lambda}_{01} \pm$ ci	$\overline{\lambda}_{10} \pm$ ci
0.040 ± 0.002	0.119 ± 0.002	0.183 ± 0.005
$\overline{\lambda}_{11} \pm$ ci	$\overline{\lambda}_{20} \pm$ ci	$\overline{\lambda}_{21} \pm$ ci
0.005 ± 0.008	0.009 ± 0.004	0.493 ± 0.007
$\overline{\psi}_{00} \pm$ ci	$\overline{\psi}_{01} \pm$ ci	$\overline{\psi}_{10} \pm$ ci
-0.513 ± 0.042	-2.971 ± 0.044	9.899 ± 0.113
$\overline{\psi}_{11} \pm$ ci	$\overline{\psi}_{20} \pm$ ci	$\overline{\psi}_{21} \pm$ ci
-17.041 ± 0.323	-3.405 ± 0.068	9.396 ± 0.827

units: λ_{kq} = [Abs L^{k+q} $\mathrm{g}^{-(k+q)}$], ψ_{kq} = [mdeg L^{k+q} $\mathrm{g}^{-(k+q)}$]
ci: confidence interval

The model was rewritten to test the hypothesis:

$$\begin{cases} \mathrm{S}_{UV,r} = & \lambda_{00,r} + \lambda_{01,r}C_{D,r} + \\ & +\lambda_{10,r}C_{L,r} + \lambda_{21,r}C_{L,r}^2C_{D,r} \quad R^2 = 0.98 \\ \mathrm{S}_{CD,r} = & \sum_{k=0}^{2}\sum_{q=0}^{1}\{\psi_{kq,r}\hat{C}_{L,r}^k\hat{C}_{D,r}^q\} \quad R^2 = 0.99 \end{cases} \tag{3.22}$$

The equation related to UV absorption in Equation 3.22 was modified, but the CD absorption equation has not changed compared to Equation 3.14. The predictability of the modified model has not changed compared to the original model, as can be seen in Figure 3.4. As the modified model gave good predictions with fewer parameters, it was the chosen model to read enantiomer concentrations in the range of 0 and 1.25 gL^{-1}.

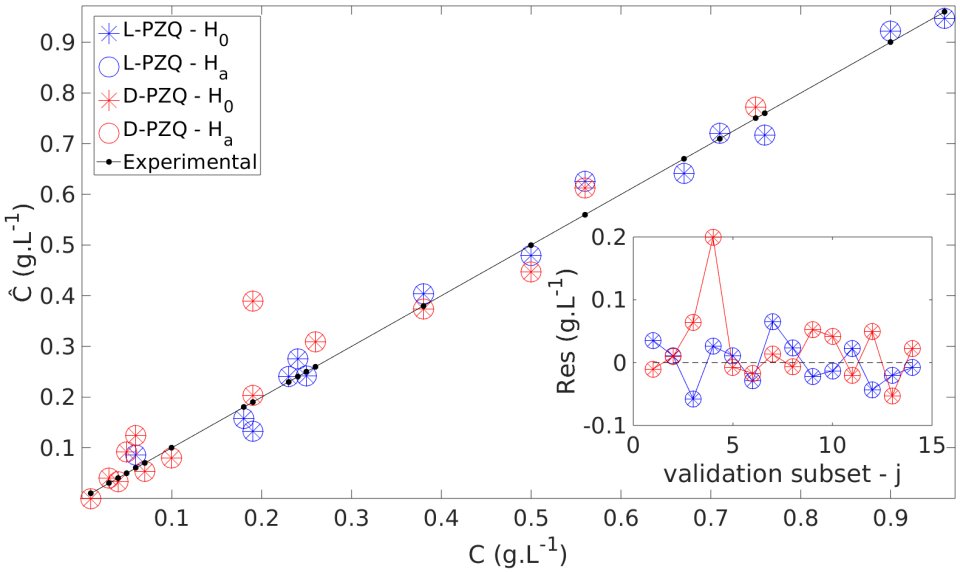

Figure 3.4: **Outer plot:** comparison between predicted data ($\hat{C}$) and experimental data (C) of the original (H_0) and modified model (H_a). The line is the experimental data identity line. **Inner plot:** residuals of the original (H_0) enantiomers concentrations and modified model (H_a).

The system's nonlinearity is also highlighted when observing the point with coordinate (0.19,0.39) of D-PZQ in Figure 3.4. The mixture with 0.19 g.L^{-1} of D-PZQ and 0.06 g.L^{-1} of L-PZQ (line 4 in Table H.2) presented an ellipticity of -1.3±0.1 *mdeg*, which lies in-between ellipticity of -1.1±0.2 and -1.5±0.1 *mdeg* observed for pure D-PZQ solutions with 0.25 and 0.50 g.L^{-1}, respectively (Table H.1), but the D-PZQ concentration in the mixture does not remain between the two pure D-PZQ concentrations. This phenomenon shows that PZQ mixtures near the limit of pure D-PZQ solutions present a high nonlinear relationship between the signal and D-PZQ concentration.

It is essential to highlight that simultaneous absorption of UV-vis and CD still takes place; what changed compared to previous works is how the data were processed. When both information is processed together in the dissymmetry factor, part of the information is lost because just one independent equation is generated. On the other hand, when both information is processed independently (*i.e.*, two independent equations are generated), both enantiomeric concentrations can be calculated (*i.e.*, two independent variables).

3.4 Conclusions

The relationship between the signal and the mixtures with low L-PZQ concentration showed high nonlinearity. Confidence interval analysis and the approach developed in this work proved to be essential allies in determining enantiomeric concentrations

in solutions with D- and L-PZQ. The results could be applied to higher concentrations to quantify enantiomers in a given stream of any separation processes, especially for the online monitoring of enantiomer purities desired for automatic control purposes.

Chapter 4

Open-loop SMB dynamics study

4.1 Introduction

Although the SMB concept was created approximately 60 years ago [42], the model-based control science related to SMB started in the 90s. Long time delays, distributed parameters, and mixed discrete and continuous time are some of the odd characteristics associated with the SMB process [103]. Nowadays, it is common to operate SMB units, not in the optimal operating point, but at a reasonable distance due to control difficulties [44, 104]. Many works are investigating different control strategies, and most of them are purely computational studies. Computational studies are essential to mature control strategies or to develop new ones. Figure 4.1 helps visualize important features that computer efforts could help, for instance, the definition of objective functions, choosing a suitable model, optimization and parameter estimation strategies, and which variables should be controlled or manipulated.

Nevertheless, there is a gap in which computational studies make a minimal contribution, the online monitoring systems. Available online monitoring systems should shape computational studies imposed by the limitations of the former. Bearing in mind the necessity to work in a closed-loop to design control strategies, it is crucial to have a reliable online measuring of enantiomer concentrations in the outlet streams. This problem is still an open issue in SMB literature, and it is going to be discussed in the following paragraphs.

MARTEAU *et al.* [105] was the first work in open literature dealing with online measurement in an SMB plant. A Raman spectroscopy was used to measure four different points of the concentration profile of the SMB unit, which was used to correct the operating variables. Data acquisition happened every 15 seconds. However, this system did not aim to separate optical isomers, it separated C8 aromatics, and p-xylene was the compound of interest. ZENONI *et al.* [98] used a UV detector and polarimeter in series to measure the enantiomer concentration in the extract and

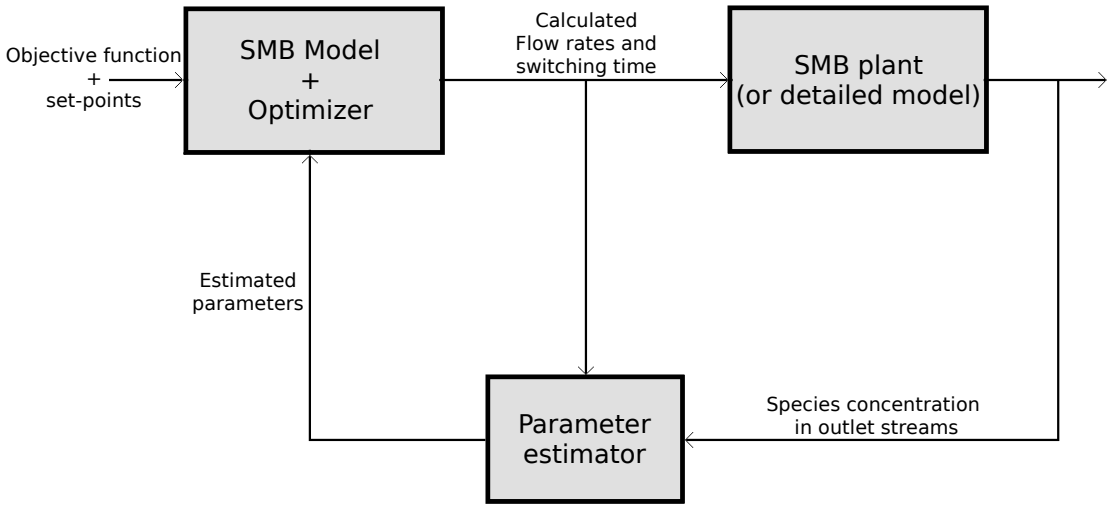

Figure 4.1: MPC general block diagram usually adopted for SMBs.

raffinate stream. The enantiomer used was the Tröger's base. The validation of the method was achieved by comparing it with off-line chiral HPLC analysis. Tröger's base enantiomer is a well-known enantiomer, and it presents linear absorption of UV light at small concentrations, which facilitates its online monitoring. KLATT *et al.* [106] used a combination of a polarimeter and a densimeter to calculate the fructose and glucose concentrations (details about the experimental setup were presented elsewhere [107]). Their work used simulated data from a rigorous process model to generate a model-based control by model identification. MIHLBACHLER *et al.* [108] used four detectors, two of them were UV detectors installed in the outlet streams, and the other two were a third UV detector and a polarimeter in series installed at the outlet of one of the columns. Tröger's base enantiomers were used to study the SMB separation. Good results were found comparing experimental data available by the online monitoring system and the simulated data using an equilibrium-dispersive model. ERDEM *et al.* [109] used an actual SMB plant to separate uridine from guanosine using two multi-wavelength UV detectors as sensors. As both substances have different UV spectra, two different signals were obtained (one for each species); therefore, two equations could be constituted. These equations had two unknown variables (concentrations of each species). Thus, a zero degree of freedom system could be solved for the concentration of the individual species at each measurement. The equations used in calibration had a linear relationship between concentrations. A time-varying linear model of the SMB process was obtained by linearizing the equilibrium dispersive SMB model described elsewhere [110, 111]. SONG *et al.* [112] used the same online measurement system from previous work to separate uridine from guanosine using a real SMB plant. The difference from previous work was the applied control strategy. The mathematical

model used a linear input/output data-based model. This sort of model is used in the problem of a relatively straightforward least square, which is very fast; on the other hand, the choice of the input and output sets of variables, the identification of the process, and the determination and validation of the input/output data-based prediction model are additional steps to be accomplished. AMANULLAH *et al.* [113] implemented a 'cycle to cycle' optimizing control for chiral separation in a laboratory SMB plant. The online measurement system was presented earlier by [98]. The guaifenesin enantiomers were used in lower concentrations, allowing, therefore, a linear calibration. A time delay between UV and polarimeter was observed, and, consequently, only incomplete information was obtained from the last cycle. Time delay is inevitable when sensors are in series. This forces any control strategy to act at each cycle and not at each switching time during an SMB operation. Once again, a simplified model was used as an SMB model to take actions in a model-based predictive control. According to GROSSMANN *et al.* [114], the polarimeter accuracy is affected by pressure fluctuations or impurities; therefore, a new monitoring system was proposed. They developed a monitoring system consisted of automated online HPLC monitoring sending as feedback information to the control system the concentrations of uridine and guanosine coming from the raffinate and extract streams over one cycle. The main advantages of this new monitoring system are its accuracy and precision and the fact that impurities little affect the measurement. On the other hand, a significant time delay is now observed once the measurement starts at the end of the cycle. The time interval to execute the analysis is in the order of magnitude of the cycle time. Once more, the model used by the controller was a simplified state-space linear time-varying model. Other works from the same research group using the same online monitoring and control strategy, but different solutes can be found elsewhere [115, 116]. ARAUJO *et al.* [117] tested a proposed online monitoring system using the Tröger's base racemate. This online monitoring system was composed of two UV detectors; one was located at the outlet of one of the columns, and the other one was placed at the outlet of the analytical HPLC column. The former had the role of measuring the total concentration of enantiomers, and the latter aimed to give information about the quantity of each enantiomer. This online monitoring system allowed the conversion into enantiomer concentrations. MAO *et al.* [118] used circular dichroism and UV detector in series to measure the enantiomer concentration of raffinate and extract continuously. A 10 port dual external sampling injection with two 10μL loops was used to measure both outlet streams during the same experiment. It was the first time that circular dichroism spectra were used in the online monitoring system of an SMB plant. The racemic mandelic acid was used in this study. A first-principle model called linear driving force was used to compare experimental to simulated data. Furthermore,

the unit worked in an open-loop configuration, *i.e.*, the flow rate leaving zone 4 was collected in an appropriate glass, and fresh desorbent was introduced into zone 1. SUVAROV *et al.* [119] used two UV sensors to determine retention times in each zone of the SMB plant. This retention time fed a model based on the moving fronts of concentrations; more details could be found in [120, 121].

Based on the literature review, some critical points could be highlighted; when non-enantiomeric isomer or similar compounds were separated, the monitoring systems presented some advantages related to enantiomeric isomers. ERDEM *et al.* [109] separated guanosine from uridine using the UV spectra difference between both. Two multi-wavelength UV detectors were enough to identify their composition located at an outlet stream of the process. When a racemate needs to be separated, only the UV spectrum is not enough anymore because UV absorption is similar for both enantiomers; therefore, UV detectors should give the total concentration and not the concentration of each species. Hence, equipment capable of detecting any change in polarized light should be necessary to complete the information needed to differentiate each of the enantiomers. Usually, polarimeters or circular dichroism were used to get this additional information. However, depending on the adopted strategy, the HPLC process can separate the enantiomers and give the desired quantity of enantiomers at some point in the SMB processes.

The novelty of this chapter is the possibility of online measurement of concentrations by using the *chiral detector* equipment, which allowed to analyze the dynamics of the SMB unit in each experiment.

4.2 Materials and methods

4.2.1 Materials

- Ethanol HPLC grade was the solvent, provided by Biograde (Brazil);
- Racemic mixture of praziquantel with pharmaceutical-grade was manufactured by Yixing Xingyu Medical Chemical Co. and provided by Farmanguinhos (Rio de Janeiro, Brazil).

4.2.2 Step experiments

The built-in-house chromatographic unit was presented in Figure 2.8. However, the *chiral detector* equipment presented in Section 3.2.2 was coupled alternately in the raffinate or extract stream to online monitoring of the concentration (see Figure 4.2).

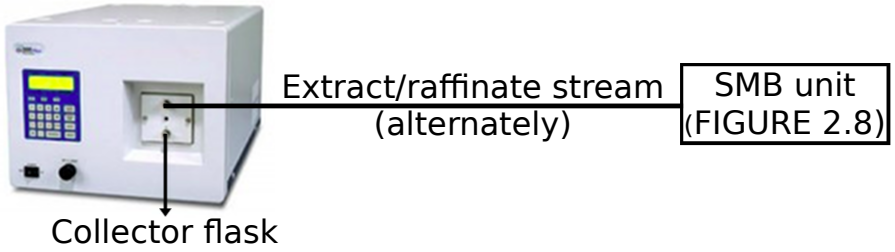

Figure 4.2: Chiral detector equipment coupled to the SMB unit outlet streams.

The experiments were carried out just once, and they were divided into three stages: (1) SMB running with solvent in both inlet streams for 1 cycle (see Figure 2.9a), (2) SMB running with solvent and solute(s) for 5 cycles before perturbation and (3) SMB running with solvent and solute(s) for 6 cycles after perturbation was applied in one of the flow rates (Q_2, Q_F or Q_D), totaling 12 cycles per experiment. The valves switching time and the pumps flow rate of each experiment before the perturbation were the same (*i.e.*, in the first and second stages); therefore, they were considered as if they were just one experiment that was repeated 5 times ($\{n \in \mathbb{N}^* \ / \ 1 \leq n \leq 5\}$) and named as *Run 6*. In other words, *Run 6* can be interpreted as a feed concentration step experiment that changed from 0 to 3 gL^{-1}. Just in the third stage (after step perturbation), the experiments differ from each other. The experiments were named as follows:

- *Run 6*: step from 0 to 3 gL^{-1} in the feed concentration (second stages);
- *Run 7*: step of +10% in the Q_2 pump (third stage)[1];
- *Run 8*: step of -10% in the Q_2 pump (third stage);
- *Run 9*: step of -10% in the Q_D pump (third stage);
- *Run 10*: step of +10% in the Q_F pump (third stage);
- *Run 11*: step of -10% in the Q_F pump (third stage).

First Stage:

The same methodology presented in Section 2.6.2 was applied in the first stage.

After this stage, the average of the extract ($\overline{Q}_{X,s,n}$) and raffinate ($\overline{Q}_{R,s,n}$) flow rates for all switching times ($\{s \in \mathbb{N}^* \ / \ 1 \leq s \leq 6\}$) was performed in the first stage

[1]The only experiment carried out twice while measuring the raffinate stream.

of each n experiment:

$$\overline{Q}_{X,n} = \frac{\sum_{s=1}^{6} Q_{X,s,n}}{6}, \tag{4.1a}$$

$$\overline{Q}_{R,n} = \frac{\sum_{s=1}^{6} Q_{R,s,n}}{6}. \tag{4.1b}$$

The flow rates above are the average of the calculated flow rates in each s switching time of the nth experiment.

Second Stage:

The same methodology presented in Section 2.6.2 was applied in the second stage. From the measured outlet flow rates, the other external ones were calculated as follows:

$$\overline{Q}_{F,n} = \frac{\overline{C}_{i,X,n}\overline{Q}_{X,n} + \overline{C}_{i,R,n}\overline{Q}_{R,n}}{\overline{C}_{i,F,n}} \tag{4.2}$$

and

$$\overline{Q}_{D,n} = \overline{Q}_{X,n} + \overline{Q}_{R,n} - \overline{Q}_{F,n}. \tag{4.3}$$

The entire volume of each outlet stream in the sixth switching time of the sixth cycle was collected; in the sequence, part of the collected volume was conditioned in separated vials and analyzed in the HPLC following the filtration and experimental procedures presented in Section 2.6.1. The concentrations measured in HPLC are available in Table C.2.

To determine the internal flow rates, one of them must be known as a priori; in this case, Q_2 is known because an HPLC pump can set it. Unlike the external flow rates that could be determined experimentally (or inferred), the internal flow rate could not be measured or inferred; therefore, a posteriori adjustment of Q_2 was made as discussed in Section 2.6.3 and presented in Section 4.2.4. Once Q_2 was set, the other internal flow rates could be calculated:

$$\overline{Q}_{1,n} = \overline{Q}_{2,n} + \overline{Q}_{X,n} \tag{4.4a}$$

$$\overline{Q}_{3,n} = \overline{Q}_{2,n} + \overline{Q}_{F,n} \tag{4.4b}$$

$$\overline{Q}_{4,n} = \overline{Q}_{2,n} + \overline{Q}_{F,n} - \overline{Q}_{R,n}. \tag{4.4c}$$

After the five experiments were carried out, all the flow rates and their experi-

mental dispersions were calculated:

$$\overline{Q} = \frac{\sum_{n=1}^{5} \overline{Q}_n}{5} \tag{4.5a}$$

$$\delta\overline{Q} = \sqrt{\frac{\sum_{n=1}^{5} \left(\overline{Q}_n - \overline{Q}\right)^2}{4}}, \tag{4.5b}$$

where Q represents the flow rates ($mL.min^{-1}$), they were displayed in Table C.2. The flow rate $\overline{Q}$ is the average for all n calculated flow rates ($\overline{Q}_n$), and the former was differentiated from the latter by removing the letter n from the index notation.

Third Stage:

It is the SMB experiments used to study its dynamics after step disturbance of +/- 10% in the Q_2, Q_F, or Q_D flow rates.

After perturbations with the aid of a 5 mL volumetric flask and a stopwatch, the flow rates of the outlet streams were measured for each switching time in the first cycle after perturbation (*i.e.*, 6 flow rates of each outlet stream were obtained). The average flow rates and their experimental dispersions represent the operation in the 6 switching times of the same single experiment:

$$\overline{Q} = \frac{\sum_{s=1}^{6} Q_s}{6} \tag{4.6a}$$

$$\delta Q = \sqrt{\frac{\sum_{s=1}^{6} \left(Q_s - \overline{Q}\right)^2}{5}}, \tag{4.6b}$$

The calculated flow rates were displayed in Tables C.3.

From these flow rates, the other external ones were calculated as follows:

$$\overline{Q}_F = \frac{\overline{C}_{i,X}\overline{Q}_X + \overline{C}_{i,R}\overline{Q}_R}{\overline{C}_{i,F}} \tag{4.7}$$

and

$$\overline{Q}_D = \overline{Q}_X + \overline{Q}_R - \overline{Q}_F. \tag{4.8}$$

To determine the internal flow rates, one of them must be known as a priori; in this case, Q_2 was previously adjusted. Once Q_2 was set, the other internal flow rates

were calculated:

$$\overline{Q}_1 = \overline{Q}_2 + \overline{Q}_X \tag{4.9a}$$

$$\overline{Q}_3 = \overline{Q}_2 + \overline{Q}_F \tag{4.9b}$$

$$\overline{Q}_4 = \overline{Q}_2 + \overline{Q}_F - \overline{Q}_R. \tag{4.9c}$$

The experimental dispersion of each volumetric flow rate was calculated using Equation 4.6b.

The signals (UV/vis and CD) acquired by the *chiral detector* equipment, as well as the instantaneous concentrations calculated from online measurements of these signals, are available in Appendix J.

4.2.3 Simulation of SMB experiments

The simulated data from the second and third stages were carried out by the software SiMoBed and SiMoCon. Both software was developed during the dissertation of ANDRADE [59] using MatLab® R2016a (student license). The details about the simulation were presented in Section 2.6.3.

Table 4.1 shows the provided information to the software to run the simulations in this chapter.

4.2.4 Adjustment of volumetric flow rate of zone 2 (Q_2) in the *Run 6*

As discussed in Section 2.6.3, it was previously assumed that the HPLC pump in zone 2 delivered exactly the set value, but this may not be true. In the light of it, the experimental flow rates, switching time, and racemic concentration, together with the Henry constants and porosity, were used to simulate *Run 6*. After that, the simulated outlet concentrations were compared to experimental ones obtained by offline HPLC measurements by using the **R**oot of **S**um of **S**quared **R**esiduals (RSSR), γ:

$$\gamma = \sqrt{\left(\overline{C}_{A,X} - \overline{C}^{sim}_{A,X}\right)^2 + \left(\overline{C}_{B,X} - \overline{C}^{sim}_{B,X}\right)^2 + \left(\overline{C}_{A,R} - \overline{C}^{sim}_{A,R}\right)^2 + \left(\overline{C}_{B,R} - \overline{C}^{sim}_{B,R}\right)^2}, \tag{4.10}$$

where the superscript *sim* denotes the simulated data, the absence of superscript in the equation above implies that the data is experimental. The dynamics of the richest component of each output stream in each experiment was compared with the

Table 4.1: Simulation parameters

More- and Less-retained components parameters (A and B)			
Thermodynamic parameters		$C_{A,F}(g.mL^{-1})$	$C_{B,F}(g.mL^{-1})$
Table 2.8 and Table F.1		Tables C.2 and C.3	Tables C.2 and C.3
Column parameters			
L_{column} (cm)	D_{column} (cm)	ρ_{ads} (g.cm^{-3})	$\epsilon_{t,j}$ (-)
10	1	1.00	Table 2.8
SMB parameters			
Nº of columns	Columns per zone [z_1 z_2 z_3 z_4]		Nº of cycles
6	[1 2 2 1]		5 (2^{nd} stage)/6 (3^{rd} stage)
t_{switch} (min)		$Q^{SMB}_{1,2,3,4}$ (mL.min^{-1})	
Tables C.2 and C.3		Tables C.2 and C.3	
Solver control			
Nº of internal elements		Jacobian	
120		Numerical	
Abs. tolerance		Rel. tolerance	
10^{-8}		10^{-8}	
Integrator			
ode15s - Variable order BDF method			
Discretization method			
First order backwards finite difference			

corresponding simulated curve through the slope of the line drawn on the inflection point of the curve; therefore the metric used was:

$$\Gamma_{i,out} = |\phi_{i,out} - \phi^{sim}_{i,out}|; \tag{4.11a}$$

$$\Gamma = |\Gamma_{B,R} - \Gamma_{A,X}|, \tag{4.11b}$$

where $\phi_{i,out}$ was the slope of the line drawn from the experimental curve ($gL^{-1}t^{-1}_{switch}$) and the $\phi^{sim}_{B,R}$ was the slope of the line drawn from the simulated curve ($gL^{-1}t^{-1}_{switch}$) both for the component i in one of the outlet streams that was being measured.

Fourteen simulations were carried out, where steps were applied to Q_2. They were: -25%, -20%, -15%, -12%, -10%, -5%, -1%, 1%, 5%, 10%, 12%, 15%, 20% and 25%. The original runs can be found in Appendix C. As Q_2 changed, the other internal flow rates were recalculated, to satisfy the mass balance. Figure 4.4 shows the region of separation and regeneration in which the experiment is inserted after adjusting of the internal flow rates.

4.3 Results and discussion

As pointed out in Section 4.2.2, all the experiments were similar before the step disturbance; therefore, this part of the experiments was analyzed as a unique one called *Run 6*.

4.3.1 Adjustment of volumetric flow rate of Q_2 in *Run 6*

Before comparing experimental and simulated data (see Section 4.3.3), the adjustment of volumetric flow rate Q_2 was made to find the most accurate value when comparing the experimental and the simulated step responses. The comparisons were performed first using the metric γ that compares the simulated concentrations with those observed experimentally through a measurement carried out by the HPLC when both streams achieve the CSS. Furthermore, the dynamics of the SMB have been revealed due to the online measurement of the *chiral detector* equipment. With that, the dynamics of the simulations performed considering nonlinear isotherm were compared with that obtained experimentally through a specific metric, Γ, as explained in Section 4.2. The Γs were calculated just for the simulations that compose the plateau, and, from Table G.6, it is possible to see that the smallest Γs were found when Q_2 changed from -1% to 10%. Once more, the 5% and 10% changes were among the minimum values observed, as happened in most of the runnings carried out in Chapter 2. The value of 5% was chosen because it presented the lowest value of $\Gamma_{B,R}$ between the two choices. Table 4.2 highlights the new internal flow rates after the adjustment.

Table 4.2: New internal flow rates after Q_2 adjustment

$\overline{Q}_1$	$\overline{Q}_2$	$\overline{Q}_3$	$\overline{Q}_4$
8.29±0.02	5.32	6.72±0.09	4.49±0.11
$\overline{Q}_X$	$\overline{Q}_F$	$\overline{Q}_R$	$\overline{Q}_D$
2.97±0.02	1.40±0.09	2.23±0.02	3.80±0.09

4.3.2 Chiral detector validation in the SMB unit - *Run 6*

From this section on, the simulations carried out in the nonlinear region presented in Table 4.2 were adopted as the reference one to the steps applied to the variables to study the SMB dynamics. Before the Q_2 change (second stage), these experiments were designed to operate inside the triangle of separation and rectangle of regeneration. It is convenient to test the developed methodology presented in Chapter 3 because almost pure outlet streams should be produced from the SMB unit in *Run*

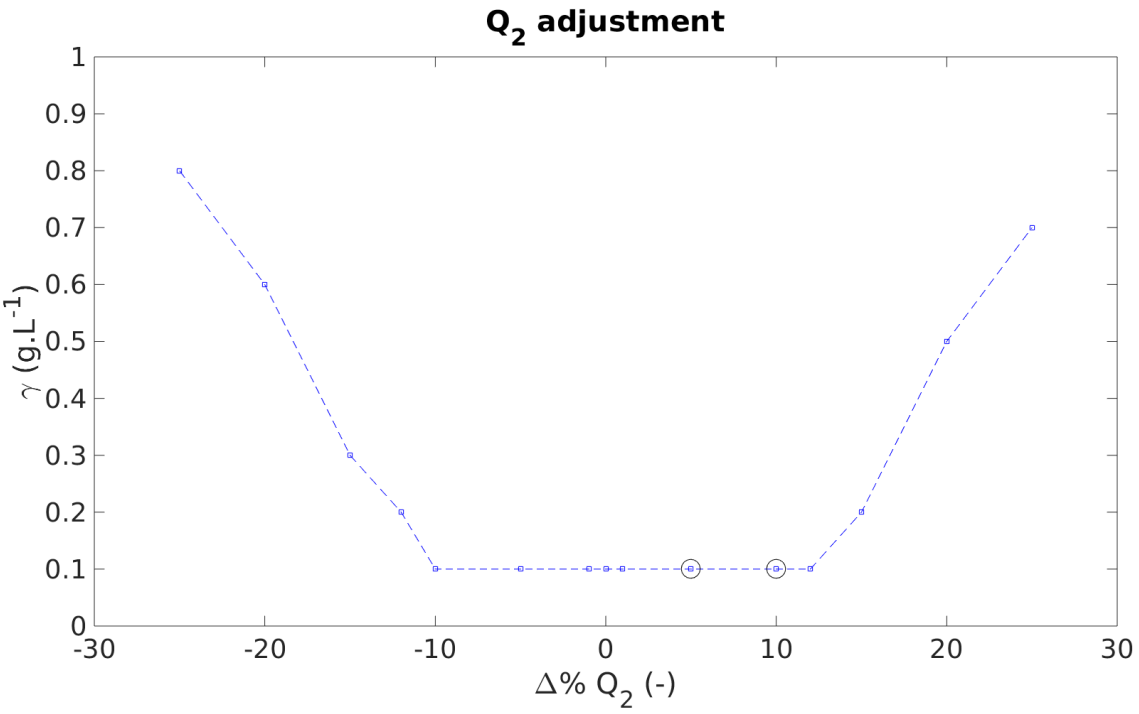

Figure 4.3: Behavior of γ versus $\Delta\%$ Q_2 in the *Run 6*.

6. This test is an important scenario to validate the calibration by comparing it with an established methodology used in the HPLC.

Comparison between HPLC and Chiral detector measurements

Figure 4.5, in addition to presenting the first dynamic information of the built SMB unit, allows validating the concentration measurement made by the *chiral detector* equipment with the classic one made by HPLC. The magenta points in Figure 4.5 represent the enantiomeric concentration measurements made by the HPLC in the sixth switching time of the fifth cycle, and they were compared with the L- and D-PZQ concentration measurements acquired by the *chiral detector* (the last blue and red points of the experimental curves). The proximity of the means and the superposition of the experimental error bars indicate that both techniques result in similar measurements of enantiomeric concentration, which serves as additional validation besides the one performed in Chapter 3.

From the concentrations measured from HPLC, it was possible to calculate the purities of each enantiomer in each outlet stream in the CSS. Table 4.3 shows that the SMB unit presented slight contamination in the raffinate stream, while the extract stream achieved optical purity of 100% considering the experimental error. The scenario depicted by the equilibrium theory that considers a nonlinear isotherm allows a satisfactory forecast of slight contamination of the raffinate stream (see Table C.2 to check the experimental conditions).

Table 4.3: Purities in *run 6* after reaching the CSS

	HPLC
$Pur_{A,X}$	99±1
$Pur_{B,R}$	98±1

Furthermore, the SMB unit operation oscillates thanks to small changes in the volumetric flow rates delivered by the pumps, the thermodynamic coefficients, and the porosity differences among all the chromatographic columns. This scenario makes the SMB unit operating out of the separation area sometimes (see Figure 4.4). This situation results in contamination of the raffinate stream.

4.3.3 Experimentation versus simulation

It is helpful to compare the experimental data with model predictions to validate the model and understand some phenomena involved during experimentation.

First of all, the dead time difference between the experimented and simulated curves was calculated by the time axis distance between the tangents drawn on the two L-PZQ (D-PZQ) curves in the raffinate (extract) stream illustrated in *Run* 6.

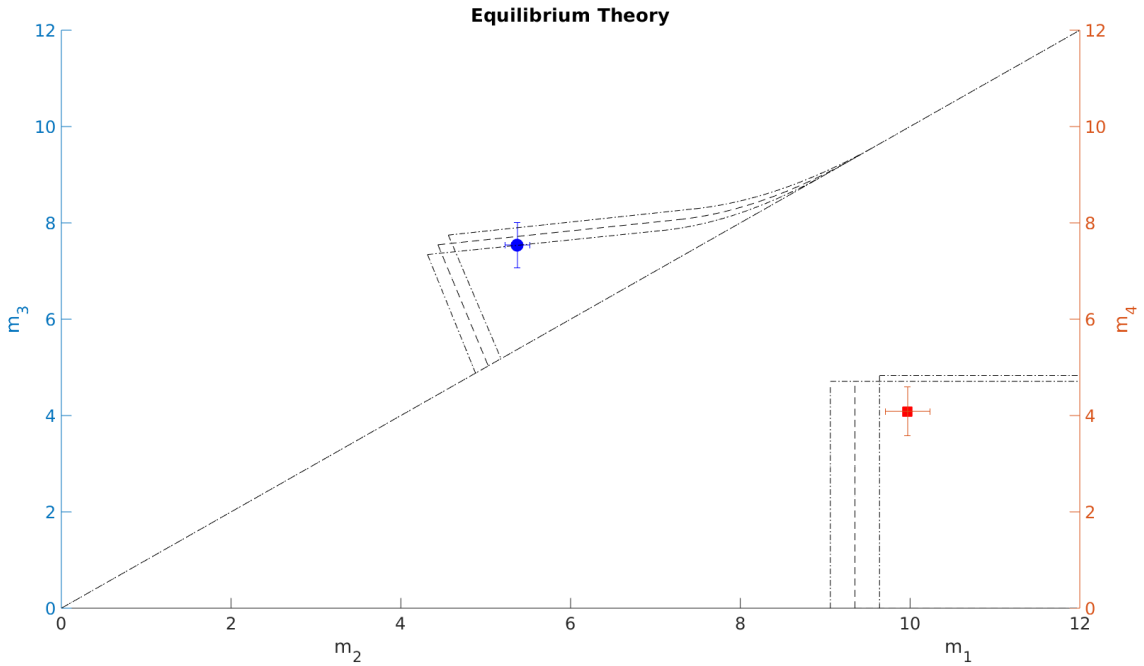

Figure 4.4: Equilibrium theory calculated for *run 6* considering the nonlinear isotherm. **Blue circle (m_2,m_3):** inside the separation zone and **orange square (m_1,m_4):** inside the regeneration zone. The dashed line on the diagonal is the identity line. The variation in the separation- and regeneration-region frontiers represented by dotted lines are due to thermodynamic parameters uncertainties and feed concentration experimental errors.

The dead-time values were (see Figure 4.5):

$$t_{d,R} \approx 4 \times \text{n}^o \text{ of switching time;} \tag{4.12a}$$

$$t_{d,X} \approx 4 \times \text{n}^o \text{ of switching time.} \tag{4.12b}$$

After the slight adjustment of Q_2, it was possible to point out two main differences from the comparison between experimental and simulated data (see Figure 4.5). The first one was translating the experimental data about the simulated one; this showed that the dead volume did not play a crucial role in mass transfer resistances in the experiments. The second one was evidenced by the differences in D-PZQ concentrations in the raffinate stream; this happens due to fluctuations intrinsic to the nature of the experiments that allow the unit to operate inside the raffinate-contaminated area (see Figure 4.4). Once the mathematical model used was a first-principle model developed in our group ([49, 59]) and it did not account for dead volume effects, this is an interesting result because it showed that a relatively simple model could give good predictions about the dynamic behavior of the built SMB unit. This result corroborates with the previous analyzes made in Section 2.7.2. The *Péclet* number was analyzed for each enantiomer for each column. It was found that the advective transport rate is at least 2340 times greater than the diffusive transport rate inside the chromatographic column for any species and column. Another dimensionless number used was the mass transfer units (see Table C.2), which shows that mass transfer surrounding the stationary phase inside the column is at least 138 times faster than the advection rate of solid phase in an equivalent TMB process. Furthermore, Table A.1 shows that approximately 3% of the total SMB volume is considered tubing dead volume, which is small enough to determine the influence on the SMB dynamic.

The experiments shown in the next section were designed to study the dynamics of the SMB unit under different step disturbances. All the perturbations were applied after the SMB unit has achieved the CSS in *Run 6*.

4.3.4 + 10% Q_2 step in the SMB unit - *run 7*

The first perturbation experiment consisted of applying a step of +10% in the Q_2 variable. It is interesting first to analyze the shifting in the CSS region promoted by the step change in the SMB unit before analyzing its dynamics. According to the equilibrium theory, Figure 4.6 showed a qualitative prediction of the CSS that the SMB unit should achieve under the conditions found in *Run 7* (see Table C.3). It can be observed that the unit operated outside the triangle of separation (more precisely in the raffinate-contaminated area) and in the border between the

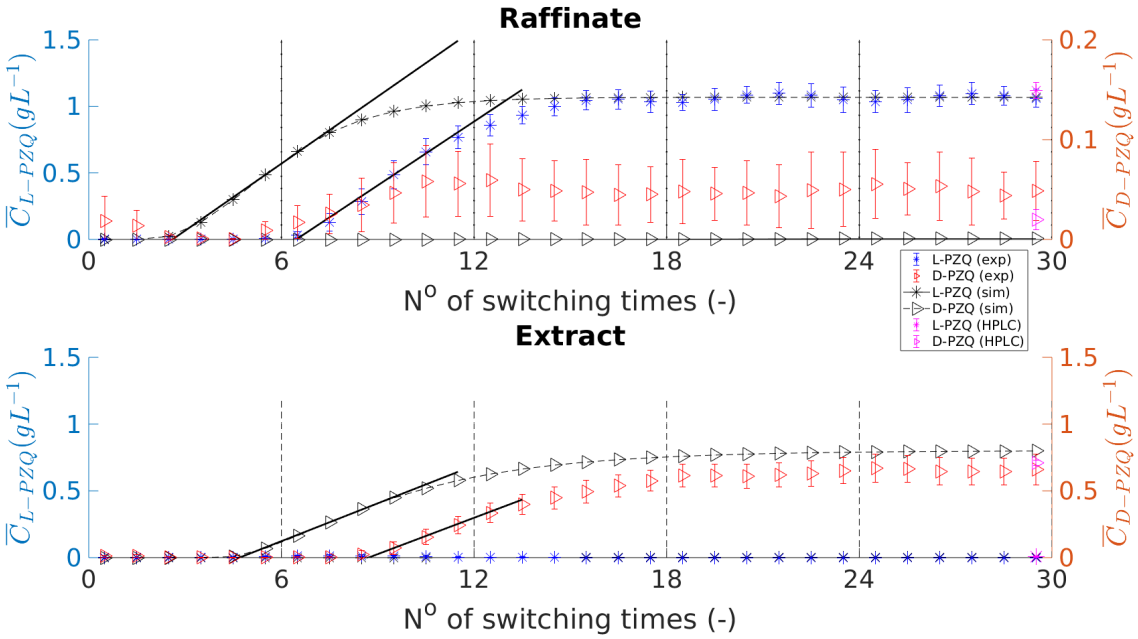

Figure 4.5: Comparison of the concentrations given by HPLC and by the *chiral detector* - coupled to the raffinate (**upper**) and the extract stream (**lower**) alternately - and computational simulations considering nonlinear isotherm.

rectangle of regeneration and the non-regenerated-liquid-phase area. From Figure 4.7 and Figure 4.8, it can be observed, when the unit achieved the CSS, that the contamination in the raffinate stream increased more than twice. In contrast, the extract stream maintained without contaminants, showing total agreement with what was predicted by the equilibrium theory.

The dynamics of the output streams were also shown in Figure 4.7 and Figure 4.8. A maximum peak was observed in the raffinate stream after approximately 4 switching times, followed by a decrease until near the initial concentration. The tendency to return to the original value was expected once the inlet and outlet flow rates remained the same values and there was, practically, no L-PZQ getting out in the extract stream. The maximum peak of L-PZQ concentration observed in Figure 4.7 can be explained by the lower residence time of enantiomers inside the chromatographic column, which means more L-PZQ molecules were dragged out due to the increased internal flow rates. Consequently, there is even more significant growth in the concentration of L-PZQ in the zone 3 and after that in the raffinate stream. The mathematical model based on the first principles showed good agreement with the experimental data for the L-PZQ in the raffinate stream. However, the D-PZQ enantiomer presented a smoother dynamic than that predicted by the model. Once the model did not predict contamination in the raffinate and, therefore, the dynamics showed a steeper increase trying to arrive at the same level of stationary state observed experimentally. On the other hand, the experimental dynamics were smoother since it started from a higher level due to the contamination

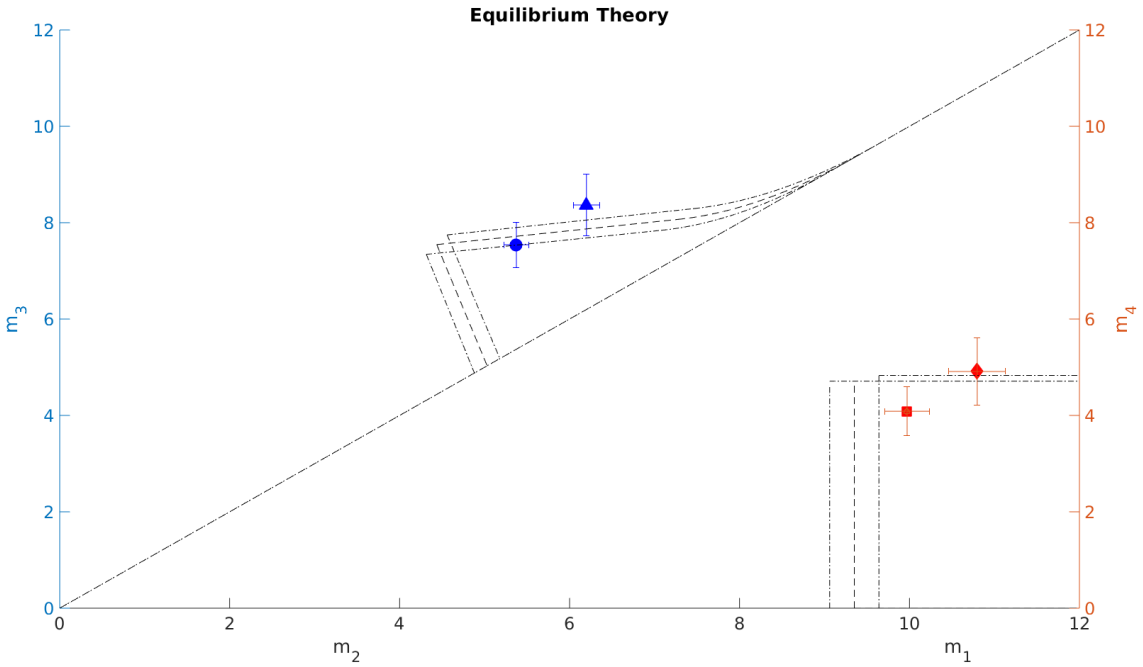

Figure 4.6: Comparison in the separation triangle of *run 6* (blue circle) and *run 7* (blue triangle) and regeneration rectangle of *run 6* (red circle) and *run 7* (red diamond).

observed in the raffinate before perturbation.

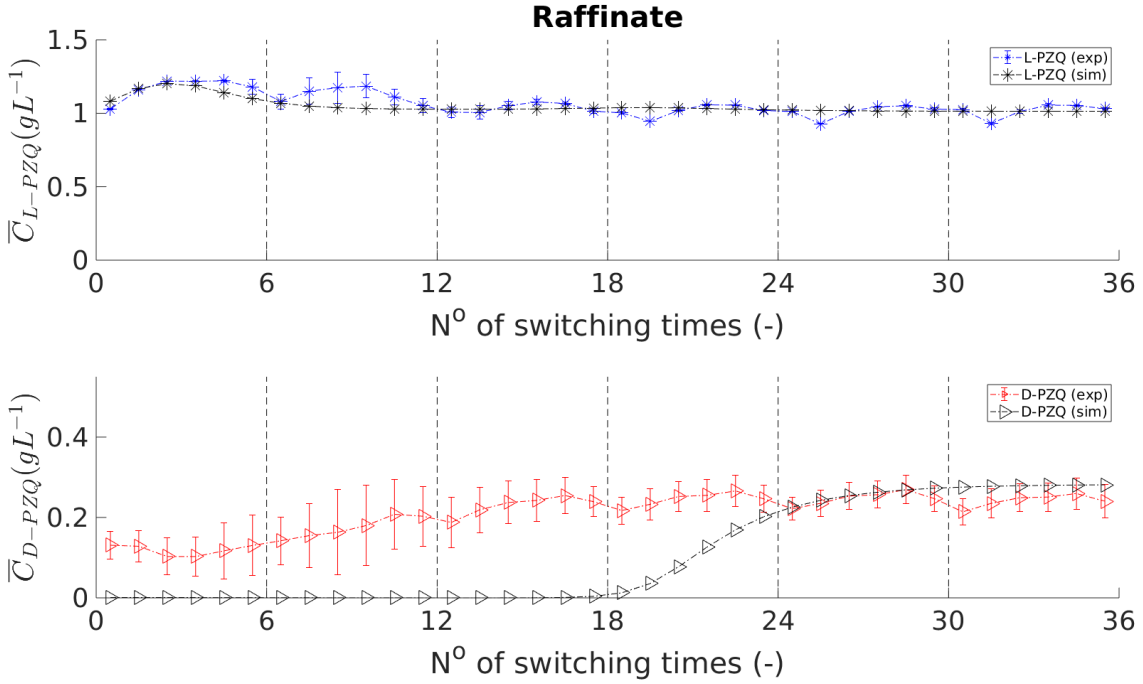

Figure 4.7: Raffinate stream dynamic after a +10% step perturbation in the zone-2 pump, Q_2 (*run 7*).

In Figure 4.8, a discrepancy between the experimented and the observed data was observed; the former showed no contamination in the extract stream by the L-PZQ.

At the same time, the latter predicted slight contamination, but the contamination was too small to be a problem, especially when working far from analytical purposes. No dynamics were observed in the experimental D-PZQ curve, although the model showed a small dynamic after the disturbance of Q_2. The experimental error related to the extract stream of *Run 6* (see Figure 4.5) suggests that because it is very subtle, the dynamics after the disturbance may have been hidden by the experimental error.

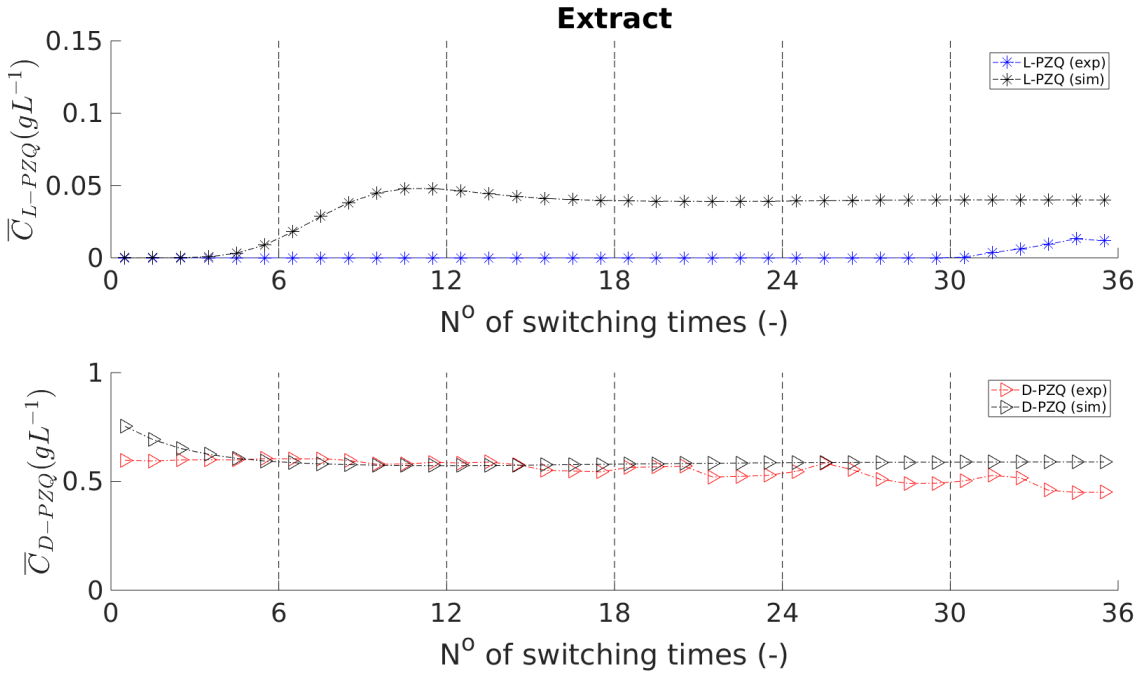

Figure 4.8: Extract stream dynamic after a +10% step perturbation in the zone-2 pump, Q_2 (*run 7*).

4.3.5 - 10% Q_2 step in the SMB unit - *Run 8*

The second perturbation experiment consisted of applying a step of -10% in the Q_2 variable. As explained in the *Run 7* experiment, the shifting in the CSS region promoted by the step change in the SMB unit was first analyzed before analyzing its dynamics. Figure 4.9 shows the CSS achieved by the SMB unit under the conditions found in *Run 8* (see Table C.3). It can be observed that the stationary state shifted from the border between the contaminated-raffinate area and the triangle-of-separation area to the border between the contaminated-extract area and the triangle-of-separation area in the m_3 x m_2 plane, and it shifted from inside the regenerating area to the border of the solid-phase-non-regenerating area and the rectangle-of-regeneration area in the m_4 x m_1 plane, culminating in slight raffinate contamination after some switching time. The frequent occurrence of non-regeneration of the solid phase will cause the contamination of the raffinate a few switching times later, since the D-PZQ enantiomer accumulated in zone 1, will pass

to zone 2, later, reaching zone 3 and, finally, contaminating the raffinate stream. Still, it is important to note in Figure 4.9 that the operating points, both before and after the disturbance, highlight the average behavior of the unit. However, there are natural fluctuations in both flow rates and thermodynamic coefficients that can cause the unit to operate in conditions other than expected by just analyzing the average values. Bearing that in mind, when analyzing Figure 4.9, it was observed that before the step-change in Q_2, minor contamination of the raffinate should be a possibility indicated by the experimental error and experimentally confirmed by Figure 4.5. After the step change, the unit should run towards a less contaminated raffinate if the regeneration point was inside the regeneration area. However, the regeneration point was inside the solid-phase-non-regenerating area, and this situation was responsible for contaminating the raffinate stream.

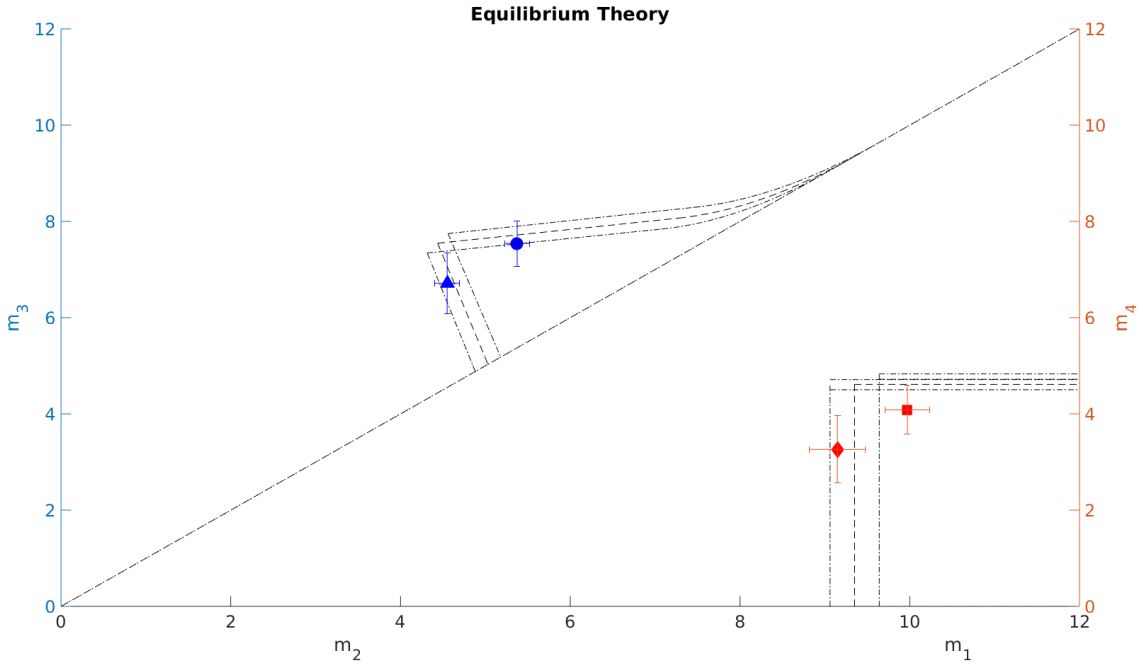

Figure 4.9: Comparison in the separation triangle of *run 6* (blue circle) and *run 8* (blue triangle) and regeneration rectangle of *run 6* (red circle) and *run 8* (red diamond).

The dynamics of the output streams are shown in Figure 4.10 and Figure 4.11. The only experimental curve that did not agree with the simulated curve was the D-PZQ curve in the raffinate stream. Not coincidentally it was the only situation in this experiment in which the observed initial steady-state was different from the predicted one (see Figure 4.5). As the initial steady-state presented higher D-PZQ concentration in relation to the final one, the dynamics were shaped in a smooth decreasing of D-PZQ quantity in the raffinate.

The dynamics of the L-PZQ concentration in the raffinate stream decreased after the negative step change in Q_2. All the internal flow rates decreased after the step

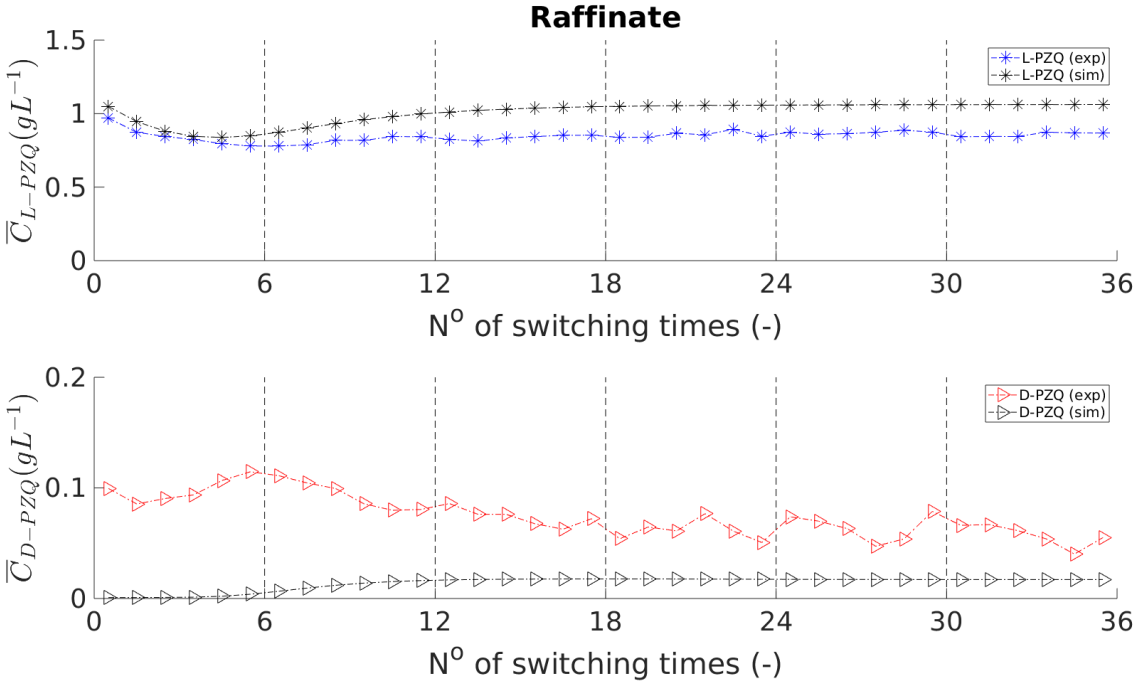

Figure 4.10: Raffinate stream dynamic after a -10% step perturbation in the zone-2 pump, Q_2 (*run 8*).

change and, consequently, the residence time of the enantiomers inside each zone increased, culminating in a decrease in the amount of L-PZQ leaving zone 3 (*i.e.*, being delivered to the raffinate outlet).

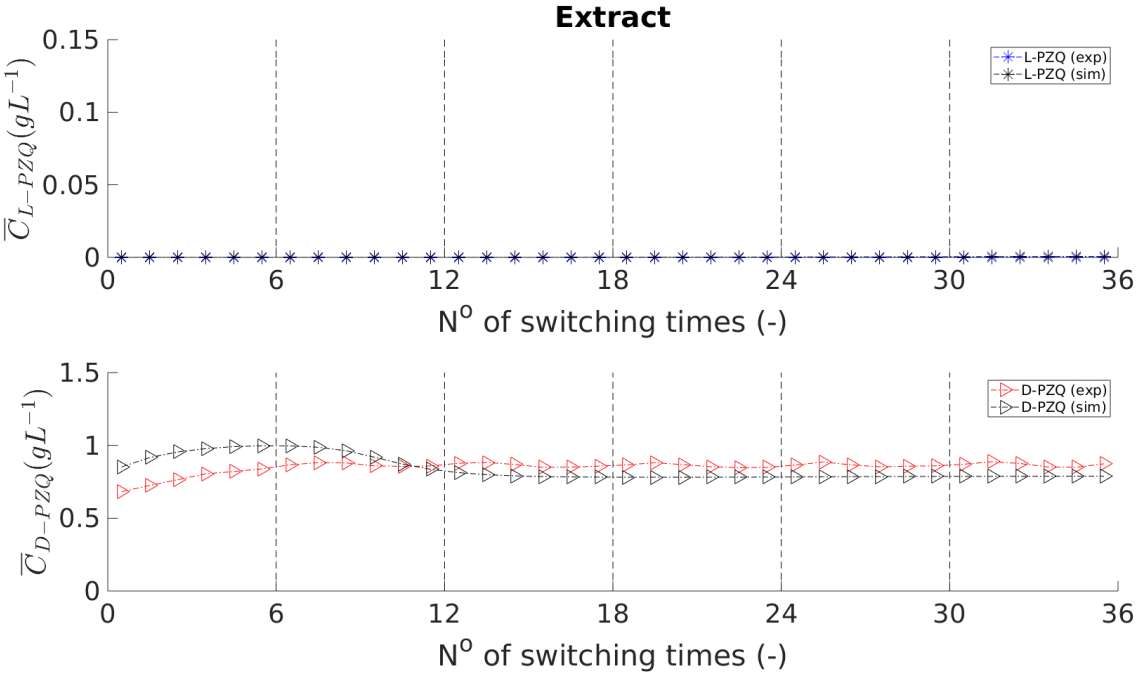

Figure 4.11: Extract stream dynamic after a -10% step perturbation in the zone-2 pump, Q_2 (*run 8*).

4.3.6 - 10% Q_D step in the SMB unit - *Run 9*

The third perturbation experiment consisted of applying a step of -10% in the Q_D variable. The discussion starts with the analysis in the CSS, followed by the analysis of the dynamics. Figure 4.12 shows the qualitative information about the CSS achieved by the SMB unit. It can be observed that the stationary state did not shift in the m_3 x m_2 plane, and it shifted to a higher m_4 position (m_1 remained unchanged) in the m_4 x m_1 plane. In order to keep the internal flow rate of zone 1 constant, the internal flow rate of zone 4 had to increase in the face of the decrease suffered by Q_D, which had a direct consequence in decreasing the flow rate of the raffinate. It is important to mention that the flow rate in zone 1 and 3 could not be reduced because both were composed of two flow rates determined by HPLC pumps, which maintained their nominal flow even after disturbance. After the step change, the unit started to run in the border between the regenerating area and the non-regenerating-liquid-phase area.

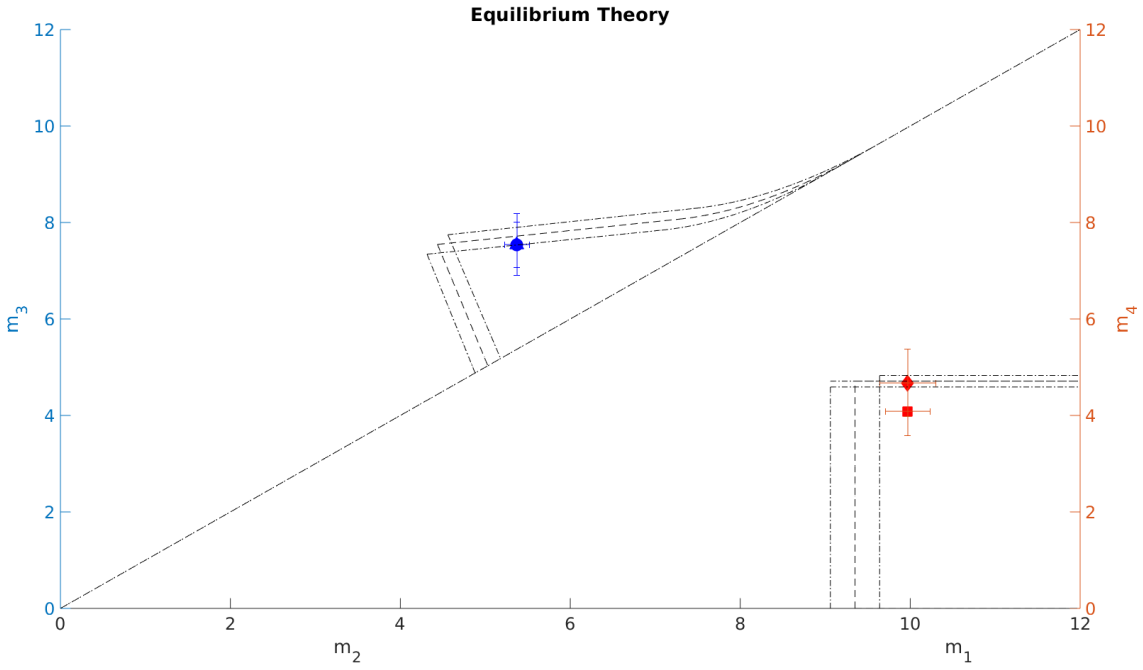

Figure 4.12: Comparison in the separation triangle of *run 6* (blue circle) and *run 9* (blue triangle) and regeneration rectangle of *run 6* (red circle) and *run 9* (red diamond).

In Figure 4.14, no trace of L-PZQ was found in the extract stream for the experimented data, while the simulated data accused contamination. However, the contamination was so minor that the stream could be considered practically pure. D-PZQ enantiomer showed an oscillating behavior, but taking into consideration the experimental error involved in the D-PZQ curve presented in Figure 4.5, approximately ± 0.1, and considering that the difference between the maximum and

the minimum values of this D-PZQ curve was approximately 0.27 gL^{-1}, it can be assumed that the oscillation was due to experimental errors.

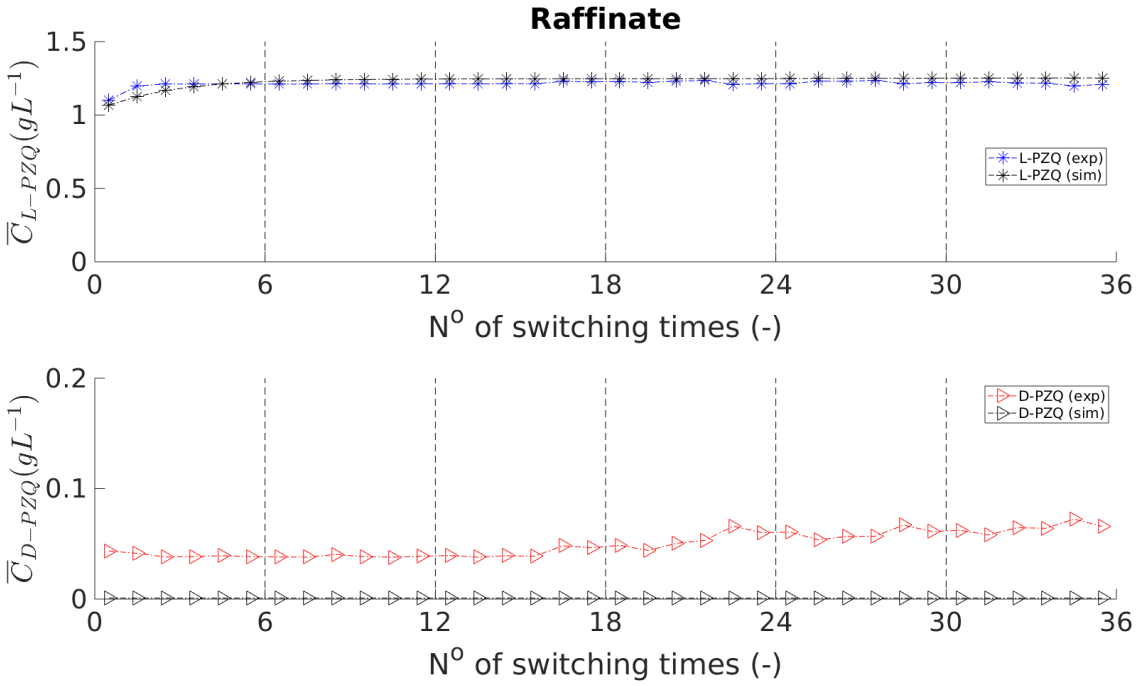

Figure 4.13: Raffinate stream dynamic after a -10% step perturbation in the desorbent pump, Q_D (*run 9*).

The raffinate stream maintained the same level of contamination in comparison to the experiment before the disturbance. Considering the fluctuations imposed by the thermodynamic parameters and by the flow rates experimental errors, the D-PZQ could likely contaminate the raffinate, which was effectively observed in Figure 4.13. The concentration of L-PZQ in the raffinate stream increased because it became more concentrated, thanks to less desorbent quantity coming in the unit. The D-PZQ concentration in the extract stream did not change because the quantity of D-PZQ coming in the unit did not change and all the zones, but the zone 4, flow rates remained unchanged.

4.3.7 + 10% Q_F step in the SMB unit - *Run 10*

The fourth perturbation experiment consisted of applying a step of +10% in the Q_F variable. The discussion starts with the analysis in the CSS, followed by the analysis of the dynamics. Figure 4.15 shows the qualitative information about the CSS achieved by the SMB unit. It can be observed that the stationary state slightly shifted to a higher m_3 position (m_2 remained unchanged) in the m_3 x m_2 plane, and it did not shift in the m_4 x m_1 plane. It is essential to mention that the flow rates in zone 1, 2, and 4 could not be changed because they were determined by HPLC pumps, which maintained their nominal flow even after disturbance. The only flow

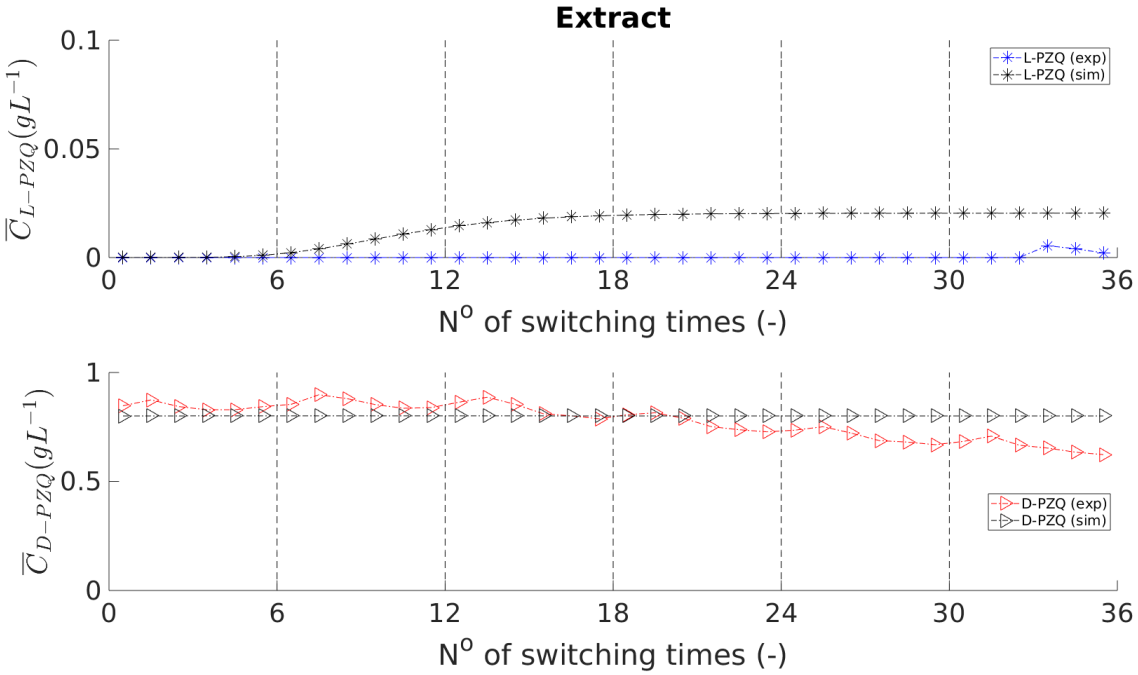

Figure 4.14: Extract stream dynamic after a -10% step perturbation in the desorbent pump, Q_D (*run 9*).

rate allowed to change was the one in zone 3 (see Figure 4.15), culminating in an increased flow of raffinate.

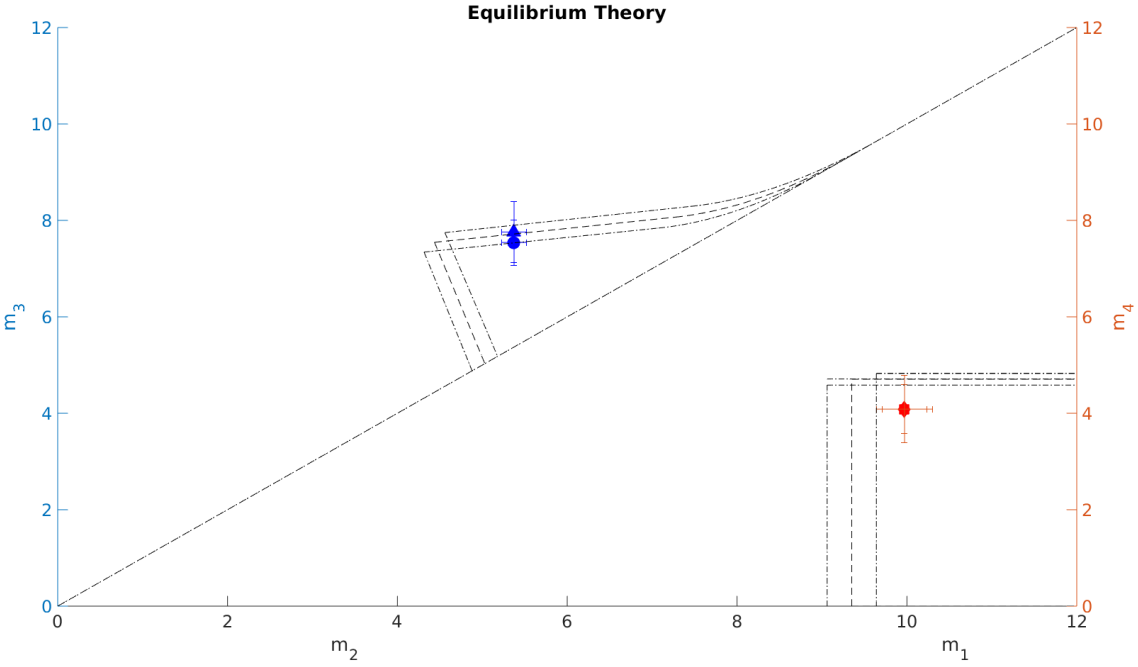

Figure 4.15: Comparison in the separation triangle of *run 6* (blue circle) and *run 10* (blue triangle) and regeneration rectangle of *run 6* (red circle) and *run 10* (red diamond).

It is important to highlight that the operating points in Figure 4.15 represent the average behavior of the unit. However, thanks to fluctuations discussed earlier;

the unit can operate in conditions other than expected. If the simulated scenario had occurred, the raffinate would not have been contaminated, as seen in Figure 4.16. However, taking into account the experimental errors, working outside the separation area was plausible and happened. As the unit started working in a condition closer to the borderline, the contamination by D-PZQ increased. Besides, the D-PZQ contamination in the raffinate was not predicted by the model thanks to this model's inability to consider the intrinsic fluctuations; the L-PZQ dynamic in the raffinate stream showed good agreement between the experimented and the simulated data.

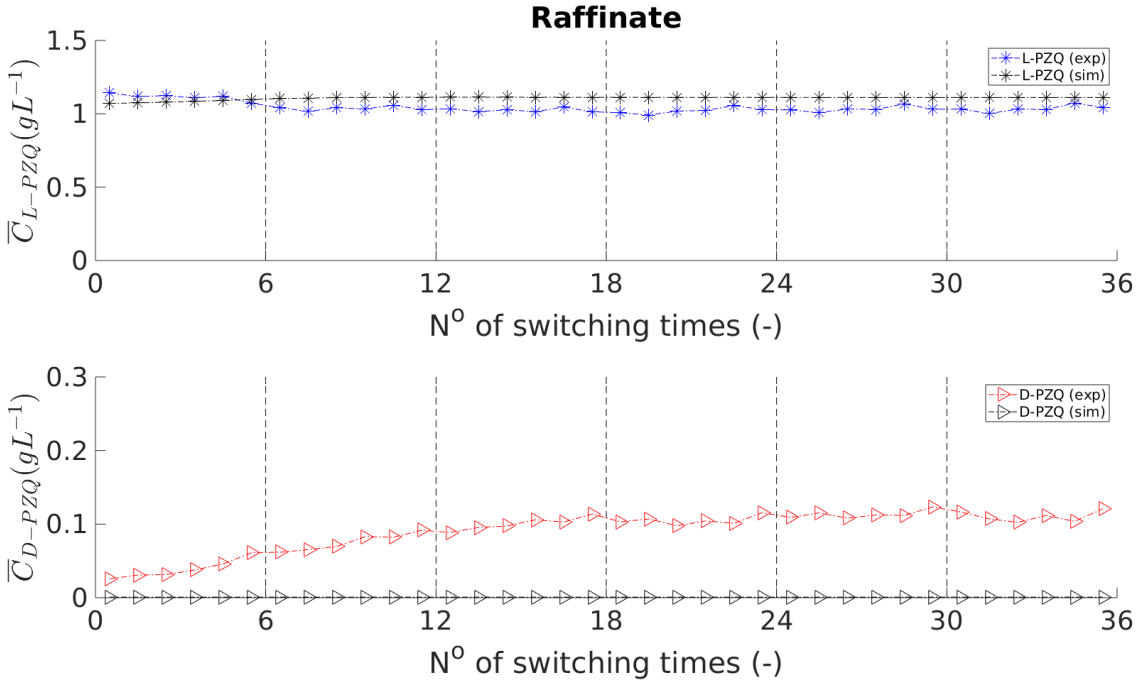

Figure 4.16: Raffinate stream dynamic after a +10% step perturbation in the feed pump, Q_F (*run 10*).

D-PZQ curve in the extract stream (see Figure 4.17) presented similar behavior to that observed for the D-PZQ curve in the extract stream of Figure 4.14, but in a baseline lower than the predicted by the model. It can be explained by the exit of part of the D-PZQ as a contaminant in the raffinate, therefore decreasing the amount that leaves in the extract.

4.3.8 - 10% Q_F step in the SMB unit - *Run 11*

The fifth perturbation experiment consisted of applying a step of -10% in the Q_F variable. The discussion starts with the analysis in the CSS, followed by the analysis of the dynamics. Figure 4.18 shows the qualitative information about the CSS achieved by the SMB unit. It can be observed that the stationary state slightly shifted to a lower m_3 position (m_2 remained unchanged) in the m_3 x m_2 plane, and

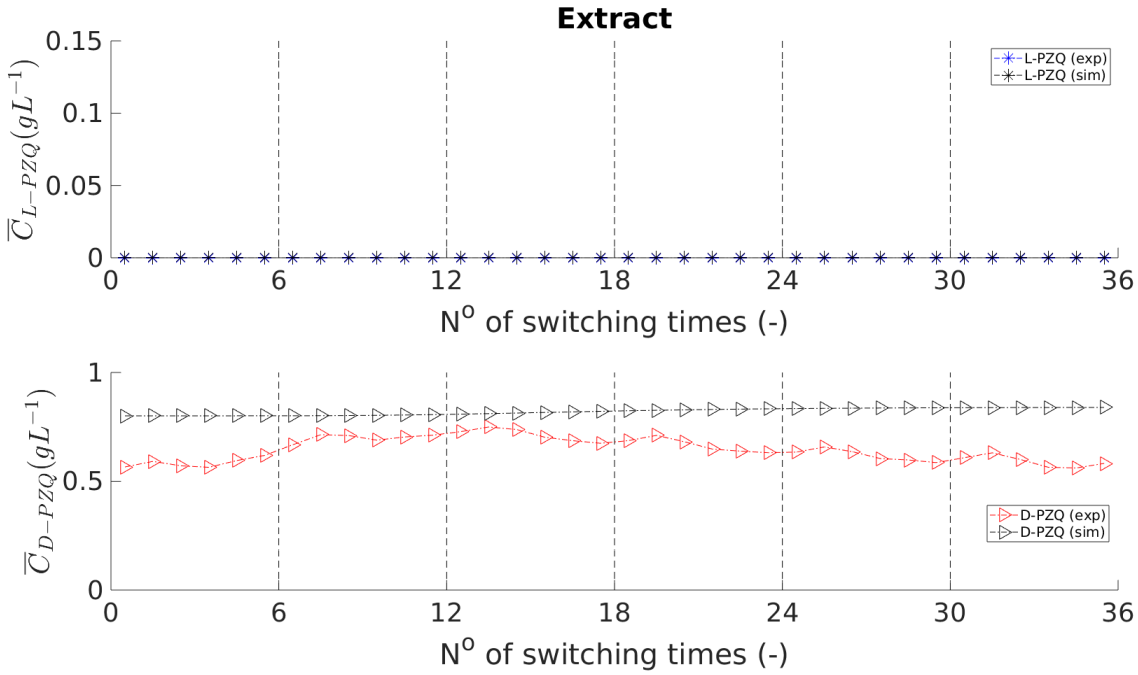

Figure 4.17: Extract stream dynamic after a +10% step perturbation in the feed pump, Q_F (*run 10*).

it did not shift in the m_4 x m_1 plane. It is important to mention that the flow rates in zone 1, 2, and 4 could not be changed for the same reasons previously discussed in *Run 10*. The only flow rate allowed to change was the one in zone 3 (see Figure 4.18), culminating in decreased flow of raffinate.

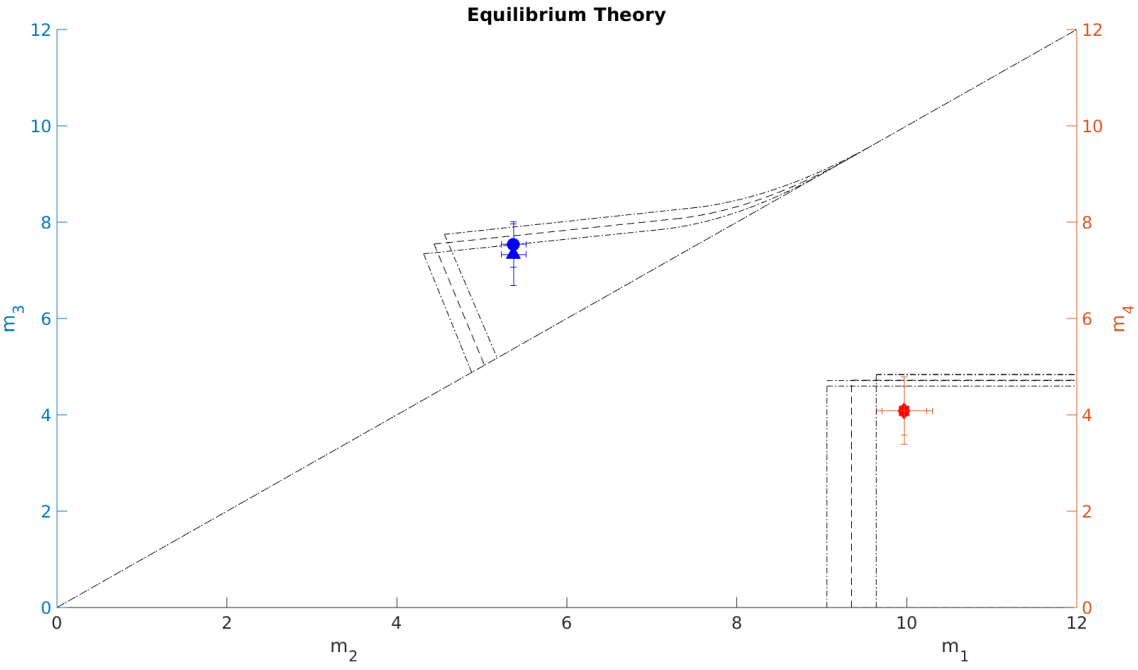

Figure 4.18: Comparison in the separation triangle of *run 6* (blue circle) and *run 11* (blue triangle) and regeneration rectangle of *run 6* (red circle) and *run 11* (red diamond).

Figure 4.19 showed good agreement between the predicted and the simulated data. The slight contamination of D-PZQ remained unchanged, corroborating with the situation exposed by Figure 4.18, which shows the unit running not far from the conditions before the perturbation.

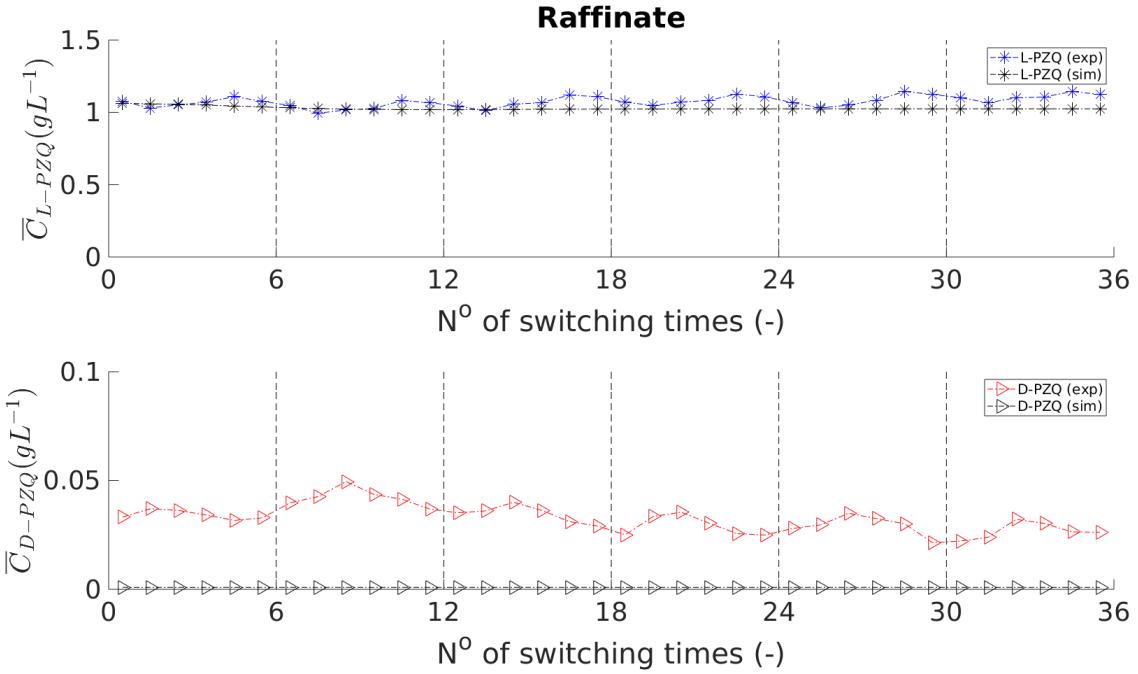

Figure 4.19: Raffinate stream dynamic after a -10% step perturbation in the feed pump, Q_F (*run 11*).

The D-PZQ curve in the extract stream (see Figure 4.20) presented similar behavior to that observed for the D-PZQ curve in the extract stream of Figure 4.14 due to experimental errors. The extract stream was not contaminated by the L-PZQ as predicted by the model and by the equilibrium theory.

The results above indicate the possibility to use a first-principle mathematical model mainly after counting the observed dead time, which opens a broad perspective once its usage for real-time applications is still scarce, thanks to the high computational costs required by the nonlinear behavior of the SMB. Usually, the mathematical model is a linear input/output data-based model. This sort of model has a low computational cost, but the choice of the input and output sets of variables, the identification of the process, and the determination and validation of the input/output data-based prediction model are additional and cumbersome steps, besides leaving the model hostage to a specific operating point.

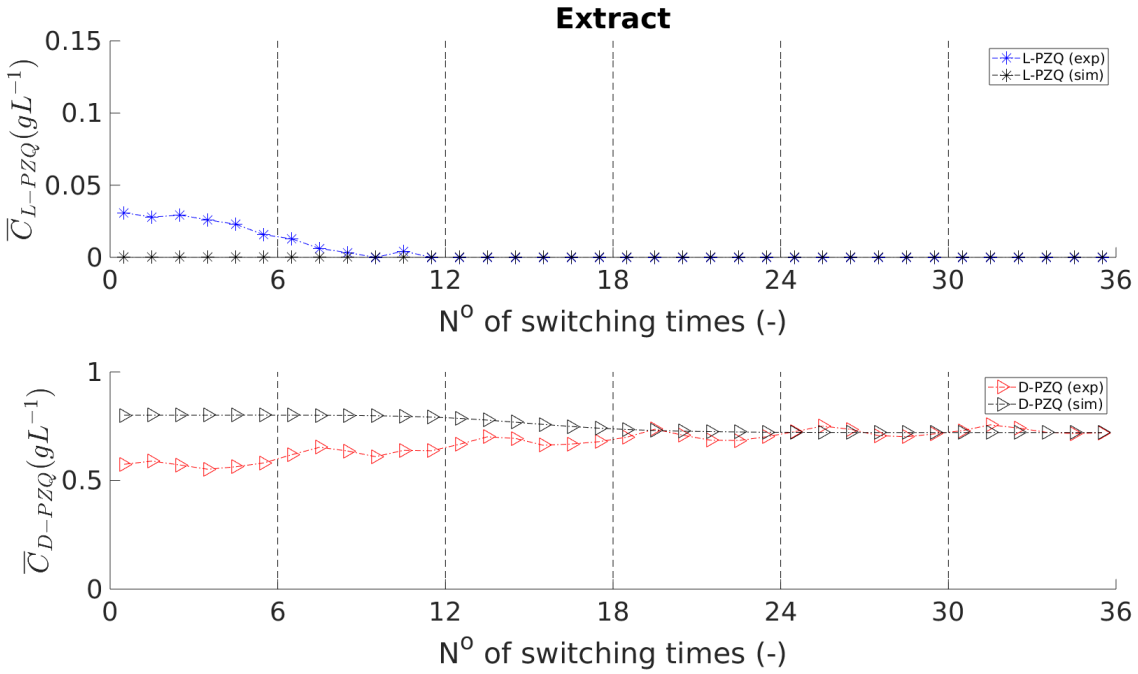

Figure 4.20: Extract stream dynamic after a -10% step perturbation in the feed pump, Q_F (*run 11*).

4.4 Conclusions

Despite tubes, pumps, and valves between the columns, the comparison between simulated and experimental data showed that axial dispersion effects related to the passage through the tubes and the mixing effects related to the passage through the valves and pumps could be neglected without loss of information. The only influence of them was reflected in the dead time observed for both extract and raffinate streams, but in the future, this could be easily accounted for in our software.

The comparison between simulated and experimental data evidenced an excellent agreement between analyses made in Chapter 2, which disregard the mass transfer resistances inside the chromatographic columns and the tubing influence inside the SMB unit (see Appendix A). As the calibration made in the *chiral detector* equipment was designed to detect streams richer in L-PZQ (*i.e.*, raffinate streams), the L-PZQ dynamics were conveniently captured by the online measurement of the raffinate stream.

The light of equilibrium theory could explain all the runnings with the help of experimental errors, which proved to be a vital feature in the prediction of the experiments carried out in the SMB. When the step concentration was applied at the beginning of the second stage of the experiment, a dead time was observed in the outlet streams, indicating that dead time should be taken into account in the simulation software when step changes in concentration were applied, but, for step changes in the flow rate, no dead time was observed. The D-PZQ dynamics in the

extract stream were also conveniently captured since the starting conditions (*Run 6*), and the applied perturbations moved the operating condition of the unit most of the time near (or in) the conditions of contaminated raffinate.

Chapter 5

Conclusions

The built-in-house SMB unit has been validated by passing tests that made the unit operate on purpose in the different operating conditions proposed by the equilibrium theory. The characterization of the chromatographic columns showed that mass transfer resistance could be neglected during the SMB operations. Furthermore, the small percentage of tubing volume (<3%) indicates that it could be neglected during the operation time. These hypotheses were confirmed when the SMB dynamics were revealed by the *chiral detector* equipment coupled in the raffinate and extract streams alternately by comparing of L-PZQ (D-PZQ) dynamics in the raffinate (extract) stream. The step disturbances applied in the flow rates showed good agreement between experimental and simulated data, as they could be explained taking into account the equilibrium theory and experimental fluctuations. The step-change in the concentration presented dead time in both outlets. However, the dynamics were similar to the simulation results, and, therefore, dead time could be easily accounted for in the simulation software.

The presented features of the SMB unit, chromatographic columns with cellulose tris(3-chloro-4-methyl-phenylcarbamate) (Chiralcel^{TM} OZ) as a chiral stationary phase, allowed to get superior performance in the separation of PZQ racemate. Compared to reference works in literature, the latter used high concentration, 50 g.L^{-1} of the racemic mixture in the feed stream, while our SMB unit used low rac-PZQ concentration.

The *chiral detector* equipment was calibrated using pure D- and L-PZQ and solutions with mixtures of both. Most of the mixtures were richer in L-PZQ, and this was made purposefully to use, preferably the equipment in the raffinate stream. The relationship between the signal and the mixtures with low L-PZQ concentration showed higher nonlinearity, which can be a problem when using it in the raffinate stream, but further investigations are needed. Confidence interval analysis and the approach developed during the calibration/validation work proved to be essential allies in determining enantiomeric concentrations in solutions with D- and L-PZQ.

The coupling of the SMB unit with the chiral detection equipment allows designing control strategies to be taken at the end of each switching time, unlike the usual control strategies that make decisions at the end of each cycle. In addition, the faster dynamics of separation of the PZQ enantiomers compared to the literature could allow the design of more efficient control strategies.

5.1 Suggestions for further developments

The possible further developments of this work are:

- study of the behavior of the SMB unit in even higher concentrations of PZQ (nonlinear region of the isotherm);
- use of another enantiomer that has no nonlinearities like the ones presented by PZQ enantiomer, in order to better characterize the SMB unit;
- execution of experiments with molecules that have no interactions with the CSP in order to characterize how the dynamics could be without the separation;
- further improvements in the calibration methodology (*e.g.*, neural networks);
- studies of different control strategies in closed-loop with and without models to predict the unit's behavior;
- application of wider steps in the SMB unit to prove the generality of the model used in the simulations, as well as new starting points could be used;
- test performance in different SMB modes of operation;
- execution of experiments with longer duration.

References

[1] CHING, C., LIM, B., LEE, E., et al. "Preparative resolution of praziquantel enantiomers by simulated counter-current chromatography", *Journal of Chromatography*, v. 634, pp. 215–219, 1993.

[2] LIM, B.-G., CHING, C.-B., TAN, R. B. H., et al. "Recovery of (-)-Praziquantel from racemic mixtures by continuous chromatography and crystallisation", *Chemical Engineering Science*, v. 14, pp. 2289–2298, 1995.

[3] Centers for Diasease Control and Prevention. "Neglected Tropical Diseases". 26 nov 2016. Disponível em: <`https://www.cdc.gov/globalhealth/ntd/fastfacts.html`>.

[4] World Health Organization. "Neglected Tropical Diseases". 25 nov 2016. Disponível em: <`http://www.who.int/neglected_diseases/diseases/en/`>.

[5] MAHMOUD, A. A. *Schistosomiasis*. 1 ed. London, Imperial College Press, 2001.

[6] RIDI, R. E. *Parasitic Diseases - Schistosomiasis*. 1 ed. Croatia, InTech, 2013.

[7] World Health Organization. "Schistosomiasis". 29 nov 2016. Disponível em: <`http://www.who.int/mediacentre/factsheets/fs115/en/`>.

[8] P S MBABAZI, A. O. "Examining the relationship between urogenital schistosomiasis and HIV infection", *PLoS Negl Trop Dis*, v. 5, n. 12, pp. 1396, Dec 1996.

[9] World Health Organization. "Strategy". 07 dec 2016. Disponível em: <`http://www.who.int/schistosomiasis/strategy/en/`>.

[10] World Health Organization. "Statistics". 07 dec 2016. Disponível em: <`http://apps.who.int/neglected_diseases/ntddata/sch/sch.html`>.

[11] World Health Organization. "WHO convenes experts to sustain progress against soil-transmitted helminthiases and schistosomiasis". 04 feb

2017. Disponível em: <http://www.who.int/neglected_diseases/news/WHO_convenes_experts_to_sustain_progre/en/>.

[12] LIA HASENCLEVER, E. A. *Economia Industrial de Empresas Farmacêticas*. 1 ed. Rio de Janeiro, E-papers, 2010.

[13] FAPERJ. "Fiocruz avança nos testes da vacina contra a esquistossomose". 06 feb 2017. Disponível em: <http://www.faperj.br/?id=3249.2.3>.

[14] World Health Organization. "Schistosomiasis: population requiring preventive chemotherapy and number of people treated in 2010". 07 dec 2016. Disponível em: <http://www.who.int/wer/en/>.

[15] REICH, M. R., GOVINDARAJ, R., DUMBAUGH, K., et al. *International strategies for tropical disease treatments. Experiences with praziquantel*. 1 ed. -, Harvard University, 1998.

[16] World Health Organization. "WHO Model List of Essential Medicines". 11 jan 2018. Disponível em: <http://www.who.int/medicines/publications/essentialmedicines/en/>.

[17] BUSTINDUY, A. L., WRIGHT, S., JOEKES, E. C., et al. "One hundred years of neglect in paediatric schistosomiasis", *Parasitology*, v. 144, n. 12, pp. 1613–1623, 2017.

[18] BUSTINDUY, A. L., WATERHOUSE, D., DE SOUSA-FIGUEIREDO, J. C., et al. "Population Pharmacokinetics and Pharmacodynamics of Praziquantel in Ugandan Children with Intestinal Schistosomiasis: Higher Dosages Are Required for Maximal Efficacy", *American Society for Microbiology*, v. 7, n. 4, pp. –, 2016.

[19] WHO. "The pediatric formulation". 15 jan 2018. Disponível em: <https://www.pediatricpraziquantelconsortium.org/node/36>.

[20] MEYER, T., SEKLJIC, H., FUCHS, S., et al. "Taste, A New Incentive to Switch to (R)-Praziquantel in Schistosomiasis Treatment", *PLoS Negl Trop Dis*, v. 3, pp. 357, 2009.

[21] DA FONSECA, L. B., VIÇOSA, A. L., MATTOS, A. C. A., et al. "Development of a brazilian nanoencapsulated drug for schistosomiasis treatment", *Revista Visa em debate*, v. 1, pp. 82, 2013.

[22] FONSECA, L. B., NELE, M., VOLPATO, N. M., et al. "Production of PMMA Nanoparticles Loaded with Praziquantel Through 'In Situ' Miniemulsion Polymerization", *Macromolecular Reaction Engineering*, v. 7, pp. 54, 2013.

[23] MALHADO, M., PINTO, D. P., SILVA, A. C., et al. "Preclinical pharmacokinetic evaluation of praziquantel loaded in poly (methyl methacrylate) nanoparticle using a HPLC-MS/MS", *Journal of Pharmaceutical and Biomedical Analysis*, v. 117, pp. 405, 2016.

[24] PAIVA, T., VIEIRA, L., MELO, P., et al. "In Situ Incorporation of Praziquantel in Polymer Microparticles through Suspension Polymerization for Treatment of Schistosomiasis", *Macromolecular Reaction Engineering*, v. 13, pp. 1, 2019.

[25] WHO. "Pediatric Praziquantel Consortium". 15 jan 2018. Disponível em: <https://www.pediatricpraziquantelconsortium.org/>.

[26] DOENHOFF, M. J., KUSEL, J. R., COLES, G. C., et al. "Resistance of Schistosoma mansoni to praziquantel: is there a problem?" *Transactions of the royal society of tropical medicine and hygiene*, v. 96, pp. 465, 2002.

[27] MELMAN, S. D., STEINAUER, M. L., CUNNINGHAM, C., et al. "Reduced Susceptibility to Praziquantel among Naturally Occurring Kenyan Isolates of Schistosoma mansoni", *Neglected Tropical Diseases*, v. 3, pp. e504, 2009.

[28] BOTROS, S., SAYED, H., AMER, N., et al. "Current status of sensitivity to praziquantel in a focus of potential drug resistance in Egypt", *International Journal for Parasitology*, v. 35, pp. 787, 2005.

[29] DOENHOFF, M. J., CIOLI, D., UTZINGER, J. "Praziquantel: mechanisms of action, resistance and new derivatives for schistosomiasis", *Current Opinion in Infectious Diseases*, v. 21, pp. 659, 2008.

[30] FALLON, P. G., STURROCK, R. F., CAPRON, A., et al. "Short Report: Diminished Susceptibility to Praziquantel in a Senegal Isolate of Schistosoma mansoni", *The American Journal of Tropical Medicine and Hygiene*, v. 53, pp. 61, 1995.

[31] GUGLIELMO, S., CORTESE, D., VOTTERO, F., et al. "New praziquantel derivatives containing NO-donor furoxans and related furazans as active agents against Schistosoma mansoni", *European Journal of Medicinal Chemistry*, v. 84, pp. 135, 2014.

[32] DONG, Y., CHOLLET, J., VARGAS, M., et al. "Praziquantel analogs with activity against juvenile Schistosoma mansoni", *Bioorganic and Medicinal Chemistry Letters*, v. 20, pp. 2481, 2010.

[33] WEN DUAN, W., JIE QIU, S., ZHAO, Y., et al. "Praziquantel derivatives exhibit activity against both juvenile and adult Schistosoma japonicum", *Bioorganic and Medicinal Chemistry Letters*, v. 22, pp. 1587, 2012.

[34] RONKETTI, F., RAMANA, A. V., CHAO-MING, X., et al. "Praziquantel derivatives I: Modification of the aromatic ring", *Bioorganic and Medicinal Chemistry Letters*, v. 17, pp. 4154, 2007.

[35] LAURENT, S. A.-L., BOISSIER, J., COSLEDAN, F., et al. "Synthesis of 'Trioxaquantel' Derivatives as Potential New Antischistosomal Drugs", *European Journal of Organic Chemistry*, v. -, pp. 895, 2008.

[36] ZHENG, Y., DONG, L., HU, C., et al. "Development of chiral praziquantel analogues as potential drug candidates with activity to juvenile Schistosoma japonicum", *Bioorganic and Medicinal Chemistry Letters*, v. 24, pp. 4223, 2014.

[37] Our experiment alpha. "Racemization of PZQ and PZQamine". 8 mar 2019. Disponível em: <`http://www.ourexperiment.org/rac_pza`>.

[38] LIANG, Y.-S., COLES, G. C., DOENHOFF, M. J., et al. "In vitro responses of praziquantel-resistant and -susceptible Schistosoma mansoni to praziquantel", *International Journal for Parasitology*, v. 31, pp. 1227, 2001.

[39] LIANG, Y.-S., WANG, W., DAI, J.-R., et al. "Susceptibility to praziquantel of male and female cercariae of praziquantel-resistant and susceptible isolates of Schistosoma mansoni", *Journal of Helminthology*, v. 84, pp. 202, 2010.

[40] CUNHA, F. C., SECCHI, A. R., DE SOUZA JR., M. B., et al. "Separation of praziquantel enantiomers using simulated moving bed chromatographic unit with performance designed for semipreparative applications", *Chirality*, v. 31, pp. 583–591, 2019.

[41] CUNHA, F., DE HOLANDA, R., SECCHI, A., et al. "Simultaneous absorption of UV/vis and circular dichroism to measure enantiomeric concentrations of praziquantel under nonlinear conditions", *Spectrochimica Acta Part A: Molecular and Biomolecular Spectroscopy*, v. 241, 2020.

[42] D B BROUGHTON, G. G. G. "Continuous sorption process employing fixed bed of sorbent and moving inlets and outlets". 23 may 1961. US 2985589.

[43] P S GOMES, M MINCEVA, A. E. R. "Simulated moving bed technology: old and new", *Adsorption*, v. 12, pp. 375–392, 2006.

[44] A RAJENDRAN, G PAREDES, M. M. "Simulated moving bed chromatography for the separation of enantiomers", *Journal of chromatography A*, v. 1216, pp. 709–738, 2009.

[45] RODRIGUES, A. E., PEREIRA, C., MINCEVA, M., et al. *Simulated Moving Bed Technology*. 1 ed. United States of America, Elsevier Inc., 2015.

[46] RUTHVEN, D. M., CHING, C. B. "Counter-Current And Simulated Counter-Current Adsorption Separation Processes", *Chemical Engineering Science*, v. 44, pp. 1011–1038, 1989.

[47] MAZZOTTI, M., STORTI, G., MORBIDELLI, M. "Robust Design of Countercurrent Adsorption Separation Processes: 2. Multicomponent Systems", *AIChE Journal*, v. 40, pp. 1825–1842, 1994.

[48] MAZZOTTI, M., STORTI, G., MORBIDELLI, M. "Robust Design of Countercurrent Adsorption Separation Processes: 3. Nonstoichiometric Systems", *AIChE Journal*, v. 42, pp. 2784–2796, 1996.

[49] ANDRADE, A., SECCHI, A., SOUZA, M., et al. "Nonlinear model predictive control applied to the separation of praziquantel in simulated moving bed chromatography", *Journal of Chromatography A*, v. 1470, pp. 42, Sep 2016.

[50] LIM, B.-G., CHING, C.-B. "Preliminary design of a simulated counter-current chromatographic system for the separation of praziquantel enantiomers", *Journal of Chromatography A*, v. 734, pp. 247–258, 1996.

[51] LIM, B.-G., CHING, C.-B. "Modelling studies on the transient and steady state behaviour of a simulated counter-current chromatographic system", *Separations Technology*, v. 6, pp. 29–41, 1996.

[52] LAMMERHOFER, M., LINDNER, W. "Recent developments in liquid chromatographic enantioseparation". In: *Separation Methods in Drug Synthesis and Purification*, 6 ed., cap. 9, -, Elsevier Science B. V., 2000.

[53] CHANKVETADZE, B., YASHIMA, E., OKAMOTO, Y. "Tris(chloro- and methyl-disubstituted phenylcarbamate)s of Cellulose as Chiral Stationary Phases for Chromatographic Enantioseparation", *Chemistry Letters*, v. 22, pp. 617–620, 1993.

[54] CHANKVETADZE, B., YASHIMA, E., OKAMOTO, Y. "Dimethyl-, dichloro- and chloromethylphenylcarbamates of amylose as chiral stationary phases for high-performance liquid chromatography", *Journal of Chromatography A*, v. 694, pp. 101–109, 1995.

[55] CHANKVETADZE, B. "Recent developments on polysaccharide-based chiral stationary phases for liquid-phase separation of enantiomers", *Journal of Chromatography A*, v. 1269, pp. 26–51, 2012.

[56] SWEETMAN, S. C. *Martindale. The Complete Drug Reference.* 36 ed. -, Pharmaceutical Press, 2009.

[57] HENNER SCHMIDT-TRAUB, E. A. *Preparative Chromatography.* 2 ed. Germany, Wiley-VCH Verlag GmbH and Co. KGaA, 2012.

[58] GUIOCHON, G., FELINGER, A., SHIRAZI, D. G., et al. *Fundamentals of Preparative and Nonlinear Chromatography.* 2 ed. -, Elsevir Inc., 2006.

[59] ANDRADE, A. S. *Modeling, control, and optimization of the enantiomeric separation of praziquantel in simulated moving bed.* Master thesis, Chemical Engineering Program at COPPE/Federal University of Rio de Janeiro, Rio de Janeiro, Brazil, 2015.

[60] SANTOS, R. C. D. *Estudo do Equilíbrio de Adsorção entre os Enantiômeros do Praziquantel e a fase Sólida Celulose Tris 3-Cloro, 4-Metil Fenilcarbamato por meio de Regressão Não Linear de Modelos de Isotermas.* Master thesis, Escola de Química/Federal University of Rio de Janeiro, Rio de Janeiro, Brazil, 2016.

[61] CUNHA, F., DOS SANTOS, R., CURITIBA, C., et al. *Overload experiments using the Chiralcel-OZ chromatographic column to separate praziquantel.* Internal report, 2021.

[62] GOMES, P. S. *Advances in Simulated Moving Bed: New operating modes; new design methodologies; and product (FlexSMB-LSRE ®) development.* Phd thesis, Department of Chemical Engineering, Porto, Portugal, 2009.

[63] ABEL, S., ERDEM, G., AMANULLAH, M., et al. "Optimizing control of simulated moving beds - experimental implementation", *Journal of Process Control*, v. 1092, pp. 2–16, 2005.

[64] CHANKVETADZE, B., YASHIMA, E., OKAMOTO, Y. "Chloromethylphenylcarbamate derivatives of cellulose as chiral sta-

tionary phases for high-performance liquid chromatography", *Journal of Chromatography A*, v. 670, pp. 39–49, 1994.

[65] DA SILVA JUNIOR, I. J., SARTOR, J. P., ROSA, P. C. P., et al. "High-performance liquid chromatographic separation of rolipram, bupivacaine and omeprazole using a tartardiamide-based stationary phase. Influence of flow rate and temperature on the enantioseparation", *Journal of Chromatography A*, v. 1162, pp. 97–102, 2007.

[66] ANTELO, F., SANTANA, C. C., ALVES, T. L. M., et al. "Thermodynamic Study of Enantioseparation of Mitotane by Supercritical Fluid Chromatography", *Separation Science and Technology*, v. 47, pp. 636–640, 2012.

[67] PAVIA, D. L., LAMPMAN, G. M., KRIZ, G. S., et al. *Introduction to Spectroscopy*. Cengage Learning, 2008.

[68] SALAVATI-NIASARI, M., LOGHMAN-ESTARKI, M. R., DAVAR, F. "Controllable synthesis of nanocrystalline CdS with different morphologies by hydrothermal process in the presence of thioglycolic acid", *Chemical Engineering Journal*, v. 145, pp. 346–350, 2008.

[69] DARGAHI, M., MASTERI-FARAHANI, M., SHAHSAVARIFAR, S., et al. "Microemulsion-mediated preparation of $Ce_2(MoO_4)_3$ nanoparticles for photocatalytic degradation of crystal violet in aqueous solution", *Environmental Science and Pollution Research*, v. 27, pp. 12047–12054, 2020.

[70] NGAMDEE, K., NGEONTAE, W. "Circular dichroism glucose biosensor based on chiral cadmium sulfide quantum dots", *Sensors and Actuators B: Chemical*, v. 274, pp. 402–411, 2018.

[71] WANG, J., XU, X., QIU, X., et al. "Yolk-shell structured Au@Ag@mSiO 2 as a probe for sensing cysteine enantiomers and Cu 2+ based on circular dichroism", *Analyst*, v. 144, pp. 7489–7497, 2019.

[72] LIU, K., DU, G., YE, L., et al. "A chiroptical nanoprobe for highly selective recognition of histidine enantiomers in aqueous media", *Sensors and Actuators B: Chemical*, v. 284, pp. 55–62, 2019.

[73] GUO, P., WANG, Y., ZHUANG, Q. "Highly sensitive and selective biosensor for heparin detection with rhodamine B-labelled peptides as fluorescent bioreceptors", *Sensors and Actuators B: Chemical*, v. 299, pp. 126873, 2019.

[74] LUO, Y., WU, L., YANG, B., et al. "A novel potential primary method for quantification of enantiomers by high performance liquid chromatography-circular dichroism", *Scientific Reports*, v. 8, pp. 7390, 2018.

[75] HE, Z., WU, F., XIA, W., et al. "Separation and detection of cyproconazole enantiomers and its stereospecific recognition with chiral stationary phase by high-performance liquid chromatography", *Analyst*, v. 144, pp. 5193–5200, 2019.

[76] TAKASU, K., KUSHIRO, K., HAYASHI, K., et al. "Polymer brush biointerfaces for highly sensitive biosensors that preserve the structure and function of immobilized proteins", *Sensors and Actuators B: Chemical*, v. 216, pp. 428–433, 2015.

[77] ANGIOLINI, L., BENELLI, T., GIORGINI, L., et al. "Chiroptical and optical thermoplastic acid sensors based on chiral methacrylic polymers containing azoaromatic moieties", *Sensors and Actuators B: Chemical*, v. 126, pp. 56–61, 2007.

[78] REN, D.-M., GUO, H.-F., WANG, S.-Q., et al. "Separation and structure determination of two diastereomeric pairs of enantiomers from Dracocephalum rupestre by high-performance liquid chromatography with circular dichroism detection", *Journal of Chromatography A*, v. 1161, pp. 334–337, 2007.

[79] ANDERSSON, S., NELANDER, H., OHLEN, K. "Preparative Chiral Chromatography and Chiroptical Characterization of Enantiomers of Omeprazole and Related Benzimidazoles", *Chirality*, v. 19, pp. 706–715, 2007.

[80] BERTUCCI, C., ANDRISANO, V., CAVRINI, V., et al. "Reliable Assay of Extreme Enantiomeric Purity Values by a New Circular Dichroism Based HPLC Detection System", *Chirality*, v. 12, pp. 84–92, 2000.

[81] PURDIE, N., SWALLOWS, K. A. "Analytical applications of polarimetry, optical rotatory dispersion, and circular dichroism", *Analytical Chemistry*, v. 61, pp. 77–89, 1989.

[82] VELLUZ, L., LEGRAND, M. "Zirkulardichroismus und Raumstruktur: Neuere Ergebnisse im Steroid-Gebiet", *Angewandte Chemie*, v. 73, pp. 603–611, 1961.

[83] VELLUZ, L., LEGRAND, M. "Progress in Optical Circular Dichroism", *Angewandte Chemie International Edition*, v. 4, pp. 838–845, 1965.

[84] BEROVA, N., BARI, L. D., PESCITELLI, G. "Application of electronic circular dichroism in configurational and conformational analysis of organic compounds", *The Royal Society of Chemistry*, v. 36, pp. 914–931, 2007.

[85] BEROVA, N., POLAVARAPU, P. L., NAKANISHI, K., et al. *Comprehensive Chiroptical Spectroscopy*, v. 1. JOHN WILEY & SONS, INC, 2012.

[86] KOTT, L., HOLZHEUER, W. B., WONG, M. M., et al. "An evaluation of four commercial HPLC chiral detectors: A comparison of three polarimeters and a circular dichroism detector", *Journal of Pharmaceutical and Biomedical Analysis*, v. 43, pp. 57–65, 2007.

[87] BOBBITT, D. R., LINDER, S. W. "Recent advances in chiral detection for high performance liquid chromatography", *Trends in Analytical Chemistry*, v. 20, pp. 111–123, 2001.

[88] BERTUCCI, C., TEDESCO, D. "Advantages of electronic circular dichroism detection for the stereochemical analysis and characterization of drugs and natural products by liquid chromatography", *Journal of Chromatography A*, v. 1269, pp. 69–81, 2012.

[89] DRAKE, A. F., GOULD, J. M., MASON, S. F. "Simultaneous Monitoring of Light-Absorption and Optical Activity in the Liquid Chromatography of Chiral Substances", *Journal of Chromatography*, v. 202, pp. 239–245, 1980.

[90] BERTUCCI, C., DOMENICI, E., SALVADORI, P. "Circular dichroism detection in high-performance liquid chromatography: evaluation of the anisotropy factor", *Journal of Pharmaceutical and Biomedical Analysis*, v. 8, pp. 843–846, 1990.

[91] SALVADORI, P., BERTUCCI, C., ROSINI, C. "Circular Dichroism Detection in HPLC", *Chirality*, v. 3, pp. 376–385, 1991.

[92] ZUKOWSKI, J., TANG, Y., BERTHOD, A., et al. "Investigation of a circular dichroism spectrophotometer as a liquid chromatography detector for enantiomers: sensitivity, advantages and limitations", *Analytica Chimica Acta*, v. 258, pp. 83–92, 1992.

[93] SANCHEZ, F. G., DIAZ, A. N., DE VICENTE, A. B. M. "Enantiomeric resolution of bupivacaine by high-performance liquid chromatography and chiroptical detection", *Journal of Chromatography A*, v. 1188, pp. 314–317, 2008.

[94] LECOEUR-LORIN, M., DELEPEE, R., ADAMCZYK, M., et al. "Simultaneous determination of optical and chemical purities of a drug with two chiral centers by liquid chromatography-circular dichroism detection on a non-chiral stationary phase", *Journal of Chromatography A*, v. 1206, pp. 123–130, 2008.

[95] SONG, S., SUN, L., YUAN, L., et al. "Method to determine enantiomeric excess of glucose by nonchiral high-performance liquid chromatography using circular dichroism detection", *Journal of Chromatography A*, v. 1179, pp. 125–130, 2008.

[96] HAN, S., MARTIN, S. M. "Enantioselective cholesteric liquid crystalline membranes characterized using nonchiral HPLC with circular dichroism detection", *Journal of Membrane Science*, v. 367, pp. 1–6, 2011.

[97] TANG, Q., ZHAO, L., XIE, J., et al. "Deviations from Beer's law in electronic absorption and circular dichroism: Detection for enantiomeric excess analysis", *Chirality*, v. 31, pp. 492–501, 2019.

[98] ZENONI, G., PEDEFERRI, M., MAZZOTTI, M., et al. "On-line monitoring of enantiomer concentration in chiral simulated moving bed chromatography", *Journal of Chromatography A*, v. 888, pp. 73–83, 2000.

[99] JR., A. G. B., DA SILVA JR., I. J., DOS SANTOS, M. A. G., et al. "Modeling, Simulation, and Experimental Evaluation of Continuous Chromatographic Separation of Ketamine Enantiomers on MCTA", *Journal of Liquid Chromatography and Related Technologies*, v. 31, pp. 3057–3076, 2008.

[100] SKOOG, WEST, HOLLER, F. J., et al. *Fundamentals of Analytical Chemistry*. 9 ed. , Cengage Learning, 2013.

[101] MAYERHOFER, T. G., HOFER, S., POPP, J. "Deviations from Beer's law on the microscale - Nonadditivity of absorption cross sections", *Physical Chemistry Chemical Physics*, v. 21, pp. 9793–9801, 2019.

[102] LEWIS, G. F. *Analytical Chemistry: An Introduction*. 2 ed. London, MacMillan, 1985.

[103] ENGELL, S., TOUMI, A. "Optimisation and control of chromatography", *Computers and Chemical Engineering*, v. 29, pp. 1243–1252, 2005.

[104] I.-H SONG, E. A. "Identification and predictive control of a simulated moving bed process: Purity control", *Chemical Engineering Science*, v. 61, pp. 1973–1986, 2006.

[105] MARTEAU, P., HOTIER, G., ZANIER-SZYDLOWSKI, N., et al. "Advanced control of C8 aromatics separation process with real-time multipoint online Raman spectroscopy", *Process Control and Quality*, v. 6, pp. 133, 1994.

[106] KLATT, K.-U., HANISCH, F., DUNNEBIER, G. "Model-based control of a simulated moving bed chromatographic process for the separation of fructose and glucose", *Journal of Process Control*, v. 12, pp. 203–219, 2002.

[107] ALTENHONER, U., MEURER, M., STRUBE, J., et al. "Parameter estimation for the simulation of liquid chromatography", *Journal of Chromatography A*, v. 769, pp. 59–69, 1997.

[108] MIHLBACHLER, K., SEIDEL-MORGENSTERN, A., GUIOCHON, G. "Detailed Study of Troger's Base Separation by SMB Process", *AIChE Journal*, v. 50, pp. 611, 2004.

[109] ERDEM, G., ABEL, S., AMANULLAH, M., et al. "Automatic Control of Simulated Moving Beds —Experimental Verification", *Adsorption*, v. 11, pp. 573, 2005.

[110] ERDEM, G., ABEL, S., MORARI, M., et al. "Automatic Control of Simulated Moving Beds", *Ind. Eng. Chem. Res.*, v. 43, pp. 405, 2004.

[111] ABEL, S., ERDEM, G., MAZZOTTI, M., et al. "Optimizing control of simulated moving beds:linear isotherm", *Journal of Chromatography A*, v. 1033, pp. 229–239, 2004.

[112] SONG, I.-H., AMANULLAH, M., ERDEM, G., et al. "Experimental implementation of identification-based optimizing control of a simulated moving bed process", *Journal of Chromatography A*, v. 1113, pp. 60–73, 2006.

[113] AMANULLAH, M., GROSSMANN, C., MAZZOTTI, M., et al. "Experimental implementation of automatic 'cycle to cycle' control of a chiral simulated moving bed separation", *Journal of Chromatography A*, v. 1165, pp. 100–108, 2007.

[114] GROSSMANN, C., ERDEM, G., MORARI, M., et al. "'cycle to cycle' Optimizing Control of Simulated Moving Beds", *AIChE Journal*, v. 54, pp. 194–208, 2007.

[115] LANGEL, C., GROSSMANN, C., MORBIDELLI, M., et al. “Implementation of an automated on-line high-performance liquid chromatography monitoring system for ‘cycle to cycle’ control of simulated moving beds”, *Journal of Chromatography A*, v. 1216, pp. 8806–8815, 2009.

[116] LANGEL, C., GROSSMANN, C., JERMANN, S., et al. “Experimental Optimizing Control of the Simulated Moving Bed Separation of Troger’s Base Enantiomers”, *Ind. Eng. Chem. Res.*, v. 49, pp. 11996–12003, 2010.

[117] ARAUJO, J. M., RODRIGUES, R., EUSEBIO, M. F., et al. “’On-line enantiomeric analysis using high-performance liquid chromatography in chiral separation by simulated moving bed”, *Journal of Chromatography A*, v. 1189, pp. 292–301, 2008.

[118] MAO, S., ZHANG, Y., ROHANI, S., et al. “Enantioseparation of Racemic Mandelic Acid by Simulated Moving Bed Chromatography Using Chiralcel-OD Column”, *THE CANADIAN JOURNAL OF CHEMICAL ENGINEERING*, v. 92, pp. 1283–1292, 2014.

[119] SUVAROV, P., LEE, J.-W., WOUWER, A. V., et al. “Online estimation of optimal operating conditions for simulated moving bed chromatographic processes”, *Journal of Chromatography A*, v. 1602, pp. 266–272, 2019.

[120] FUTTERER, M. *On Design and Control of Simulated Moving Bed Plants*. Phd thesis, Fakultat Elektrotechnik und Informationstechnik der Otto-von-Guericke-Universitat Magdeburg, Magdeburg, Germany, 2010.

[121] SUVAROV, P., WOUWER, A., LEE, J., et al. “Control of incomplete separation in simulated moving bed chromatographic processes”, *International Federation of Automatic Control*, v. 49, pp. 153–158, 2016.

[122] CAZES, J., SCOTT, R. P. W. *Chromatography Theory*. 1 ed. USA, Marcel Dekker, Inc., 2002.

Appendix A

Constructed Simulated Moving Bed unit

This chromatographic unit was built in the **LAB**oratory of **C**hromatography and **ADS**orption (**LABCADS**) [1]. The general steps to build this unit were:

1. Design steps:
   (a) 3D project using AutoCad®2016;
   (b) Project of the electrical part;
   (c) Project of the electronic part;
2. Construction steps:
   (a) Assembly of the physical parts:
      - skid;
      - degasser;
      - six 8-way valves;
      - six 2-way valves;
      - two relief valves;
      - six chromatographic columns;
      - four HPLC pumps; and
      - sixteen meters of stainless steel tubing of 1/16" OD;
   (b) Development of the interface using LabView ®2012 SP1:
      - prior the interface, each piece of equipment was individually automated using LabView software and proper protocol communication.

[1] LABCADS composes the complex of laboratories called ATOMS, which congregates professors, researchers, and students of two academic units of the Federal University of Rio de Janeiro (UFRJ): (1) The School of Chemistry and (2) the Chemical Engineering Program (PEQ). The latter belonging to Alberto Luiz Coimbra Institute for Graduate Studies (COPPE)

(c) integration of the physical part, the developed interface, electrical and electronic parts. In order to reproduce the Simulated Moving Bed concept.

The constructed SMB unit was composed of four zones and 6 chromatographic columns with the configuration [**1 2 2 1**], which means **one** column for zone 1, **two** columns for zone 2, **two** columns for zone 3, and **one** column for zone 4. An HPLC pump was allocated in zone 2. Previous experiences coming from [62] were used to choose the configuration adopted in this work. The pipes connecting the columns, valves, and pumps should be as small as possible because there is no separation inside them. Two side effects could come out: (1) depending on the tube size (length and diameter), the dead volume could promote axial dispersion, and (2) the valves and pumps could promote back mixing effects. The constructed unit has approximately 3% of pipe volume considered as dead volume. Table A.1 shows the dead volume for each zone, and the general view of the unit is illustrated in Figure 2.8.

Table A.1: Pipes dead volume (V_{tub}), useful volume (V_{uv}) and porcentage of dead volume (%) in each zone.

Volume (cm^3)	Zone 1	Zone 2	Zone 3	Zone 4
V_{tub}	0.16	0.42	0.22	0.22
V_{uv}	5.82	11.66	11.66	5.83
%	2.67	3.48	1.85	3.64

A.1 Electrical part

In Figure A.1, the electrical part of the SMB unit is represented. Two spots in socket 4 are empty because this unit was designed for eight chromatographic columns, but just six columns have been used in this work. Two empty spots could also be observed in socket 8. The main reason is to allow the installation of at least one circular dichroism (and at *maximum* two) to give online measurements of the outlet streams. This installation is of fundamental importance because it could allow automatic control, like *Model Predictive Control* (MPC), to promote the better performance of the unit.

A.2 Electronic part

The switching command of the valves and the flow rate of the pumps can be changed from the developed supervisory system, thanks to the electronic part, whose diagram is represented in Figure A.2.

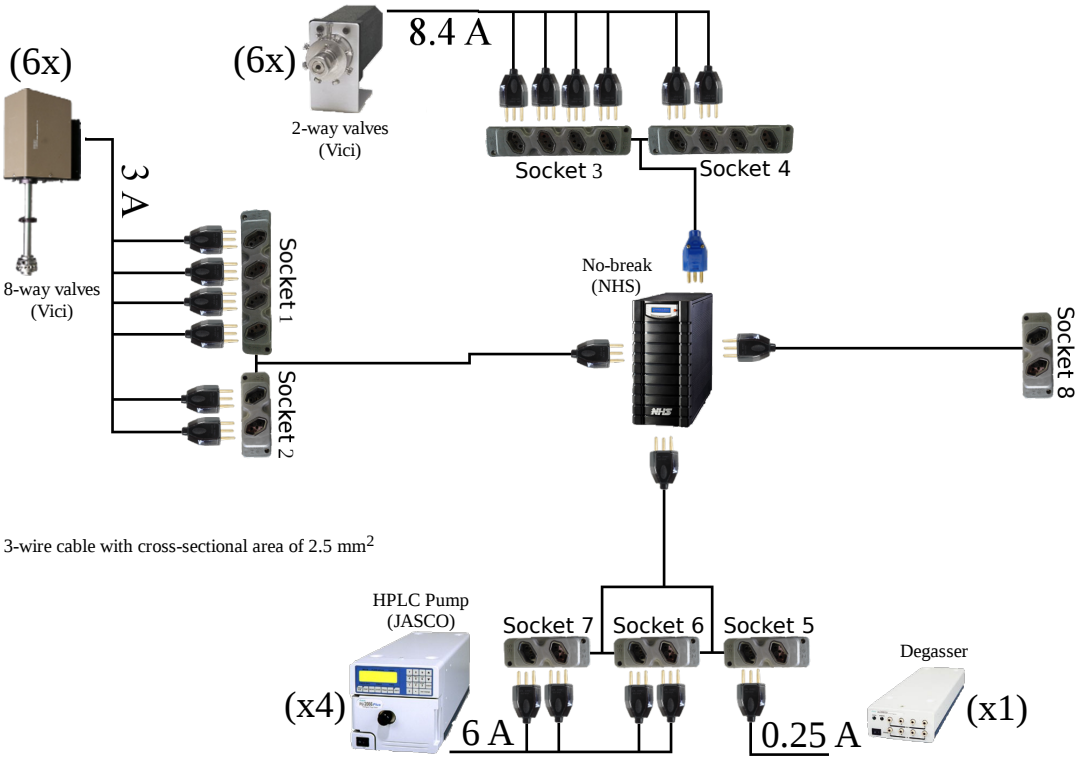

Figure A.1: Electrical part of the SMB unit.

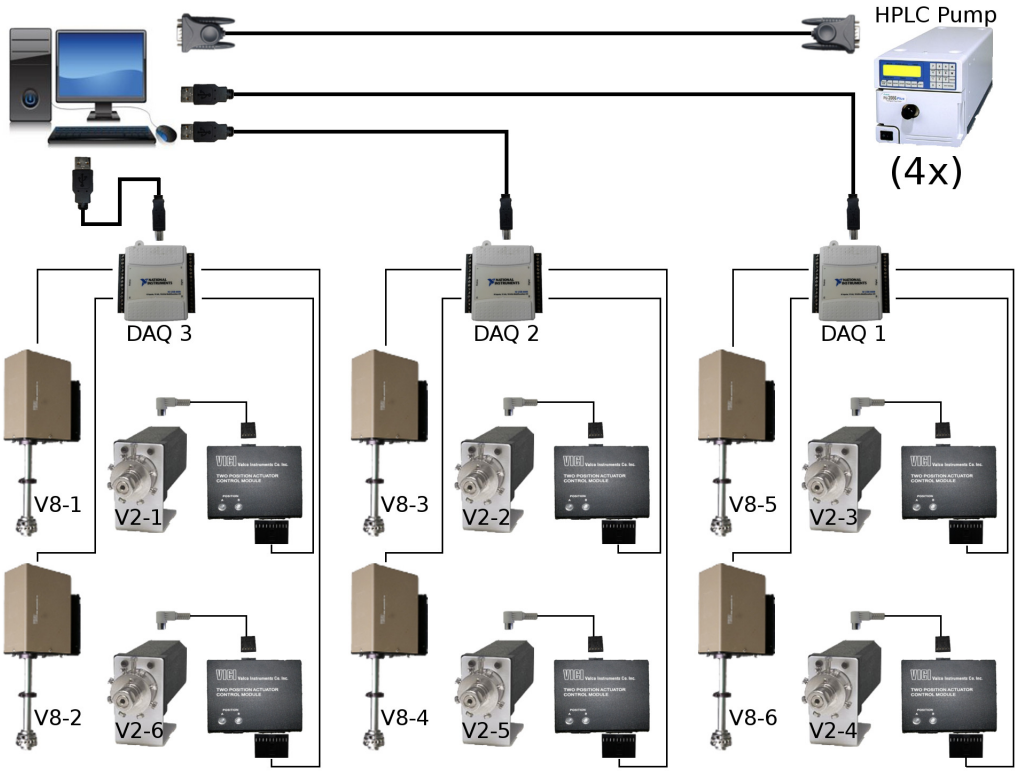

Figure A.2: Electronic part of the SMB unit.

As mentioned earlier, this SMB unit was designed to accommodate up to eight columns (*i.e.*, eight 2-way valves). Figure A.2 shows six 2-way valves, but the **D**ata

Ac**Q**uisition**s** (**DAQs**) could undoubtedly hold more 2-way valves, if necessary.

It is important to mention that the electronic and electric parts were accommodated in different electrical wire channels, because in the former, the wires have a voltage of approximately 5 volts and, in the latter, wires have a voltage of approximately 110 volts. If a bare wire of one touches a bare wire of the other, some equipment could be seriously damaged.

A.3 Supervisory system

The supervisory system was the main result of the final project to meet the course requirements of the undergraduate student, Rômulo Holanda [2]. This supervisory system allows the user to set pump flow rates and valve switching time, as well as monitoring the pump pressure, valve position and the number of cycles. In the subsequent figures, some features of the developed supervisory system are given.

Figure A.3 illustrates the main supervisory system tab, the "Simulated Moving Bed (Process Diagram)". In this tab, it can be observed at the top left corner the measured pressure in the pumps downstream. In the lower right and left corner, the 8-way valve position, and in the top right corner, the position of the 2-way valve. In the middle of the tab, a diagram showing which parts of the tubing are active at the moment of running. For instance, when this picture was captured, the eluent stream was fed into column 3 and the feed stream in column 6. While the outlet streams of extract and raffinate were withdrawn right after columns 3 and 1, respectively. The role of the 8-way valves can be better understood from Figure A.3, as described below:

- **Valve 8.1** directs the eluent stream to column 3;
- **Valve 8.2** directs the racemic solution to column 6;
- **Valve 8.3** withdraws the stream from **valve 8.5** and directs it to column 4 (*i.e.*, right after the column that received the eluent - column 3);
- **Valve 8.6** withdraws the stream from **valve 8.4** and directs it to column 2 (*i.e.*, right after the column that received the racemic mixture - column 1).

It is worth mentioning that in-between valves 8.5 and 8.3, there is the extract stream, and in-between valves 8.4 and 8.6, there is the raffinate stream. The eluent feed inlet, racemic mixture inlet, extract outlet, and the flow rate in zone 2 were set, respectively, by 4 HPLC pumps. The position of the 8-way valves points out in

[2] Rômulo Holanda's work has been advised by Felipe Coelho Cunha and Professor Amaro Gomes Barreto Júnior

which position in a cycle the running is (to know in which cycle the running is, it is necessary to check the "Cycles counter" in the tab named "Valves Controls and Indicators" (Figure A.4)). The 2-way valves are responsible for directing the stream to extract and raffinate outlet, as observed in Figure A.3. When valves 2.1 and 2.3 are closed, the only options available are the way out in the raffinate and extract outlet, respectively. The switching time could be set in the "Valves Controls and Indicators" tab, in the tab named "Controls - Eight-way valves" (see Figure A.4). The flow rate and the maximum operating pressure of each pump could be set in the tab named "Pump Controls and Indicators" (see Figure A.5). The dynamic of the measured pressure could be observed in plots situated in the middle of this tab, and on the right side, there is the option to record the dynamic behavior of the pressure in a .txt file.

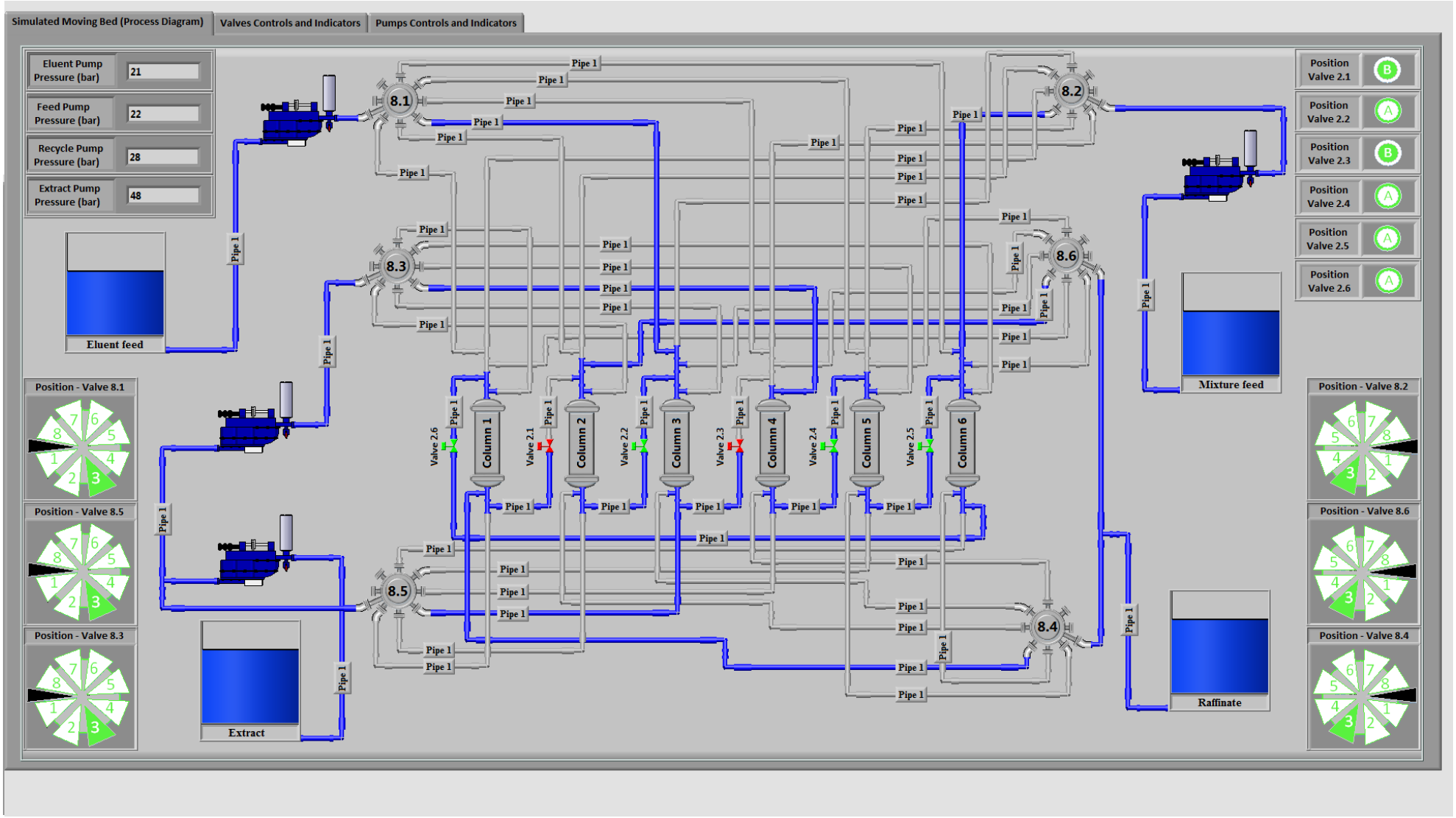

Figure A.3: Part of the supervisory system responsible to show the pressure in the pumps downstream, the valves position and in which tube is the flux.

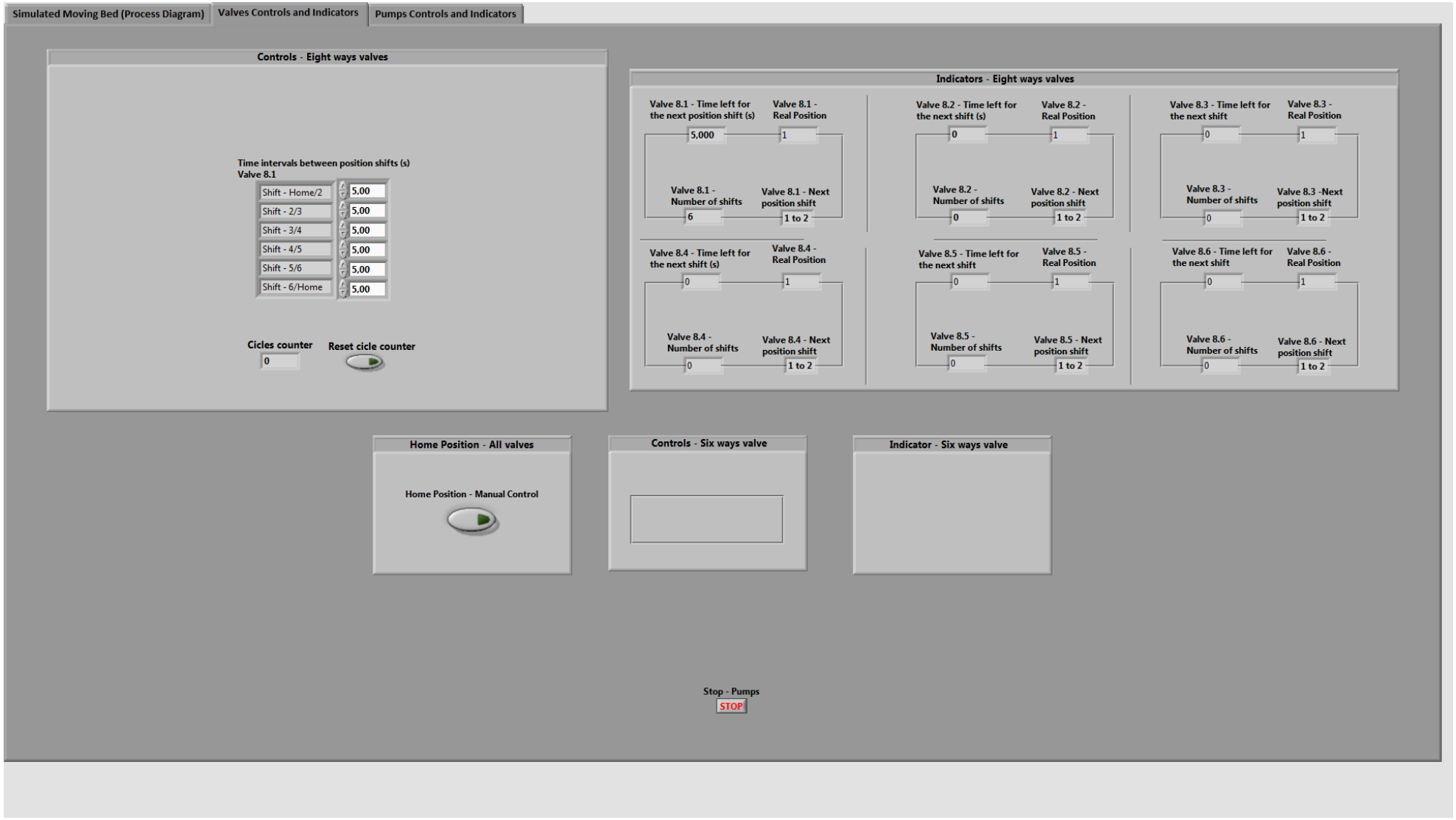

Figure A.4: Part of the supervisory system responsible to set the switching time of the valves, to show the remaining time to switch the valves and the completed cycles.

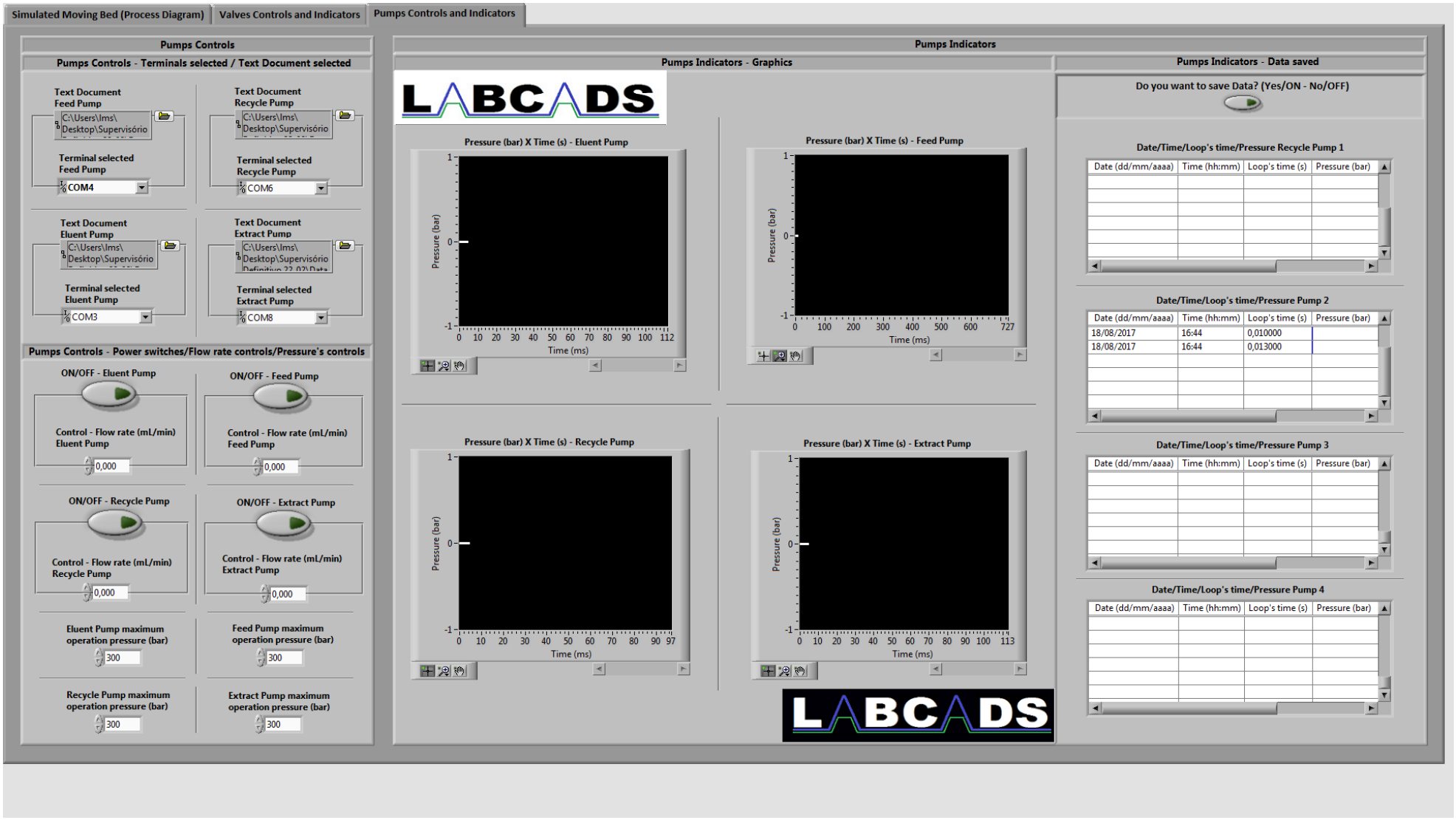

Figure A.5: Part of the supervisory system responsible to set the flow rate of the pumps and to observe the downstream pressure in the pumps.

Appendix B

Calculated errors

This appendix shows how errors were calculated throughout the text.

B.1 Bed Porosity ($\epsilon_{bed,j}$)

$$\delta\epsilon_{bed,j} = \pm\left\{\sum_{n=1}^{7}\left[\frac{\partial\epsilon_{bed,j}}{\partial t_{o,j,n}}\cdot\delta t_{o,j,n}\right]^2\right\}^{0.5}, \tag{B.1}$$

where,

$$\frac{\partial\epsilon_{bed,j}}{\partial t_{o,j,n}} = \frac{\dot{V}_n}{V_{column}}. \tag{B.2}$$

B.2 Henry constant ($\mathbf{H}_{i,j}$)

$$\delta H_{i,j} = \pm\left\{\sum_{n=1}^{7}\left[\frac{\partial H_{i,j}}{\partial t_{i,j,n}}\cdot\delta t_{i,j,n}\right]^2 + \sum_{n=1}^{7}\left[\frac{\partial H_{i,j}}{\partial t_{o,j,n}}.\delta t_{o,j,n}\right]^2 + \sum_{n=1}^{7}\left[\frac{\partial H_{i,j}}{\partial\epsilon_{bed,j,n}}.\delta\epsilon_{bed,j,n}\right]^2\right\}^{0.5}, \tag{B.3}$$

where,

$$\frac{\partial H_{i,j}}{\partial t_{i,j,n}} = \frac{\epsilon_{bed,j}}{1-\epsilon_{bed,j}}.\frac{1}{t_{o,j,n}} \tag{B.4a}$$

$$\frac{\partial H_{i,j}}{\partial t_{o,j,n}} = -\frac{t_{i,j,n}}{t_{o,j,n}^2}.\frac{\epsilon_{bed,j}}{1-\epsilon_{bed,j}} \tag{B.4b}$$

$$\frac{\partial H_{i,j}}{\partial\epsilon_{bed,j,n}} = \left[\frac{t_{i,j,n}}{t_{o,j,n}} - 1\right].\left[\frac{1}{1-\epsilon_{bed,j}} - \frac{\epsilon_{bed,j}}{(1-\epsilon_{bed,j})^2}\right]. \tag{B.4c}$$

B.3 Binary Langmuir isotherm parameter (b_i)

$$\delta b_i = \pm\left\{\left[\frac{\partial b_i}{\partial H_i}\delta H_i\right]^2 + \left[\frac{\partial b_i}{\partial q_m}\delta q_m\right]^2\right\}^{0.5}, \tag{B.5}$$

where,

$$\frac{\partial b_i}{\partial H_i} = \frac{1}{q_m} \tag{B.6a}$$

$$\frac{\partial b_i}{\partial q_m} = -\frac{H_i}{q_m^2}. \tag{B.6b}$$

$$\delta q_{e,i} = \pm \left\{ \sum_{i=A,B} \left[\left(\frac{\partial q_{e,i}}{\partial \overline{C}_i} \delta \overline{C}_i \right)^2 + \left(\frac{\partial q_{e,i}}{\partial b_i} \delta b_i \right)^2 \right] \right\}^{0.5} \tag{B.7}$$

where

$$\frac{\partial q_{e,i}}{\partial \overline{C}_i} = \frac{q_m b_i}{1 + \sum\limits_{i=A,B} \left(b_i \overline{C}_i \right)} \left[1 - \frac{b_i}{1 + \sum\limits_{i=A,B} \left(b_i \overline{C}_i \right)} \right] \tag{B.8a}$$

$$\frac{\partial q_{e,i}}{\partial b_i} = \frac{q_m \overline{C}_i}{1 + \sum\limits_{i=A,B} \left(b_i \overline{C}_i \right)} \left[1 - \frac{\overline{C}_i}{1 + \sum\limits_{i=A,B} \left(b_i \overline{C}_i \right)} \right]. \tag{B.8b}$$

(B.8c)

B.4 Axial diffusion ($D_{axial,i,j}$) and effective mass transfer coefficients ($k_{eff,i,j}$)

$$\delta u_{int,j,n} = \pm \left\{ \left[\frac{\partial u_{int,j,n}}{\partial \epsilon_{bed,j}} \cdot \delta \epsilon_{bed,j} \right]^2 \right\}^{0.5}, \tag{B.9}$$

where,

$$\frac{\partial u_{int,j,n}}{\partial \epsilon_{bed,j}} = -\frac{\overline{Q}_n}{\epsilon_{bed,j}^2 . A_{sc}}. \tag{B.10}$$

$$\delta D_{axial,i,j,n} = \pm \left\{ \left[\frac{\partial D_{axial,i,j,n}}{\partial u_{int,j,n}} \cdot \delta u_{int,j,n} \right]^2 \right\}^{0.5}, \tag{B.11}$$

where,

$$\frac{\partial D_{axial,i,j,n}}{\partial u_{int,j,n}} = \frac{A_{i,j}}{2}. \tag{B.12}$$

$$\delta k_{eff,i,j} = \pm \left\{ \left[\frac{\partial k_{eff,i,j}}{\partial \epsilon_{bed,j}} \cdot \delta \epsilon_{bed,j} \right]^2 + \left[\frac{\partial k_{eff,i,j}}{\partial H_{i,j}} \cdot \delta H_{i,j} \right]^2 \right\}^{0.5}, \tag{B.13}$$

where,

$$\frac{\partial k_{eff,i,j}}{\partial H_{i,j}} = \frac{2}{\overline{C}_{i,j}} \cdot \frac{k_{o,i,j} - 1}{(k_{o,i,j} + 1)^3} \cdot \frac{1 - \epsilon_{bed,j}}{\epsilon_{bed,j}}, \tag{B.14a}$$

$$\frac{\partial k_{eff,i,j}}{\partial \epsilon_{bed,j}} = \frac{2}{\overline{C}_{i,j}} \cdot \frac{k_{o,i,j} - 1}{(k_{o,i,j} + 1)^3} \cdot \frac{H_{i,j}}{\epsilon_{bed,j}}. \tag{B.14b}$$

B.5 k liquid internal flow rate, $\overline{Q}_h$, the solid flow rate, $\overline{Q}_{solid}$, and the flow rate ratios, m_h

The error of each k liquid internal flow rate, $\overline{Q}_h$, the solid flow rate, $\overline{Q}_{solid}$, and the flow rate ratios, m_h, were calculated as follows:

$$\delta \overline{Q}_k^{TMB} = \pm \left[\left(\frac{\partial \overline{Q}_k^{TMB}}{\partial \overline{Q}_k^{SMB}} \cdot \delta \overline{Q}_k^{SMB} \right)^2 + \left(\frac{\partial \overline{Q}_k^{TMB}}{\partial \epsilon_{int}} \cdot \delta \epsilon_{int} \right)^2 \right]^{0.5} \tag{B.15a}$$

$$\delta \overline{Q}_{solid} = \pm \left(\frac{\partial \overline{Q}_{solid}}{\partial \epsilon_{int}} \cdot \delta \epsilon_{int} \right) \tag{B.15b}$$

$$\delta m_k = \left[\left(\frac{\partial m_k}{\partial \overline{Q}_k^{TMB}} \cdot \delta \overline{Q}_k^{TMB} \right)^2 + \left(\frac{\partial m_k}{\partial \overline{Q}_{solid}} \cdot \delta \overline{Q}_{solid} \right)^2 \right]^{0.5}. \tag{B.15c}$$

where,

$$\frac{\partial \overline{Q}_k^{TMB}}{\partial \overline{Q}_k^{SMB}} = 1 \tag{B.16a}$$

$$\frac{\partial \overline{Q}_k^{TMB}}{\partial \epsilon_{int}} = \frac{V_{column}}{t_{switch}} \tag{B.16b}$$

$$\frac{\partial \overline{Q}_{solid}}{\partial \epsilon_{int}} = -\frac{V_{column}}{t_{switch}} \tag{B.16c}$$

$$\frac{\partial m_k}{\partial \overline{Q}_k^{TMB}} = \frac{1}{\overline{Q}_{solid}} \tag{B.16d}$$

$$\frac{\partial m_k}{\partial \overline{Q}_{solid}} = -\frac{\overline{Q}_k^{TMB}}{\overline{Q}_{solid}^2}. \tag{B.16e}$$

The experimental dispersion of the switching time, δt_{switch}, is negligible compared to the other process variables.

B.6 SMB performance parameters

$$\delta Pur_{i,out} = \pm \left[\sum_{h=A,B} \left(\frac{\partial Pur_{i,out}}{\partial \overline{C}_{h,out}} \cdot \delta \overline{C}_{h,out} \right)^2 \right]^{0.5}, \tag{B.17a}$$

$$\delta Rec_{i,out} = \pm \left\{ \sum_{h=F,out} \left[\left(\frac{\partial Rec_{i,out}}{\partial \overline{Q}_h} \cdot \delta \overline{Q}_h \right)^2 + \left(\frac{\partial Rec_{i,out}}{\partial \overline{C}_{i,h}} \cdot \delta \overline{C}_{i,h} \right)^2 \right] \right\}^{0.5}, \tag{B.17b}$$

$$\delta Pr_i = \pm (60 \cdot 24) \left[\left(\frac{\partial Pr_i}{\partial \overline{Q}_{out}} \cdot \delta \overline{Q}_{out} \right)^2 + \left(\frac{\partial Pr_i}{\partial \overline{C}_{i,out}} \cdot \delta \overline{C}_{i,out} \right)^2 \right]^{0.5}, \tag{B.17c}$$

$$\delta DC = \pm \left[\sum_{h=D,F} \left(\frac{\partial DC}{\partial \overline{Q}_h} \cdot \delta \overline{Q}_h \right)^2 + \sum_{h=A,B} \left(\frac{\partial DC}{\partial \overline{C}_{h,F}} \cdot \delta \overline{C}_{h,F} \right)^2 \right]^{0.5}. \tag{B.17d}$$

where,

$$\frac{\partial Pur_{i,out}}{\partial \overline{C}_{h,out}}|_{i=h} = \frac{\overline{C}_{h,out}}{\left(\sum_{h=A,B} \overline{C}_{h,out}\right)^2} 100 \tag{B.18a}$$

$$\frac{\partial Pur_{i,out}}{\partial \overline{C}_{h,out}}|_{i\neq h} = -\frac{\overline{C}_{i,out}}{\left(\sum_{h=A,B} \overline{C}_{h,out}\right)^2} 100 \tag{B.18b}$$

$$\frac{\partial Rec_{i,out}}{\partial \overline{Q}_{out}} = \frac{\overline{C}_{i,out}}{\overline{C}_{i,F}\overline{Q}_F} \tag{B.18c}$$

$$\frac{\partial Rec_{i,out}}{\partial \overline{C}_{i,out}} = \frac{\overline{Q}_{out}}{\overline{C}_{i,F}\overline{Q}_F} \tag{B.18d}$$

$$\frac{\partial Rec_{i,out}}{\partial \overline{Q}_F} = -\frac{\overline{C}_{i,out}\overline{Q}_{out}}{\overline{C}_{i,F}\overline{Q}_F^2} \tag{B.18e}$$

$$\frac{\partial Rec_{i,out}}{\partial \overline{C}_{i,F}} = -\frac{\overline{C}_{i,out}\overline{Q}_{out}}{\overline{C}_{i,F}^2\overline{Q}_F} \tag{B.18f}$$

$$\frac{\partial Pr_i}{\partial \overline{Q}_{out}} = \frac{\overline{C}_{i,out}}{m_{ads}N_{column}} \tag{B.18g}$$

$$\frac{\partial Pr_i}{\partial \overline{C}_{i,out}} = \frac{\overline{Q}_{out}}{m_{ads}N_{column}} \tag{B.18h}$$

$$\frac{\partial DC}{\partial \overline{Q}_D} = \frac{1}{\overline{Q}_F \sum_{h=A,B} \overline{C}_{h,F}} \tag{B.18i}$$

$$\frac{\partial DC}{\partial \overline{Q}_F} = -\frac{\overline{Q}_D}{\overline{Q}_F^2 \sum_{h=A,B} \overline{C}_{h,F}} \tag{B.18j}$$

$$\frac{\partial DC}{\partial \overline{C}_{h,F}} = -\frac{\overline{Q}_D + \overline{Q}_F}{\overline{Q}_F \left(\sum_{h=A,B} \overline{C}_{h,F}\right)^2} \tag{B.18k}$$

(B.18l)

B.7 Mass balance check-up

The errors were calculated using the equations below:

$$\delta \dot{m}_{k,i} = \pm \left\{ \left[\frac{\partial \dot{m}_{k,i}}{\partial \overline{Q}_k} \cdot \delta \overline{Q}_k \right]^2 + \left[\frac{\partial \dot{m}_{k,i}}{\partial \overline{C}_{k,i}} \cdot \delta \overline{C}_{k,i} \right]^2 \right\}^{0.5}, \tag{B.19}$$

where

$$\frac{\partial \dot{m}_{k,i}}{\partial \overline{Q}_k} = \overline{C}_{k,i} \tag{B.20a}$$

and (B.20b)

$$\frac{\partial \dot{m}_{k,i}}{\partial \overline{C}_{k,i}} = \overline{Q}_k. \tag{B.20c}$$

Appendix C

Calculated flow rates and switching time

Table C.1 shows the flow rates, switching times, concentrations in the CSS, and adimensional coefficients for *Run 1*, *Run 2*, *Run 3*, *Run 4*, and *Run 5*. From *Run 6* on, the *chiral detector* equipment started monitoring online the concentrations in the outlet streams; therefore, in addition to the information previously mentioned, the slope near the inflection points of the dynamic curves for the richest enantiomer in the output streams (*i.e.*, raffinate and extract) were also shown (see Table C.2).

Table C.1: Runnings in the SMB unit presented in Chapter 2 *,#

Run 1				Run 2			
$\overline{Q}_1$	$\overline{Q}_2$	$\overline{Q}_3$	$\overline{Q}_4$	$\overline{Q}_1$	$\overline{Q}_2$	$\overline{Q}_3$	$\overline{Q}_4$
8.141±0.009	5.063	6.012±0.046	4.038±0.057	3.270±0.004	2.046	2.966±0.099	1.584±0.093
$\overline{Q}_D$		$\overline{Q}_F$	t_{switch}	$\overline{Q}_D$		$\overline{Q}_F$	t_{switch}
4.103±0.053		0.949±0.046	3.57	1.686±0.089		0.919±0.099	8.82
$\overline{Q}_X$		$\overline{C}_{A,X}$	$\overline{C}_{B,X}$	$\overline{Q}_X$		$\overline{C}_{A,X}$	$\overline{C}_{B,X}$
3.078±0.009		0.16±0.03	< 0.06	1.224±0.004		0.18±0.01	<0.06
$\overline{Q}_R$		$\overline{C}_{A,R}$	$\overline{C}_{B,R}$	$\overline{Q}_R$		$\overline{C}_{A,R}$	$\overline{C}_{B,R}$
1.974±0.045		-	0.28±0.02	1.382±0.006		0.17±0.02	0.37±0.01
$Pe_{i,j}$			$\alpha_{i,j}$	$Pe_{i,j}$			$\alpha_{i,j}$
>2340			>157	>2340			<388
Run 3				Run 4			
$\overline{Q}_1$	$\overline{Q}_2$	$\overline{Q}_3$	$\overline{Q}_4$	$\overline{Q}_1$	$\overline{Q}_2$	$\overline{Q}_3$	$\overline{Q}_4$
4.364±0.004	2.266	3.258±0.041	2.195±0.043	3.325±0.012	1.830	2.833±0.140	1.682±0.151
$\overline{Q}_D$		$\overline{Q}_F$	t_{switch}	$\overline{Q}_D$		$\overline{Q}_F$	t_{switch}
2.188±0.040		0.973±0.041	6.62	1.643±0.141		1.003±0.140	8.75
$\overline{Q}_X$		$\overline{C}_{A,X}$	$\overline{C}_{B,X}$	$\overline{Q}_X$		$\overline{C}_{A,X}$	$\overline{C}_{B,X}$
2.098±0.004		0.26±0.02	< 0.06	1.495±0.012		0.22±0.04	< 0.06
$\overline{Q}_R$		$\overline{C}_{A,R}$	$\overline{C}_{B,R}$	$\overline{Q}_R$		$\overline{C}_{A,R}$	$\overline{C}_{B,R}$
1.064±0.003		-	0.53±0.01	1.150±0.012		0.12±0.01	0.39±0.03
$Pe_{i,j}$			$\alpha_{i,j}$	$Pe_{i,j}$			$\alpha_{i,j}$
>2340			>291	>2340			>385
Run 5				Ching *et al.*** [1]			
$\overline{Q}_1$	$\overline{Q}_2$	$\overline{Q}_3$	$\overline{Q}_4$	$\overline{Q}_1$	$\overline{Q}_2$	$\overline{Q}_3$	$\overline{Q}_4$
8.109±0.030	5.063	6.243±0.141	4.243±0.128	na	na	na	na
$\overline{Q}_D$		$\overline{Q}_F$	t_{switch}	$\overline{Q}_D$		$\overline{Q}_F$	t_{switch}
3.866±0.153		1.181±0.141	3.57	4.10		0.30	45.0
$\overline{Q}_X$		$\overline{C}_{A,X}$	$\overline{C}_{B,X}$	$\overline{Q}_X$		$\overline{C}_{A,X}$	$\overline{C}_{B,X}$
3.046±0.030		0.70±0.03	< 0.06	2.60		2.71	0.30
$\overline{Q}_R$		$\overline{C}_{A,R}$	$\overline{C}_{B,R}$	$\overline{Q}_R$		$\overline{C}_{A,R}$	$\overline{C}_{B,R}$
2.000±0.015		< 0.06	1.25±0.02	1.80		0.25	3.74
$Pe_{i,j}$			$\alpha_{i,j}$	$Pe_{i,j}$			$\alpha_{i,j}$
>2340			>157	na			na

*Q=[mL.min^{-1}], t_{switch}=[min], C=[g.L^{-1}]

** dispersion of the experiments **n**ot **a**vailable (na)

A and B are the D-PZQ and L-PZQ, respectively

Table C.2: *Run 6* in the SMB unit presented in Chapter 4 *,#

Run 6			
$\overline{Q}_1$	$\overline{Q}_2$	$\overline{Q}_3$	$\overline{Q}_4$
8.03±0.03	5.07	6.47±0.09	4.24±0.11
$\overline{Q}_D$	$\overline{Q}_F$	$\overline{C}_F$	
3.79±0.09	1.40±0.09	1.69±0.04	
$\overline{Q}_X$		$\overline{Q}_R$	
2.96±0.03		2.23±0.03	
$\overline{C}_{A,X}^{HPLC}$	$\overline{C}_{B,X}^{HPLC}$	$\overline{C}_{A,R}^{HPLC}$	$\overline{C}_{B,R}^{HPLC}$
0.74±0.07	<0.06	<0.06	1.12±0.06
$\overline{C}_{A,X}^{chiral}$	$\overline{C}_{B,X}^{chiral}$	$\overline{C}_{A,R}^{chiral}$	$\overline{C}_{B,R}^{chiral}$
0.66±0.11	-	0.05±0.03	1.06±0.07
$\phi_{A,X}/\phi_{B,R}$	t_{switch}	$Pe_{i,j}$	$\alpha_{i,j}$
0.09/0.16	3.14	> 2340	> 138

*Q=[mL.min^{-1}], t_{switch}=[min], C=[g.L^{-1}]

A and B are the D-PZQ and L-PZQ, respectively

Table C.3: Runnings in the SMB unit presented in Chapter 4 *,#

Run 7				Run 8			
$\overline{Q}_1$	$\overline{Q}_2$	$\overline{Q}_3$	$\overline{Q}_4$	$\overline{Q}_1$	$\overline{Q}_2$	$\overline{Q}_3$	$\overline{Q}_4$
8.75±0.06	5.76	7.26±0.02	5.01±0.04	7.55±0.06	4.56	6.14±0.01	3.89±0.06
$\overline{Q}_D$	$\overline{Q}_F$	$\overline{C}_F$	t_{switch}	$\overline{Q}_D$	$\overline{Q}_F$	$\overline{C}_F$	t_{switch}
3.74±0.02	1.50±0.02	1.66±0.02	3.14	3.66±0.01	1.58±0.01	1.66±0.02	3.14
$\overline{Q}_X$		$\overline{Q}_R$		$\overline{Q}_X$		$\overline{Q}_R$	
2.99±0.06		2.25±0.05		2.99±0.06		2.26±0.05	
$\overline{C}^{chiral}_{A,X}$	$\overline{C}^{chiral}_{B,X}$	$\overline{C}^{chiral}_{A,R}$	$\overline{C}^{chiral}_{B,R}$	$\overline{C}^{chiral}_{A,X}$	$\overline{C}^{chiral}_{B,X}$	$\overline{C}^{chiral}_{A,R}$	$\overline{C}^{chiral}_{B,R}$
0.45	0.01	0.24 ± 0.04	1.03 ± 0.01	0.87	0.00	0.06	0.87
	$Pe_{i,j}$		$\alpha_{i,j}$		$Pe_{i,j}$		$\alpha_{i,j}$
	>2340		> 138		>2340		> 138

Run 9				Run 10			
$\overline{Q}_1$	$\overline{Q}_2$	$\overline{Q}_3$	$\overline{Q}_4$	$\overline{Q}_1$	$\overline{Q}_2$	$\overline{Q}_3$	$\overline{Q}_4$
8.07±0.06	5.07	6.51±0.01	4.67±0.04	8.05±0.05	5.07	6.67±0.01	4.31±0.03
$\overline{Q}_D$	$\overline{Q}_F$	$\overline{C}_F$	t_{switch}	$\overline{Q}_D$	$\overline{Q}_F$	$\overline{C}_F$	t_{switch}
3.34±0.15	1.44±0.01	1.72±0.03	3.14	3.74±0.02	1.60±0.01	1.72±0.03	3.14
$\overline{Q}_X$		$\overline{Q}_R$		$\overline{Q}_X$		$\overline{Q}_R$	
3.00±0.06		1.84±0.05		2.98±0.05		2.36±0.04	
$\overline{C}^{chiral}_{A,X}$	$\overline{C}^{chiral}_{B,X}$	$\overline{C}^{chiral}_{A,R}$	$\overline{C}^{chiral}_{B,R}$	$\overline{C}^{chiral}_{A,X}$	$\overline{C}^{chiral}_{B,X}$	$\overline{C}^{chiral}_{A,R}$	$\overline{C}^{chiral}_{B,R}$
0.62	0.00	0.07	1.21	0.58	0.00	0.12	1.04
	$Pe_{i,j}$		$\alpha_{i,j}$		$Pe_{i,j}$		$\alpha_{i,j}$
	>2340		> 138		>2340		> 138

Run 11			
$\overline{Q}_1$	$\overline{Q}_2$	$\overline{Q}_3$	$\overline{Q}_4$
8.00±0.04	5.07	6.34±0.01	4.25±0.04
$\overline{Q}_D$	$\overline{Q}_F$	$\overline{C}_F$	t_{switch}
3.76±0.02	1.27±0.01	1.72±0.03	3.14
$\overline{Q}_X$		$\overline{Q}_R$	
2.93±0.04		2.09±0.04	
$\overline{C}^{chiral}_{A,X}$	$\overline{C}^{chiral}_{B,X}$	$\overline{C}^{chiral}_{A,R}$	$\overline{C}^{chiral}_{B,R}$
0.72	0.00	0.03	1.12
	$Pe_{i,j}$		$\alpha_{i,j}$
	>2340		> 138

*Q=[mL.min^{-1}], t_{switch}=[min], C=[g.L^{-1}]
A and B are the D-PZQ and L-PZQ, respectively

Appendix D

Typical chromatograms

Figure D.1 and Figure D.2 show typical chromatograms obtained by rac-PZQ and TTBB injections, respectively. Figure D.3 and Figure D.4 show typical chromatograms from *Run 1* to *Run 5*.

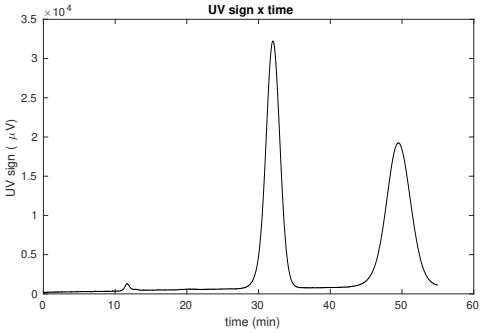

(a) 0.5 mL.min^{-1}

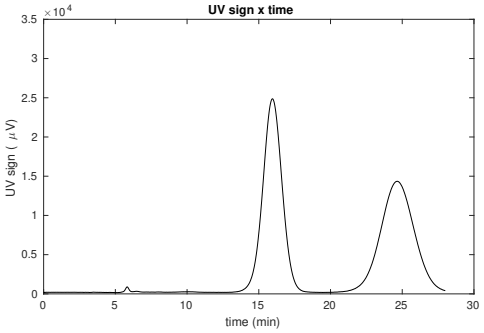

(b) 1 mL.min^{-1}

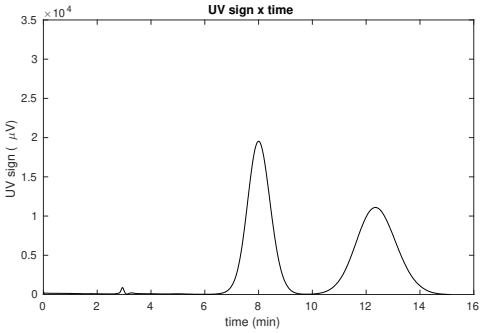

(c) 2 mL.min^{-1}

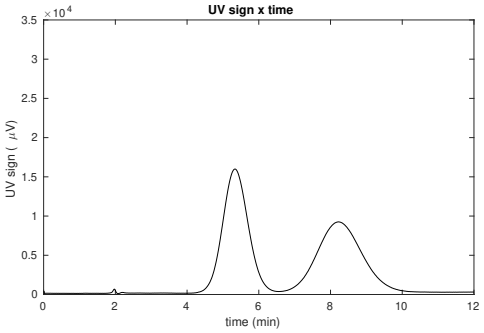

(d) 3 mL.min^{-1}

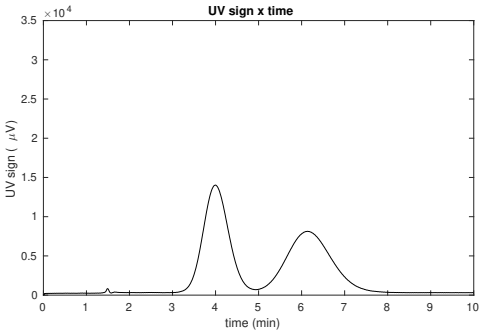

(e) 4 mL.min^{-1}

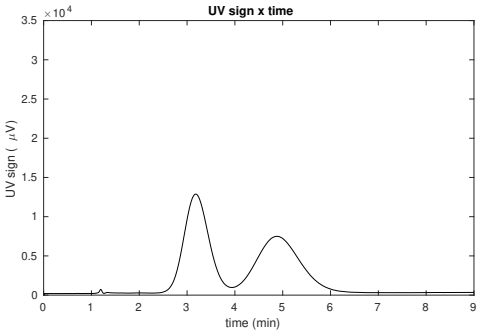

(f) 5 mL.min^{-1}

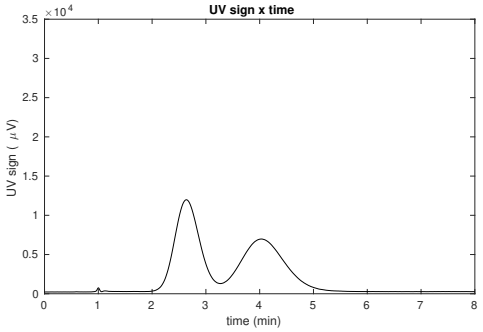

(g) 6 mL.min^{-1}

Figure D.1: Henry coefficients measurement: typical chromatograms originated with different desorbent flow rates by a 20μL of rac-PZQ injected into an HPLC using a chromatographic column Chiracel^{TM}OZ. The less-retained peak is the L-PZQ, and the other one is the D-PZQ.

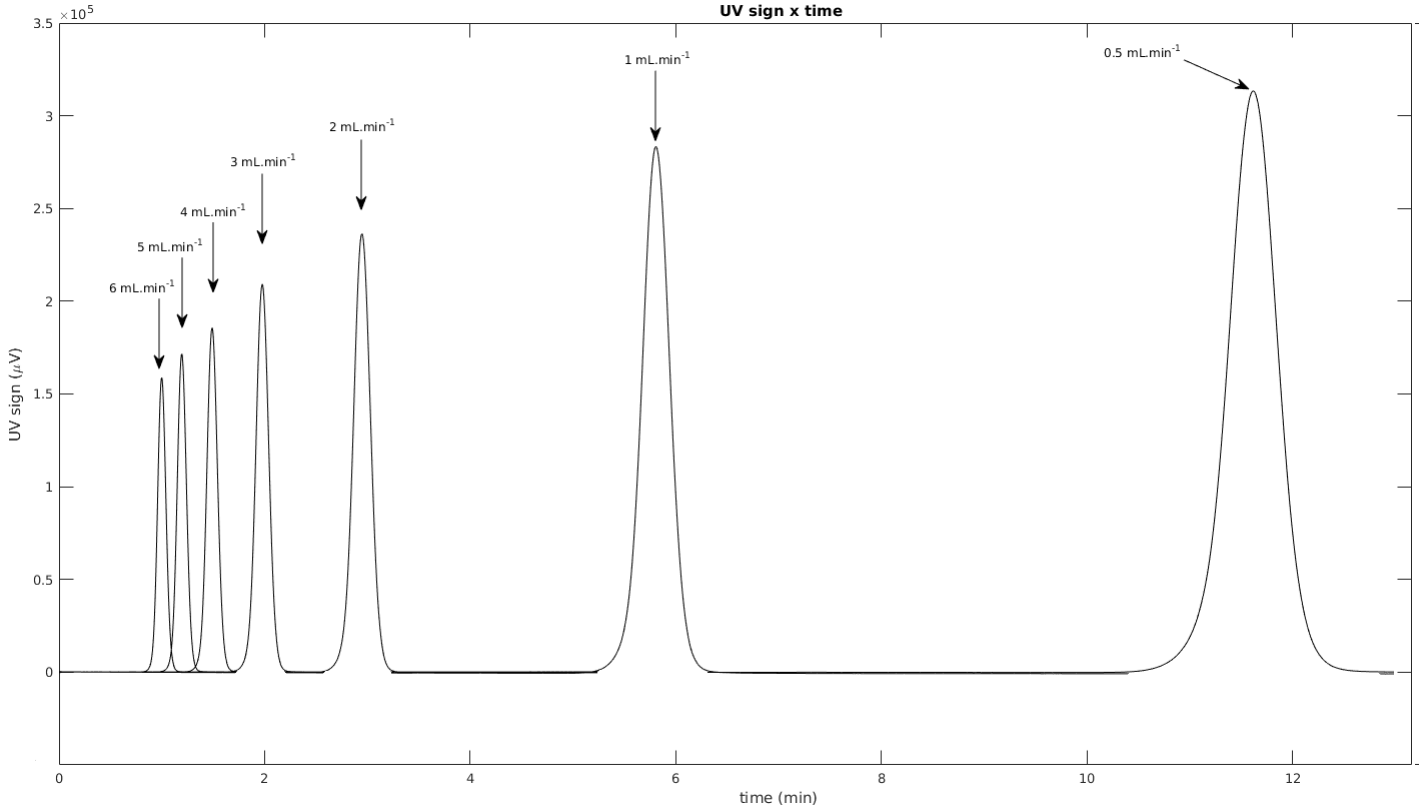

Figure D.2: Porosity measurement: typical chromatograms originated with different desorbent flow rates by a 20μL of TTBB injected into an HPLC using a chromatographic column Chiracel^{TM}OZ.

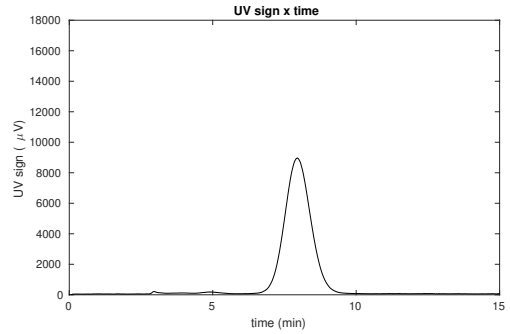

(a) *Run 1*: Raffinate

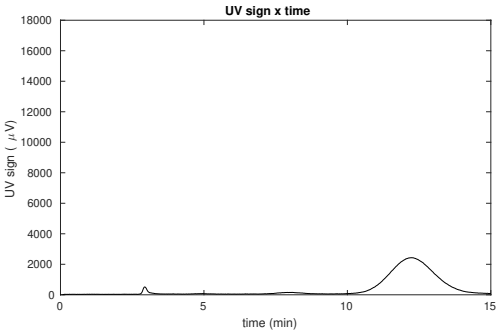

(b) *Run 1*: Extract

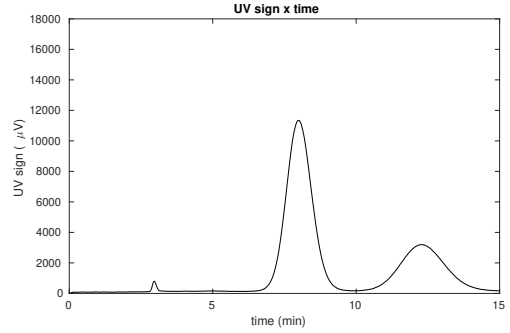

(c) *Run 2*: Raffinate

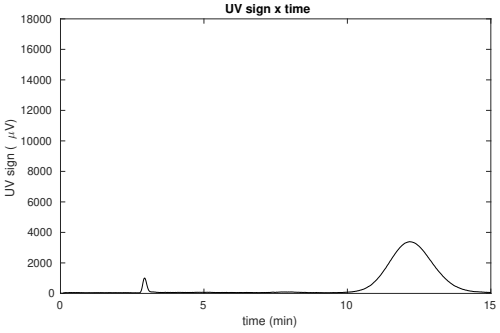

(d) *Run 2*: Extract

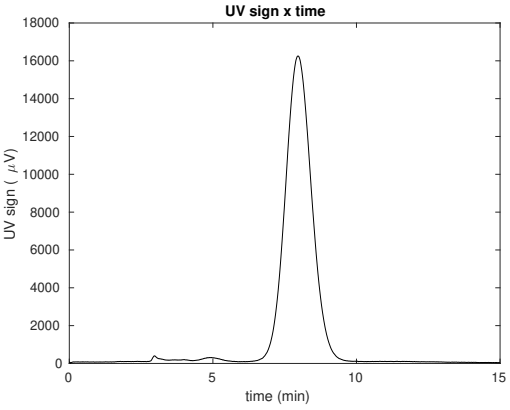

(e) *Run 3*: Raffinate

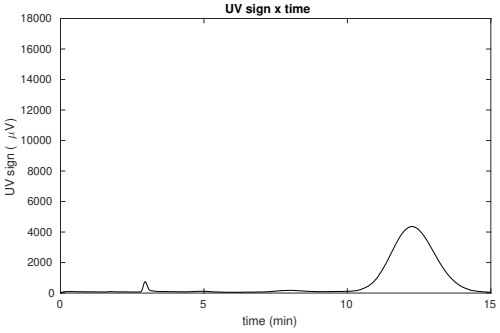

(f) *Run 3*: Extract

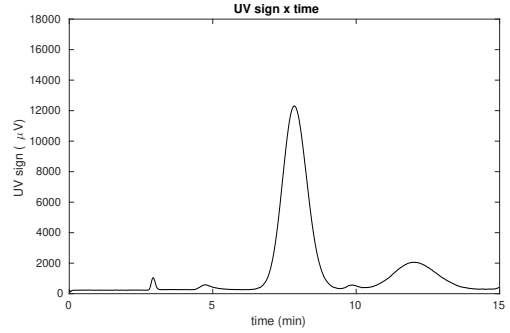

(g) *Run 4*: Raffinate

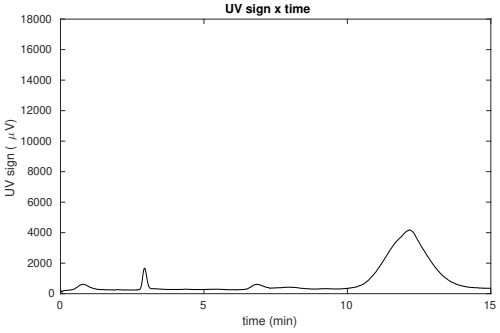

(h) *Run 4*: Extract

Figure D.3: Typical chromatograms of extract and raffinate streams of *Run 1*, *Run 2*, *Run 3*, and *Run 4*. The less-retained peak is the L-PZQ, and the other one is the D-PZQ.

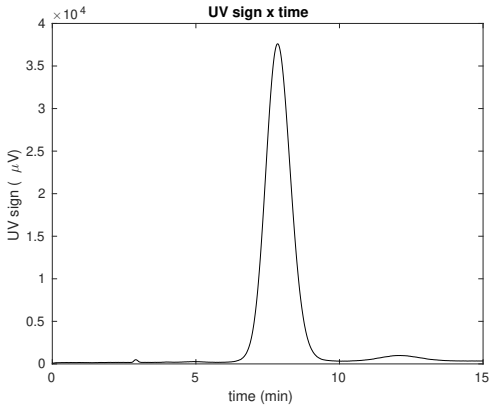

(a) Raffinate stream

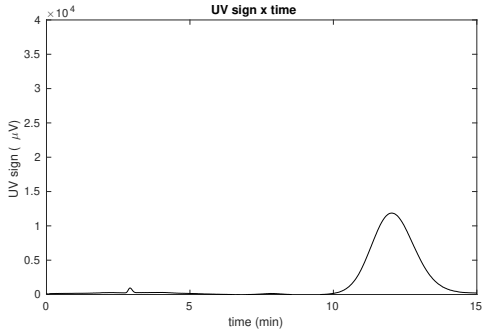

(b) Extract stream

Figure D.4: Typical chromatograms of extract and raffinate streams of *Run 5*. The less-retained peak is the L-PZQ, and the other one is the D-PZQ.

Appendix E

Plate theory and van Deemter equation

As mentioned earlier, Martin and Synge, in their theoretical studies in 1941, predicted some ideal situations that could provide better performance to chromatographic processes. Part of these theoretical studies focused on comparing the performance of one column for different experiments or comparing the performance of different columns for the same experiment. They found a practical way to solve this issue.

The proposed solution was not a first principle approach but an entirely empirical one. Despite that, it has been proven very useful and efficient in comparing chromatographic column efficiency. [58].

They divided the column into many theoretical plates in series. Inside each plate, an important consideration was made [57, 58]:

1. phases were well-mixed
2. solid and liquid phase were in equilibrium;
3. liquid phase passes from one plate to the other right after it;
4. fresh liquid phase is added just to the first plate;
5. the volume of both phases remain constant along the time; and
6. the concentration of solutes in the solid phase was proportional to the concentration of solutes in the liquid phase (*i.e.*, **linear isotherm**).

Dividing the column into N equal plates, each plate has a total volume equal to "V_{column}/N". Inside each plate, one could find a fraction of "(1 - ϵ_{bed})" of solid phase and a fraction of "ϵ_{bed}" of the liquid phase. Solving the equation resulted from the mass balance in the nth plate, considering a linear isotherm and the injection of

solute as being well described by an ideal Dirac pulse, it is possible to achieve the following analytical solution [57]:

$$f\left(t; N, N/t_{R,i}\right) = \frac{C_{i,N}}{(m_{inj}/Q)} = \frac{\left(\frac{N}{t_{R,i}}\right)^N t^{N-1} e^{-\left(N/t_{R,i}\right)t}}{(N-1)!}. \tag{E.1}$$

In this equation $m_{inj,i}$ is the injected quantity of the solute i inside the column (g), t is the time (min), and $C_{i,N}$ is the concentration of solute i at the column outlet ($g.mL^{-1}$). Equation E.1 is known as *Gamma distribution function* [1].

First and second moments of Gamma Density Function are, respectively [57]:

$$\mu_t = t_{R,i}, \tag{E.2a}$$

$$\sigma_t = \frac{t_{R,i}}{\sqrt{N}}. \tag{E.2b}$$

From Equation E.2b, it is possible to calculate the number of theoretical plates, N, of a determined chromatographic column. It is important to highlight that the above mentioned moments of the Gamma distribution are well-known after the chromatogram is obtained. It is also known that Gamma distribution tends to a Gaussian distribution for limiting cases (*i.e.*, big values of N). Therefore, getting the second moment of a Gaussian distribution is even simpler from a given chromatogram, so calculating N becomes much easier.

Commonly, N is not used directly. In practice, the length of the column, L_{column} is divided by N, in order to give the **H**igh **E**quivalent to each **T**heoretical **P**late (**HETP**). The *HETP* is commonly used to compare columns performance, its equation is [45, 57, 58]:

$$HETP = \frac{L_{column}}{N}, \tag{E.3}$$

where the L_{column} is measured in centimeters, substituting Equation E.2b into Equation E.3, it is possible to analyze some fundamental concepts related to chromatography.

$$HETP = \left(\frac{\sigma_t}{t_{R,i}}\right)^2 L_{column}. \tag{E.4}$$

Equation E.4 tells that *HETP* will become smaller as a consequence of the column efficiency increase. Thus, as the peak width (σ_t) becomes narrower, the ef-

[1] The generic equation for *Gamma distribution function* is

$$f\left(x; \alpha, \beta\right) = \frac{(\beta)^\alpha x^{\alpha-1} e^{-\beta x}}{(\alpha-1)!}$$

ficiency increases of power of two. In the limiting case, the peak chromatogram approximates the initial Dirac pulse given at the column entrance. This situation will never be achieved because, in real scenarios, efficiency problems will always be present. Bearing in mind the necessity to separate all solutes in the preparative chromatography, studying the effects that affect the width of a peak is of utmost importance.

E.1 van Deemter Equation

The efficiency of the column is intimately related to mass transfer (between solid and liquid phase) and axial dispersion coefficients throughout the column. A very famous equation that connects all these parameters is the so-called van Deemter equation. This equation is not based on first principles but on empirical ones. Despite that, it is a very useful equation,

$$HETP_i = A_i + \frac{B_i}{u_{int}} + C_i u_{int}, \tag{E.5}$$

where u_{int} is the interstitial velocity (cm.min^{-1}), A (cm), B (cm^2.min^{-1}), and C (min) are parameters that link the axial dispersion coefficient, $D_{axial,i}$, and the effective mass transfer coefficient, $k_{eff,i}$ [57, 58, 122]. Nevertheless, for preparative purposes, the B term is usually neglected (see Figure E.1). Hence,

$$HETP_i = A_i + C_i u_{int}. \tag{E.6}$$

A_i and C_i are [57, 58]:

$$A_i = \frac{2D_{axial,i}}{u_{int}}, \tag{E.7a}$$

$$C_i = 2\left(\frac{k_{0,i}}{1+k_{0,i}}\right)^2 \frac{1}{k_{0,i}k_{eff,i}}, \tag{E.7b}$$

$$k_{0,i} = H_i \frac{(1-\epsilon_{bed})}{\epsilon_{bed}}. \tag{E.7c}$$

Parameters A_i and C_i are calculated experimentally, and they are illustrated in Figure E.1. After calculating these van Deemter parameters, it is possible to calculate $D_{axial,i}$ from Equation E.7a and $k_{eff,i}$ from Equation E.7b.

It is essential to mention that the velocity calculated was not the interstitial (u_{int}), but the effective one (u_{eff}). Therefore, the dispersion calculated was the apparent ($D_{app,i}$) one, not the axial one ($D_{axial,i}$). See Section 2.6 for more details.

All these parameters were calculated H_i, $D_{app,i}$, $k_{eff,i}$, and ϵ_t. These parameters are responsible for providing sufficient information of a given chromatographic

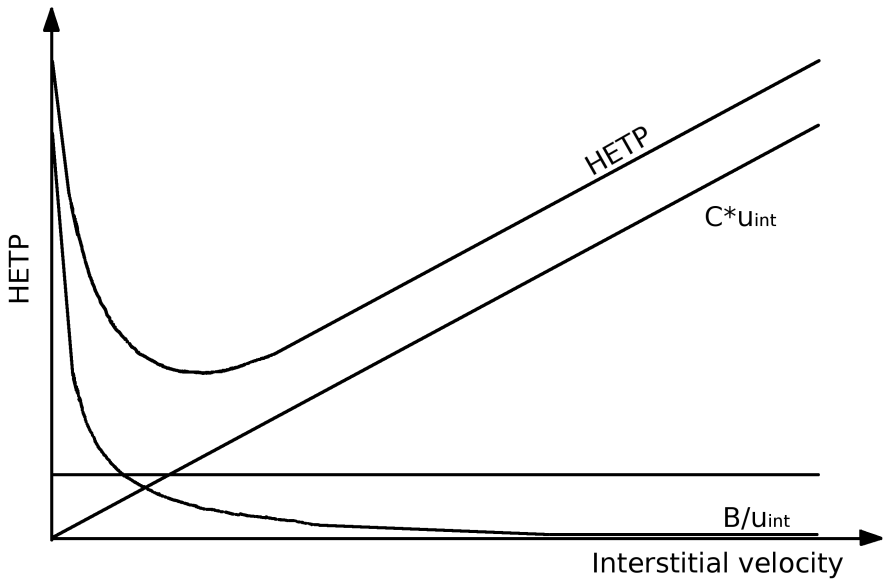

Figure E.1: Contribution of each term for the van Deemter equation (Equation E.5).

system to mathematical models.

Appendix F

Binary Langmuir isotherm parameters

The maximum adsorption capacity, q_m, estimated was:

$$q_m = 97.01\ gL^{-1}.$$

The parameter b, responsible for quantifying the adsorption interaction constant, was estimated using the inverse method; based on pulse response experiments (see Figure F.1). They are found in Table F.1:

Table F.1: Binary Langmuir thermodynamic parameter

$b_A\ (Lg^{-1})$	$b_B\ (Lg^{-1})$
0.0964 ± 0.0030	0.0519 ± 0.0015

The expressions used to compute the experimental errors are available in Appendix B.

The authors showed that isotherm was suitable to reproduce experimental data up to 5 gL^{-1} per component. Figure F.2 shows the equilibrium concentrations between the liquid and the solid phase. The experiments named *Run 1*, *Run 2*, *Run 3*, *Run 4* and *Run 5* were carried out in the nonlinear region of the isotherm.

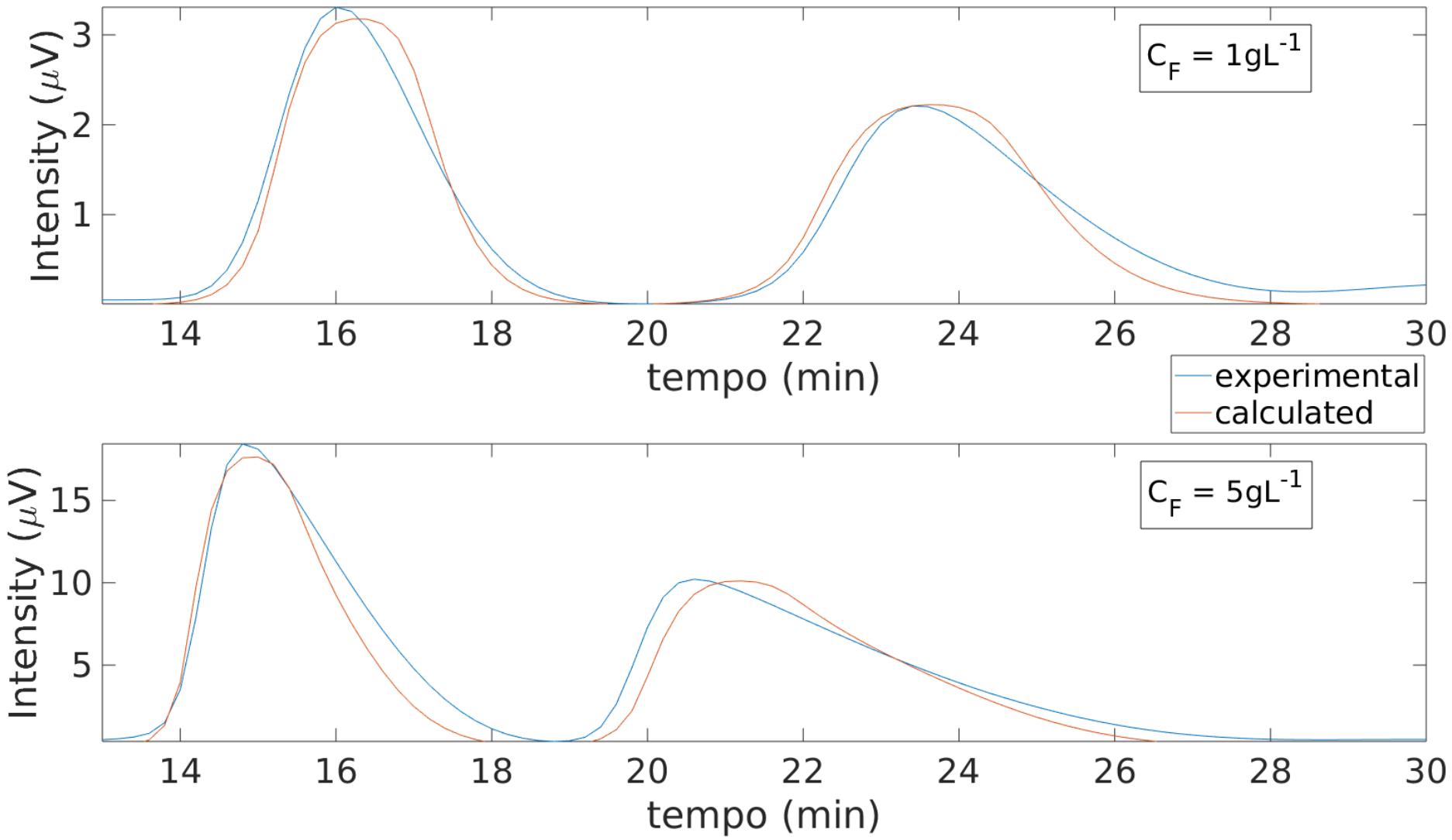

Figure F.1: Comparison between experimental and calculated data when the racemic concentration injected by the HPLC was 1g.L^{-1} (**upper**) and 5g.L^{-1} (**lower**). The injected volume was 2mL.

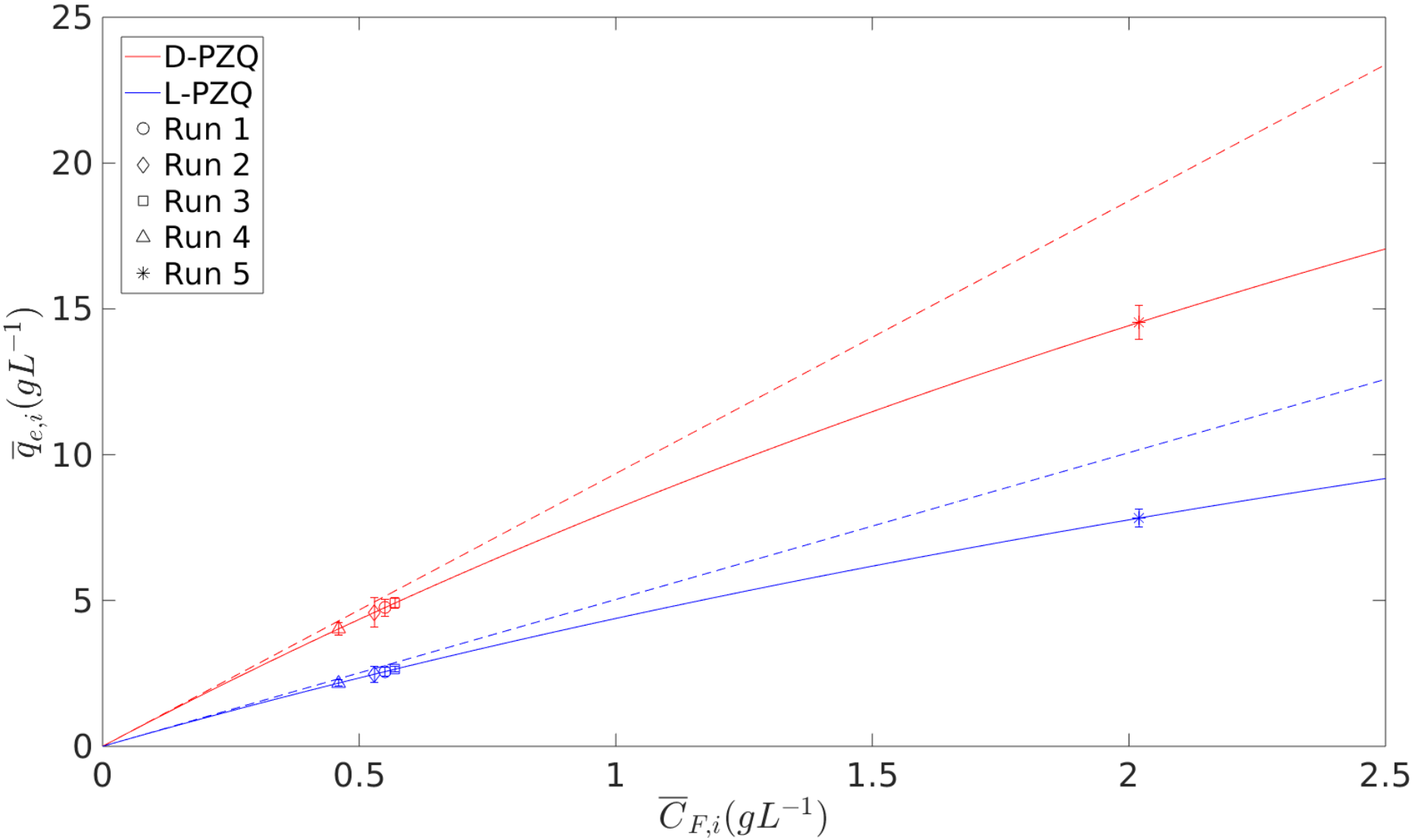

Figure F.2: **Solid lines:** Binary Langmuir isotherm; **Dashed lines:** Linear isotherm. $\overline{C}_{F,i}$ is the racemic concentration of the enantiomer i in the feed stream of each experiment carried out in the SMB unit.

Appendix G

Simulated concentrations and RSSR (γ) for each step in Q_2

Tables G.1, G.2 , G.3, G.4, and G.5 show the calculated concentrations of each enantiomer i for each outlet stream (X and R), as well as the RSSR of each step applied in the Q_2 variable.

Table G.1: Run 1 - Simulated data in the nonlinear region of isotherm and RSSR (γ) for each $\Delta\%$ Q_2^*

$\Delta\%Q_2$				
$\overline{C}_{A,X}^{\,nlin}$	$\overline{C}_{B,X}^{\,nlin}$	$\overline{C}_{A,R}^{\,nlin}$	$\overline{C}_{B,R}^{\,nlin}$	γ^{nlin}
		-25% Q_2		
0.17	0.09	<0.06	0.11	0.2
		-20% Q_2		
0.17	0.04	<0.06	0.18	0.1
		-15% Q_2		
0.17	<0.06	-	0.25	0.0
		-12% Q_2		
0.17	-	-	0.26	0.0
		-10% Q_2		
0.17	-	-	0.26	0.0
		-5% Q_2		
0.17	-	-	0.26	0.0
		-1% Q_2		
0.17	-	-	0.26	0.0
		0% Q_2		
0.17	-	-	0.26	0.0
		1% Q_2		
0.17	-	-	0.26	0.0
		5% Q_2		
0.17	-	-	0.26	0.0
		10% Q_2		
0.16	<0.06	-	0.25	0.0
		12% Q_2		
0.15	<0.06	-	0.24	0.0
		15% Q_2		
0.13	<0.06	-	0.23	0.1
		20% Q_2		
0.08	<0.06	0.10	0.22	0.1
		25% Q_2		
0.04	<0.06	0.21	0.17	0.2

* The experimental data are in Table C.1.

Table G.2: Run 2 - Simulated data in the nonlinear region of isotherm and RSSR (γ) for each $\Delta\%$ Q_2^*

$\Delta\%Q_2$				
$\overline{C}_{A,X}^{\,nlin}$	$\overline{C}_{B,X}^{\,nlin}$	$\overline{C}_{A,R}^{\,nlin}$	$\overline{C}_{B,R}^{\,nlin}$	γ^{nlin}
-25% Q_2				
0.38	0.08	<0.06	0.28	0.3
-20% Q_2				
0.39	<0.06	<0.06	0.32	0.3
-15% Q_2				
0.38	-	-	0.33	0.3
-12% Q_2				
0.36	-	<0.06	0.35	0.2
-10% Q_2				
0.34	-	<0.06	0.35	0.2
-5% Q_2				
0.30	-	0.08	0.35	0.2
-1% Q_2				
0.26	-	0.12	0.35	0.1
0% Q_2				
0.27	-	0.13	0.37	0.1
1% Q_2				
0.25	-	0.13	0.35	0.1
5% Q_2				
0.22	-	0.16	0.35	0.0
10% Q_2				
0.18	<0.06	0.19	0.35	0.0
12% Q_2				
0.16	<0.06	0.21	0.34	0.1
15% Q_2				
0.13	<0.06	0.23	0.33	0.1
20% Q_2				
0.09	<0.06	0.27	0.32	0.1
25% Q_2				
0.04	<0.06	0.31	0.31	0.2

* The experimental data are in Table C.1.

Table G.3: Run 3 - Simulated data in the nonlinear region of isotherm and RSSR (γ) for each $\Delta\%$ Q_2^*

$\Delta\%Q_2$				
$\overline{C}_{A,X}^{\,nlin}$	$\overline{C}_{B,X}^{\,nlin}$	$\overline{C}_{A,R}^{\,nlin}$	$\overline{C}_{B,R}^{\,nlin}$	γ^{nlin}
		-25% Q_2		
0.27	0.17	<0.06	0.19	0.4
		-20% Q_2		
0.27	0.14	<0.06	0.26	0.3
		-15% Q_2		
0.27	0.11	-	0.32	0.2
		-12% Q_2		
0.27	0.09	-	0.36	0.2
		-10% Q_2		
0.27	0.07	-	0.39	0.2
		-5% Q_2		
0.27	<0.06	-	0.45	0.1
		-1% Q_2		
0.27	<0.06	-	0.50	0.0
		0% Q_2		
0.27	<0.06	-	0.51	0.0
		1% Q_2		
0.27	<0.06	-	0.52	0.0
		5% Q_2		
0.27	<0.06	-	0.52	0.0
		10% Q_2		
0.27	<0.06	-	0.50	0.0
		12% Q_2		
0.26	<0.06	-	0.48	0.1
		15% Q_2		
0.25	<0.06	-	0.46	0.1
		20% Q_2		
0.22	<0.06	0.09	0.43	0.1
		25% Q_2		
0.19	0.06	0.16	0.41	0.2

* The experimental data are in Table C.1.

Table G.4: Run 4 - Simulated data in the nonlinear region of isotherm and RSSR (γ) for each $\Delta\%$ Q_2^*

$\Delta\%Q_2$				
$\overline{C}_{A,X}^{\,nlin}$	$\overline{C}_{B,X}^{\,nlin}$	$\overline{C}_{A,R}^{\,nlin}$	$\overline{C}_{B,R}^{\,nlin}$	γ^{nlin}
-25% Q_2				
0.30	0.12	<0.06	0.25	0.2
-20% Q_2				
0.31	0.09	<0.06	0.29	0.2
-15% Q_2				
0.31	0.06	-	0.32	0.2
-12% Q_2				
0.31	<0.06	-	0.35	0.2
-10% Q_2				
0.31	<0.06	-	0.36	0.1
-5% Q_2				
0.29	-	<0.06	0.39	0.1
-1% Q_2				
0.27	-	<0.06	0.40	0.1
0% Q_2				
0.26	-	0.06	0.40	0.1
1% Q_2				
0.26	-	0.07	0.40	0.1
5% Q_2				
0.23	<0.06	0.10	0.39	0.0
10% Q_2				
0.21	<0.06	0.13	0.38	0.0
12% Q_2				
0.20	<0.06	0.15	0.37	0.0
15% Q_2				
0.18	<0.06	0.17	0.36	0.1
20% Q_2				
0.18	<0.06	0.17	0.36	0.1
25% Q_2				
0.13	0.06	0.24	0.33	0.2

* The experimental data are in Table C.1.

Table G.5: Run 5 - Simulated data in the nonlinear region of isotherm and RSSR (γ) for each $\Delta\%$ Q_2^*

$\Delta\%Q_2$				
$\overline{C}_{A,X}^{\,nlin}$	$\overline{C}_{B,X}^{\,nlin}$	$\overline{C}_{A,R}^{\,nlin}$	$\overline{C}_{B,R}^{\,nlin}$	γ^{nlin}
-25% Q_2				
0.77	0.10	<0.06	1.01	0.3
-20% Q_2				
0.78	0.01	-	1.16	0.1
-15% Q_2				
0.78	-	-	1.19	0.1
-12% Q_2				
0.78	-	-	1.19	0.1
-10% Q_2				
0.78	-	-	1.19	0.1
-5% Q_2				
0.71	-	-	1.21	0.1
-1% Q_2				
0.60	<0.06	0.12	1.20	0.1
0% Q_2				
0.58	<0.06	0.25	1.18	0.3
1% Q_2				
0.55	<0.06	0.32	1.16	0.3
5% Q_2				
0.43	0.06	0.50	1.10	0.6
10% Q_2				
0.29	0.12	0.71	1.01	0.8
12% Q_2				
0.25	0.13	0.78	0.98	0.9
15% Q_2				
0.18	0.16	0.88	0.94	1.1
20% Q_2				
0.10	0.20	1.02	0.89	1.2
25% Q_2				
0.04	0.23	1.11	0.84	1.3

* The experimental data are in Table C.1.

Table G.6: *Run 6* - Simulated data and RSSR (γ) for each $\Delta\%$ Q_2^* in nonlinear isotherm region

$\overline{C}_{A,X}^{sim}$	$\overline{C}_{B,X}^{sim}$	$\overline{C}_{A,R}^{sim}$	$\overline{C}_{B,R}^{sim}$	γ	$\phi_{B,R}^{sim}$	$\Gamma_{B,R}$	$\phi_{A,X}^{sim}$	$\Gamma_{A,X}$	$\Gamma\,(=\lvert\Gamma_{B,R}-\Gamma_{A,X}\rvert)$
			$\Delta\%Q_2$						
			-25% Q_2						
0.71	0.48	0.11	0.42	0.8					
			-20% Q_2						
0.73	0.31	0.08	0.64	0.6					
			-15% Q_2						
0.75	0.13	0.06	0.86	0.3					
			-12% Q_2						
0.75	0.06	0.04	0.96	0.2					
			-10% Q_2						
0.76	0.03	0.03	1.01	0.1	0.13	0.03	0.15	0.06	0.09
			-5% Q_2						
0.78	0.00	0.02	1.06	0.1	0.15	0.01	0.14	0.05	0.06
			-1% Q_2						
0.79	0.00	0.01	1.07	0.1	0.16	0.00	0.11	0.02	0.02
			0% Q_2						
0.80	0.00	0.00	1.07	0.1	0.16	0.00	0.11	0.02	0.02
			1% Q_2						
0.80	0.00	0.00	1.07	0.1	0.16	0.00	0.11	0.02	0.02
			5% Q_2						
0.80	0.00	0.00	1.07	0.1	0.17	0.01	0.10	0.01	0.02
			10% Q_2						
0.72	0.00	0.00	1.07	0.1	0.19	0.03	0.08	0.01	0.04
			12% Q_2						
0.67	0.01	0.00	1.07	0.1	0.20	0.04	0.07	0.02	0.06
			15% Q_2						
0.59	0.04	0.21	1.02	0.2					
			20% Q_2						
0.47	0.08	0.42	0.95	0.5					
			25% Q_2						
0.33	0.13	0.58	0.89	0.7					

* The experimental data are in Table C.2.

Appendix H

Experiments carried out in the spectropolarimeter equipment

Table H.1 and Table H.2 show the data set used in Chapter 3 to cross-validate the *chiral detector* equipment.

Table H.1: Data set of pure for calibration

$\overline{S}_{UV} \pm \delta S_{UV}$	$\overline{S}_{CD} \pm \delta S_{CD}$	$C_D(g.L^{-1})$	$C_L(g.L^{-1})$	Label
0.08±0.02	2.3±0.1	0.00	0.26	ω_1^{pur}
0.13±0.02	3.7±0.1	0.00	0.51	ω_2^{pur}
0.18±0.02	4.8±0.1	0.00	0.75	ω_3^{pur}
0.23±0.02	6.0±0.1	0.00	1.01	ω_4^{pur}
0.28±0.02	6.7±0.1	0.00	1.25	ω_5^{pur}
0.06±0.02	-1.1±0.2	0.25	0.00	ω_6^{pur}
0.09±0.01	-1.5±0.1	0.50	0.00	ω_7^{pur}
0.13±0.02	-2.7±0.1	0.75	0.00	ω_8^{pur}
0.16±0.02	-3.7±0.1	1.00	0.00	ω_9^{pur}
0.19±0.01	-4.2±0.1	1.26	0.00	ω_{10}^{pur}

Table H.2: Data set of mixtures for calibration/validation

$\overline{S}_{UV} \pm \delta S_{UV}$	$\overline{S}_{CD} \pm \delta S_{CD}$	$C_D(g.L^{-1})$	$C_L(g.L^{-1})$	Label
0.08±0.02	1.9±0.1	0.01	0.24	ω_1^{mix}
0.09±0.02	1.4±0.1	0.03	0.23	ω_2^{mix}
0.08±0.01	0.2±0.1	0.06	0.19	ω_3^{mix}
0.10±0.02	-1.3±0.1	0.19	0.06	ω_4^{mix}
0.19±0.02	4.5±0.1	0.04	0.71	ω_5^{mix}
0.18±0.02	3.9±0.1	0.07	0.67	ω_6^{mix}
0.22±0.02	2.3±0.1	0.19	0.56	ω_7^{mix}
0.19±0.02	-0.2±0.1	0.38	0.38	ω_8^{mix}
0.15±0.02	-2.3±0.2	0.56	0.18	ω_9^{mix}
0.27±0.02	4.9±0.1	0.05	0.96	ω_{10}^{mix}
0.26±0.02	4.8±0.1	0.10	0.90	ω_{11}^{mix}
0.29±0.02	2.0±0.2	0.26	0.76	ω_{12}^{mix}
0.24±0.02	-0.7±0.1	0.50	0.50	ω_{13}^{mix}
0.20±0.02	-3.3±0.1	0.75	0.25	ω_{14}^{mix}

Appendix I

Range of wavelength evaluation

In this appendix, Table I.1 shows the circular dichroism signals obtained for different concentrations of pure L- and D-PZQ at different wavelengths, and Figure I.1 shows typical spectra obtained during analysis on the *chiral detector* equipment.

I.1 Range of wavelength evaluation

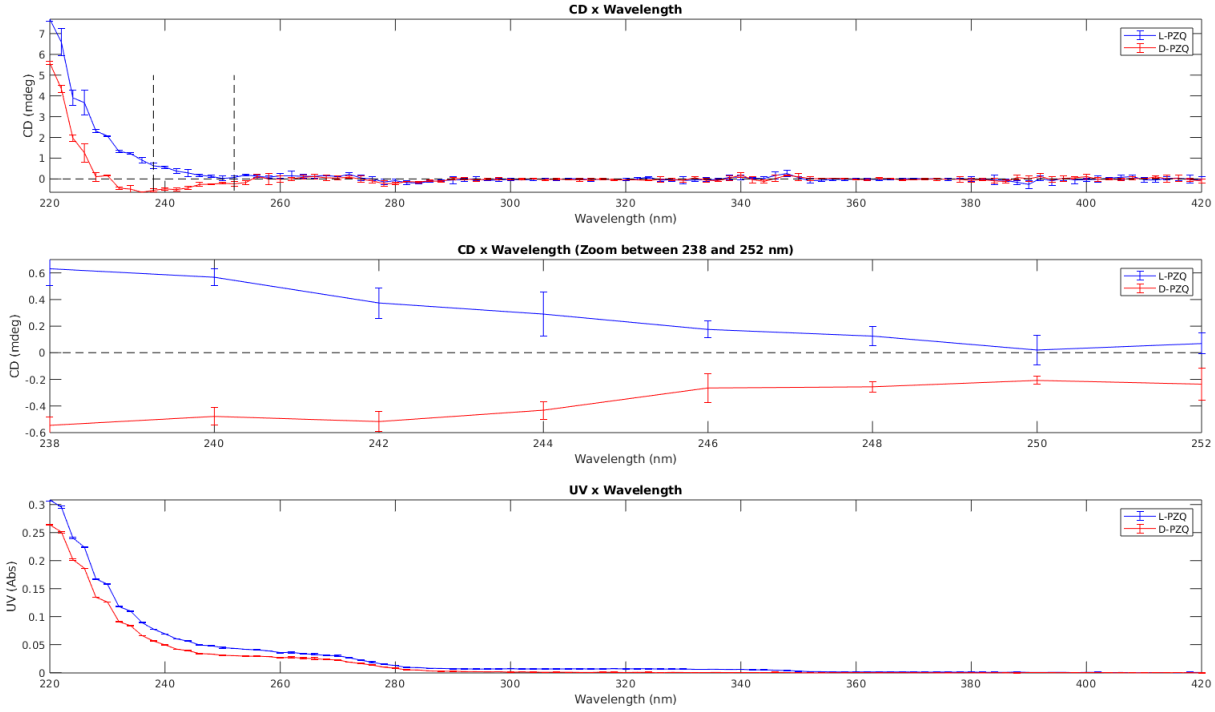

Figure I.1: Typical spectra obtained in the *Chiral Detector* equipment, e.g., 0.25 g.L^{-1} of each pure enantiomer. **Upper**: CD spectrum; **Middle**: zoom in the CD spectrum between 238 and 252 nm; **Lower**: UV spectrum.

Table I.1: CD signals for different concentrations of pure L- and D-PZQ at different wavelengths *,**

	Wavelength (nm)											
	232	234	236	238	240	242	244	246	248	250	252	254
	0.25 $g.L^{-1}$											
L-PZQ	+	+	+	+	+	+	+	+	+	+	+	+
D-PZQ	-	-	-	-	-	-	-	-	-	-	-	-
	0.50 $g.L^{-1}$											
L-PZQ	+	+	+	+	+	+	+	+	+	+	+	+
D-PZQ	-	-	-	-	-	-	-	-	-	-	-	-
	0.75 $g.L^{-1}$											
L-PZQ	+	+	+	+	+	+	+	+	+	+	+	+
D-PZQ	-	-	-	-	-	-	-	-	-	-	-	+
	1.00 $g.L^{-1}$											
L-PZQ	+	+	+	+	+	+	+	+	+	+	+	+
D-PZQ	+	-	-	-	-	-	-	-	-	-	-	+
	1.25 $g.L^{-1}$											
L-PZQ	+	+	+	+	+	+	+	+	+	+	+	+
D-PZQ	+	-	-	-	-	-	-	-	-	-	-	-
	1.75 $g.L^{-1}$											
L-PZQ	+	+	+	+	+	+	+	+	+	+	+	+
D-PZQ	+	-	-	-	-	-	-	-	-	-	-	-
	2.00 $g.L^{-1}$											
L-PZQ	+	+	+	+	+	+	+	+	+	+	+	+
D-PZQ	+	+	-	-	-	-	-	-	-	-	-	-
	2.25 $g.L^{-1}$											
L-PZQ	+	+	+	+	+	+	+	+	+	+	+	+
D-PZQ	+	+	-	-	-	-	-	-	-	-	-	-
	2.50 $g.L^{-1}$											
L-PZQ	+	+	+	+	+	+	+	+	+	+	+	+
D-PZQ	+	+	-	-	-	-	-	-	-	-	-	-
	2.75 $g.L^{-1}$											
L-PZQ	+	+	+	+	+	+	+	+	+	+	+	+
D-PZQ	+	+	-	-	-	-	-	-	-	-	-	-
	3.00 $g.L^{-1}$											
L-PZQ	+	+	+	+	+	+	+	+	+	+	+	+
D-PZQ	+	+	-	-	-	-	-	-	-	-	-	-
	3.50 $g.L^{-1}$											
L-PZQ	+	+	+	+	+	+	+	+	+	+	+	+
D-PZQ	+	+	+	-	-	-	-	-	-	-	-	+

*Light gray color: opposite CD signals between the L- and D-PZQ pure solutions.
** Dark gray color: range of wavelengths with opposite CD signals for L- and D-PZQ.

Appendix J

Signals and instantaneous concentration

This appendix contains the UV/vis and circular dichroism signals acquired by the *chiral detector* equipment and the instantaneous concentrations calculated from on-line measurements of these signals.

J.1 Second (*Run 6*) and third (*Run 7*) stages

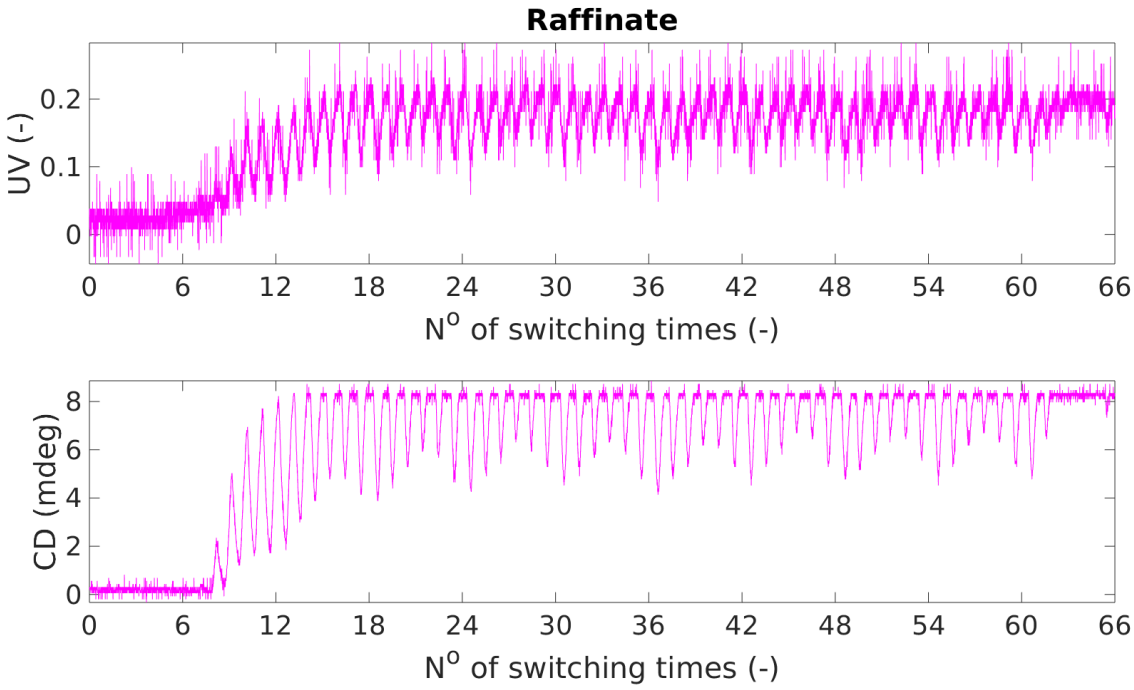

Figure J.1: Measured UV/vis and CD signals for the second (*Run 6.1*) and third (*Run 7.1*) stages.

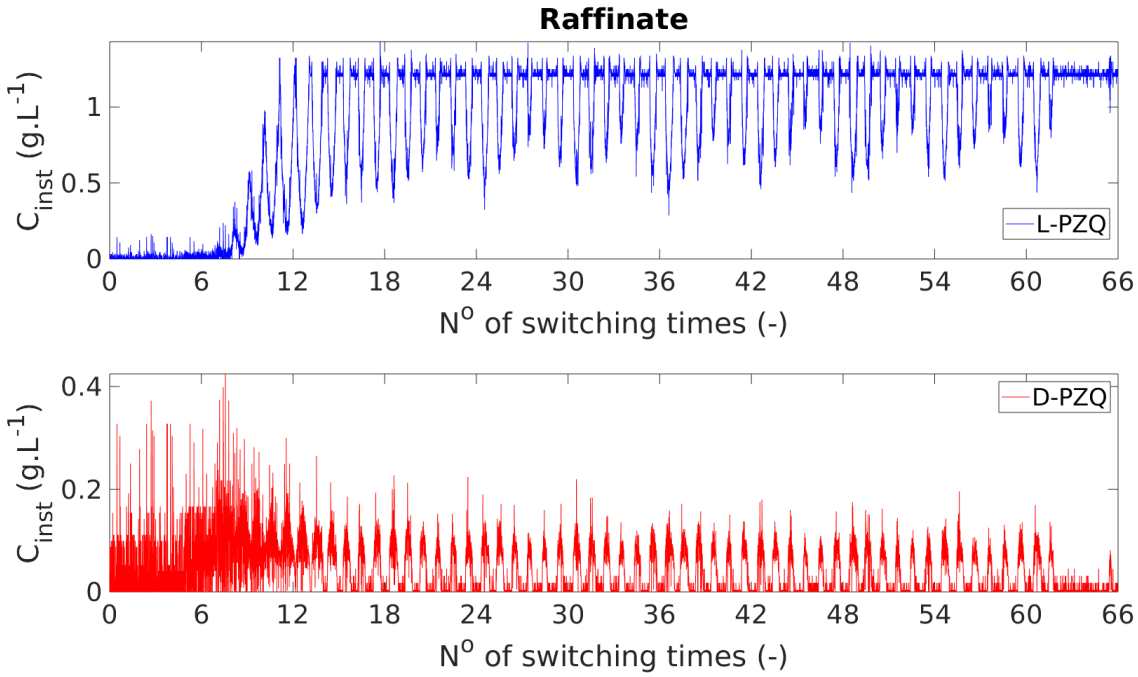

Figure J.2: Instantaneous concentrations for the second (*Run 6.1*) and third (*Run 7.1*) stages when the raffinate was measured.

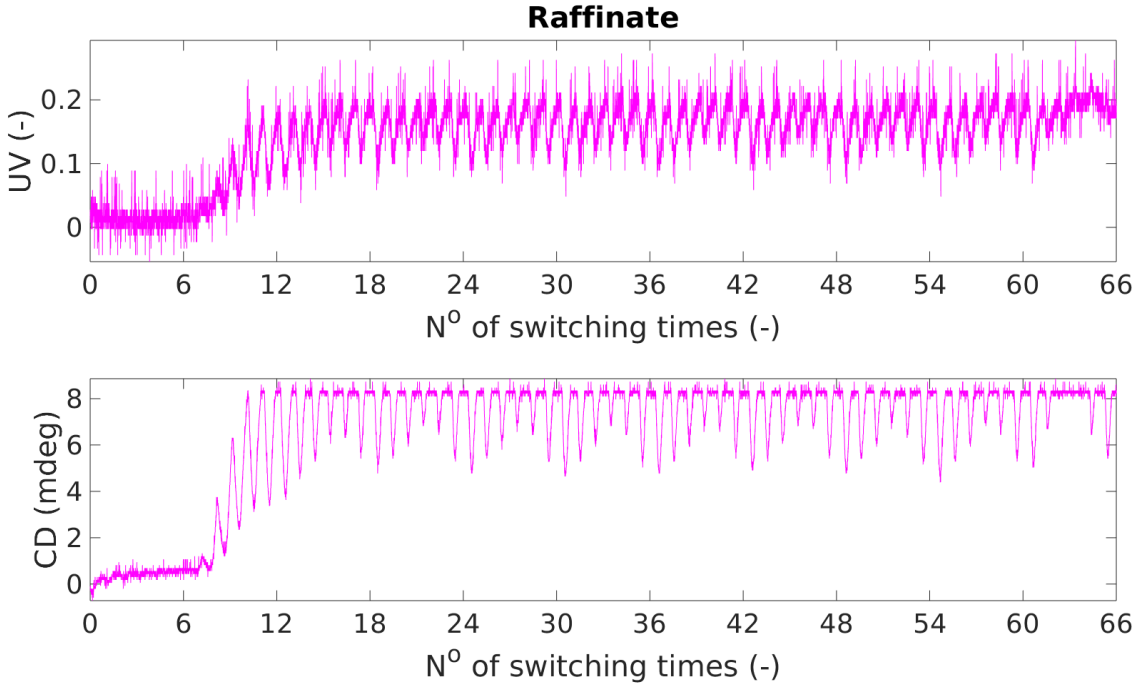

Figure J.3: Measured UV/vis and CD signals for the second (*Run 6.2*) and third (*Run 7.2*) stages.

J.2 Second (*Run 6*) and third (*Run 8*) stages

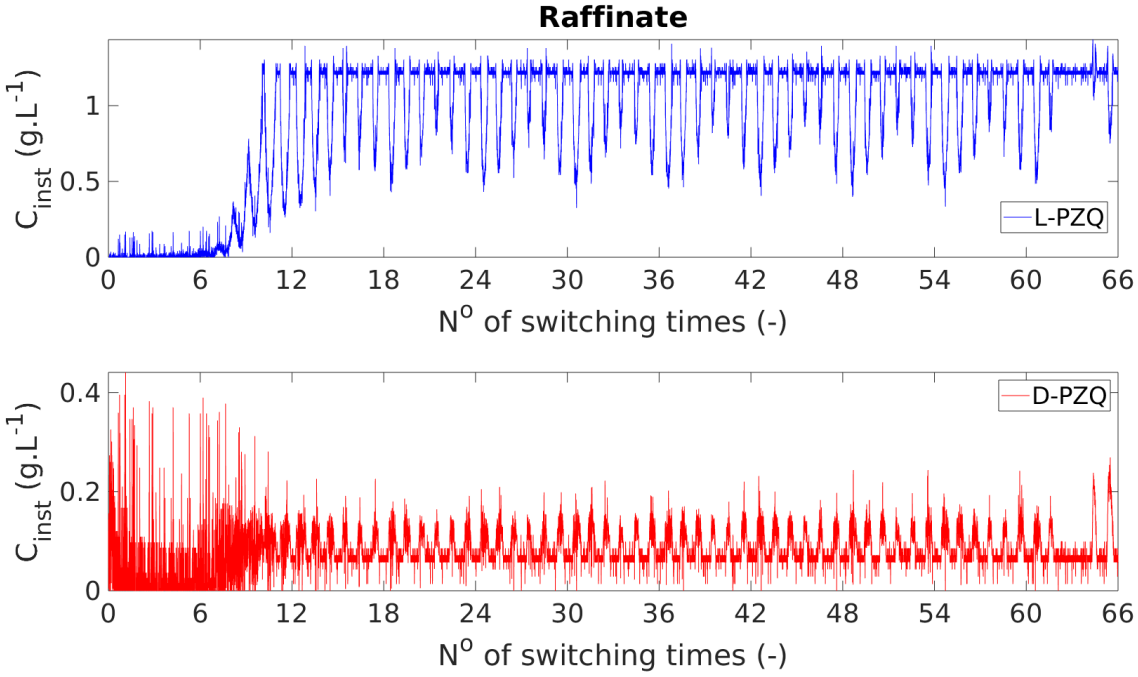

Figure J.4: Instantaneous concentrations for the second (*Run 6.2*) and third (*Run 7.2*) stages when the raffinate was measured.

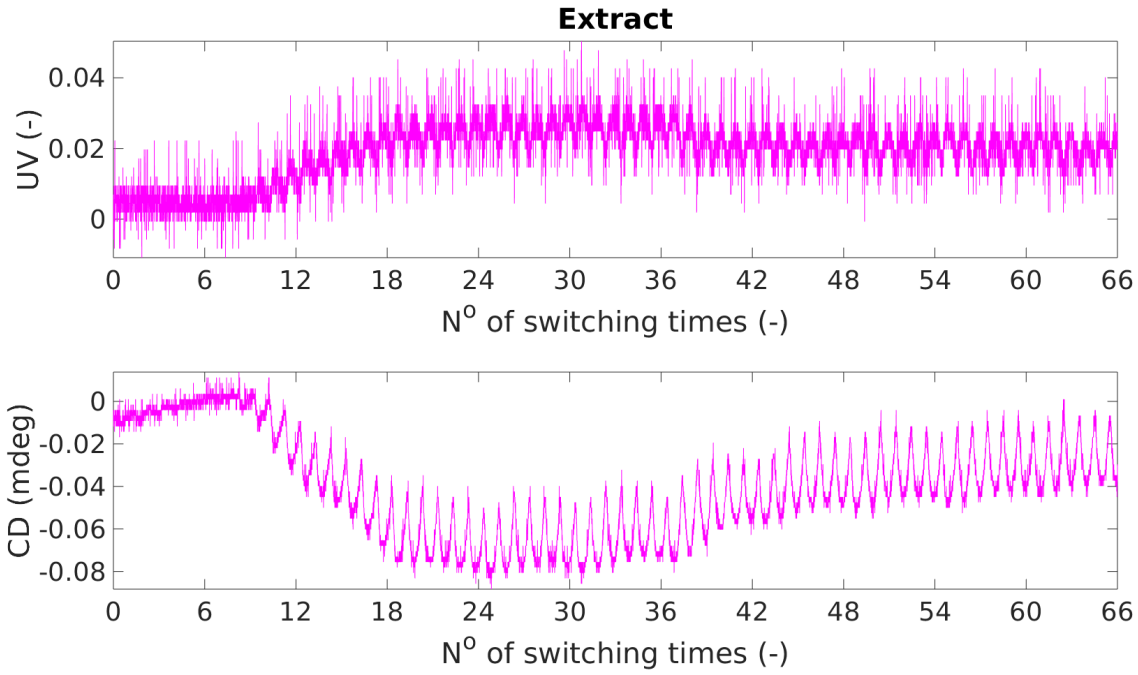

Figure J.5: Measured UV/vis and CD signals for the second (*Run 6*) and third (*Run 7*) stages.

J.3 Second (*Run 6*) and third (*Run 9*) stages

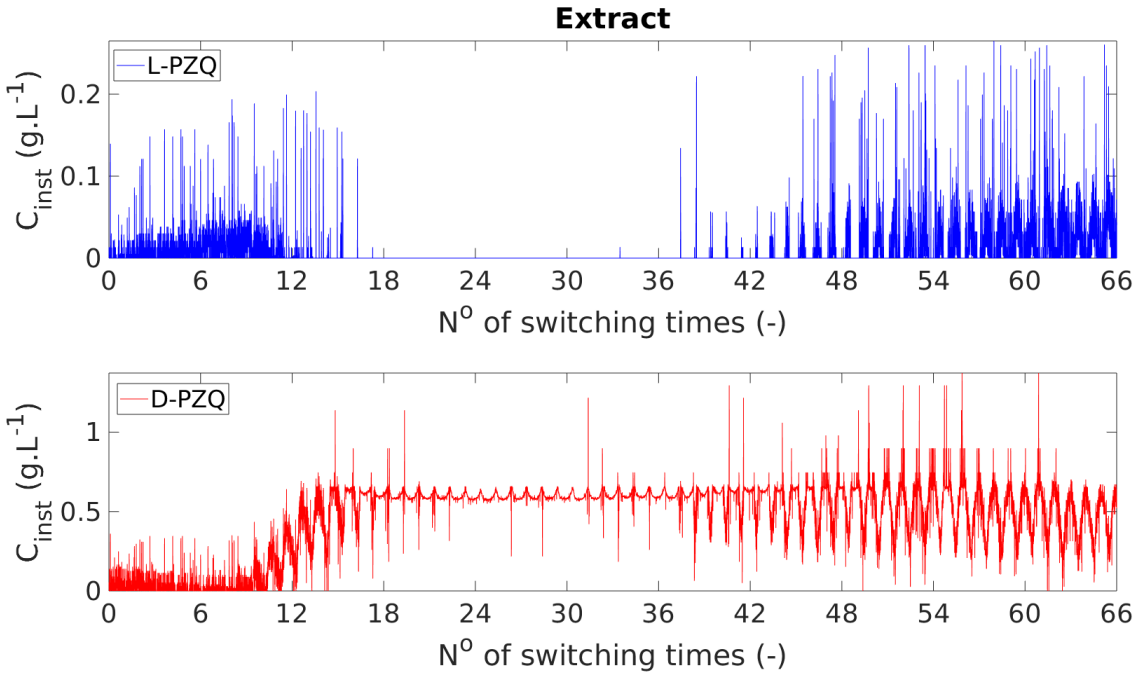

Figure J.6: Instantaneous concentrations for the second (*Run 6*) and third (*Run 7*) stages when the extract was measured.

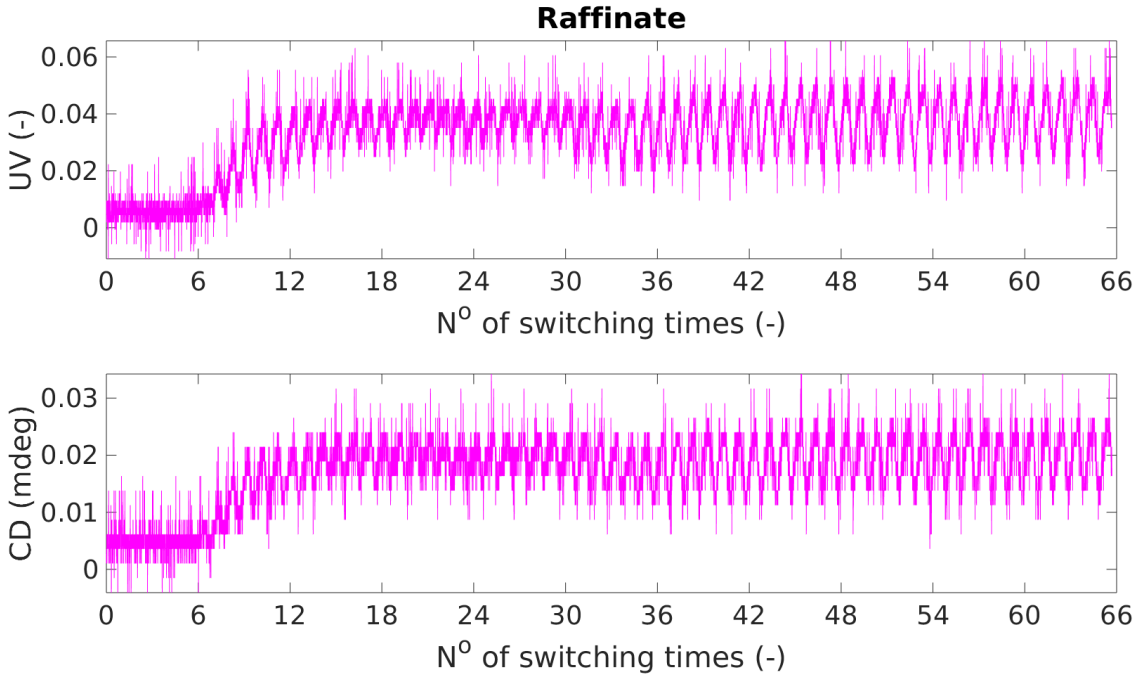

Figure J.7: Measured UV/vis and CD signals for the second (*Run 6*) and third (*Run 8*) stages.

J.4 Second (*Run 6*) and third (*Run 10*) stages

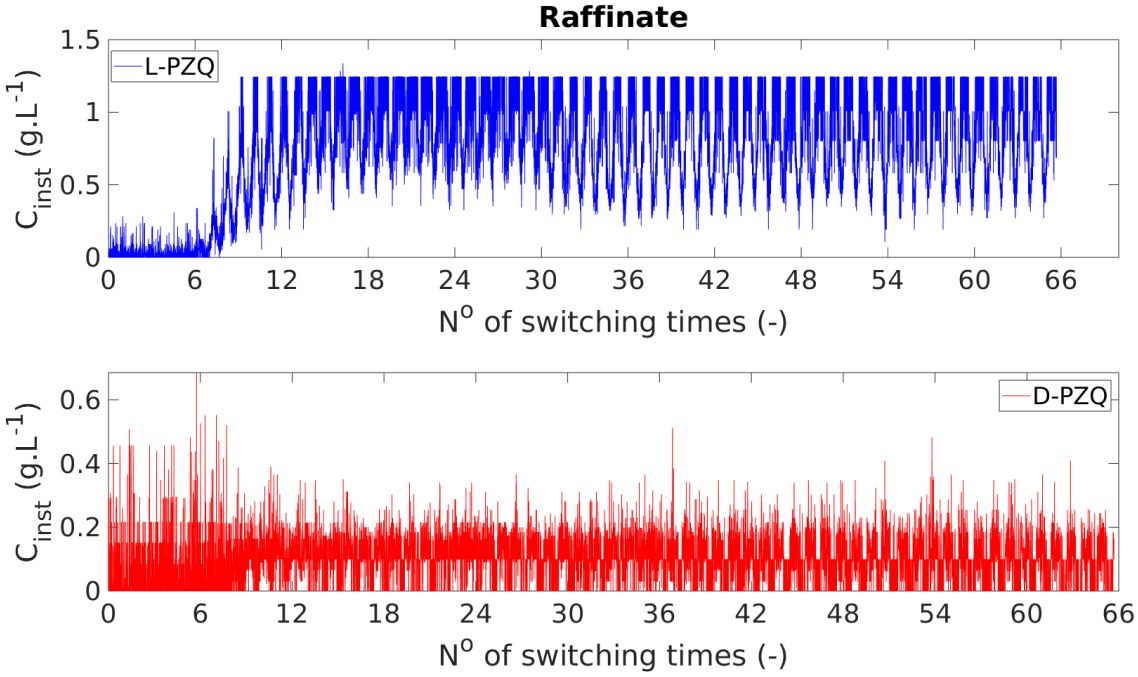

Figure J.8: Instantaneous concentrations for the second (*Run 6*) and third (*Run 8*) stages when the raffinate was measured.

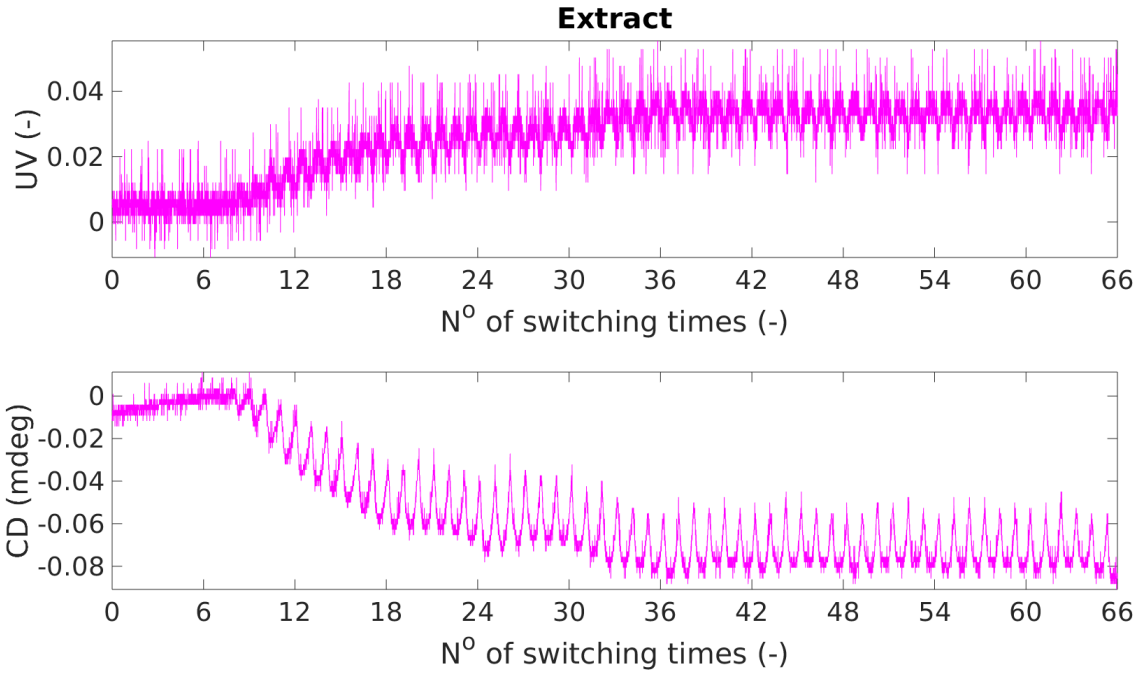

Figure J.9: Measured UV/vis and CD signals for the second (*Run 6*) and third (*Run 8*) stages.

J.5 Second (*Run 6*) and third (*Run 11*) stages

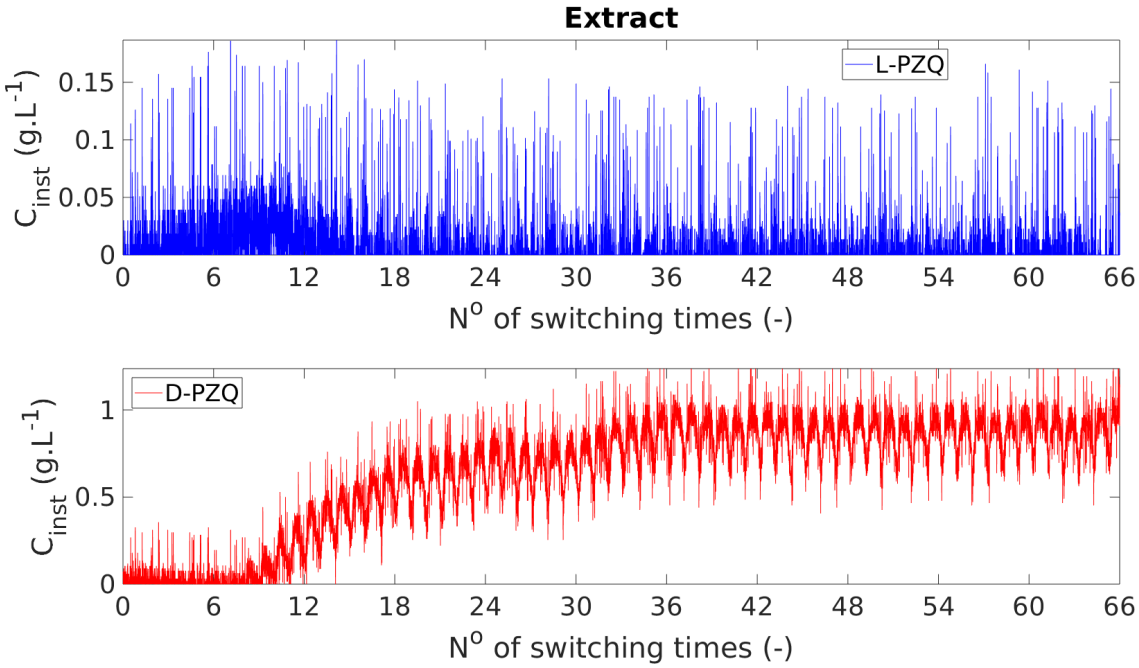

Figure J.10: Instantaneous concentrations for the second (*Run 6*) and third (*Run 8*) stages when the extract was measured.

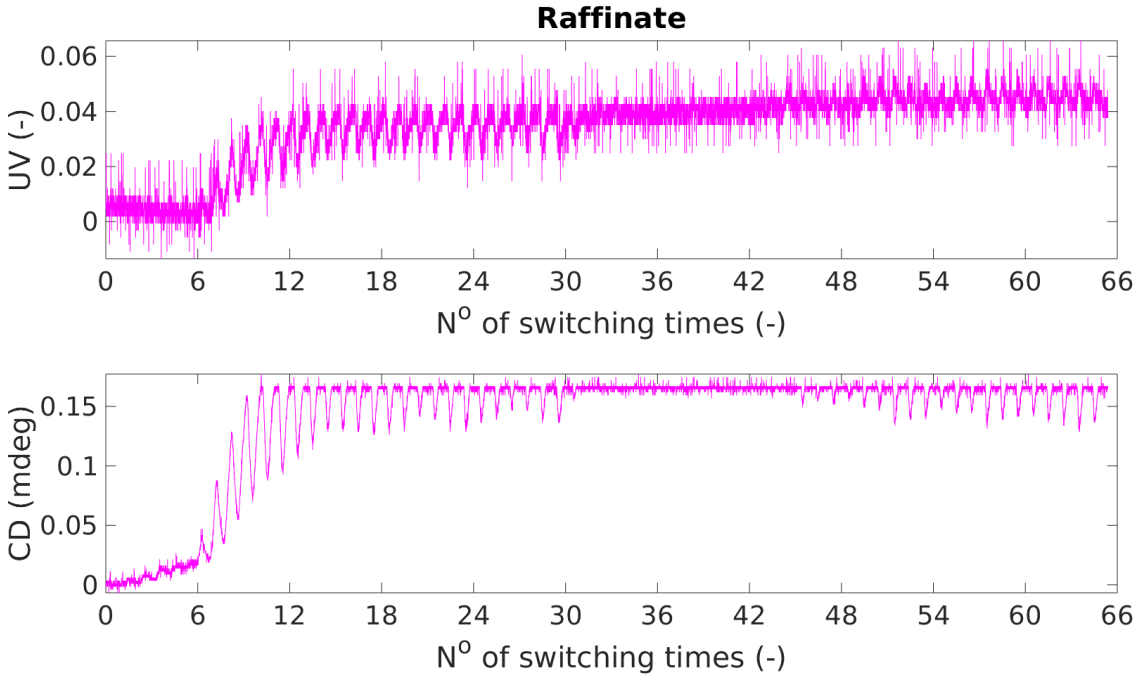

Figure J.11: Measured UV/vis and CD signals for the second (*Run 6*) and third (*Run 9*) stages.

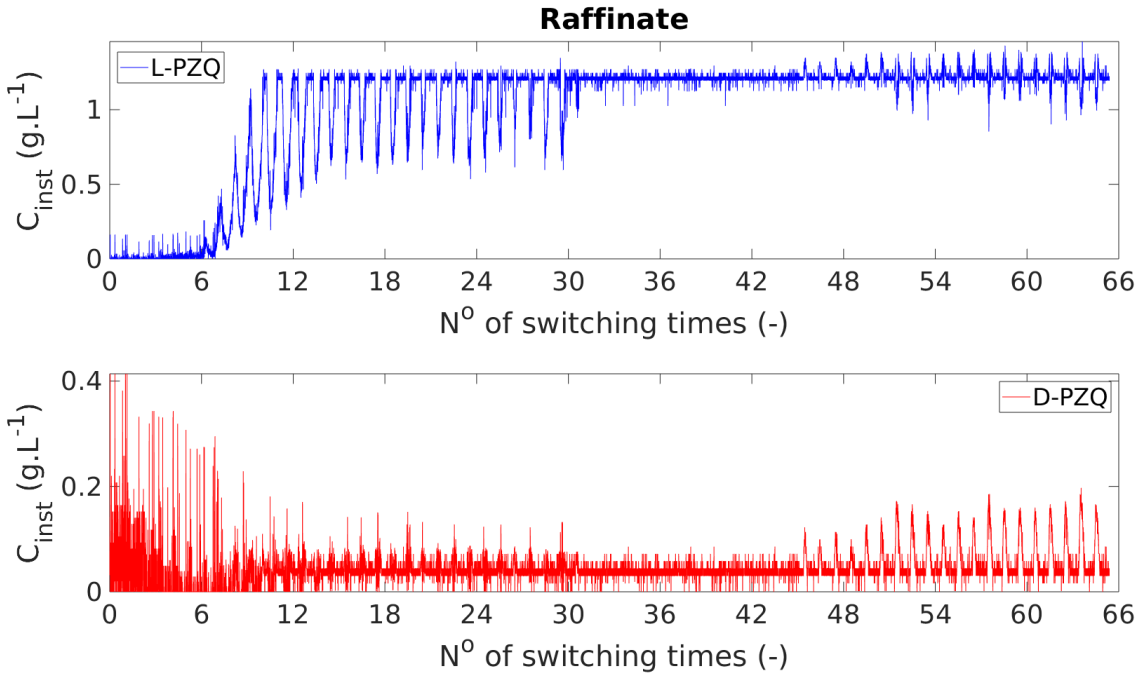

Figure J.12: Instantaneous concentrations for the second (*Run 6*) and third (*Run 9*) stages when the raffinate was measured.

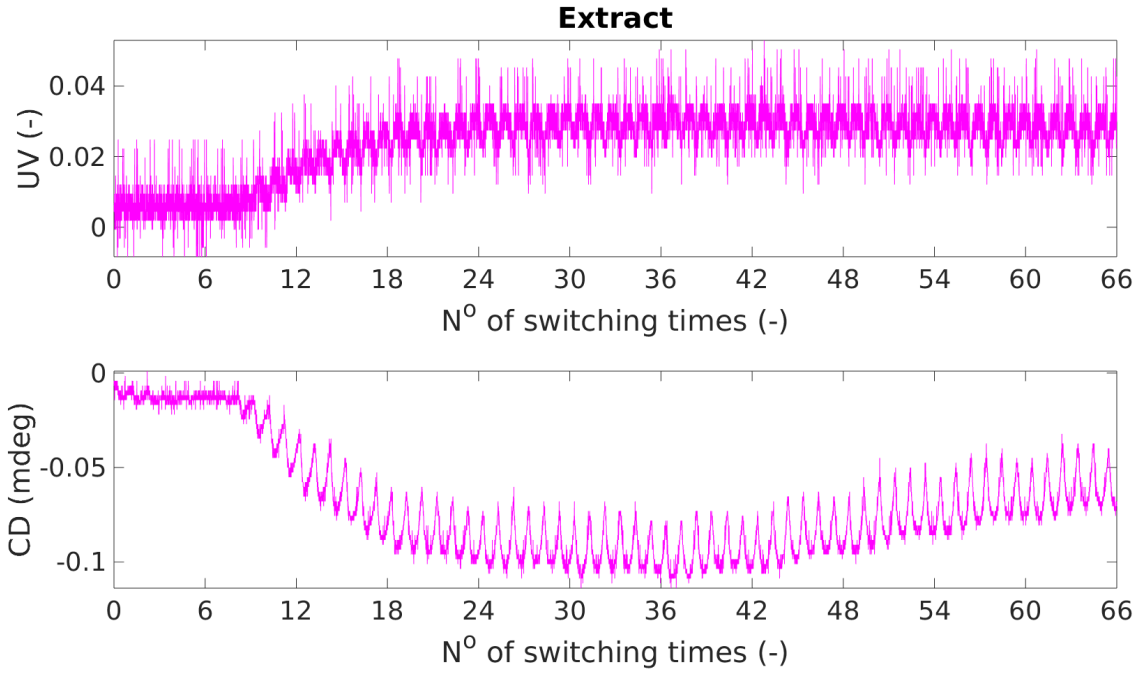

Figure J.13: Measured UV/vis and CD signals for the second (*Run 6*) and third (*Run 9*) stages.

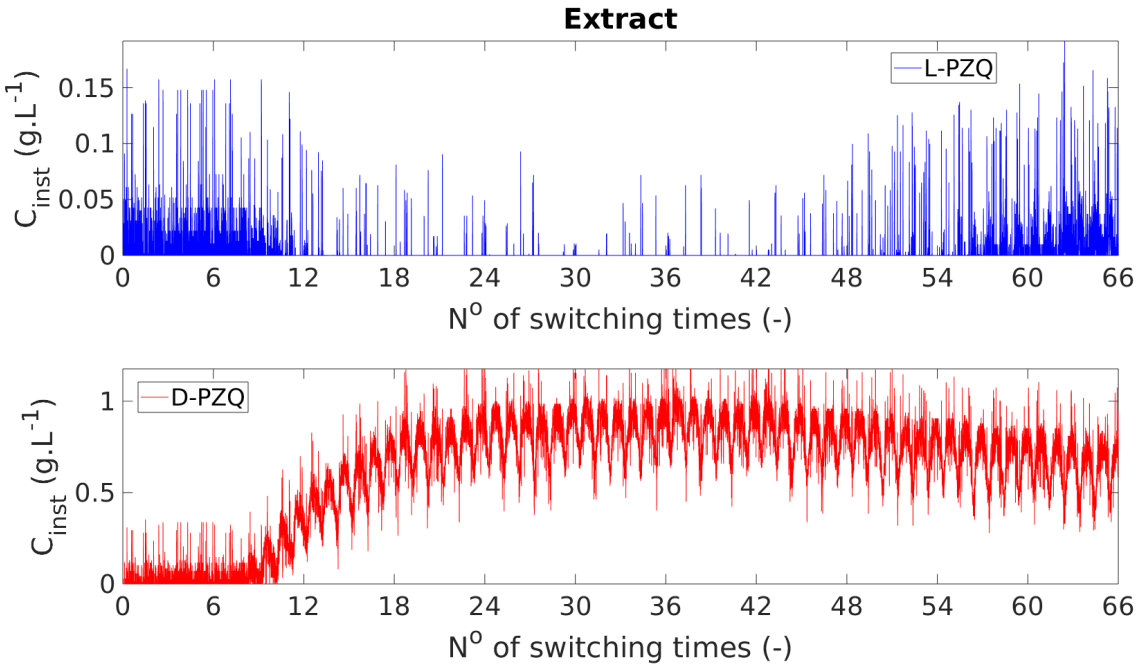

Figure J.14: Instantaneous concentrations for the second (*Run 6*) and third (*Run 9*) stages when the extract was measured.

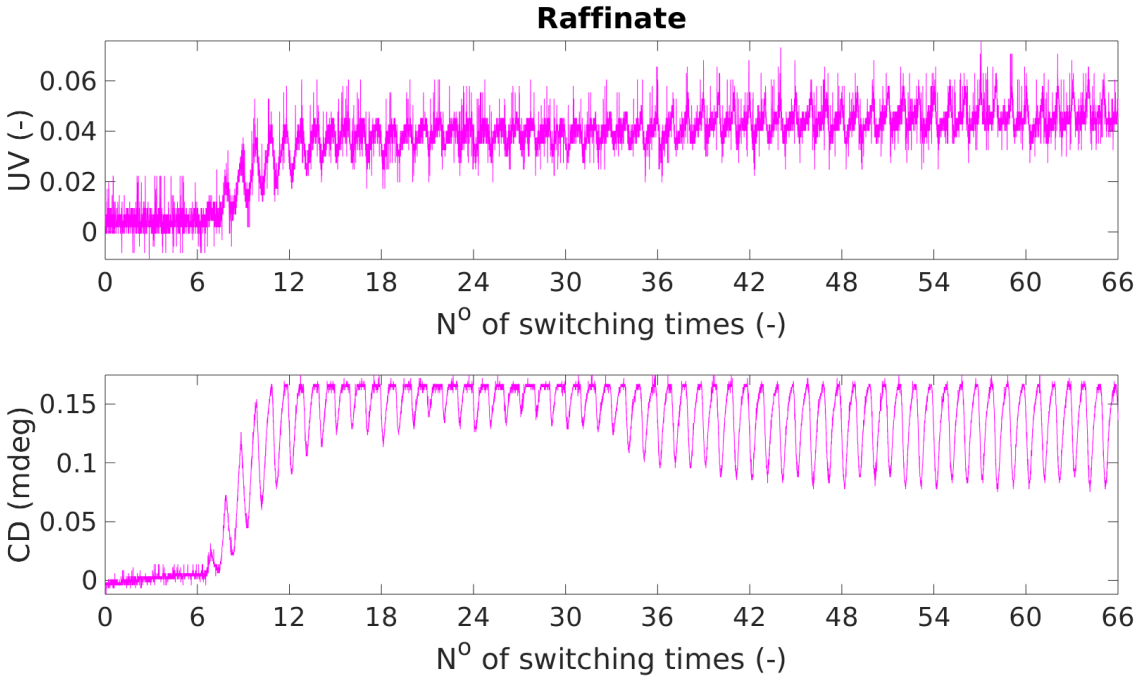

Figure J.15: Measured UV/vis and CD signals for the second (*Run 6*) and third (*Run 10*) stages.

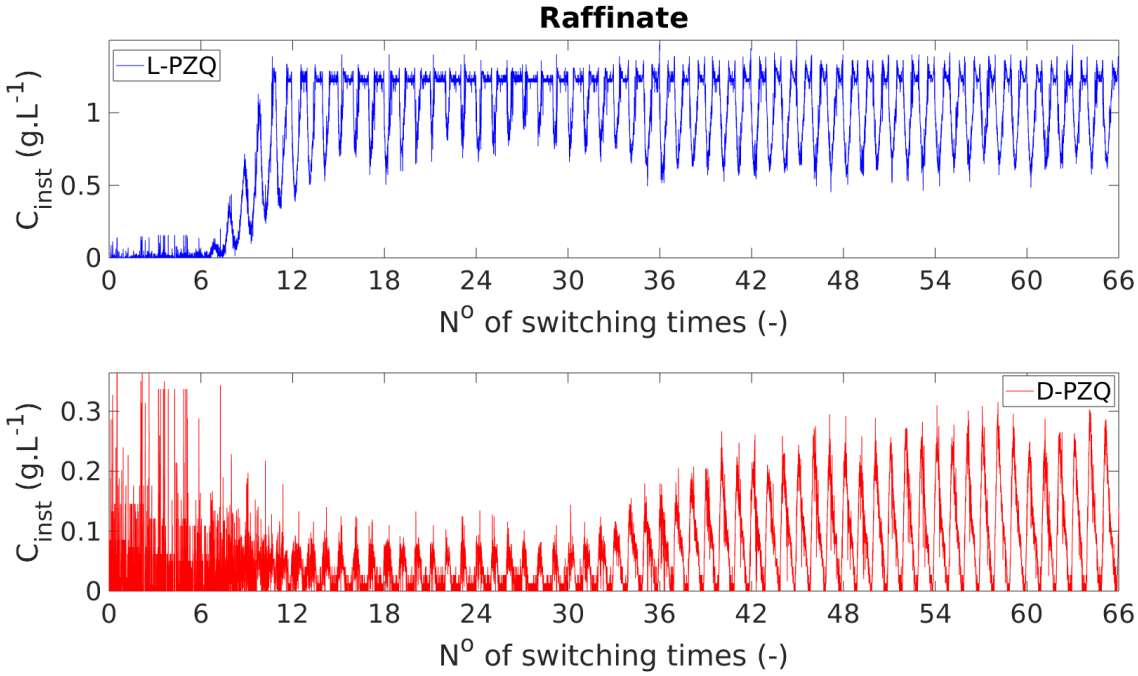

Figure J.16: Instantaneous concentrations for the second (*Run 6*) and third (*Run 10*) stages when the raffinate was measured.

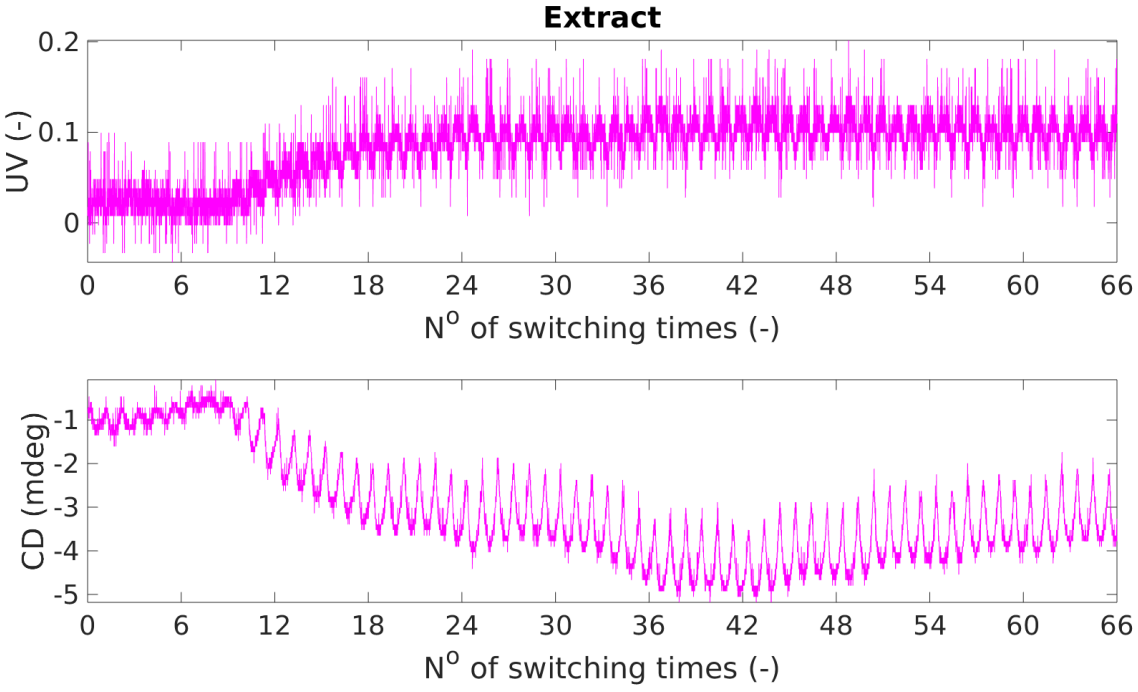

Figure J.17: Measured UV/vis and CD signals for the second (*Run 6*) and third (*Run 10*) stages.

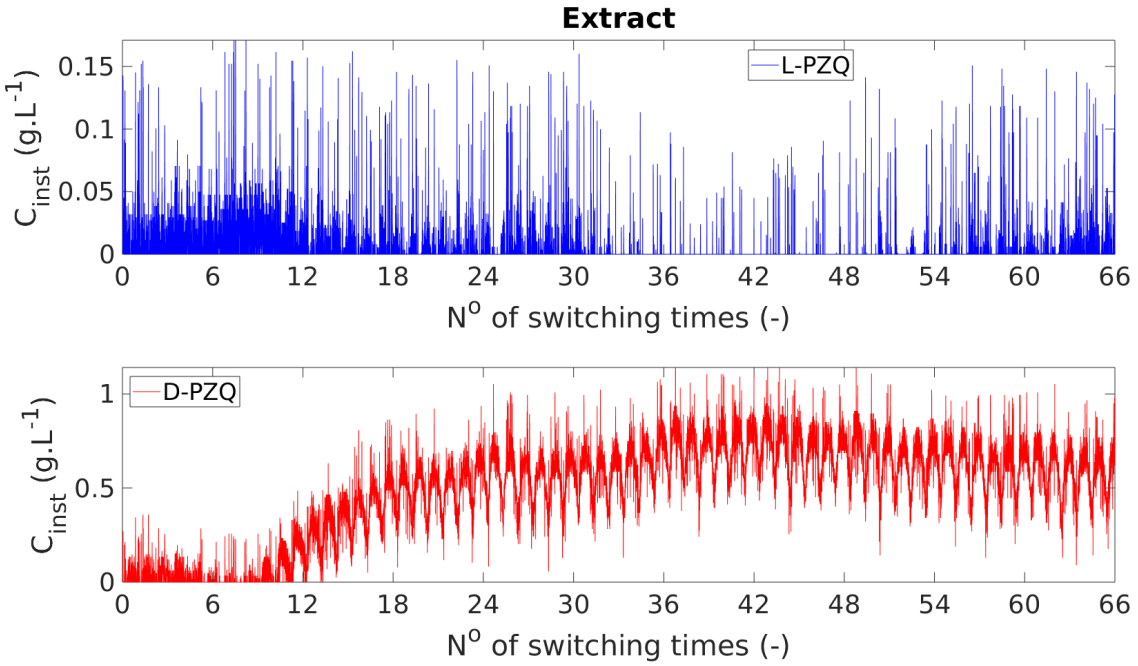

Figure J.18: Instantaneous concentrations for the second (*Run 6*) and third (*Run 10*) stages when the extract was measured.

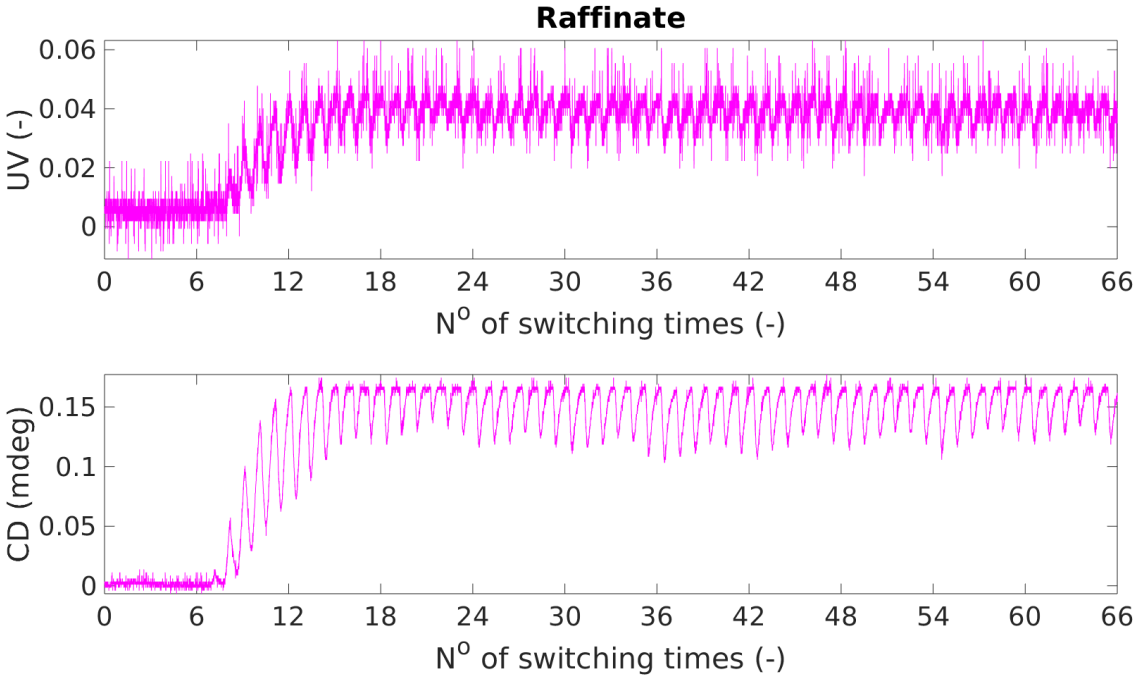

Figure J.19: Measured UV/vis and CD signals for the second (*Run 6*) and third (*Run 11*) stages.

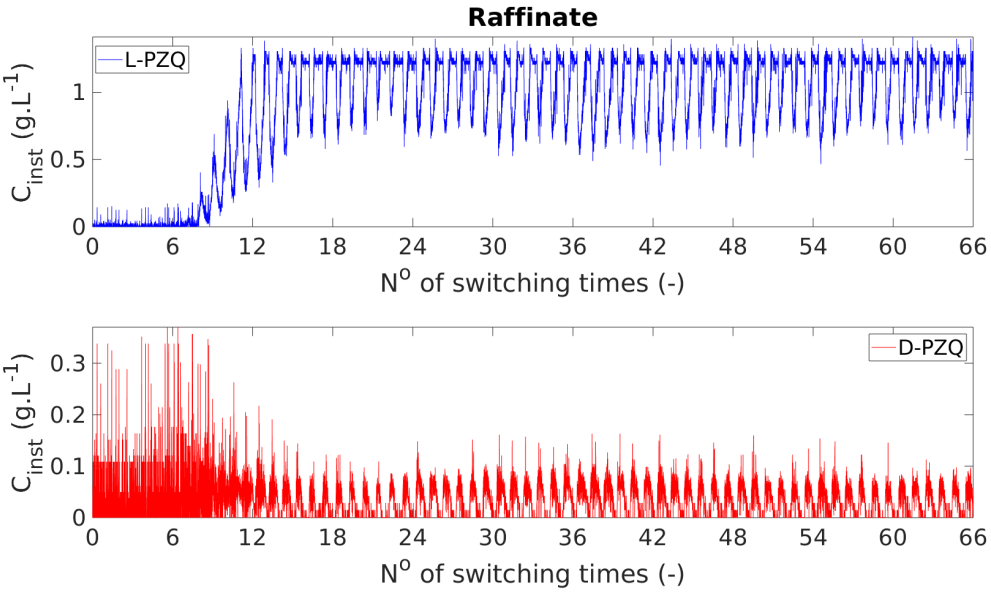

Figure J.20: Instantaneous concentrations for the second (*Run 6*) and third (*Run 11*) stages when the raffinate was measured.

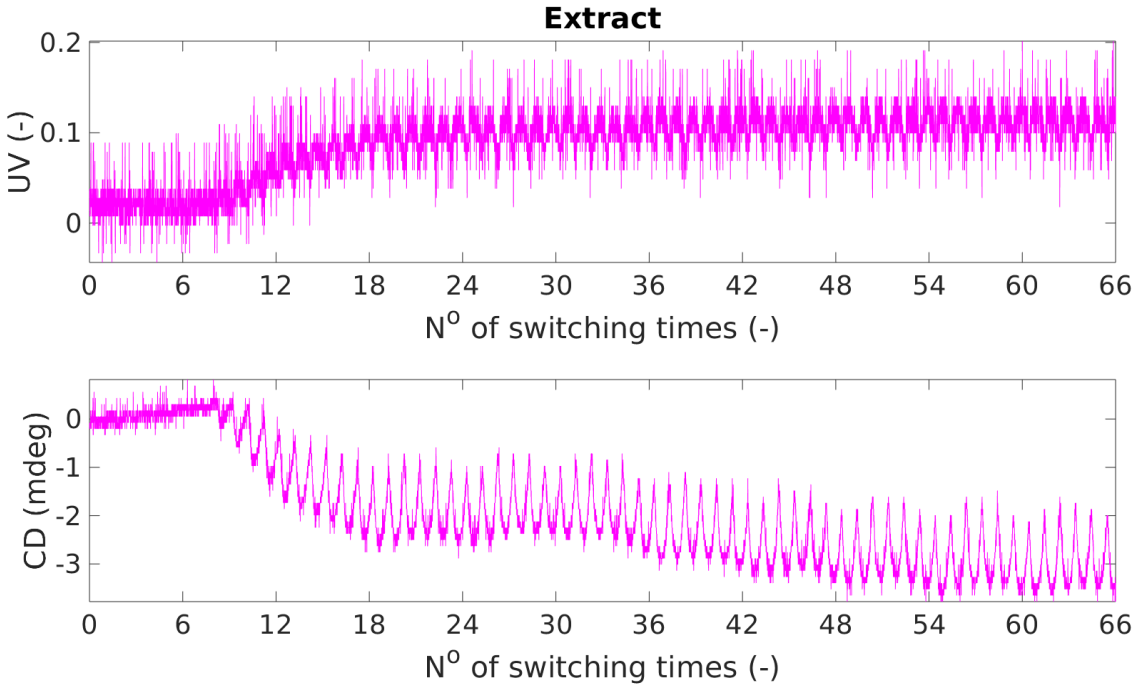

Figure J.21: Measured UV/vis and CD signals for the second (*Run 6*) and third (*Run 11*) stages.

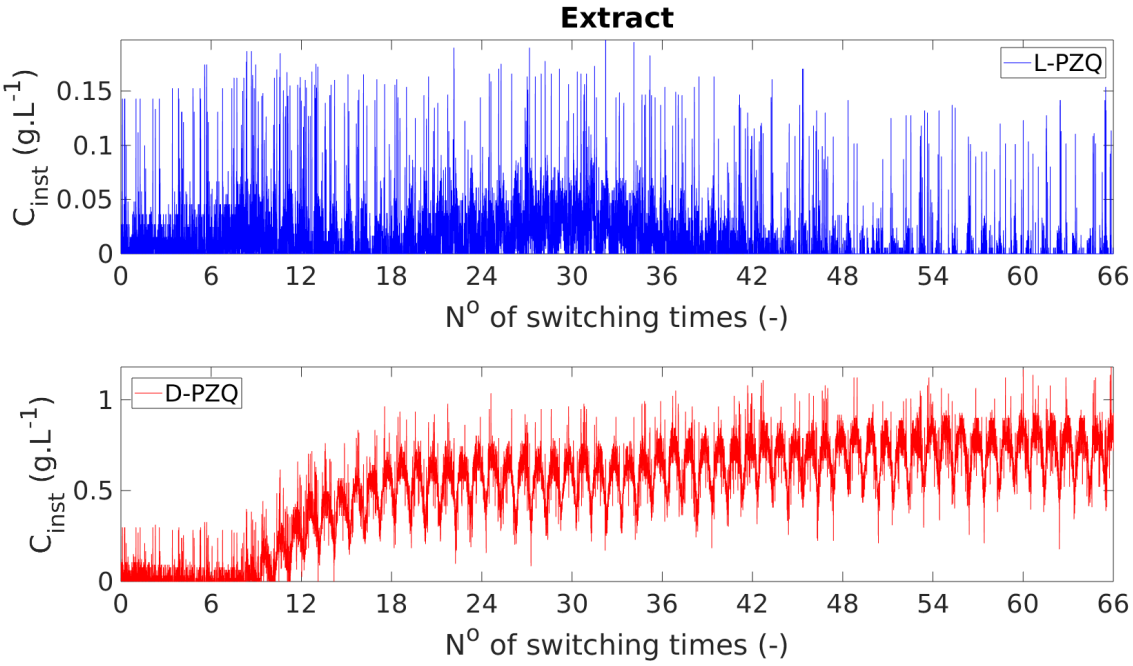

Figure J.22: Instantaneous concentrations for the second (*Run 6*) and third (*Run 11*) stages when the extract was measured.

Appendix K

Automation of a Simulated Moving Bed Chromatographic Process

This appendix shows the next article to be submitted. The main issue of this work is the supervisory system developed for the built SMB.

Development in LabVIEW of a Supervisory System for the Automation of a Simulated Moving Bed Chromatographic Process

R.C. de Holanda, A.G. Barreto Jr, F.C. Cunha, A.R. Secchi

***Abstract* – Praziquantel (PZQ) is a racemic mixture prescribed for Schistosomiases disease treatment. However only the enantiomer (R)-PZQ presents a proven treatment efficiency against the infirmity, the (S)-PZQ causing cases of sickness and vomiting due to its bitter taste. The Simulated Moving Bed chromatographic system (SMB) is a well stablish separation process applied in many branches of the chemical industry, from drug purification stages to food processing systems. In order to implement and operate a SMB unity for the PZQ separation, allowing the production of a medication with proven efficiency and without side effects, it was developed a LabVIEW supervisory system. The automation software was capable of controlling remotely all the equipment present in the operational unit, such as automatic pumps, multiposition valves for flowrates position readjustments, and a Circular Dichroism Chiral Detector, allowing the imposition of a specific behavior for each one of the process components. Two different experiments were conducted so that it was possible to verify the system operational behavior and efficiency. The first set of results demonstrated that the data acquisition programming was capable of retrieving information constantly, evidencing a direct correlation between the internal liquid pressure and the valving system position, with mean pressure values around 50 bar. The second set of results demonstrated the SMB process efficiency, the Raffinate stream presenting (R)-PZQ high concentration values with a low presence of (S)-PZQ, with experimental values equal to 1.0 g/L and 0 g/L respectively.**

Keywords – Chemical Engineering, LabVIEW, Separation process, Simulated Moving Bed

I. INTRODUCTION

Racemic mixtures are solutions composed by two molecules that have the same molecular formula one being the mirror image of the other, therefore they cannot be overlapped. These molecules are known as enantiomers and are identified by the initials “R” and “S” [1]. Different racemic mixtures are produced daily in many branches of the economy, from the food processing stages up to the pharmaceutical industry [2]. One example is the medicament Praziquantel (PZQ), prescribed for the combat and treatment of Schistosomiasis disease. Only the (R)-PZQ has a proven pharmacological action against the disease, the (S)-PZQ providing a significant bitterness to the drug causing cases of seasickness and vomiting [3]. In the last decades many investments in research and development have been made targeting the creation of new technologies capable of producing a drug with a high purity percentage of (R)-PZQ, increasing the medicament efficiency [4]. Among all proposed technologies, the Simulated Moving Bed chromatography process (SMB) shows as a prominent candidate [4].

Differently from the traditional batch chromatographic process, the SMB simulates the adsorptive phase displacement in an opposite direction of the feed stream [5]. In a fixed group of chromatographic columns two inlet streams (Eluent and Mixture feed) and two outlet streams (Raffinate and Extract) have their position in the system systematically changed, in the same sense of the fluid stream flow. These position shifts happen according to a time specified by the operator being the responsible for the displacement simulation of the adsorbent phase [6]. This operational behavior change allows the process to work continuously improving the system productivity, decreasing simultaneously the feedstock consumption, such as the quantity of eluent utilized [6].

The SMB system setup consists basically of a valving system of a single or multiple valve responsible for input and output streams position rearrangement in each chromatographic column, and pumps controlling the process flowrates values [7]. The valving system is considered the SMB separation process core and it can be designed as a central or distributed valve system, depending of the flexibility the SMB system must operate with, each design having its own advantages [8]. Therefore, the design and equipment assembly of a SMB unit is complex once that depending of the mixture separation to be

This paragraph of the first footnote will contain the date on which you submitted your paper for review. It will also contain support information, including sponsor and financial support acknowledgment. For example, “This work was supported in part by the U.S. Department of Commerce under Grant BS123456.”

The next few paragraphs should contain the authors’ current affiliations, including current address and e-mail. For example, F. A. Author is with the National Institute of Standards and Technology, Boulder, CO 80305 USA (e-mail: author@ boulder.nist.gov).

S. B. Author, Jr., was with Rice University, Houston, TX 77005 USA. He is now with the Department of Physics, Colorado State University, Fort Collins, CO 80523 USA (e-mail: author@lamar.colostate.edu).

T. C. Author is with the Electrical Engineering Department, University of Colorado, Boulder, CO 80309 USA, on leave from the National Research Institute for Metals, Tsukuba, Japan (e-mail: author@nrim.go.jp).

carried out, the most suitable system configuration must be identified among a considerable quantity of valves, pumps and transfer lines combinations [9]. Once the system architecture design is defined the process automation becomes the next challenge to be overcome. Any laboratorial/industrial unit automation is a critical task, and concerning a SMB system, it's even more crucial once that the unit's operation and flexibility relies in its automation routine and control algorithm [10].

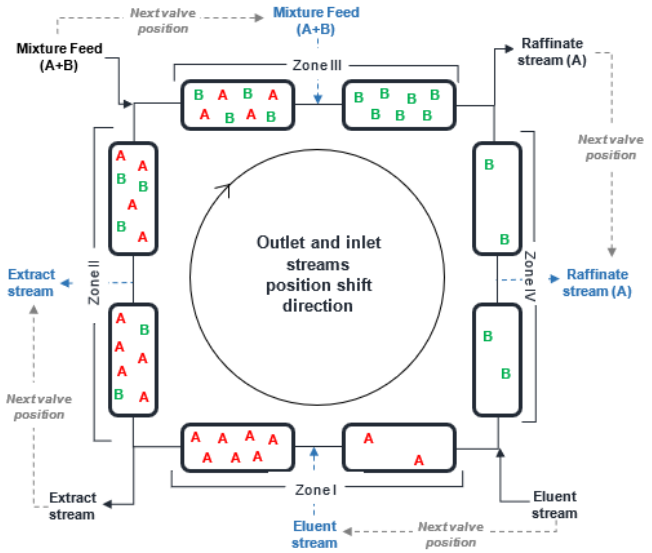

Fig. 1. Simulated moving bed behavior and inlet and outlet streams rearrangement according to valve position.

Control strategies are import for the operation of a SMB process once that the optimized unit operation is highly sensitive to disturbances, such as temperature or feed composition changes for example, affecting the operation efficiency [11]. However, in order to stablish a control procedure over the process behavior is necessary to fully automate the system setup, controlling remotely the equipment and monitoring the process parameters [12]. LabVIEW is a well-known supervision and control software used for SMB unit automation, being applied in many projects and experiments involving the separation of racemic mixtures, each one demanding specific equipment assemblies and operation modes. [13] developped a SMB unit, controlled by a LabVIEW-based supervision system, operating with a multiple valving system for the resolution of cis(R, S)-FTC-ester racemic mixtures, achieving purity values of 99.8% for the S-FTC-ester enantiomere. [14] evaluated and described the operation of a SMB unit using microcrystalline cellulose triacetate (MCTA) columns and automated by a LabVIEW supervisory system for the chiral separation of ketamine enantiomers, obtaining purities values above 99.5% in the raffinate stream ((S)-ketamine) and 97.7% for (R)-ketamine in the extract stream. [15] described the operation of a SMB unit controlled by a LabVIEW-based program for the separation of a racemic Praziquantel mixture, reporting optimum purity values of 100,0 % for the R-PZQ in the raffinate stream, the extract stream having a 96.0% of purity for the (S)-PZQ.

In this paper we make a comprehensive description of the development and experimental evaluation of a supervisory system in LabVIEW for the operation of a SMB process capable of retrieving both PZQ enantiomers separately, in different streams and with high purity thus allowing the production of a drug with fewer side effects.

II. MATERIALS AND METHODS

A. *Materials*

For the experiments a racemic mixture of Praziquantel with pharmaceutical grade was provided by Farmanguinhos (Rio de Janeiro, Brazil) and produced by Yixing Xingyu Medical Chemical Co.

As a solvent it was used Ethanol HPLC grade, provided by Biograde (Brazil).

B. *Equipment*

The Simulated Moving Bed chromatography system is comprised of four pumps PU-2086 provide by Jasco Company. The communication between the equipment and the PC unit is made through a standard RS-232 data connection, allowing to an external supervisory system a remote control over the equipment functionalities.

TABLE I
JASCO PU-20186 PUMP SERIAL COMMUNICATION SETTINGS AND PROTOCOL

Serial communication settings	
Baud Rate (bits/s)	4800
Data bits (bit)	8
Parity	None
Stop bits (bits)	2
Flow control	RTS/CTS
Serial communication protocol	
Retrieve pressure measurement	*press 1 load p*
Outlet stream value adjustment	*value flowrate set*
Outlet stream start and stopping	0 pump set (Start) 1 pump set (Stop)

This SMB experimental setup operates with two different types of valves provided by Valco Co., the E8 multiposition valve and the two-ways valve. The operation of the E8 valve is performed by an electronic actuator designed around a microcontroller that operates in 110VCA and consisting of the actuator itself, a control box with LED/display and 20 conductor interfacial cable. The control is performed by a 20-pin using TTL digital input/output signals. A BCD-encoded logic level signal was used in order to access randomly each position of the valve and recognize its real position, as it's described in TABLE II. The control scheme only uses the "Home" and "Step" wires for the sake of simplicity.

TABLE II
BCD-ENCODED LOGIC USED FOR E8 VALVE REMOTE CONTROL AND MONITORING

BCD logic for position random access	
Next position	*Pin "STEP"*
Position 1 (Home)	*Pin $\bar{1}$'s*
BCD logic for position monitoring	
Position 1 (Home)	*Pin 1's*
Position 2	*Pin 2s*
Position 3	*Pins 1's and 2's*
Position 4	*Pin 4's*
Position 5	*Pins 4's and 1's*
Position 6	*Pins 4's and 2's*

The six two-ways-valves (one per each column) also operates according to an assembly composed by a control module, a stepper motor/gearbox and a manual controller, connected to a 24 VDC power supply. A pin 10-pin connector performs the control by means of TTL digital input/output signals. By asserting input pin 5 the actuator goes to Position A, and asserting input pin 6 it goes to Position B. The microcontroller indicates that the valve is in Position A driving output pin 3 to a logic low, maintaining output pin 4 at a logic high. The opposite behavior is imposed once that the two-ways-valve is in Position B.

TABLE III
DIGITAL INPUT/OUTPUT COMMUNICATION PROCEDURE FOR POSITION REMOTE CONTROL AND REAL TIME POSITION MONITORING

Digital pin for position monitoring	
Pin 3	*OUTPUT: Position A*
Pin 4	*OUTPUT: Position B*
Digital pins for valve position remote control	
Pin 5	*INPUT: Position A*
Position 6	*INPUT: Position B*

A Circular Dichroism Chiral Detector CD-2095 provide by Jasco Co. was used in order to quantify the presence of each enantiomer in the Raffinate stream, through simultaneous UV-Vis and circular dichroism (CD) signals measurement. Voltage signals proportional to both the CD and UV-vis signals are produced by the equipment's internal control system and retrieved through a Terminal Block.

Both digital and analog signals transmitted or received from the equipment are interfaced by a NI DAQ USB-6501 acquisition device, which communicates to the PC Unit through a USB port.

C. Experimental Setup

The SMB experimental unit was set up according to the flowsheet shown in Fig. 2. The inlet and outlet tee-connectors connect the columns to the multiposition and dead-end valves responsible for the streams periodic position shift. The E8 valves V-8.2, V-8.1 e V-8.3 connected simultaneously to the column's inlet T-connectors and pumps deliver respectively feed, eluent and a recycled stream retrieved from the extract fluid, in order to control the zones inner streams. The valve V-8.6 is responsible for recycling the fluid phase. The two remaining multiposition valves (V-8.4 e V-8.5) are connected to the outlet T-connectors, collecting the products streams. Both streams are connected to relief valves assuring safe operational conditions and maximum pressure values. The raffinate stream passes then through a Circular Dichroism Chiral Detector being analyzed.

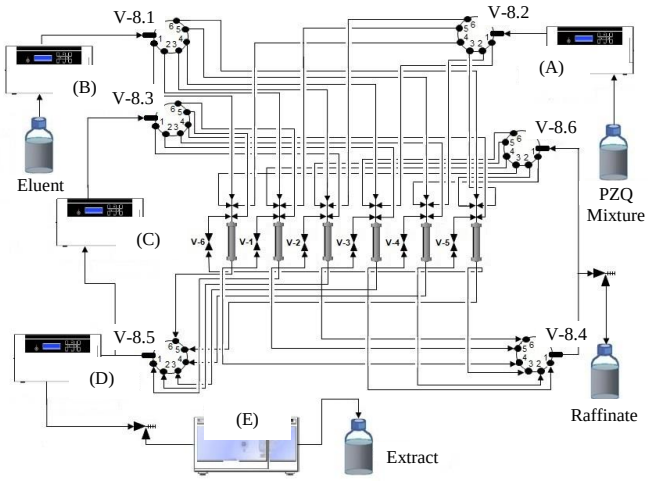

Fig. 2. Flowsheet of the experimental setup consisting of four pumps (A, B, C and D), six chromatographic columns, one Circular Dichroism Chiral Detector (E), six dead-end valves positioned between the columns, six E8 valves (V-8.1 up to V-8.6) and streamlines representing the unit tubbing.

The software used for the development of the supervisory system responsible for the SMB unit equipment remote control and measured data acquisition was the LabVIEW 2015.

D. LabVIEW programming development

1) Jasco PU-2086 pump:

Once one knows the equipment RS232 communication settings and protocol it's possible to stablish a connection between the equipment and the pc unit as so the development of the supervision programming logic. In the present application for the serial data transmission and receiving it was used the VISA block programming tools.

First the RS-232 settings were selected using the VISA Configure Serial Port block. In order to retrieve the pressure measured by the pump, to adjust the outlet stream value and to start or stop the pumping it's necessary to write to the serial port the commands specified by the serial communication protocol. That is done by using the VISA Write Block. Once the pressure measurement is requested all the bytes sent by the pumps internal control system are interpreted using simultaneously the Bytes at Port function and the VISA Read Block.

As it isn't possible to change simultaneously all three parameters defined by the communication protocol, it was necessary to define an internal hierarchy between them. As the process streams are constant during major part of a given experiment and the stream is switched on or off only in specific

situations the pressure value requisition is defined as the priority command.

This behavior was accomplished using different LabVIEW tools and functions. Once the supervisory is activated, in each interaction all parameter's values are stored (Shift Register) and then compared with the new ones retrieved in the next interaction (Equal Logical Comparison). If they are equal the command responsible for the pressure measurement is sent to the Visa Write Block (Select Function). Otherwise the command that had its command value changed will be the one to be sent.

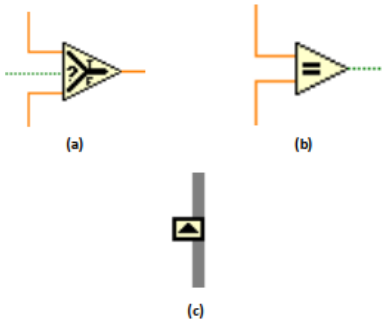

Fig. 3. LabVIEW tools used for the Jasco pump supervisory system programming: (a) Select Function, (b) Equal, (c) Shift Register.

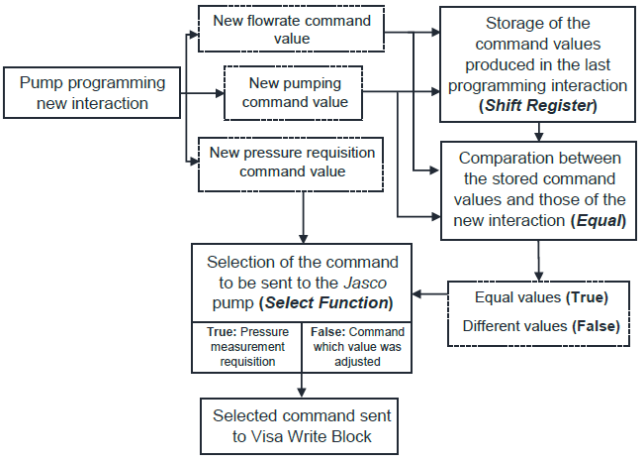

Fig. 4. Logic developed for the selection of the command send to the Visa Write Block.

2) Valco Multiposition Valve E8:

Differently from the supervisory programming developed for the four pumps operation, both dead-end and E8 valves signal transmission and acquisition are configurated by NI DAQmx Tools. To retrieve or send a digital or analog signal it's necessary to select the NI DAQ device and specify the port to which one given wire of the interfacial cable is connected. That's accomplished by selecting DAQmx Start Task block. In order the read and send a signal to the valve microcontroller it was used the DAQmx Read and DAQmx Write blocks respectively.

At each chromatographic operation cycle the E8 valves must switch positions six times. The position rearrangement from the first up to the sixth position is controlled by voltage signal drop over Wire "Step". Once the E8 valves are in the sixth position the wire 1's is taken to 0 volts sending the outlet stream back to the first position.

All E8 valves must stay in each of the six positions for a given time period. The control over these six periods of time is made by a time control matrix. This matrix is connected to a time counter and at each of the first five time lapses is produced a logical False signal. At this moment the Wire "Step" is taken to 0 volt switching the valve outlet stream to the next position, maintaining the wire '1s' at 5 volts. At the same time a shift position counter is incremented switching the time controller present in the time control matrix. Once the sixth time lapse happens the wire 1's and 'Step' are maintained at 0 and 5 volts respectively, returning the valve's outlet stream to the first position and resetting both shift position counter and control matrix.

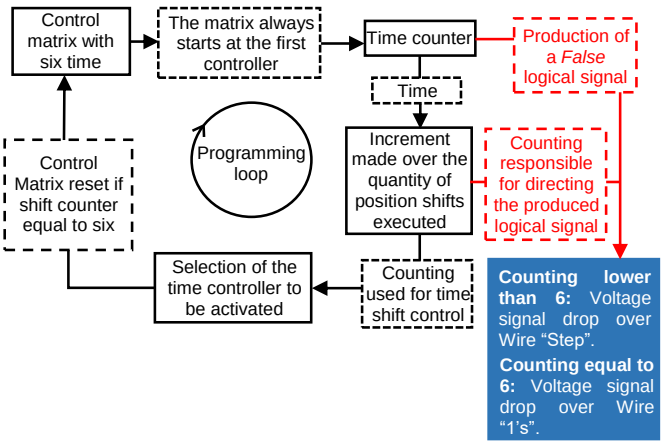

Fig. 5. Programming logic developed for E8 valve position shifting control.

By retrieving the signals transmitted by the second section wires it is possible to define the valve operational outlet position. For the first, second and fourth positions, the E8 internal controller drops the voltage signal of a single wire. For positions 3, 5 and 6 the same controller drops the voltage signal of two specific wires at the same time.

After receiving and reading the voltage signals transmitted by wires 1's, 2's and 4's the DAQmx Read block produces logical signals, being True and False correlated to 5 and 0 volt respectively. The three signals are grouped according to the equipment instrumentation described in TABLE II. and compared by the tools *And Function* and *Equal? Function*.

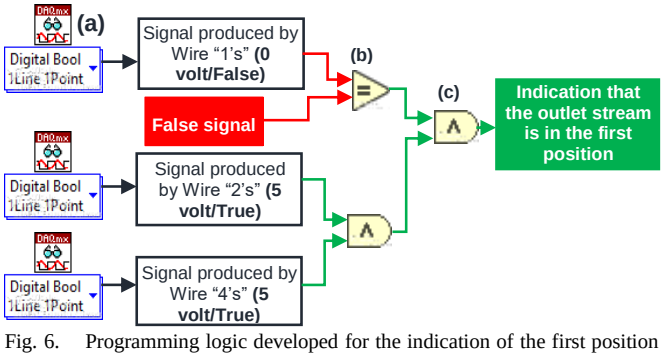

Fig. 6. Programming logic developed for the indication of the first position (a: DAQmx Read; b: Equal? Function; c: And Function).

3) Valco two-ways valve:

In this process the two ways valve operates as a dead-end valve allowing (position A) or blocking (position B) the flow of a given stream. Differently from the E8 valves the supervisory system for the dead-end valves wasn't developed in order to create a time shift control matrix. Instead it was created a logical correlation between the position adjustment of the dead-end valves and the operational position of one given E8 valve. This logical correlation defines if a specific dead-end valve will or not block a stream in function of the E8 valve 8.1 operational position.

TABLE III
CORRELATION BETWEEN VALVE 8.1 OPERATIONAL POSITION AND ALL DEAD-END VALVES OPENING AND CLOSURE BEHAVIOR.

Valve 8.1 position	Dead-end valves operational position					
	2.1	2.2	2.3	2.4	2.5	2.6
1	B	A	A	A	B	A
2	A	B	A	A	A	B
3	B	A	B	A	A	A
4	A	B	A	B	A	A
5	A	A	B	A	B	A
6	A	A	A	B	A	B

The E8 valve 8.1 logical position indicators signals were obtained through the usage of a programming block called *Local Variable.* This tool allows the user to retrieve a signal of a given indicator or controller in order to avoid the creation of new dataflow lines.

Once the time counter responsible for the valve 8.1 shifting position lapses, the produced logical *False* signal is compared to two positions logical signals groupings retrieved from valve 8.1, one related to position A and the other to position B.

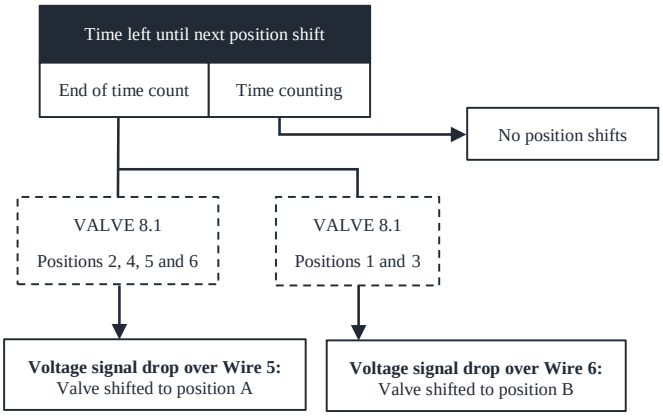

Fig. 7. Programming logic developed for remotely control valve 2.1 position shifting.

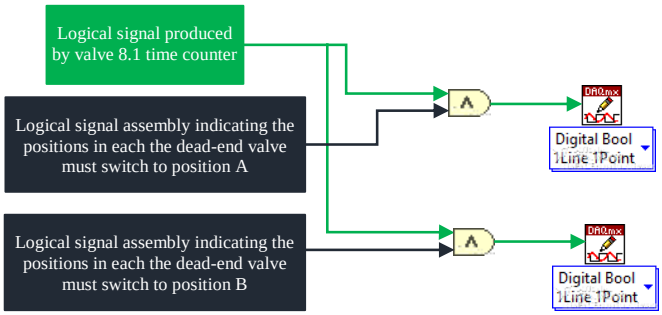

Fig. 8. Comparation between logical signals in order to adjust the position of a specific dead-end valve.

To retrieve the signals transmitted from the dead-valves microcontroller it was only used two programming tools: *DAQmx Start Task* and *DAQmx Read* blocks. The valve microcontroller indicates the equipment operational position taking to a logical low level the respective wire. Once the valve is in position A the microcontroller drops the voltage signal of wire 3, maintaining wire 4 at 5 volts. The opposite happens if the valve is in position B. *The DAQmx Read* block identify High and low levels as True and False logical signals respectively, indicating to the operator through which operational position the equipment outlet stream is flowing through.

4) Circular Dichroism Chiral Detector:

Once the voltage signals acquired by the NI device are proportional to CD and UV values it's possible to retrieve the enantiomers concentrations in the Raffinate stream. The equipment was already calibrated in order to analyze and quantify both enantiomers. As during the calibration procedure, the CD and UV ranges were set to 0.0005 deg·$(10mV)^{-1}$ and 0.04 AU·$(10mV)^{-1}$ respectively, the acquired voltage signals are adjusted, the UV voltage signal being multiply by 50.0 and the CD signal by 4.0.

A MATLAB script containing an empiric model that calculates enantiomer concentrations data from CD and UV values allows the supervisory system to quantify the presence of each enantiomers in a given stream. The Circular dichroism calibration procedure and the scientific work responsible for the cited empiric model development are described in [16].

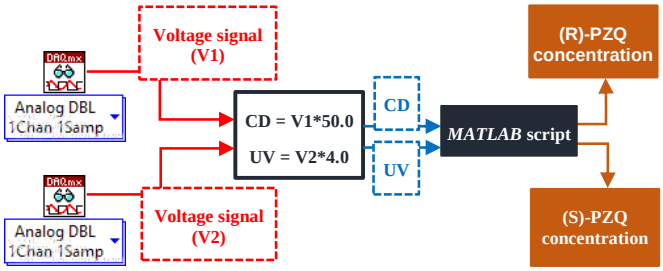

Fig. 9. UV-Vis and CD signals transformed into enantiomers concentration data.

III. Experiments and Results

A. Experiment 1: SMB process pressure variation over experiment time:

The first experiment evaluated if the supervisory system was capable of executing simultaneously all its programmed functions, adjusting all valves operational positions and retrieving the measured pressure data from the four pumps. It was analyzed the measured pressure variation according to each of the six E8 valves position shifts during two operational cycles. The SMB process was operated maintaining all E8 valves in each of the six positions during 10 seconds and the four flowrates with constant values equal to 1.0 g·min^{-1}.

The pressure variation measured by the Eluent, Recycle and Feed pumps reaches a maximum value every time the last position shift is executed as it can be seen in Fig. 10. Once that downstream of each one of these three pumps it is located a given E8 valve, during the last position shift the flowrate is maintained obstructed for a longer period of time, causing this high-pressure variation as it's shown in Fig. 10. The same operational behavior isn't observed for the Extract pump once that a relief valve is located downstream of the equipment.

The actuator takes normally 4.0 seconds to rotate completely, taking so 0.5 seconds to go from one position to the next in the case of the E8 valve. Once the Time Counter of each E8 valve only starts counting when the valve reaches a specific position, this mechanical behavior causes a growing time delay related to the position shifts execution at each operational cycle.

B. Experiment 2: Enantiomers concentrations of the Raffinate outlet stream:

The second experiment observed the CD and UV values variations in function of the process supervised operational behavior, following the evolution of each enantiomer concentration over time in the Raffinate stream. The process was operated as an open loop-system where the four flowrates values are independent of the measured enantiomers concentrations. In this experiment the Recycle pump flowrate has its value changed at the end of the fifth cycle and maintained constant until the end of the experiment as it can be seen in TABLE IV. All E8 and dead-end valves were kept in each position during 3.14 minutes.

TABLE IV
OPERATING FLOWRATE VALUES FOR THE FOUR PUMPS PRESENT IN THE SYSTEM (1.0 G·MIN^{-1}).

Cycles	Feed	Eluent	Extract	Recycle
First to fifth cycle	1.433	3.768	3.006	5.068
Sixth cycle forward	1.499	3.690	2.986	5.575

The oscillatory profile of the two concentrations values calculated from the UV and CD measurements happens in function of the cyclic position shifts. To better interpret the evolution of these oscillatory values, they were treated using a Moving Average Filter (MAF) as it's shown in Fig. 11.

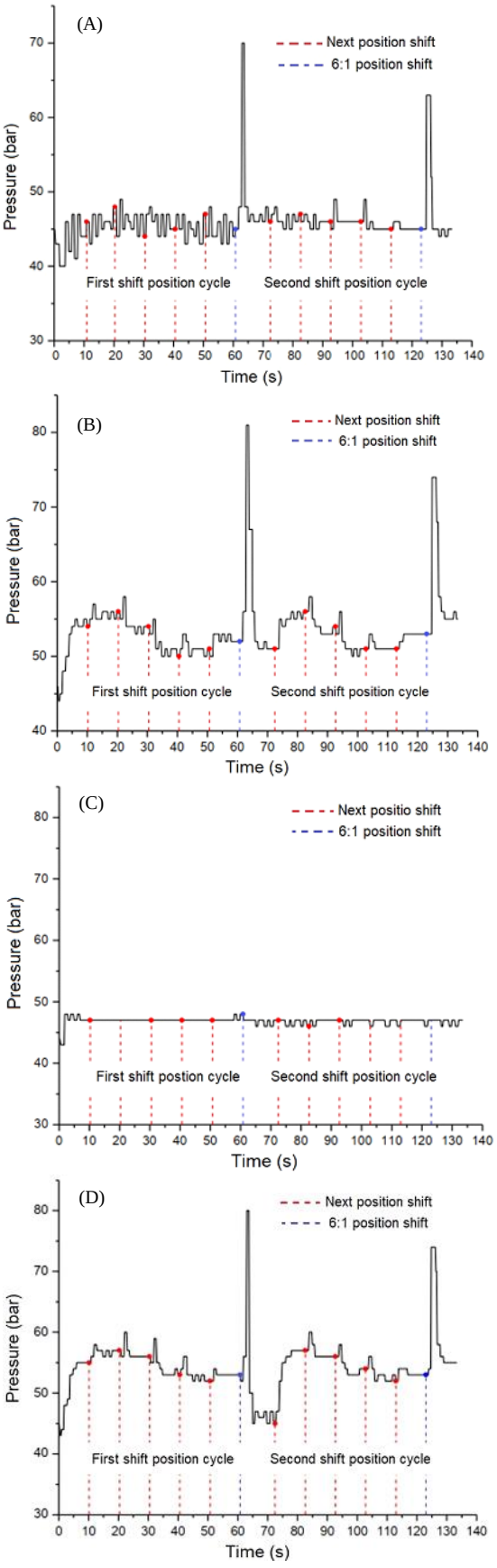

Fig. 10. Measured pression variation over time (A: Eluent pump; B: Feed pump; C: Recycle pump; D: Extract pump).

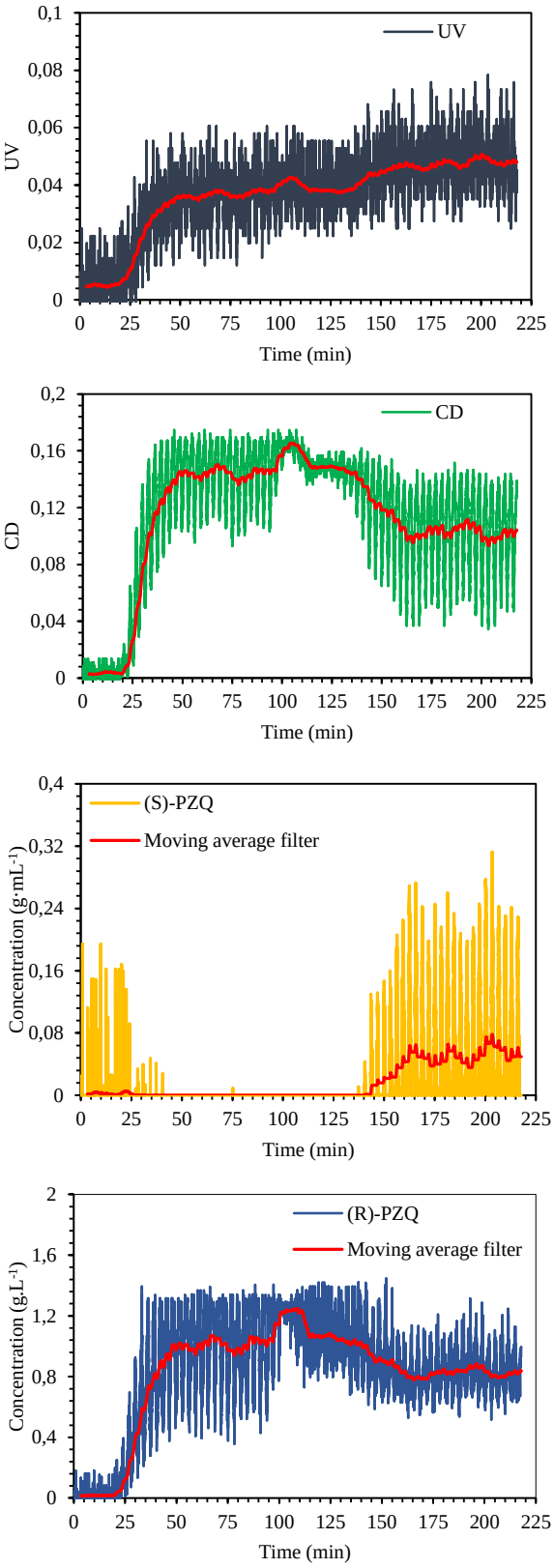

Fig. 11. Experimental results showing UV, CD, (R)-PZQ and (S)-PZQ values variation over process time

At the first 20 minutes of the experiment both concentrations are close to zero do not showing a variance on their values, indicating that the enantiomers aren't yet present in the Raffinate stream. Between 20 and 50 minutes the filtered data of (R)-PZQ concentration shows a constant growth reaching a maximum value of 1.0 $g \cdot L^{-1}$ with the (S)-PZQ concentration value still being close to zero, indicating at a first moment that the SMB is actuating as expected. This steady-state is maintained until the flowrate value change of all four pumps is made, that happening after 95 minutes or at the end of the fifth cycle. After this disturbance in the system both concentrations start having their values altered. Between 120 and 160 minutes the (R)-PZQ concentration start dropping slightly reaching a minimum value of 0.80 $g \cdot L^{-1}$ with the (S)-PZQ concentration having an augmentation of $g \cdot L^{-1}$ in its value. This steady-state is maintained until the end of the experiment.

IV. CONCLUSION

The supervisory system developed in LABVIEW for the operation a SMB unit was capable of keep a cyclic position shift behavior in all six E8 and dead-end valves, through a direct connection between the transmitted and acquired data from all valves microcontrollers, and operate remotely the four pumps, retrieving constantly the measured pressure data and adjusting its flowrate according to the operator needs.

Once that the SMB unit can also acquire data from the Circular Dichroism Chiral Detector and interpret it by means of an empiric mathematic model written in MATLAB code, it was possible to evaluate the system efficiency. The experimental data indicates that the supervisory system was capable of imposing in the process the behavior expected for a SMB chromatographic unit once that it was possible to retrieve in the Raffinate stream a solution with a significative difference between the (R) and (S)-PZQ concentrations. The system reached two different steady-states in function of a step given in the Recycle pump outlet stream. In the first steady-state the (R) and (S)-PZQ concentrations mean values were equal respectively to 1.0 $g \cdot L^{-1}$ and 0.0 $g \cdot L^{-1}$, and 0.80 $g \cdot L^{-1}$ and 0.05 $g \cdot L^{-1}$ for the second one.

REFERENCES

[1] D. Klein, Organic Chemistry as a Second Language, 3ª ed., Wiley, 2012.

[2] J. Clayden, N. Greeves e S. Warren, Organic Chemistry, 2ª ed., Nova Iorque: Oxford University Press, 2012.

[3] J. R. Coura e M. J. Conceição, "Specific schistosomiasis treatment as a strategy for disease control," *Memorias do Instituto Oswaldo Cruz*, vol. 105, nº 4, pp. 598-603, 2010.

[4] T. Meyer, H. Sekljic, S. Fuchs, H. Bothe, D. Schollmeyer e C. Miculka, "Taste, a new incentive to switch to (R)-praziquantel in schistosomiasis treatment," *PLoS Neglected Tropical Diseases*, vol. 3, nº 1, pp. 3-7, 2009.

[5] J. Blehaut e R. M. Nicoud, “Recent aspects in simulated moving bed,” *Analusis,* vol. 26, nº 7, 1998.

[6] A. E. Rodrigues, C. Pereira, M. Minceva, L. S. Pais, A. M. Ribeiro, A. Ribeiro e M. Silva, Simulated Moving Bed Technology: Principle Design and Process Applications, C. Owen, Ed., Elsevier Inc., 2015.

[7] Y. C. Chin e N.-H. L. Wang, “Simulated Moving Bed Equipment Designs,” *Separation & Purification Reviews,* pp. 77-155, Agosto 2007.

[8] J. P. S. Aniceto e C. M. Silva, “Simulated Moving Bed Strategies and Designs: From Established Systems to the Latest Developments,” *Separation & Purification Reviews,* pp. 41-73, 2015.

[9] R. P. Faria e A. E. Rodrigues, “Instrumental aspects of Simulated Moving Bed chromatography,” *Journal of Chromatography A,* vol. 1421, pp. 82-102, 2015.

[10] S. G. Pedro, “Advances in Simulated Moving Bed (Ph.D thesis),” 2009.

[11] G. Erdem, S. Abel, M. Morari, M. Mazzoti, M. Morbidelli e J. h. Lee, “Automatic Control of Simulated Moving Beds,” *Industrial & Engineering Chemistry Research,* vol. 43, pp. 405-421, Dezembro 2003.

[12] J. M. M. Araújo, R. C. R. Rodrigues, M. F. Eusébio e J. P. Mota, “On-line enantiomeric analysis using high-performance liquid chromatography in chiral separation by simulated moving bed,” *Journal of Chromatography A,* vol. 1189, pp. 292-301, 2008.

[13] Y. Xie, B. Hritzko, C. Y. Chin e N.-H. L. Wang, “Separation of FTC-Ester Enantiomers Using a Simulated Moving Bed,” *Industrial & Engineering Chemistry Research,* vol. 42, pp. 4055-4067 , Julho 2003.

[14] A. G. Barreto, I. J. da Silva, M. A. G. dos Santos, V. de Veredes e C. C. Sanatana, “Modeling, Simulation, and Experimental Evaluation of Continuous Chromatographic Separation of Ketamine Enantiomers on MCTA,” *Journal of Liquid Chromatography & Related Technologies,* vol. 31, pp. 3057-3076, 2008.

[15] F. C. Cunha, A. R. Secchi, M. B. de Souza e A. G. Barreto, “Separation of praziquantel enantiomers using simulated moving bed chromatographic unit with performance designed for semipreparative applications,” *Chirality,* vol. 31, nº 8, pp. 583-591, Maio 2019.

[16] F. C. Cunha, R. C. Holanda, A. R. Secchi, M. B. de Souza Jr e A. G. Barreto Jr, “Simultaneous absorption of UV–vis and circular dichroism to measure enantiomeric concentrations of praziquantel under nonlinear conditions,” *Spectrochimica Acta Part A: Molecular and Biomolecular Spectroscopy,* vol. 241, 2020.